

AN ABSTRACT OF THE THESIS OF

Logan Strid for the degree of Master of Science in Mechanical Engineering presented on September 25, 2013

Title: Passive Pumping in Pool and Open Channel Configurations via Meso-Scale Asymmetric Surface Patterning

Abstract approved:

Vinod Narayanan

The research presented in this thesis is a continuation of collaboration between Oregon State University and Auburn University studying the feasibility of passively pumping liquid during boiling in a preferential direction using meso-scaled asymmetric surface patterns. Such a passive phase-change mechanism has great potential for thermal management in spacecraft and in zero-gravity environments.

Fluid pumping is demonstrated in two configurations—one in which the patterned surface is immersed in a pool of liquid, and a second in which two patterned surfaces form the vertical walls of an open channel. The surface pattern consists of 60-30 degree millimeter scale ratchets. In the pool configuration, ratchets have a cavity on the 30 degree slope of the ratchets for preferential nucleation.

In the pool configuration, the asymmetric geometry causes bubbles to preferentially grow normal to the surface rather than in a vertical direction. A semi-empirical model predicting resultant liquid velocities is validated with particle tracking velocimetry. A single bubble was found to have an area of influence on the surrounding liquid equal to the average projected area of the bubbles during its growth cycle and was capable of imparting average fluid velocities of $75 \text{ mm}^1\text{s}^{-1}$ at an angle 32.7° from vertical.

In the open channel configuration, high-speed videos document the dramatic preferential motion of vapor slugs with velocities ranging from $13.4 \text{ mm}^1\text{s}^{-1}$ to $96.3 \text{ mm}^1\text{s}^{-1}$ under both diabatic and flash boiling conditions. Four regimes of channel flow are identified and bubble kinematics is presented. A thin liquid film is observed to exist in between the ratchet wall and the vapor slug. A model to determine slug velocities based on a balance of the net Young-Laplace pressure gradient in the thin liquid film and the viscous drag of the channel walls is put forth.

©Copyright by Logan Strid

September 25, 2013

All Rights Reserved

Passive Pumping in Pool and Open Channel Configurations via Meso-Scale Asymmetric
Surface Patterning

by

Logan Strid

A THESIS

submitted to

Oregon State University

in partial fulfillment of
the requirements for the
degree of

Master of Science

Presented September 25, 2013

Commencement June 2014

Master of Science thesis of Logan Strid presented on September 25, 2013

APPROVED:

Major Professor, representing Mechanical Engineering

Head of the School of Mechanical, Industrial, and Manufacturing Engineering

Dean of the Graduate School

I understand that my thesis will become part of the permanent collection of Oregon State University libraries. My signature below authorizes release of my thesis to any reader upon request.

Logan Strid, Author

ACKNOWLEDGEMENTS

I would first like to thank my advisor Dr. Vinod Narayanan for giving me the opportunity to work on such a challenging and stimulating project. Dr. Narayanan provided excellent guidance from start to finish. I appreciate the confidence he had in me to design and fabricate the many complex components and assemblies utilized during the project. He also provided immeasurable guidance throughout the project. I am continually awed by his vast knowledge of thermal-fluid sciences and the speed and efficiency with which he works.

I would also like to thank our collaborators—Dr. Sushil Bhavnani and Naveenan Thiagarajan at Auburn University. Our regular conference calls were essential to the success of this project. It was the experience of a lifetime to participate in the Reduced Gravity Program with them and it is something I will never forget.

The success of this project is also a result of the tremendous support of my past and present lab mates: Ruander Cardenas, Preeti Mani, Mohammad Ghazvini, Erfan Rasoulli, Shashank Natesh, Aaron Wilson, and Thomas L’Estrange. I must give a special thanks to Florian Kapsenberg for leaving me with an excellently organized account of his work; to Eric Truong for machining and fabricating countless components for me when I did not have the time or the skills; and to Bryan Kilgore for the years of classes and projects we worked together on.

I owe many thanks to Brian Jensen and Gary Borntreger of the MIME Machining and Product Realization Laboratory for the expertise on machining and rapid prototyping.

To my friends Marcus Collins, Allison Dethlefs, Jason Noland, and Erick Edtl for providing the much needed distractions from academia over the last six years, many thanks.

Finally, I must thank my family Dean, Deb, and Whitney Strid for their love and support. I would not be where I am today without you.

Financial assistance for the project was provided by NSF under grant number 0854503 and by NASA under grant number NNX09AJ98G.

TABLE OF CONTENTS

	<u>Page</u>
1. INTRODUCTION	1
2. LITERATURE REVIEW	3
2.1. Gravity Driven Pumpless Closed Loop	3
2.2. Inertial Micropump	5
2.3. Self-Propelled Leidenfrost Film Boiling Droplets	8
2.4. Lateral Motion Induced in Nucleate Pool Boiling	11
2.5. Conclusions on Literature Review	18
3. SCOPE AND OBJECTIVES.....	19
3.1. Adiabatic Single Bubble Study Objectives	19
3.2. Open-Channel Pump Study Objectives.....	20
PART I: ADIABATIC SINGLE-SINGLE BUBBLE	21
4. EXPERIMENTAL FACILITY.....	22
4.1. Test Section.....	22
4.2. Chamber	23
4.3. Test Facility	24
4.4. Flow Visualization and Illumination Components	26

TABLE OF CONTENTS (Continued)

	<u>Page</u>
5. EXPERIMENTAL PROCEDURES.....	28
5.1. Test Section Assembly	28
5.2. High-Speed Camera & Lighting.....	30
5.3. Filling the Chamber.....	31
5.4. Gas Injection	32
5.5. Flow Visualization	32
5.6. Shut-down.....	32
6. DATA ANALYSIS	33
6.1. Particle Tracking Velocimetry Algorithm	33
6.2. Bubble Growth Image Processing.....	33
6.2.1. Bubble Diameter and Center of Mass.....	34
6.2.2. Bubble Height Growth Rate.....	37
6.3. Calibration and Uncertainty.....	41
6.3.1. Particle Tracking Velocimetry Uncertainty	41
6.3.2. Image Processing and Model Uncertainty.....	43
7. RESULTS AND DISCUSSIONS.....	45
7.1. Semi-Empirical Model.....	45
7.2. Bubble Growth Force Model	48
7.3. Particle Tracking Velocimetry	59
7.4. Model Validation	93

TABLE OF CONTENTS (Continued)

	<u>Page</u>
PART II: Open-Channel Pump	97
8. EXPERIMENTAL FACILITY.....	98
8.1. Test Section Assembly	98
8.2. Test Chamber.....	104
8.3. Test Facility	107
8.4. High Speed Imaging & Lighting.....	110
8.5. Data Acquisition (DAQ).....	111
9. EXPERIMENTAL PROCEDURES.....	113
9.1. Start-up.....	113
9.1.1. Spacing the Test Section Assembly.....	113
9.1.2. Securing the Chamber	114
9.1.3. Filling the Chamber.....	114
9.1.4. High-Speed Camera and Lighting.....	115
9.2. Flash Boiling	117
9.3. Diabatic Boiling	117
9.4. Sub-Atmospheric Diabatic Boiling	118
9.5. Capturing Videos.....	118
9.6. Shut-down.....	118
9.6.1. High-Speed Camera and Lighting.....	118
9.6.2. Draining the Chamber.....	119

TABLE OF CONTENTS (Continued)

	<u>Page</u>
10. DATA ANALYSIS	120
10.1. Bubble Slug Tracking	120
10.1.1. Center of Mass Tracking	120
10.1.2. Leading Edge Tracking	121
10.1.3. Slug Velocity and Acceleration	123
10.2. Calibration and Uncertainty	124
10.2.1. Pressure Transducer Calibration and Uncertainty	124
10.2.2. K-type Thermocouple Uncertainty	126
10.2.3. Subcooling Uncertainty	127
10.2.4. Pixel Resolution Calibration and Uncertainty	128
10.2.5. Velocity Uncertainty	129
10.2.6. Heat Flux Uncertainty	130
11. RESULTS AND DISCUSSIONS	131
11.1. Qualitative Visualization	131
11.1.1. Churn Flow Regime	133
11.1.2. Intermittent Slug Flow Regime	139
11.1.3. Walking Bubble Regime	156
11.1.4. Homogeneous-Slug Flow Regime	175
11.2. Bubble-Slug Kinematics	180
11.2.1. Churn Flow	180
11.2.2. Intermittent Slug Flow	183
11.2.3. Walking Bubble Regime	190
11.2.4. Homogeneous Slug Flow	197
11.3. Slug Transport Mechanism	200

TABLE OF CONTENTS (Continued)

	<u>Page</u>
12. CONCLUSIONS.....	213
12.1. Adiabatic Single-Bubble	213
12.2. Open Channel Pump	214
13. Recommendations for Future Investigation	215
13.1. Adiabatic Single-Bubble	215
13.2. Open Channel Pump	215
REFERENCES.....	217
APPENDICES.....	219
Appendix A. Preparing Cospheric Microspheres.....	220
Appendix B. Bubble Tracking Algorithm	221
Appendix C. Inconel Heater Resistance	222
Appendix D. FC-72 Properties	223

LIST OF FIGURES

<u>Figure</u>	<u>Page</u>
Figure 2.1: Schematic for a gravity driven pumpless closed loop experiment.....	3
Figure 2.2: 1-D schematic of an inertial micropump.	5
Figure 2.3: A general boiling curve showing the major regimes and key transition points.	8
Figure 2.4: Schematic of a Leidenfrost droplet and asymmetric surface geometry.	9
Figure 2.5: Schematic of the structured surface with reentrant cavities.....	12
Figure 2.6: Bubble velocity field at high subcooling	13
Figure 4.1: Structured brass surface.....	23
Figure 4.2: Solid model and assembled test section.	23
Figure 4.3: Adiabatic-Single Bubble test chamber assembly.....	24
Figure 4.4: Overview of the experimental facility	25
Figure 4.5: Cole Parmer rotameter.....	26
Figure 4.6: Custom 625 LED array used for illumination of chamber.....	27
Figure 5.1: Proper alignment of the test section and chamber on the stage.....	29
Figure 5.2: Installing the chamber assembly.	29
Figure 5.3: Composite image of two frames 0.25 seconds elapsed showing stagnant seed particles.	31
Figure 6.1: Raw image of the Edmunds optical grid.....	42
Figure 7.1: Representative drawing of surface geometry showing bubble dimensions used in the semi-empirical model.....	45
Figure 7.2: Representation of the control volume used for the momentum balance.	47

LIST OF FIGURES (Continued)

<u>Figure</u>	<u>Page</u>
Figure 7.3: Bubble diameter and height plotted for the growth cycle of Bubble 1 of 14.	48
Figure 7.4: Bubble diameter and height plotted for the growth cycle of Bubble 2 of 14.	49
Figure 7.5: Bubble diameter and height plotted for the growth cycle of Bubble 3 of 14.	49
Figure 7.6: Bubble diameter and height plotted for the growth cycle of Bubble 4 of 14.	50
Figure 7.7: Bubble diameter and height plotted for the growth cycle of Bubble 5 of 14.	50
Figure 7.8: Bubble diameter and height plotted for the growth cycle of Bubble 6 of 14.	51
Figure 7.9: Bubble diameter and height plotted for the growth cycle of Bubble 7 of 14.	51
Figure 7.10: Bubble diameter and height plotted for the growth cycle of Bubble 8 of 14.	52
Figure 7.11: Bubble diameter and height plotted for the growth cycle of Bubble 9 of 14.	52
Figure 7.12: Bubble diameter and height plotted for the growth cycle of Bubble 10 of 14. ...	53
Figure 7.13: Bubble diameter and height plotted for the growth cycle of Bubble 11 of 14. ...	53
Figure 7.14: Bubble diameter and height plotted for the growth cycle of Bubble 12 of 14. ...	54
Figure 7.15: Bubble diameter and height plotted for the growth cycle of Bubble 13 of 14. ...	54
Figure 7.16: Bubble diameter and height plotted for the growth cycle of Bubble 14 of 14. ...	55
Figure 7.17: Series of 48 frames of the adiabatic single bubble growing and departing the structured surface.	60
Figure 7.18: Series of 8 frames of particle tracking results during the growth of a bubble on the surface.	68
Figure 7.19: Series of 48 frames of a single bubble growing and departing the structured surface with particle tracking results overlaid.	74

LIST OF FIGURES (Continued)

<u>Figure</u>	<u>Page</u>
Figure 7.20: Time series of magnitude of average seed particle velocity calculated by PTV for 0.4 seconds of the adiabatic single-bubble high-speed video with a 1-Dia ROI.....	89
Figure 7.21: Time series of magnitude of average seed particle velocity calculated by PTV for 0.4 seconds of the adiabatic single-bubble high-speed video with a 2-Dia ROI.....	90
Figure 7.22: Time series of magnitude of average seed particle velocity calculated by PTV for 0.4 seconds of the adiabatic single-bubble high-speed video with a 3-Dia ROI.....	91
Figure 7.23: Average fluid velocity plotted as a function of region of interest width.....	92
Figure 7.24: Comparison of particle tracking velocimetry results and model results.....	94
Figure 7.25: Percent deviation of the model predictions from the particle tracking velocimetry.	95
Figure 8.1: The test section assembly.....	99
Figure 8.2: Solid model of the test section assembly exploded to show individual layers. ...	100
Figure 8.3: Structured surface machined from brass shown with dimensions.	101
Figure 8.4: Inconel 600 heater.....	102
Figure 8.5: Wiring diagram for the heaters in the test section.	103
Figure 8.6: The construction of the test chamber without any components installed.	105
Figure 8.7: Top view of the test chamber designating the uses and location of ports in the top plate.	106
Figure 8.8: Stage and toe clamps used to elevate and secure the test chamber.....	107
Figure 8.9: Experimental facility for the open-channel pump experiment.....	108
Figure 8.10: Auxiliary components required to run the channel pump experiment.	109

LIST OF FIGURES (Continued)

<u>Figure</u>	<u>Page</u>
Figure 8.11: Thor Labs right angle prism as configured during testing.	111
Figure 9.1: Channel width dimension definition.	114
Figure 9.2: Field of view for the two different microscope objectives.....	116
Figure 10.1: Example images from the image processing performed to track the center of mass of a bubble slug.	121
Figure 10.2: Example images from the image processing performed to track the leading edge of a bubble slug.....	122
Figure 10.3: Plot of velocity with varying n for an example slug	123
Figure 10.4: Calibration curve for the Omega PX302 pressure transducer.....	126
Figure 10.5: Calibration curve for the Omega K-type thermocouple.....	127
Figure 10.6: Example images used to determine pixel resolution for the high-speed videos.	128
Figure 11.1: Plot of testing conditions of the channel pump.	132
Figure 11.2: Sequence of 20 frames exhibiting churn flow.	134
Figure 11.3: Sequence of 21 frames exhibiting intermittent slug flow.	140
Figure 11.4: Sequence of 20 frames exhibiting intermittent slug flow.	147
Figure 11.5: Sequence of 13 frames exhibiting intermittent slug flow.	152
Figure 11.6: Sequence of 20 frames exhibiting walking bubble flow.....	157
Figure 11.7: Sequence of 20 frames exhibiting walking bubble flow.....	163
Figure 11.8: Sequence of 20 frames exhibiting walking bubble flow.....	169

LIST OF FIGURES (Continued)

<u>Figure</u>	<u>Page</u>
Figure 11.9: Sequence of 13 frames exhibiting homogenous-slug flow.....	176
Figure 11.10: Position data of six slugs in the churn flow regime.	181
Figure 11.11: Velocity results of six slugs in the churn flow regime.	182
Figure 11.12: Position data of six slugs in the intermittent slug flow regime.	184
Figure 11.13: Velocity results of six slugs in the intermittent slug flow regime.....	185
Figure 11.14: Position data of six slugs in the intermittent slug flow regime.	186
Figure 11.15: Velocity results of six slugs in the intermittent slug flow regime.....	187
Figure 11.16: Position data of seven slugs in the intermittent slug flow regime.	188
Figure 11.17: Velocity results of seven slugs in the intermittent slug flow regime.	189
Figure 11.18: Position data of six bubbles in the walking bubble flow regime.	191
Figure 11.19: Velocity results of six bubbles in the walking bubble flow regime.	192
Figure 11.20: Position data of four bubbles in the walking bubble flow regime.	193
Figure 11.21: Velocity results of four bubbles in the walking flow regime.	194
Figure 11.22: Position data of four bubbles in the walking bubble flow regime.	195
Figure 11.23: Velocity results of four bubbles in the walking flow regime.	196
Figure 11.24: Position data of five slugs in the homogeneous slug flow regime.	198
Figure 11.25: Velocity results of five slugs in the homogeneous slug flow regime.....	199
Figure 11.26: Example images of showing the determination of the liquid layer thickness..	201

LIST OF FIGURES (Continued)

<u>Figure</u>	<u>Page</u>
Figure 11.27: Schematic showing ratchet topography and the interface of the bubble.	201
Figure 11.28: Radius measurements of the slug interface for a sequence of 42 consecutive frames.....	202
Figure 11.29: Liquid layer thickness between the slug and ratchet calculated for a sequence of 42 consecutive frames.....	203
Figure 11.30: Simplified shape of the bubble interface and ratchet profile. Dimensions are shown for clarity.	204
Figure 11.31: Image used to determine the width of slug interacting with the ratchet surface.	208
Figure 11.32: Schematic of a slug in the channel.	208
Figure 11.33: Plot of predicted velocity values for a range of top shear layer, hT	211
Figure 11.34: Plot of predicted slug velocity as a function of varying liquid layer thickness between the slug and ratchet.....	212
Figure D.1: Plot of FC-72 saturation temperature with respect to pressure.....	224

LIST OF TABLES

<u>Table</u>	<u>Page</u>
Table 4.1: Properties of the K2/SC microscope lens fitted with a CF-3 objective as given by the manufacturer.....	26
Table 5.1: Phantom Camera Control settings.....	30
Table 6.1: A series of images showing each image processing step of a single frame (-7714) to extract bubble diameter and center of mass.	35
Table 6.2: A series of images showing each image processing step of a single frame (-7714) to extract bubble height.	38
Table 6.3: Perturbations of the image processing for diameter of a bubble.	43
Table 6.4: Perturbations of the image processing for height of a bubble.....	44
Table 7.1: Velocity predictions made by the semi-empirical model with an area of influence of 1 average bubble diameter (n=1).....	56
Table 7.2: Velocity predictions made by the semi-empirical model with an area of influence of 1 average bubble diameter (n=2).....	57
Table 7.3: Velocity predictions made by the semi-empirical model with an area of influence of 1 average bubble diameter (n=3).....	58
Table 7.4: Average fluid velocity values over 800 frames (0.4 s) in the three varying region of interest widths.....	92
Table 7.5: Values of velocities with uncertainty errors shown for the comparison between PTV and model results.....	94
Table 7.6: Values of percent deviation of the model predictions from the particle tracking velocimetry for all three areas of interest.....	95
Table 8.1: List of components used for data acquisition.....	112
Table 9.1: Phantom Camera Control settings.....	116

Table 10.1: Summary of uncertainty analysis of the Omega PX302 pressure transducer.	125
Table 10.2: Summary of uncertainty analysis of the Omega K-Type thermocouple.....	126
Table 10.3: Summary of pixel resolution.....	129
Table 10.4: Summary of uncertainty in velocity.....	130
Table 11.1: Summary of conditions for each data set with uncertainties shown.....	131
Table 11.2: Variables used in predicting slug velocity.....	210
Table C.1: Change in resistance due to a 1 μm (2.54×10^{-5} in.) change in each heater dimension.....	222
Table D.2: Selected saturated data for FC-72.....	223

NOMENCLATURE

Part I	Part II
<i>A</i> area [m^2]	<i>A</i> area [m^2]
C_D coefficient of drag	<i>a</i> acceleration [$m \cdot s^{-2}$]
<i>d</i> bubble diameter [m]	<i>D</i> slug diameter [m]
<i>F</i> force [N]	<i>F</i> force [N]
f_d bubble departure frequency [s^{-1}]	<i>h</i> shear layer thickness [m]
<i>h</i> bubble height [m]	<i>L</i> length [m]
<i>P</i> momentum [$kg \cdot m \cdot s^{-1}$]	<i>n</i> integer
q'' heat flux [$W \cdot m^{-2}$]	<i>P</i> pressure [bar]
ΔT_{sub} pool subcooling [$^{\circ}C$]	q'' heat flux [$W \cdot m^{-2}$]
<i>u</i> uncertainty	<i>r</i> slug interface curvature [m]
<i>t</i> time [s]	<i>t</i> time [s]
\dot{V} volumetric flow rate [$L \cdot min^{-1}$]	ΔT_{sub} pool subcooling [$^{\circ}C$]
<i>v</i> velocity [$m \cdot s^{-1}$]	<i>u</i> uncertainty
 	<i>v</i> velocity [$m \cdot s^{-1}$]
Greek Symbols	<i>W</i> bubble width [m]
α ratchet angle [$^{\circ}$]	<i>w</i> channel width [m]
Δ difference	<i>x</i> position [m]
θ liquid velocity angle [$^{\circ}$]	Greek Symbols
ρ density [$kg \cdot m^{-3}$]	α ratchet angle [$^{\circ}$]
 	Δ difference
Subscripts	μ Dynamic viscosity [$P \cdot s$]
<i>inf</i> influence	ρ density [$kg \cdot m^{-3}$]
<i>l</i> liquid	σ surface tension [$N \cdot m^{-1}$]
<i>ts</i> test section	τ shear stress [$N \cdot m^{-2}$]
<i>v</i> vapor	Subscripts
 	<i>l</i> liquid
 	<i>p</i> projected
 	<i>s</i> shear
 	<i>v</i> vapor

PASSIVE PUMPING IN POOL AND OPEN CHANNEL
CONFIGURATIONS VIA MESO-SCALE ASYMMETRIC SURFACE
PATTERNING

1. INTRODUCTION

Continual advancements in electronics have rendered computerized devices ubiquitous in today's society. However, with the increase in capability in size and decrease in size, the heat production of these devices has also surged dramatically. In order to meet the new requirements for heat dissipation, innovative cooling solutions must be utilized. Current solutions include forced convection, heat sinks, microchannel heat exchangers, single-phase liquid cooling (such as immersion or jet impingement), heat pipes, and thermal ground planes.

Heat pipes and thermal ground planes work on essentially the same principle. A working fluid within the pipe or ground plane is vaporized by a hot region from which heat must be dissipated. The vapor is transported away, condensed, and the liquid phase is transported back to the hot region. These systems are closed loop and take advantage of two-phase heat transfer. Two phase heat transfer has the advantage over single-phase heat transfer in that the energy required to convert a liquid to a vapor is substantially higher than the energy required to raise the same working fluid by several degrees. Furthermore, phase change is an isothermal process—allowing these systems to be tailored to maintain a desired temperature at a given hot spot. Limitations on heat pipes and thermal ground planes include their physical size and their ability to return vapor to the hot spot as a liquid. After vapor is condensed, it is commonly returned to the hot region using capillary action. Capillary flows are often characterized by low volumetric flow rates as large pressure drops are typical in such flows.

Work completed by Kapsenberg and Thiagarajan [7][8][9] has shown an innovative means of passively inducing lateral of bubbles during pool boiling from heated asymmetric structured surfaces. The bubbles have been shown to impart momentum causing liquid lateral motion in a preferential direction and a model was proposed. Although it was only a proof-of-concept study, this means of passive pumping shows promise for improving mass transport in two-phase thermal management.

Part I of this thesis intends to build upon the work of Kapsenberg and Thiagarajan [7][8]; first, by continuing the study of bubbles from asymmetric surfaces in a pool environment. Using a similar ratchet surface geometry, isolation of a single bubble emanating from the surface is done to determine a single bubble's influence on the surround liquid. Furthermore, improvements to the existing model are done to improve predictions of liquid velocity.

Part II of this thesis focuses on applying the phenomena of two-phase fluid motion into a channel configuration. The hypothesis is that by integrating ratchet structures into the walls of a channel a net fluid velocity can be achieved through the channel in a preferred direction. This is test tested with the use of high-speed visualization of the channel and image analysis of the flow within. Finally a model is proposed which describes the mechanisms which cause fluid motion in the channel.

2. LITERATURE REVIEW

The research presented in this thesis relates directly to the passive transport of fluid present in two phases. As the results of this thesis will show, there is potential in applying passive transport of two-phase fluids in pumpless thermal management. This literature review covers the existing technologies of pumpless transport of fluid in the presence of two-phases.

2.1. Gravity Driven Pumpless Closed Loop

Simulated electronics cooling using closed loop two-phase heat transfer has been a topic of study for at least the last two decades. The simplest of configurations is a vertically oriented (two vertical legs and two horizontal legs) closed loop containing a boiler, condenser and reservoir. The boiler is positioned on one of the vertical legs (rising tube) and the condenser is located either before or in the reservoir. A generic schematic adapted from [1][2] of the closed loop is shown in Fig. 2.1.

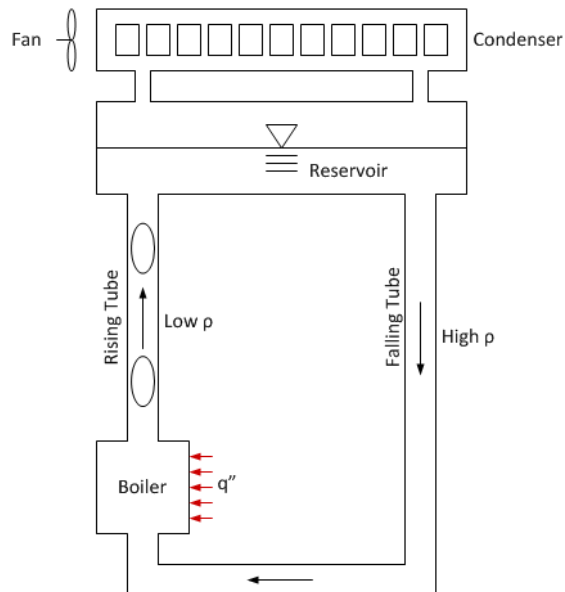


Figure 2.1: Schematic for a gravity driven pumpless closed loop experiment.

The boiler is a small chamber containing a simulated electronic device which generally takes the form of a heated copper block with optional forms of geometrical enhancements including mini- or micro-channels, fins, and boiling cavities. As heat is applied to the boiling surface, boiling occurs and bubbles exit the boiler. The presence of bubbles in the rising tube leaving the boiler reduces the density in the tube; thus, creating a hydrostatic pressure difference between the rising tube and the cold return leg on the opposite side of the loop. The pressure difference sets up a flow through the loop bringing cool liquid into the boiler to replenish the two phase mixture that exited.

Mukherjee and Mudawar [1] tested such a closed loop using FC-72 and water as the working fluid and a simulated electronic device with no surface enhancements, mini-channel surface, and micro-channel surface enhancements. Only results from FC-72 are presented as they predicted that the boiling channels would become blocked due to the large bubble diameters with water.

One advantage of using a pumpless loop system was found in a comparison of critical heat flux between pool boiling and the pumpless closed loop. The critical heat flux for FC-72 was increased by a factor of 4.5, 5.9, and 5.7 for the flat, mini-, and micro-channel surfaces, respectively. These results were also found with a very small boiling gap (distance between the surface and opposing wall) indicating that a very small amount of fluid is required in the boiler. The increase in CHF was attributed to the clearing of vapor from the hot surface which was driven by the pressure difference between the rising and falling tubes.

A model was developed for the flow of liquid in the closed loop and results for the three surfaces were presented for different input heat fluxes ranging from 10-60 W^1cm^{-2} . In general small boiling gaps produced the highest exit velocities from the boiler; however, mass flow becomes restricted with the small cross-sectional area available. Velocities ranged from as low as $\sim 2.5 m^1s^{-1}$ to as high as $\sim 20 m^1s^{-1}$.

Kuo et al. [2] performed a similar experiment and reported results from tests rather than model predictions. Furthermore, their boiling surfaces featured either boiling cavities in two different configurations (grid and offset grid) or a combination of fins with boiling cavities.

The key result of the study is the driving pressure created by the bubbles in the boiler. All three surfaces produced similar results in the range of 20 to $80 \text{ W}^1\text{cm}^{-2}$ of input heat. It was found that driving pressure increases nearly linearly with increasing heat flux ranging from $\sim 300 \text{ Pa}$ at the lowest heat flux to $\sim 1000 \text{ Pa}$ at the highest.

2.2. Inertial Micropump

Based on technology similar to that found in ink-jet printer heads, micropumps with no moving parts have been developed. One such example is that studied by Tornaiainen et al [3]. This micropump works by using the massive burst of pressure associated with bubble growth at a superheated surface within a small channel. Bubbles are initiated with an actuator (resistor) located asymmetrically within a channel. Figure 2.2 shows a 1-D schematic of the micropump.

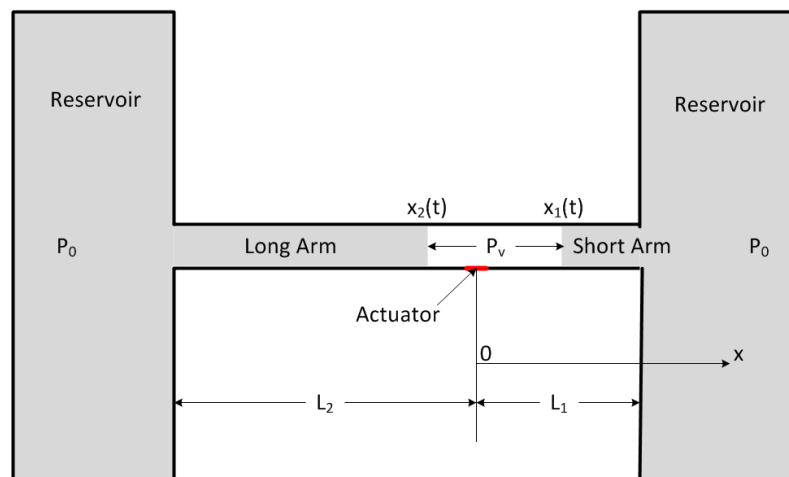


Figure 2.2: 1-D schematic of an inertial micropump.

When the actuator (heater) is activated, the vapor bubble which forms has a higher pressure than the surrounding liquid ($P_v > P_0$) and causes flow out of both the long and short arms. This is referred to as the expansion phase. As the size of the bubble increases and the actuator is deactivated, the pressure in the bubble slows and eventually drops below P_0 causing the bubble to collapse. This is referred to as the collapse phase. Once the bubble has fully collapsed, the long and short arms of liquid collide at a location x_c which is generally not equal to the location of the bubble's inception. This is referred to as the post-collapse phase.

The net flow of fluid through the channel occurs from the short arm towards the long arm after each cycle of the expansion, collapse and post collapse phase. It is important to note that the actuator must be placed either left or right of center in the channel and a centered actuator would produce a net flow of zero due to symmetry between the long and short arms.

Expressions for momentum of the short and long arms are shown in Eqs. 2.1 and 2.2, respectively, where momentum is designated by Q .

$$Q_1(t) = \rho A(L_1 - x_1)\dot{x}_1 \quad (\text{Eq. 2.1})$$

$$Q_2(t) = \rho A(L_2 - x_2)\dot{x}_2 \quad (\text{Eq. 2.2})$$

In the expansion phase, some mass from the short arm is lost to the right reservoir and must be accounted for.

$$Q_1(t + dt) = Q_1(t) - \rho A\dot{x}_1^2 dt + F_1 dt \quad (\text{Eq. 2.3})$$

An expression for force can be obtained by substituting in Eq. 2.1 into 2.3.

$$F_1(t) = \rho A(L_1 - x_1)\ddot{x}_1 \quad (\text{Eq. 2.4})$$

This expression is applicable for both the expansion and collapse phases as F_1 will simply have a different sign. A similar analysis can be done for the long arm and results in:

$$F_2(t) = \rho A(L_2 + x_2)\ddot{x}_2 \quad (\text{Eq. 2.5})$$

A similar analysis showing the same result was performed by Yin and Prosperetti [4]. The forces shown in Eqns. 2.4 and 2.5 were then applied in a model which accounts for the

driving force of the bubble pressure, viscous forces, and surface tension forces. It takes the form of

$$\rho A(L_1 - x_1)\ddot{x}_1 + \kappa(L_1 - x_1)\dot{x}_1 = (p_v - p_0)A - \frac{4\sigma A}{D_h} \quad (\text{Eq. 2.6})$$

$$\rho A(L_2 + x_2)\ddot{x}_2 + \kappa(L_2 + x_2)\dot{x}_2 = (p_0 - p_v)A + \frac{4\sigma A}{D_h} \quad (\text{Eq. 2.7})$$

where κ is viscosity and σ is surface tension.

After the collapse of the bubble the pressure and surface tensions drop out due to the absence of the bubble. Thus; during the post-collapse phase the equation becomes:

$$\rho A(L_1 + L_2)\ddot{x}_2 + \kappa(L_1 + L_2)\dot{x}_2 = 0 \quad (\text{Eq. 2.8})$$

as the short arm and long arm are not a continuous arm in the channel and are analyzed such that momentum is conserved in the collision between the two columns.

Torniainen et al. [3] performed full 3-D CFD simulations of this configuration micropump and fabricated a physical array micropumps using thermal inkjet technology. CFD and experimental results agree for a range of input energy pulses to the actuator in a channel measuring 25 μm by 17 μm . Maximum flow rate of a water-glycerol mix through the micropump were found to be approximately 2 pL per pulse at a pulse rate of 10 Hz; however, a maximum flow rate of 8 pL per pulse was estimated by varying viscosity and channel dimensions.

2.3. Self-Propelled Leidenfrost Film Boiling Droplets

A typical boiling curve is shown in Fig. 2.3 as adapted from Incropera and Dewitt [5]. Film boiling exists when the excess temperature (T_e) is greater than that at the Leidenfrost point. In film boiling, the liquid is suspended from the boiling surface by vapor and heat is transferred by radiation from the surface to the liquid.

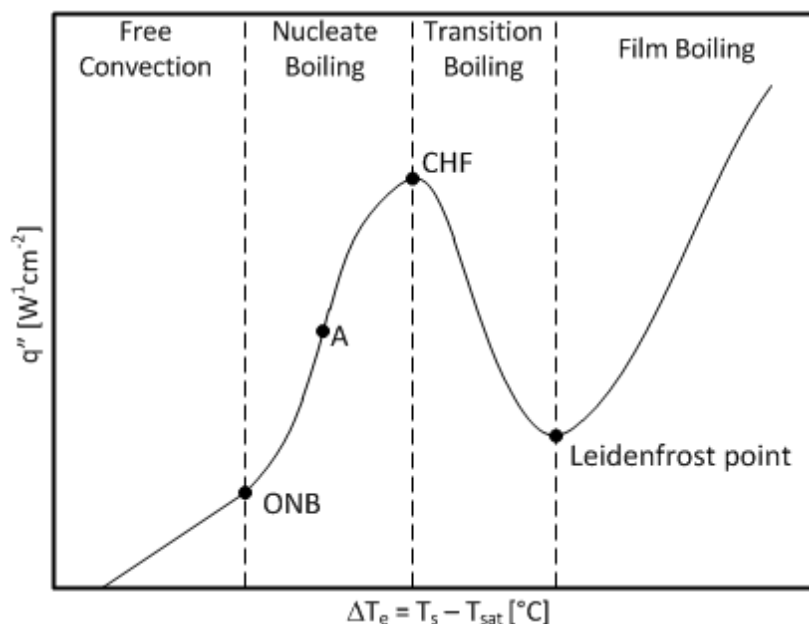


Figure 2.3: A general boiling curve showing the major regimes and key transition points.

One can observe film boiling at home with droplets of water in a hot pan. The droplets will dance erratically across the pan, driven by temperature gradients and surface condition until they evaporate completely. Linke et al. [6] showed that small droplets can be preferentially moved in this film boiling.

A droplet of liquid was placed on an asymmetric surface with ratchet-like topography. This surface temperature was controlled such that the excess temperature (T_e) was above the Leidenfrost point for the given fluid. The droplet was then observed to accelerate in the positive x direction (Fig. 2.4) until it reached a terminal velocity. A maximum terminal velocity of $5 \text{ cm}^1\text{s}^{-1}$ was observed.

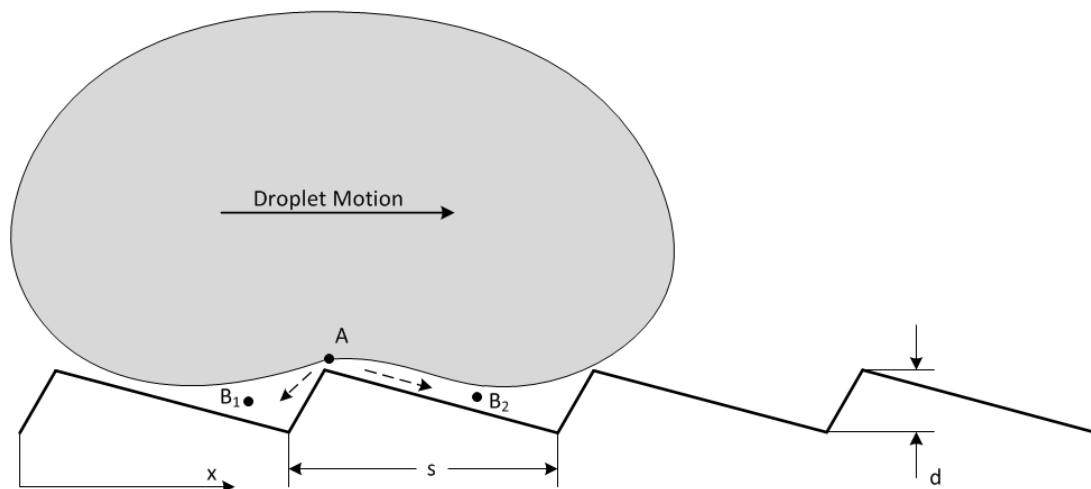


Figure 2.4: Schematic of a Leidenfrost droplet and asymmetric surface geometry.

The asymmetric surfaces tested featured pitches, s , ranging from 1 mm to 3 mm and ratchet heights, d , from 0.1 mm to 0.3 mm. A range of liquids were tested with boiling points ranging from $-196\text{ }^{\circ}\text{C}$ to $151\text{ }^{\circ}\text{C}$. These included nitrogen, acetone, methanol, ethanol, water, and hexadecane. For acceleration of a droplet to occur, it was found that it must span several ratchets as droplets sized smaller than the pitch of the ratchet did not display any motion. However, large droplets spanning many tended to break up into individual droplets as they traveled along the surface. The acceleration of the droplets was found to loosely depend on the inclination of the surface; that is, gravity only ensures that the droplet maintains contact with the surface.

A model was proposed to explain the motion of the droplets. The droplet has a distinctive shape where it is concave at the peak of a ratchet (A) and convex on either side (B_1 and B_2). This shape was used to estimate the local pressure in these regions using the Young-Laplace equation:

$$\Delta p = \frac{2\sigma}{r} \quad (\text{Eq. 2.9})$$

where r is the local radius of curvature of the droplet.

Due to the shape of the droplet over the ratchet, it can be inferred that in the vapor region, $p_A > p_B$; thus, the vapor tend to flow from A to B₁ and B₂. The flow of vapor from A to B₂ imparts a viscous drag on the droplet in the forward direction and it was assumed that the flow from A to B₁ is negligibly small as it escapes in the transverse direction.

Thus, there are two forces acting on the droplet: the shear force driving its motion and viscous drag opposing it. These forces take the form show in Eqs. 2.10 and 2.11, respectively.

$$F_1 = 0.5A_{eff}h \left| \frac{dp}{dx} \right| \cos \alpha \quad (\text{Eq. 2.10})$$

$$F_2 = - \left(\frac{\mu A_{eff}}{h} \right) v_x \quad (\text{Eq. 2.11})$$

where A_{eff} is the effective area of the droplet spanning the ratchet, h is the thickness of the vapor layer between the droplet and ratchet, α is the angle of the long ratchet face, μ is the viscosity, and v_x is the droplet velocity.

By determining radii and vapor layer thickness from high-speed video data, droplet acceleration was predicted with the above model that agrees with the experimental results within the uncertainty of the calculations.

2.4. Lateral Motion Induced in Nucleate Pool Boiling

The nucleate pool boiling regime is divided into two distinct sub-regimes: isolated bubbles and jets or columns [5]. These sub-regimes are shown in Fig. 2.3 where the isolated bubble regime is present when the excess temperature (T_e) is between points ONB (onset of nucleate boiling) and A; conversely, jets and columns are present when the excess temperature is between A and CHF (critical heat flux). It is in the nucleate boiling regime that the work of Kapsenberg et al. [7][8][10] has shown the ability of a bubble to impart lateral motion in surrounding liquid.

The experiment consisted of an asymmetric structured surface heated from below with a thin film aluminum heater and was located in a large pool filled with the water as the working fluid. The structured surface took the form of a periodic saw-tooth (or ratchet) with a shallow face angled 24° from horizontal (Fig. 2.5). It was fabricated out of silicon in several steps. The saw-tooth surface was created using grayscale lithography and deep reactive ion etching (DRIE). Furthermore, reentrant cavities were incorporated onto the faces of the ratchets using anisotropic etching [9]. Reentrant cavities have a distinct advantage over conventional cavities in that they can generally produce bubbles sustainably because substantial subcooling is required to deactivate such a site [11].

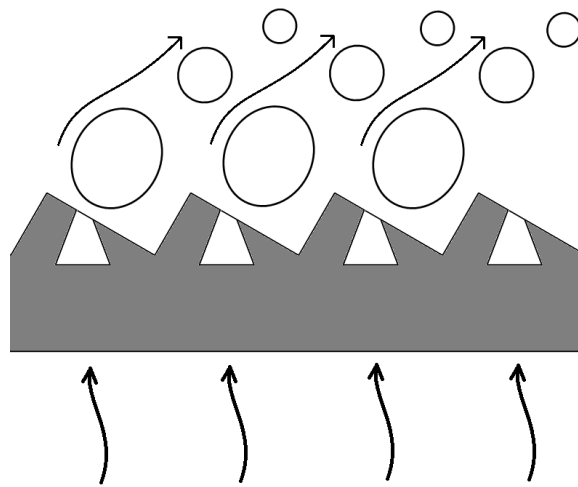


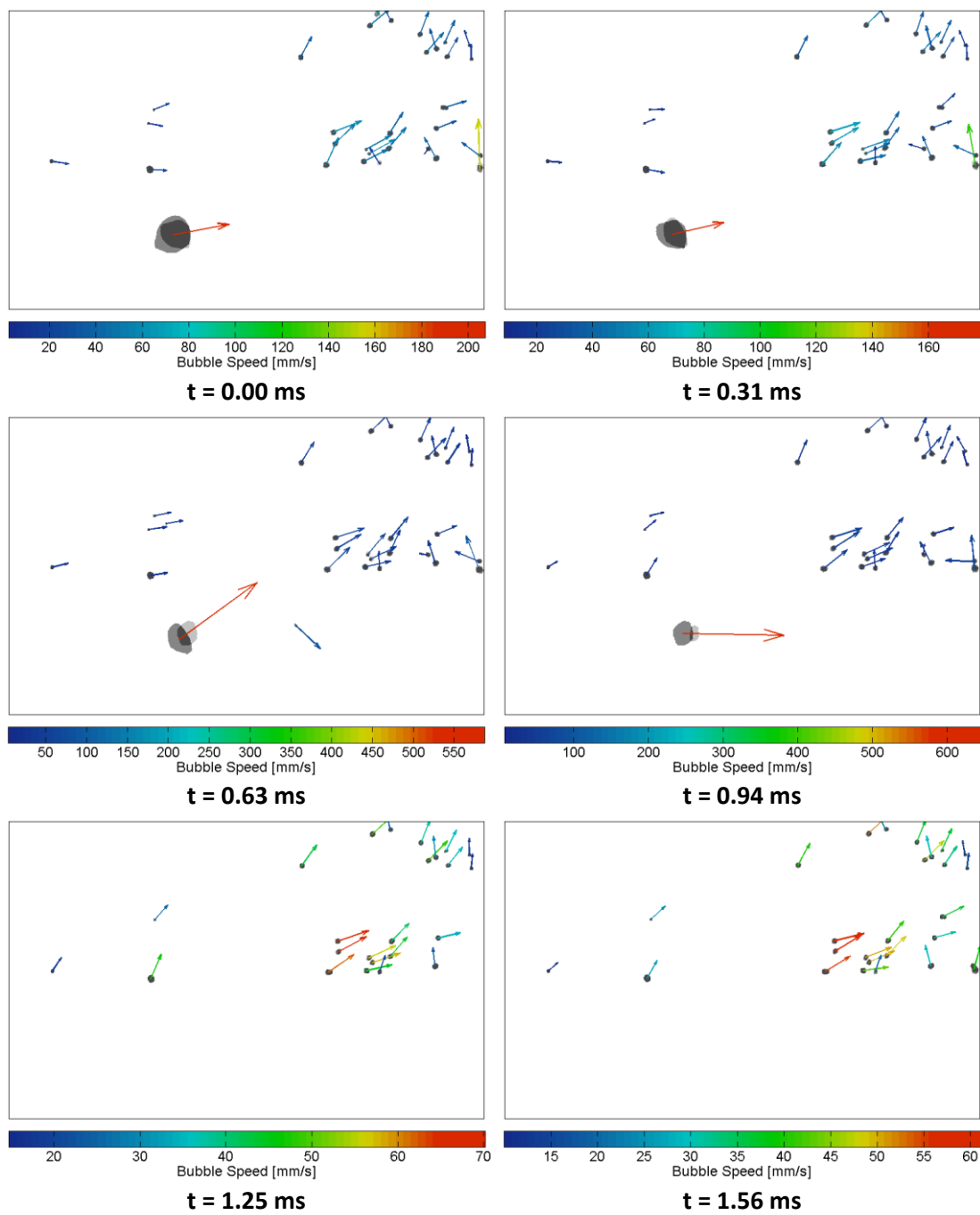
Figure 2.5: Schematic of the structured surface with reentrant cavities. Picture courtesy of Kapsenberg [8].

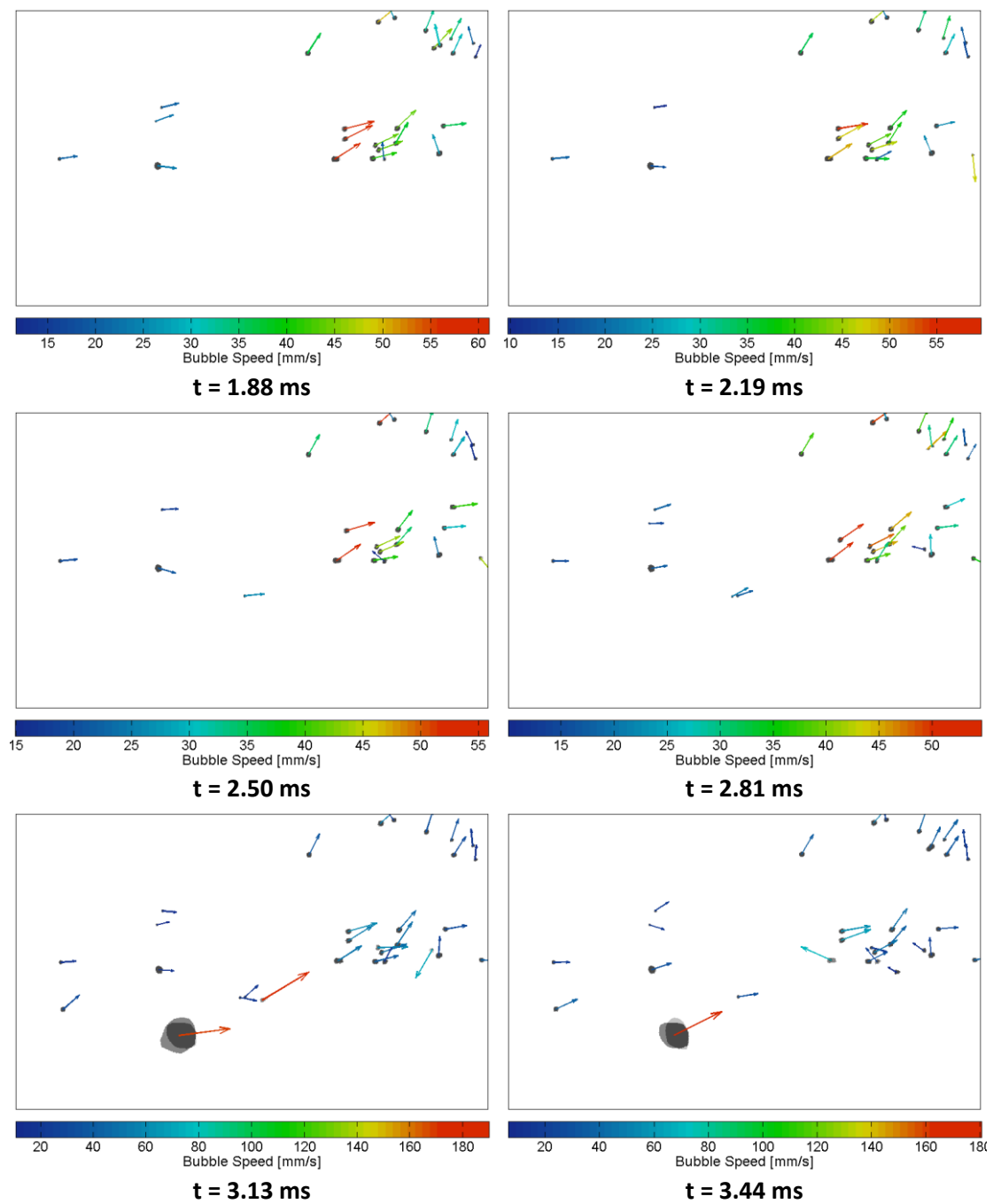
Because the reentrant cavities were located preferentially on the 24° face, bubble growth occurred at an angle normal to the face rather than vertically. Two test cases are presented by Kapsenberg [8]—a low and high pool subcooling case.

The low subcooling case yielded large bubbles from the surfaces which initially left at an angle normal to the 24° face; however, their large size caused them to generally rise vertically soon after departure. Initial departure velocities were found to be $100\text{-}250\text{ mm}^1\text{s}^{-1}$.

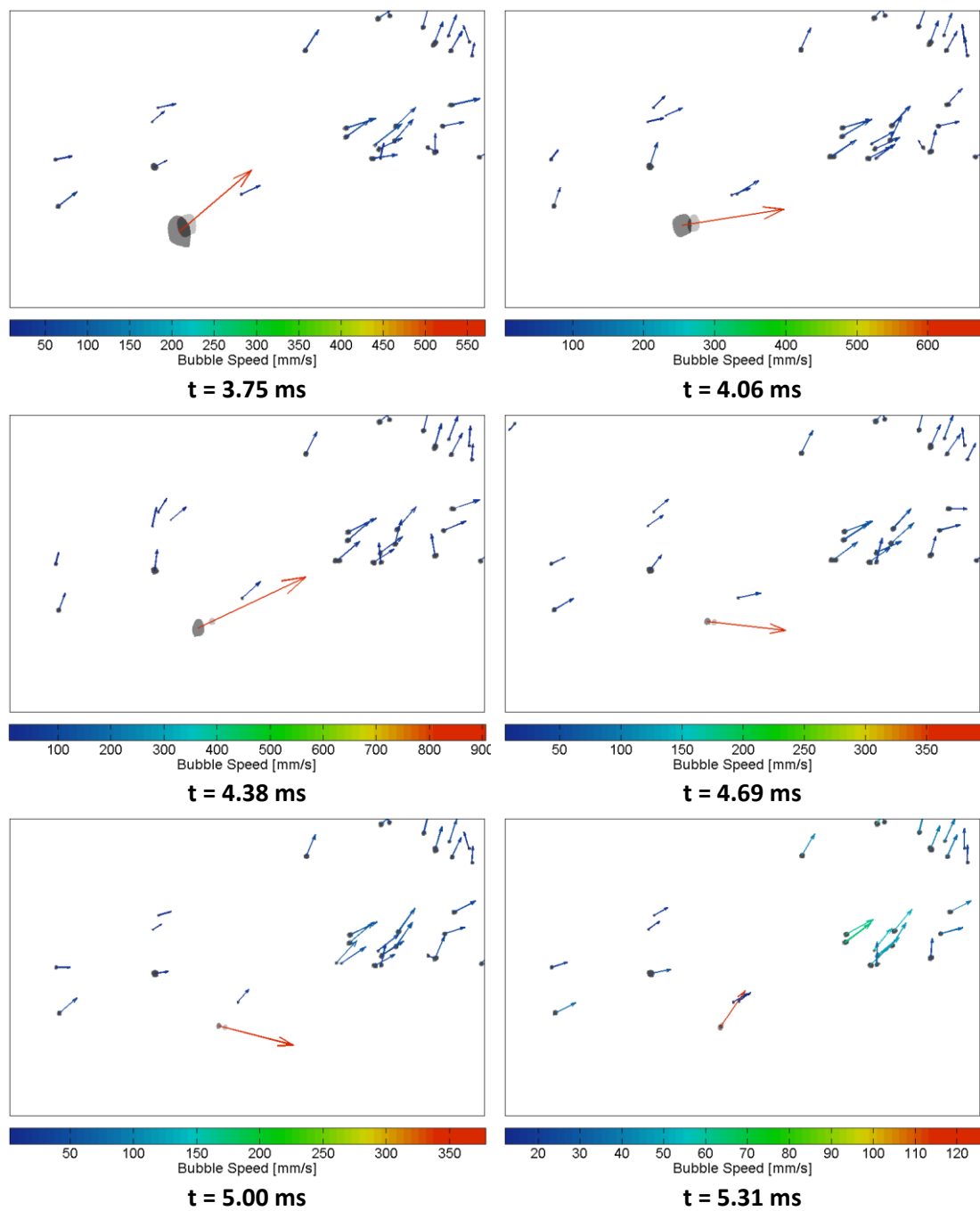
The high-subcooling test was performed at a 20°C subcooling with $18.94\text{ W}^1\text{cm}^{-2}$ of applied heat to the structured surface. Bubbles consistently grew at an angle to the face. At departure, their initial velocity ranged from 170 to $200\text{ mm}^1\text{s}^{-1}$. This was followed by an almost immediate collapse of the bubble due to the highly subcooled pool. Bubbles during this collapse exhibited rapid accelerations to the right (preferential direction) to a velocity as high as $906\text{ mm}^1\text{s}^{-1}$. Far field bubbles were measured to have velocities ranging from $30\text{-}60\text{ mm}^1\text{s}^{-1}$ with a horizontal component of velocity averaging between $25\text{-}35\text{ mm}^1\text{s}^{-1}$. Velocity measurements were performed with a bubble tracking algorithm. A sample sequence of the results excerpted from Kapsenberg [8] is shown in Fig. 2.6.

Figure 2.6: Bubble velocity field at high subcooling . $q'' = 18.94 \pm 1.26 \text{ W}^1\text{cm}^{-2}$; $\Delta T_{\text{sub}} = 20.0 \pm 0.3^\circ\text{C}$; $\Delta t = 312.5 \mu\text{s}$; exposure time = $40 \mu\text{s}$; Aperture 100% open; field of view = 8.71 mm x 5.44 mm; $\alpha = 24^\circ$.





(Figure 2.6 continued)



(Figure 2.6 continued)

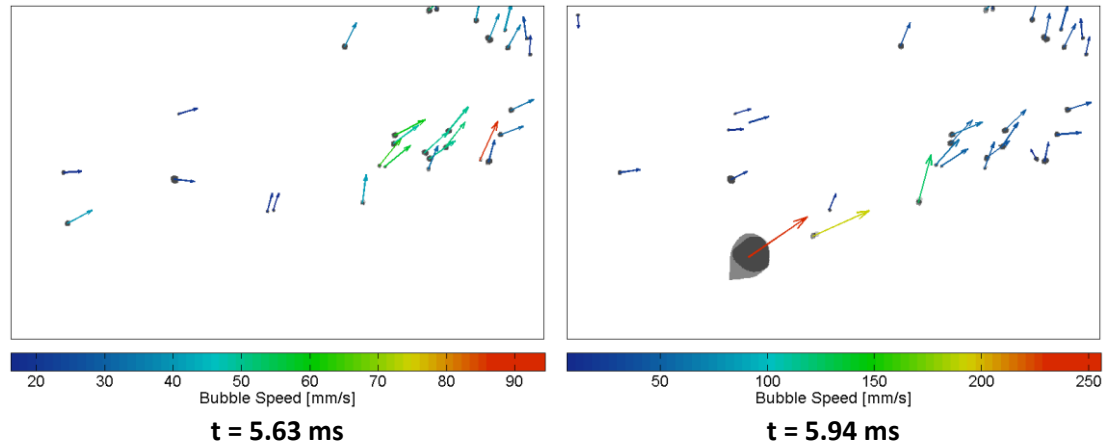


(Figure 2.6 continued)

Bubble growth data from the surface was then applied to develop a semi-empirical model intended to predict liquid velocity. The model uses a momentum balance between the bubble growth and a liquid control volume located above the reentrant cavity. The time rate of change of momentum from the bubble was equated as the drag force overcome by the bubble during each cycle whereas the liquid momentum was equated as the mass of liquid displaced multiplied by its velocity.

$$|\vec{v}_l| = \sqrt{\frac{7\pi f_d}{2A_{ts} \cos \alpha} \sum_{i=t_0}^{i=t_f-1} \bar{C}_D \left(\frac{d_i + d_{i+1}}{2}\right)^2 \left(\frac{d_{i+1} - d_i}{dt}\right)^2 dt} \quad (\text{Eq. 2.12})$$

where A_{ts} was the total area of the structured surface and f_d was bubble departure frequency.

Predictions made by the semi-empirical model for the high subcooling test were $45 \text{ mm}^1\text{s}^{-1}$ with a horizontal component of $18 \text{ mm}^1\text{s}^{-1}$.

2.5. Conclusions on Literature Review

The literature above presents a number of existing and potential technologies which utilize two-phase heat transfer and passive liquid transport. Presently, these technologies are not developed enough to be commercialized. Further research must be done to understand the driving mechanisms behind the phenomena. Ultimately these passive devices must be 'reliable, small, adaptable to a wide range of fluids, and mass producible' [3].

3. SCOPE AND OBJECTIVES

As this thesis is organized in two parts by differing configurations, the scope and objectives for each are distinguished here.

3.1. Adiabatic Single Bubble Study Objectives

As part of a continuing collaboration between Oregon State University and Auburn University, lateral motion of bubbles emanating from cavities on asymmetric surfaces is the focus of Part I. The literature review in Chapter 2 indicates previous work done by this collaboration supports the hypothesis that lateral motion of bubbles can effectively impart a net lateral velocity in the surrounding fluid as initial proof of concept experiments were successful. The objective of this continuing research is two-fold: confirm that the lateral fluid motion is caused by the asymmetric growth of a bubble from the surface and quantify the fluid region of influence on which a single bubble acts.

To achieve the first, an experiment is designed and built which isolates a single bubble in a pool as PTV or PIV is very difficult in boiling flows because of the frequent and spontaneous coalescence of bubbles. Gas injection through a typical boiling cavity-sized port provides a simple and repeatable means to create a single bubble by avoiding boiling from the surface. This experiment supports high-speed imaging of bubbles at the asymmetric surface within the pool to collect bubble growth data and particle tracking velocimetry (PTV) to improve the fluid velocity measurements. An existing PTV algorithm developed by Kapsenberg [8][1] is utilized to track seed particles.

In conjunction with the PTV measurements of velocity, quantification of the region of influence of a single bubble will be performed with a semi-empirical model also developed by Kapsenberg [8]. Refinements and modifications of the model will be made to improve its ability to predict fluid velocities in the pool. The model is then validated against the PTV data by equally altering the region of influence of a bubble for both.

3.2. Open-Channel Pump Study Objectives

The open-channel pump experiment serves as a proof-of-concept for a novel application of preferential motion of vapor slugs by a passive surface. The major objective is to test the hypothesis that asymmetric structures incorporated into channel geometry induce a net flow in a preferential direction. Once this is achieved, the subsequent steps are determining slug kinematics and the driving force behind their motion.

To test the hypothesis, an experiment is designed and fabricated which demonstrates motion of vapor slugs. Functionality requirements include pressure control and measurement of the channel environment, local heat addition to the test section, and the ability to visualize slug motion with high-speed videography.

As slug flow within a channel has not yet been actualized by the current collaborators, it is unknown how it will appear; therefore, image processing techniques must be developed to consistently quantify slug motion for the various regimes of flow which may occur. High-speed visualization must also be capable of capturing elements of the flow which may indicate the cause of the vapor motion. This data can then be applied to explain and predict velocities witnessed in the channel.

PART I: ADIABATIC SINGLE-SINGLE BUBBLE

4. EXPERIMENTAL FACILITY

This section covers the facility used to perform the adiabatic single-bubble experiments where nitrogen gas was injected into a fluid filled chamber through a structured test section. Flow visualization was incorporated to capture bubble growth and departures from a structured surface. The flow was seeded to determine liquid velocities during post processing. The ultimate goal was to relate bubble growth to fluid velocities in the immediate vicinity. The experimental rack (T-slotted frame assembly) was based on the original configuration that was used for a prior microgravity experiment. Descriptions of the test section, chamber, and auxiliary components will each be presented here.

4.1. Test Section

The test section consists of a structured surface mounted on a stainless steel substrate. The structured surface, shown in Fig. 4.1, was machined from brass and measures 10 mm (0.394 in) square with an overall height of 500 μm (0.0197 in). The top surface has a saw-tooth pattern containing nine ratchets with a pitch of 1 mm (0.0394 in) and a shallow face angle of 30 degrees. In the center of each face is a 172 μm (0.0068 in) cylindrical cavity drilled normal to the shallow face through to the bottom surface. The brass surface was affixed using double sided Kapton tape to a 76.2 mm (3.0 in) diameter stainless steel shim disc of thickness 250 μm (0.01 in). A 6.35 mm (0.25 in) diameter hole located in its center allows the flow of nitrogen through the surface. An aluminum adaptor measuring 19.05 mm (0.75 in) square and 12.7 mm (0.5 in) was epoxied to the bottom side of the shim disc and contains a 1/8 inch NPT tapped through-hole for a corresponding Swagelok compression fitting. Only one cavity was left open for the flow of nitrogen. The test section is shown in Fig.4.2.



Figure 4.1: Structured brass surface. The ratcheted surface and nine cavities on the shallow faces are visible in this image taken with a macro lens.

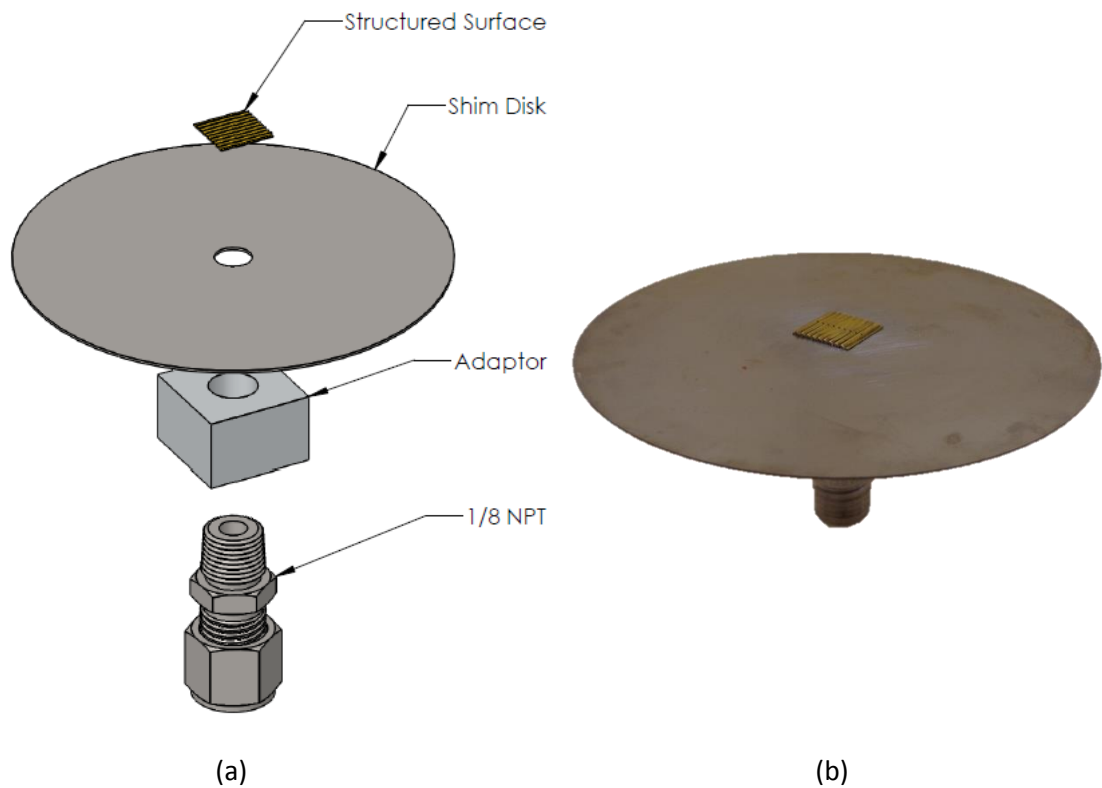


Figure 4.2: Solid model and assembled test section. (a) The solid model is exploded and annotated to identify each component. (b) The test section in its assembled form for testing.

4.2. Chamber

The chamber, shown in Fig. 4.3, used in this testing was originally designed for adiabatic and diabatic testing; therefore, some features of the chamber are not relevant for this

experiment. Four optically clear sections of polycarbonate fused together create a nearly circular unit with a centered void measuring 19.05 mm (0.75 in) square through the 50.8 mm (2.0 in) height of the component. The front, rear, left, and right faces remain flat and optically clear for illuminating and imaging. Additional features used for diabatic tests include a top recess for a heat sink, through-holes for pogo-pin electrical probes, and pathways for wires. The chamber is secured on top of a stage with the test section sandwiched between the two. A circular EPDM gasket and EPDM o-ring are used to seal the interfaces between the test section, chamber, and the stage, respectively. Eight 50.8 mm (2.0 in) #10-32 stainless steel socket head cap screws are used to compress the gasket and o-ring.

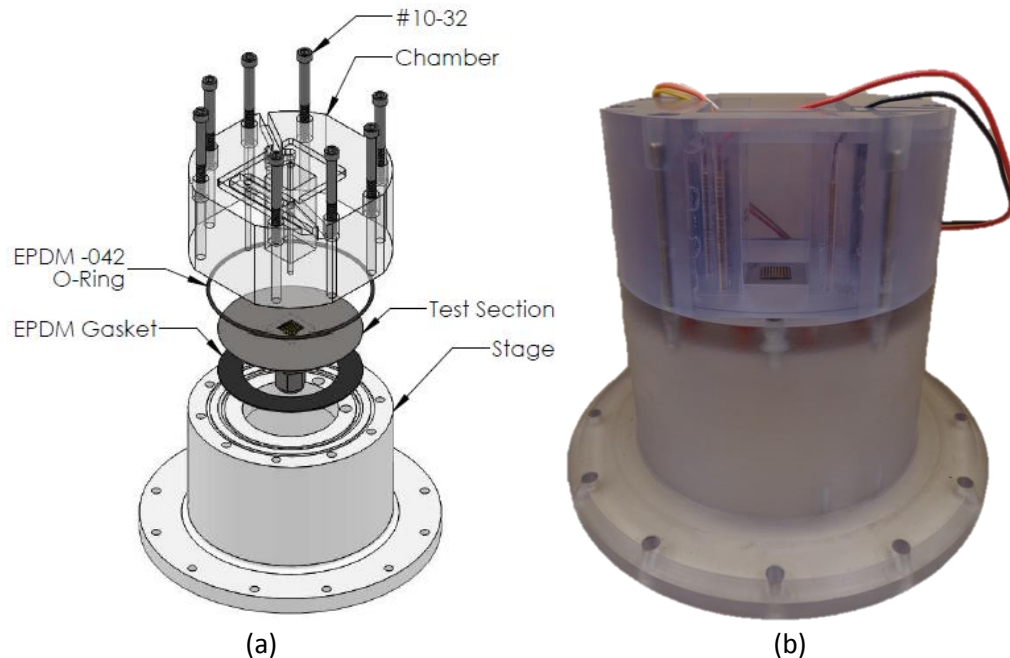


Figure 4.3: Adiabatic-Single Bubble test chamber assembly. (a) Components are exploded and annotated for clarity. (b) Picture of the test assembly in shown with test section installed. Electrical wires were not used during adiabatic testing.

4.3. Test Facility

The test facility, shown in Fig. 4.4, is constructed out of T-slotted aluminum extrusion frame (rack) and all components are affixed to this frame. The chamber was supported in the experiment rack by an aluminum plate such that the camera and lens are aligned to view the profile of the ratchet pattern. The LED array was mounted behind the chamber to provide

illumination. A DC power supply, power switch for the LED array, and a tray for a laptop were also included in the rack.

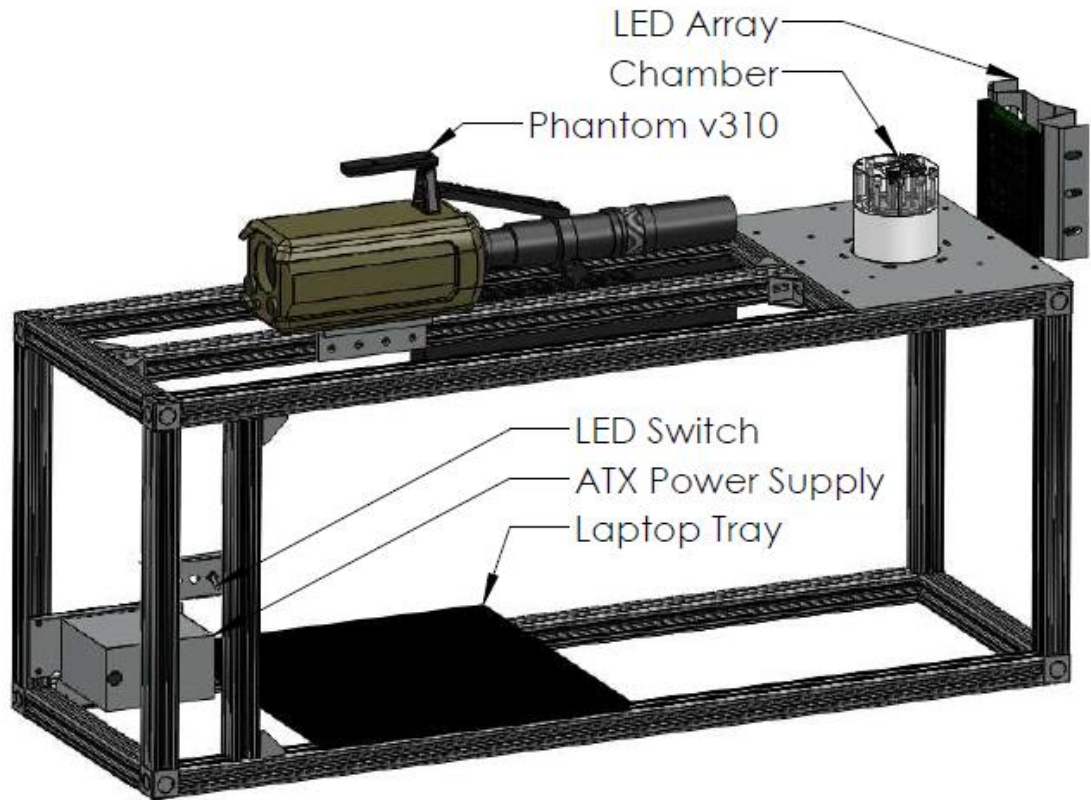


Figure 4.4: Overview of the experimental facility with major components labeled for clarity.

Nitrogen was injected into the chamber via the test section through the single cavity that was left clear. Nitrogen was supplied from a 300 liter high pressure steel supply of compressed nitrogen. Pressure at the tank is controlled with regulator. Flow to the test section is controlled using a Cole Parmer rotameter, shown in Fig. 4.5.



Figure 4.5: Cole Parmer rotameter used to regulate the flow through the test section.

4.4. Flow Visualization and Illumination Components

High-speed imaging of the gas bubbles and seed particles leaving the structured surface was done with a Vision Research Phantom v310. The camera was supported by a T-slotted aluminum extrusion and its distance from the chamber was adjusted with a double flange linear bearing designed for the extrusion. Magnification was achieved with an Infinity K2/SC microscope lens fitted with a CF-3 objective. Properties for the lens and CF-3 objective are given in Table 4.1. Videos were captured and saved using Vision Research's Phantom Camera Control (PCC 1.3) software.

Table 4.1: Properties of the K2/SC microscope lens fitted with a CF-3 objective as given by the manufacturer.

		Focus		
Property	Units	Near	Mid	Far
Field of View (FOV)	mm	8.4	10	12.4
Depth of Field (DOF)	mm	0.04	0.08	0.08

The optical method used to capture the bubbles is shadowgraphy. The backlighting is supplied by a custom designed array of LEDs (Fig. 4.6) located behind the chamber. The 625 LEDs are powered by a 350W ADX computer power supply and cooled by two 12VDC brushless fans.

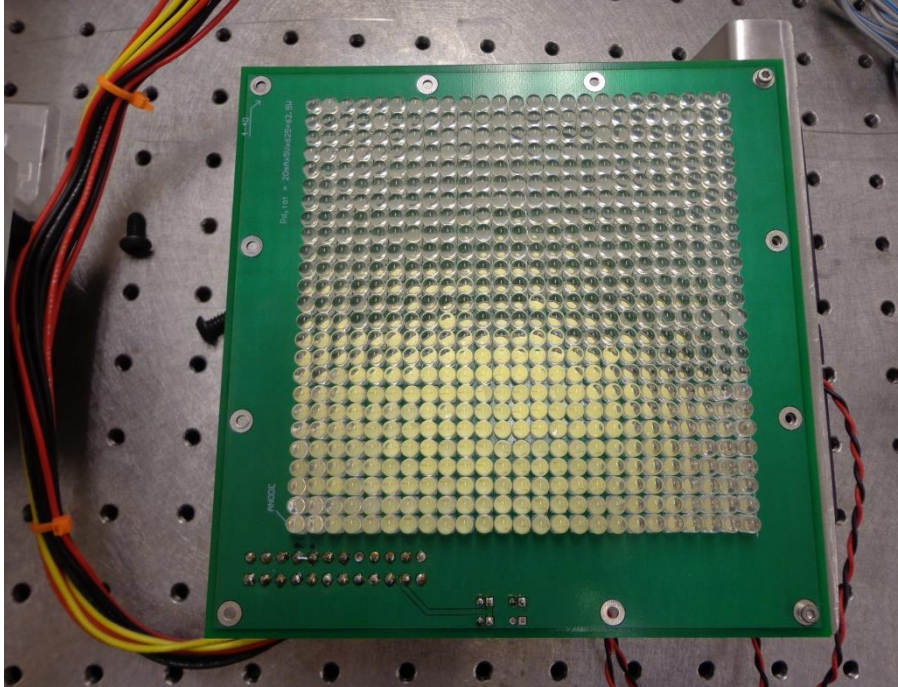


Figure 4.6: Custom 625 LED array used for illumination of chamber.

5. EXPERIMENTAL PROCEDURES

Described here are the experimental procedures followed during the adiabatic single-bubble experiments. It was imperative that these procedures are completed consistently to ensure repeatable results.

5.1. Test Section Assembly

Before installing the test section into the chamber, both were visually inspected to ensure that the chamber is clear of debris or smudges and that the brass surface is clean. If either required cleaning, it was cleaned with deionized water and a microfiber cloth. If necessary, the brass surface was cleaned with isopropyl alcohol and rinsed with deionized water.

Due to the bolting pattern of the stage and chamber, the test section must be mounted on the stage in the correct orientation in order to allow for the ratchet profile to be visualized through the chamber walls. Figure 5.1 shows this mounting procedure. Starting with the stage, the EPDM gasket was laid in the center in the same recess that locates the shim disc. The test section was placed onto the gasket, allowing the NPT fitting to pass through the center hole of the stage. The test section must be rotated such that ratchet peaks are parallel to the only line which can connect four bolt holes (two from the outer pattern and two from the inner pattern)—see Fig. 5.1a. It was not imperative that the test section is perfectly aligned at this point as the chamber assembly can rotate (10 degrees max) when installed in the experimental facility.

The EPDM-042 o-ring was installed in the gland just inside of the inner pattern of bolt holes. With the eight chamber screws located placed in their holes, the chamber was gently lowered onto the stage so that the screws rested into their corresponding holes in the stage before the chamber made contact with the test section. This procedure was to prevent unintentional rotation of the test section when securing the chamber. The chamber was aligned such that the large flat faces were the viewports for the camera and lighting (see Fig. 5.1b). Chamber screws were tightened in a crisscrossed pattern to ensure a leak free seal. Firm, but not excessive tightening is required with a standard hex head key.

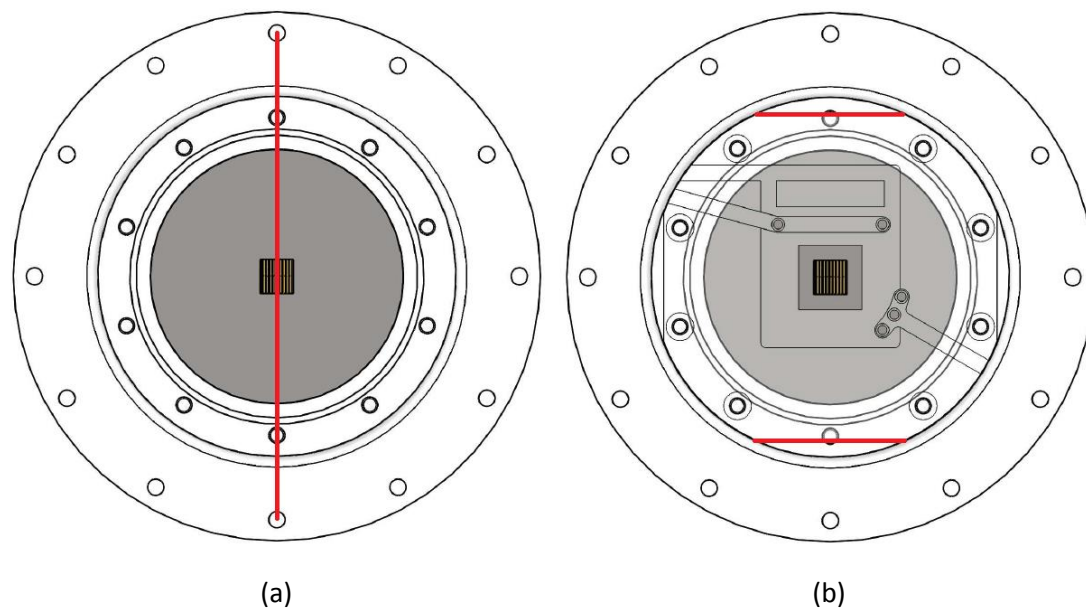


Figure 5.1: Proper alignment of the test section and chamber on the stage. Ensure that the ratchet peaks are parallel with the orientation line shown in (a) and that the chamber is aligned such that the wide faces (b) are used for imaging and lighting.

With the test section assembly completed, the chamber was then installed into the experiment rack by bolting the stage flange loosely to the aluminum deck in the slotted holes with six 22.3 mm (0.875 in) #10-32 stainless steel socket head cap screws and nuts (see Fig. 5.2). The chamber assembly must be inserted from the bottom. Using an electronic level and by adjusting the six screws the chamber is leveled. Lastly, the nitrogen flow line from the rotameter is connected to NPT fitting of the test section.

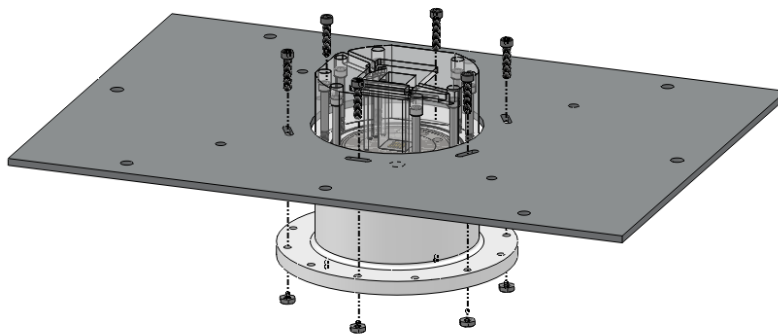


Figure 5.2: Installing the chamber assembly. The slotted bolting configuration allows for easy rotation of the test section for imaging.

5.2. High-Speed Camera & Lighting

The camera was first attached to the linear bearing using two of the mounting holes located on the bottom (refer to Fig. 4.4). The linear bearing was slid onto the T-slotted support beam aligned with the chamber and LED array (Fig. 4.4) after it is loosened at the rear. Using a measuring tape, the position of the support beam is adjusted such that it is centered and square in the facility. The Infinity K2/SC microscope lens, CF-3 objective, and lens brace are all subsequently installed.

The v310 must be powered up in a specific order. The power cable plugs into the back of the camera and LEDs begin blinking. After checking that the fan is powered on and the blinking lights are steady (approximately 30 seconds), the yellow Ethernet data cord is plugged into the back of the camera and connected to the laptop's Ethernet port. A 10 gigabit Ethernet port is required for the v310. Again, blinking LEDs must become steady before proceeding. Phantom Camera Control software is then opened and the following parameters are adjusted: resolution, sample rate, and exposure time. Table 5.1 shows these settings used for videos recorded herein. Ensuring the lens cap is on, a current session reference (CSR) was performed before taking or saving any data. Once the software is ready, lens aperture is set to 100% open, the LED array is turned on, and the camera's position and focus are adjusted until the structured surface becomes visible.

Table 5.1: Phantom Camera Control settings

Parameter	Setting
Image Resolution	1280 x 800 pixels
Sample Rate	2000 frames per second
Exposure Time	50 μ s
Aperture	100% open
Focus	Mid
Pixel Resolution	128.06 pix/mm

5.3. Filling the Chamber

The working fluid, deionized water, must be seeded with particles during the filling process because particle tracking velocimetry is used to analyze flow within the chamber. First, 10 mL (0.338 oz.) of deionized water is added to the chamber using a graduated pipette. Before adding any seed particles, the stock aqueous mixture vial of seed is agitated to suspend the settled particles by inverting the vial several times. This stock mixture is 6.25% particles by mass and the particles are Cospheric, white, polyethylene microspheres of diameter 53-63 μm (0.0021-0.0025 in), density of 1.00 g/cm^3 (62.4 lbs/ft^3), coated with Tween 80. A summary of how these particles are prepared is provided in Appendix A. Seeding is achieved by adding 0.4 mL (0.014 oz) of the stock solution to the deionized water in the chamber, resulting in a 0.25% mixture of particles by mass. After the particles become stagnant, the camera is readjusted and a short video is recorded with the Phantom v310 for verification that the particles are neutrally buoyant (see Fig. 5.3)

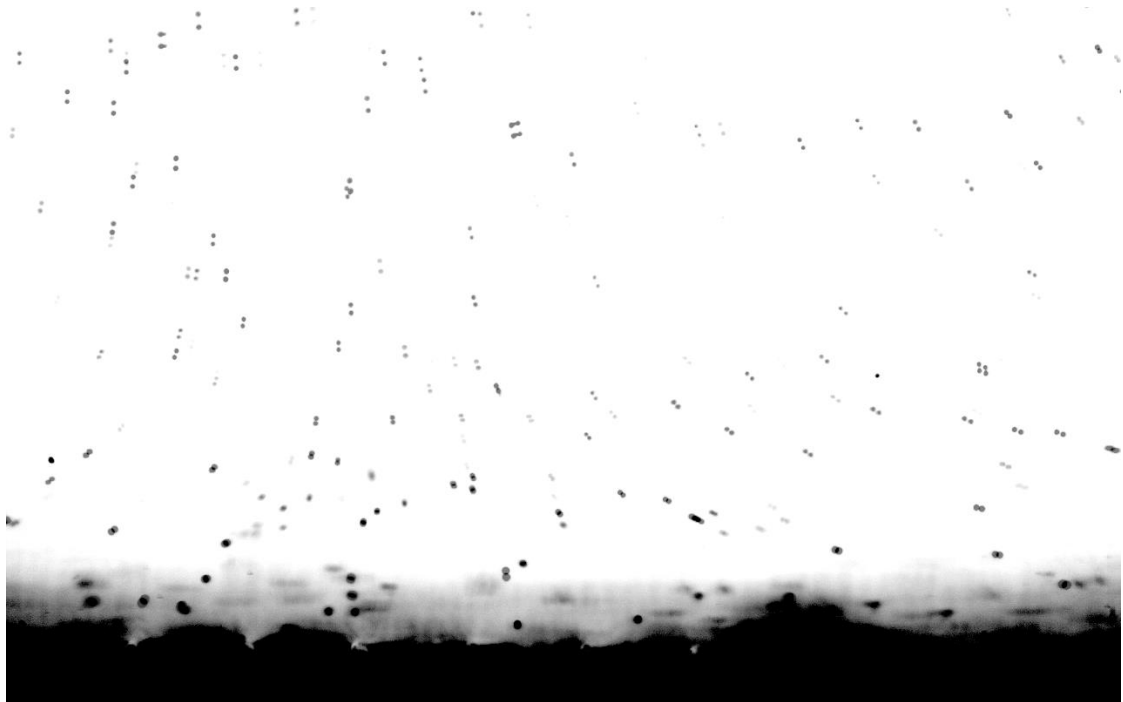


Figure 5.3: Composite image of two frames 0.25 seconds elapsed showing stagnant seed particles.

5.4. Gas Injection

With the rotameter closed, the nitrogen tank is opened and the regulator is set to approximately 15 kPa (2 psi). The rotameter is slowly opened until the ball is barely lifted and steady. This value is below the scale on the rotameter; however, its value is not a concern because the rotameter is only used to visually adjust nitrogen flow rate. It is necessary to readjust the camera position to bring the bubbles into focus since the cavity is located at the center of the structured surface (Fig 4.1).

5.5. Flow Visualization

To capture a video of the gas bubbles not only growing, but also departing the structured surface, the camera's RAM must be initialized. The RAM stores the preceding 8 GB of continuously recorded video which can be selected to save with the trigger function. When the camera is triggered, the camera activates the previously recorded images and displays them in the PCC software. After reviewing the video, a section (2000 frames/1 second) is selected and saved on the computer hard drive.

5.6. Shut-down

It is important to shut down the experiment properly to ensure the safety of the camera and cleanliness of the chamber and structured surface. The gas injection system was first shut down by closing the rotameter and nitrogen-tank valves to stop the flow of nitrogen. The visualization and illumination system is turned off by closing the Phantom Control Software, followed by removing the Ethernet cord from the computer, and finally by powering off the v310. The LED array was shut off at this time as well. The fluid in the chamber was disposed in a dedicated waste container. After removing the chamber assembly from the facility, the chamber was rinsed with deionized water and stored.

6. DATA ANALYSIS

This chapter covers the data analysis performed for the results presented in Chapter 7 on the adiabatic single-bubble study. From the high-speed videos, fluid velocity was determined by tracking seed particles in a control volume centered at the active cavity using particle tracking velocimetry (PTV). Bubble growth on the surface was measured with common image processing techniques on a sequence of high-speed video frames. The bubble growth was then related to fluid velocities using a semi-empirical model. A general description of the PTV algorithm, overview of the image processing, calibration, and uncertainty analysis are all included in this chapter.

6.1. Particle Tracking Velocimetry Algorithm

The PTV algorithm used was originally written by Kapsenberg [8] to track bubbles departing from surfaces to the one presented in this thesis. Therefore, no changes were necessary to apply the algorithm. An 800 frame series of images in the range of [-7800 to -7000] containing fourteen bubble growths and departures were analyzed for the data presented in this thesis. A detailed description of the algorithm can be found in Kapsenberg's thesis and an outline of the operations completed is located in Appendix B.

Particle tracking velocimetry was performed on the high-speed video of the single bubble over three regions of interest. In each repetition the region of interest was centered over the cavity of interest while all other parameters remained constant. The region of interest was a rectangle measuring one, two, and three bubble diameters in width and was rotated 30 degrees to align with shallow slope of the ratcheted surface. The PTV results with the different regions of interest will be used to determine the *area of influence* of a bubble (refer to Chapter 7.1).

6.2. Bubble Growth Image Processing

The same 800 frame series showing fourteen bubble growths and departures analyzed with PTV were also processed to measure bubble growth rates. The goals of the image processing

were to extract bubble diameter, height, and center of mass while the bubble was still attached to the surface. All image processing was performed in National Instruments Vision Assistant software. Two different processes were required to determine the diameter and height and are described below.

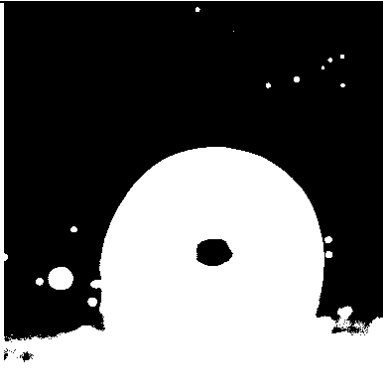
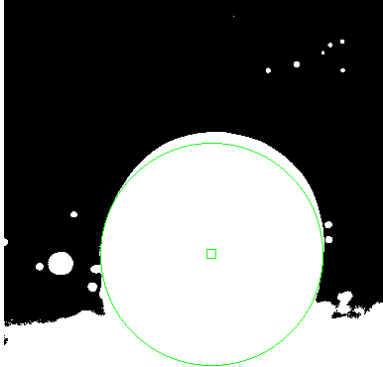
6.2.1. Bubble Diameter and Center of Mass

A series of image processing steps were performed to each of the fourteen bubble growth cycles which extracted the bubble diameter and center of mass. The original image (stored in a multipage TIFF file) was imported into the Vision Assistant program. Table 6.1 shows a series of example images from the image processing and parameters set in each step. A threshold was applied to binarize the image. The binary image was then inverted to—making the bubble a ‘bright object’ as the backlit experiment images objects as dark objects. The image was then cropped to region of interest containing only the bubble being measured. This decreased the processing time when performing batch processing. Holes in the bubble image were filled and the built in circle detection function was applied. The result of the circle detection returned the bubble radius, center x location, and center y location in pixels. With the pixel resolution (128.0 pixels/mm) known, these measurements were converted to physical dimensions. The circle detected showed an overlay which extended into the ratchet surface; however, this diameter still represents the desired measurement which will later be used to determine the projected area of the bubble.

Table 6.1: A series of images showing each image processing step of a single frame (-7714) to extract bubble diameter and center of mass. Images are displayed in the left column and the parameters of the process are shown in the right.

	<p>Original Image</p> <ul style="list-style-type: none">• No Parameters
	<p>Binary Threshold</p> <ul style="list-style-type: none">• Manual Threshold• Look For: Bright Objects• Threshold Range: Minimum 128
	<p>Binary Image Inversion</p> <ul style="list-style-type: none">• No Parameters

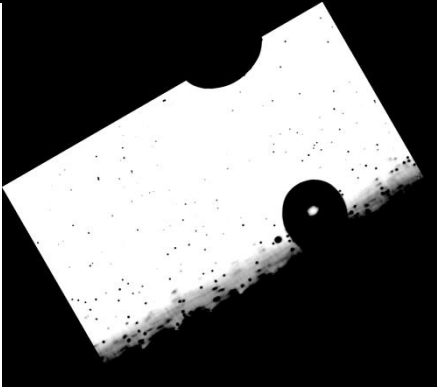
(Table 6.1 continued)

	<p>Crop (Image Mask)</p> <ul style="list-style-type: none">• Extract Masked Region Outside the Region of Interest (ROI)• ROI: [679, 357];[1063, 745] = 2.5 mm x 2.5 mm
	<p>Fill Holes</p> <ul style="list-style-type: none">• No Parameters
	<p>Circle Detection</p> <ul style="list-style-type: none">• Minimum Radius: 20 pixels• Maximum Radius: 250 pixels

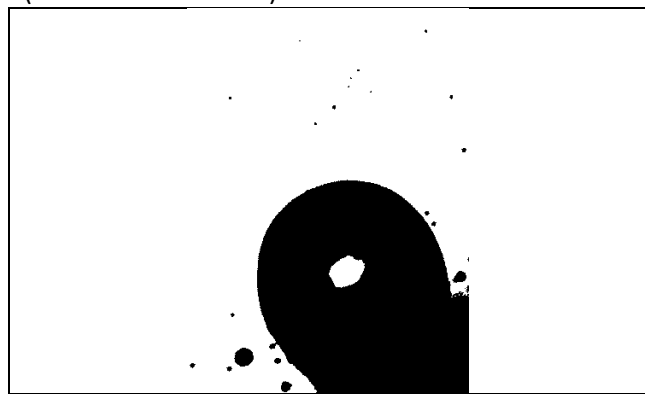
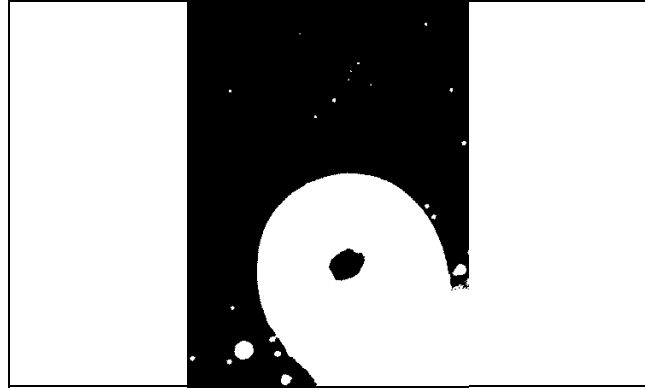
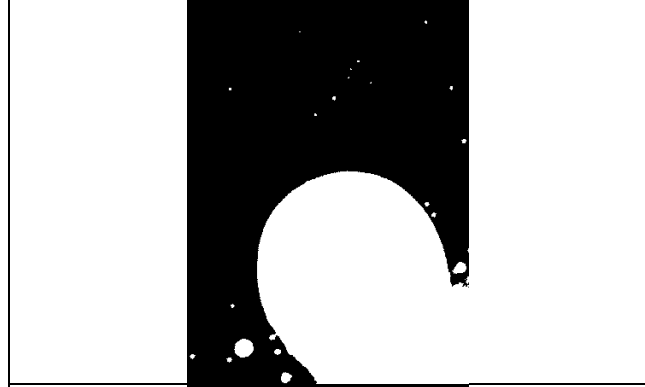
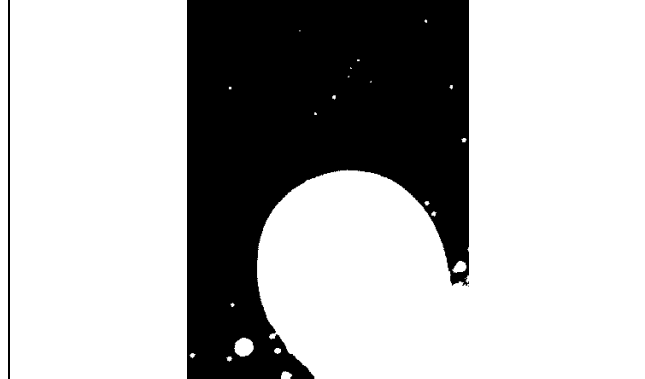
6.2.2. Bubble Height Growth Rate

A different series of image processing steps were performed to evaluate the bubble height growth rate in the fourteen bubbles analyzed. The original image was imported into the Vision Assistant program and was rotated 30 degrees counter clockwise. This was done to orient the image such that the shallow ratchet face was horizontal. Therefore; the measurement of bubble height growth rate was in the direction normal to the shallow face. The image was then cropped to a region containing only the bubble being measured. As before, the image was binarized, inverted, and holes in the bubble were filled. The bubble was separated from the previous bubble (not present in all frames) and the seed particles were removed from the images. Any remaining unwanted regions were removed by a particle filter set to keep only regions coincident with the bottom edge of the region of interest. This step removed departed bubbles and only retained the bubble growing at the surface. The height of the bubble was then measured with a bounding rectangle with the particle analysis tool. The height of the bubble was equated by the difference between the bottom and top bounds of the bubble. The bottom bound of the bubble did not physically correspond to the surface of the ratchet; however, because the bottom bound remained constant, rate of change in height depends only on the top bound. With the pixel resolution (128.06 pixels/mm) known, the height was converted to a physical dimension. Table 6.2 shows a series of example images from the image processing and parameters set in each.

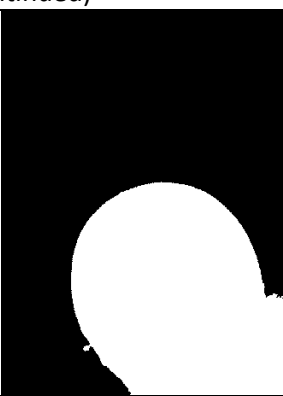
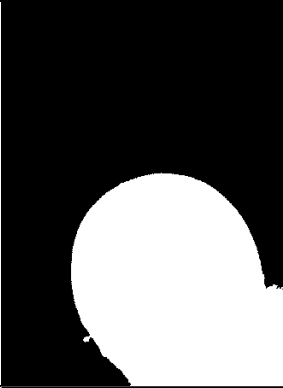
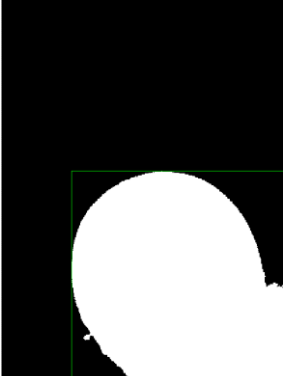
Table 6.2: A series of images showing each image processing step of a single frame (-7714) to extract bubble height. Images are displayed in the left column and the parameters of the process are shown in the right.

	<p>Original Image</p> <ul style="list-style-type: none"> • No Parameters
	<p>Rotate Image</p> <ul style="list-style-type: none"> • 30° CCW
	<p>Crop (Image Mask)</p> <ul style="list-style-type: none"> • Extract Masked Region Outside the Region of Interest (ROI) • ROI: [890, 414];[1220, 865] = 3.72 mm x 2.77 mm

(Table 6.2 continued)

	<p>Binary Threshold</p> <ul style="list-style-type: none">• Manual Threshold• Look For: Bright Objects• Threshold Range: Minimum 10
	<p>Binary Image Inversion</p> <ul style="list-style-type: none">• No Parameters
	<p>Fill Holes</p> <ul style="list-style-type: none">• No Parameters
	<p>Separate Objects</p> <ul style="list-style-type: none">• Size: 7• Iterations: 7

(Table 6.2 continued)

		<p>Remove Small Objects</p> <ul style="list-style-type: none">• Iterations: 20
		<p>Particle Filter</p> <ul style="list-style-type: none">• Parameter: Bounding Rectangle Bottom• Range: 450-452 pixels• Action: Keep
		<p>Object Analysis</p> <ul style="list-style-type: none">• Measurements: Bounding Rectangle Top, Bounding Rectangle Bottom

6.3. Calibration and Uncertainty

To provide confidence in the results of the adiabatic single-bubble experiment, calibration and uncertainty analyses were performed. Uncertainty analysis was performed for the PTV algorithm and the image processing.

A pixel resolution calibration was performed to relate the camera field of view to a physical field of view. The v310 pixel intensity calibration is a built in function through the Phantom Camera Control software. It was performed each time the experiment was run before recording any high-speed videos. After allowing the camera to run for several minutes with the lens cap on, the Current Session Reference (CSR) button was clicked. The CSR computes and applies pixel offsets for the current image such that all pixels read the same intensity with the lens cap on. The CSR was repeated if any acquisition parameter was changed.

6.3.1. Particle Tracking Velocimetry Uncertainty

Uncertainty in the particle tracking is assumed to arise from two sources; namely, the timing of the camera frame rate and pixel resolution. The Phantom v310 has a 20 ns timing resolution; thus, the uncertainties in frame rate are assumed to be orders of magnitude lower than any other source.

The pixel resolution of the v310 was used in not only the PTV algorithm, but also in the image processing for bubble dimensions. Pixel resolution provides a means to convert pixel measurements in an image to a physical measurement. It could be determined in three ways: in situ measurement, calculation, or optical grid measurement.

In situ measurement requires a physical object of known dimension to be in the field of view and focus of the camera during testing. A pixel measurement of that physical object is then compared to its known physical dimension to determine pixel resolution. In the case of the adiabatic-single bubble experiment, the only logical physical object to measure was the ratchet pitch of the structured surface; however, the camera settings to capture images of

the bubble caused the ratchets to be out of focus during testing and , hence, this calibration method could not be used..

Calculation of the pixel resolution was performed using data for the K2/SC lens [14]. The manufacturer published data for the K2/SC lens was based on a 12.7 mm (0.5 in.) camera sensor. The v310 contains a 50.8 mm (2.0 in.) camera sensor; therefore, the conversion factor for the supply data is 4. The calculated pixel resolution was determined to be 128.0 pixels/mm (3253.7 pixels/in.) for the CF-3 objective to the middle focus setting; however, no accuracy for the data was given by the manufacturer.

The pixel resolution was chosen to be determined by using an optical grid. An image was taken at the middle focus setting of an Edmunds Optics (Product Number: 58-509) optical grid containing a 25.0 mm (0.984 in.) square grid of 0.0625 mm (0.0025 in.) diameter dots with 0.125 mm (0.0049 in.) center-to-center spacing. A square region in the center was chosen for the calibration containing 625 dots (Fig. 6.1). Particle detection using National Instruments Vision Assistant was performed to measure the center-to-center distance between each dot. The resulting analysis resulted in a pixel resolution of 128.0 ± 0.78 pixels/mm (3253.7 ± 10.5 pixels/in.). This 1.28 mm/s represents the bias error in PTV velocity determination.

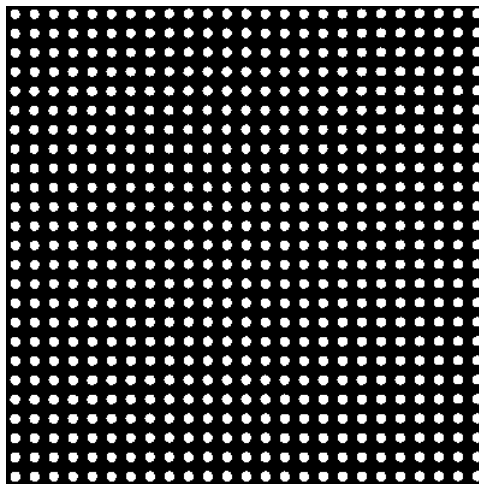


Figure 6.1: Raw image of the Edmunds optical grid used to determine pixel resolution for the Phantom v310 equipped with the Infinity K2/SC microscope lens and CF-3 objective.

6.3.2. Image Processing and Model Uncertainty

The image processing steps performed to measure bubble diameter and height have inherent uncertainties because these steps may alter the image slightly during the process. Furthermore, the extent of an image modification is directly dependent upon the parameters set for any given operation and these parameters are user defined; therefore, human error is also attributed to the uncertainty of the image processing. Because two different image processes were used for diameter and height, respectively, each uncertainty was determined independently by a perturbation method. Some image processing steps could not be perturbed because no parameters were necessary (see Table 6.1 and Table 6.2); for example, binary image inversion and fill holes. Furthermore, some steps require input parameters, but did not affect the diameter or height measurements for example, image mask, circle detection, particle filter, and remove small particles. Thus, the image processing performed to extract diameter measurements was only perturbed by the binary threshold minimum limit. Table 6.3 below shows the perturbation results for the diameter image processing. It was found that the binary threshold could be altered by over 50% with limited impact on the diameter.

Table 6.3: Perturbations of the image processing for diameter of a bubble. The only step which altered the diameter was the threshold parameter when binarizing the image.

	Threshold	Diameter [pix]	Δd [pix]	Max Δd
Original	128	224		2
Perturbations	56	222	-2	
	100	222	-2	
	200	226	2	

In the image processing for height measurement, it was found that the binary threshold limit could be drastically changed (increased 10-fold) with no change to the height of the bubble. The bubble height; however, changed with the rotation of the image. The original rotation was set to 30 degrees—equal to the angle of the ratchet. If any error was present in the position of the camera relative to the ratchet position, it would render the image rotated

slightly before image processing which would, in turn, change the measured height of the bubble. Therefore, the rotation of the image was perturbed and the results are shown in Table 6.4. Small variations in the rotation of the image only alter the resultant height by a maximum of 1 pixel.

Table 6.4: Perturbations of the image processing for height of a bubble. The only step which altered the diameter was the threshold parameter when binarizing the image.

	Rotation [deg]	Height [pix]	Δh [pix]	Max Δh
Original	30	250		1
Perturbations	28	249	-1	
	29	249	-1	
	31	249	-1	
	32	251	1	

As will be shown in the next chapter, the velocity of the liquid is determined using a semi-empirical model based on Kapsenberg [8] as:

$$\bar{v}_l = \sqrt{\frac{\pi f_d}{8A_{in} \cos \alpha} \sum_{i=t_0+1}^{t_f} \bar{C}_D \left(\frac{d_i + d_{i-1}}{2}\right)^2 \left(\frac{h_i + h_{i-1}}{dt}\right)^2 dt} \quad (\text{Eq. 6.1})$$

The uncertainties in bubble diameter and height were then propagated through the bubble force model using the Kline and McClintock method along with the pixel resolution uncertainty.

$$u_V = \sqrt{\left(\frac{\partial V}{\partial(res)} u_{res}\right)^2 + \left(\frac{\partial V}{\partial(d)} u_d\right)^2 + \left(\frac{\partial V}{\partial(h)} u_h\right)^2} \quad (\text{Eq. 6.2})$$

7. RESULTS AND DISCUSSIONS

This chapter presents the results from the adiabatic single-bubble study. All data was taken with water at ambient room temperature, injection pressure of approximately 0.14 bar (2 psia), and a flow rate of approximately 0.01 Lpm ($0.01 \text{ in}^3/\text{s}$). First, the bubble growth model of Kapsenberg [8] along with modification is presented. Next, the results from the bubble growth model particle tracking velocimetry and are presented. A comparison between the two results concludes the chapter. Due to the high quantity of frames analyzed for this experiment only an example set of images from one bubble growth and departure will be shown; however, data values reflect all bubbles analyzed.

7.1. Semi-Empirical Model

A semi empirical model was developed by Kapsenberg [8] to predict the velocity imparted to the liquid due to bubble growth. Slight modifications have been applied to the model as improvements. The model hypothesizes that the growth of a bubble from an asymmetric surface imparts momentum on a control volume of fluid in the region above it and affects a net fluid velocity in that control volume. Figure 7.1 serves as a guide for the following description of the model.

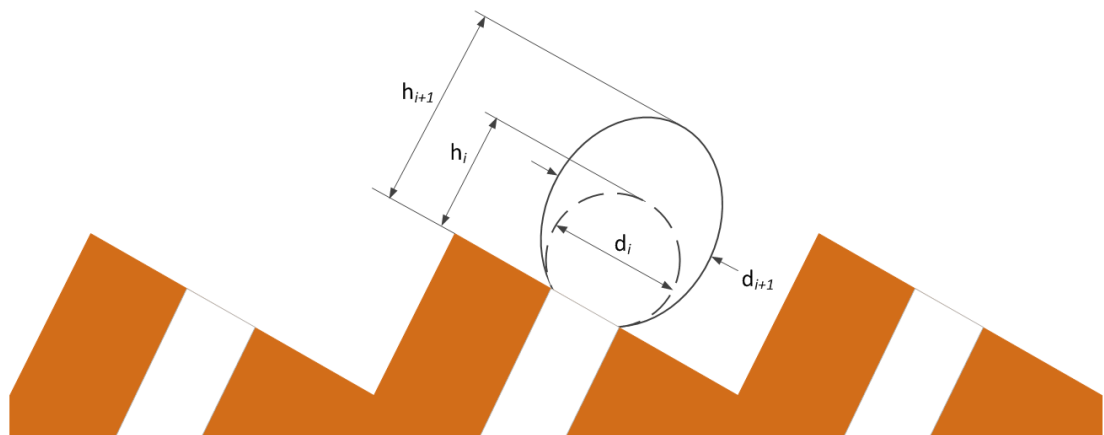


Figure 7.1: Representative drawing of surface geometry showing bubble dimensions used in the semi-empirical model.

Kapsenberg [8] presented that the force due to bubble growth is equal to the time rate of change in momentum imparted to the liquid. The force was equated as being the drag force of bubble sphere moving at the bubble diameter growth rate. The first modification to the model replaced the bubble diameter growth rate with the bubble height growth rate (Eq. 7.1), as the bubbles were observed to grow in a non-spherical manner. The diameter was required for drag force.

$$-\vec{F}_g = \frac{d\vec{P}_l}{dt} = \frac{1}{8}\pi\rho_l C_D d^2 \left(\frac{\partial \vec{h}}{\partial t}\right)^2 \quad (\text{Eq. 7.1})$$

Equation 7.1 was discretized for each time step (time between two consecutive video frames). Because bubble height growth rate is determined between two frames, the diameter was estimated as the average diameter between the two frames. The Reynolds number for this time step is a function of this average diameter and bubble height growth rate and was used to determine the drag coefficient C_D [13]. Thus, total momentum from a bubble growth cycle was determined to take the form shown in Eq. 7.2.

$$\vec{P}_l = \frac{1}{8}\pi\rho_l \sum_{i=t_0+1}^{t_f} C_D \left(\frac{d_i + d_{i-1}}{2}\right)^2 \left(\frac{h_i + h_{i-1}}{dt}\right)^2 dt \quad (\text{Eq. 7.2})$$

A control volume of fluid being influenced by the momentum of the bubble was then established. In the original model, the structured surface contained twenty-eight individual cavities, and the control volume cross sectional area was assumed to be 1/28 of the angled face area. The structured surface in this thesis only possesses one cavity; thus, the second change to the model was a new control volume cross sectional area. How this area was determined will be presented in the next chapter, but will be referred to as the *area of influence*— A_{inf} (Fig. 7.2).

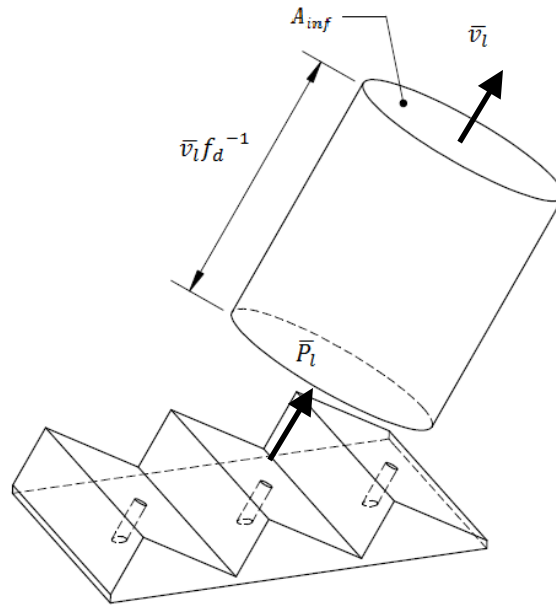


Figure 7.2: Representation of the control volume used for the momentum balance.

The momentum balance on the control volume takes the form of:

$$\bar{P}_l = m_l \bar{v}_l = (\rho_l A_{inf} f_d^{-1}) \cdot \bar{v}_l \quad (\text{Eq. 7.3})$$

By setting Eqs. 7.2 and 7.3 equal to each other and rearranging, a prediction of fluid velocity was obtained.

$$\bar{v}_l = \sqrt{\frac{\pi f_d}{8 A_{inf}} \sum_{i=t_0+1}^{t_f} \bar{C}_D \left(\frac{d_i + d_{i-1}}{2} \right)^2 \left(\frac{h_i + h_{i-1}}{dt} \right)^2 dt} \quad (\text{Eq. 7.4})$$

7.2. Bubble Growth Force Model

The bubble growth force model described in Chapter 7.1 was applied to the 800 frames presented in the previous section. Bubble diameter and height determined in each frame are shown per bubble below in Figs. 7.3-7.16. Bubble height consistently grows larger than the diameter in the same time, indicating, on average, a greater growth rate. The height grows normal to the shallow surface; thus imparting momentum onto the surrounding liquid in that direction. Some irregularities are apparent in some bubble growth cycles which can be attributed to coalescence near the surface and liquid-vapor interface undulations near the end of the growth cycle.

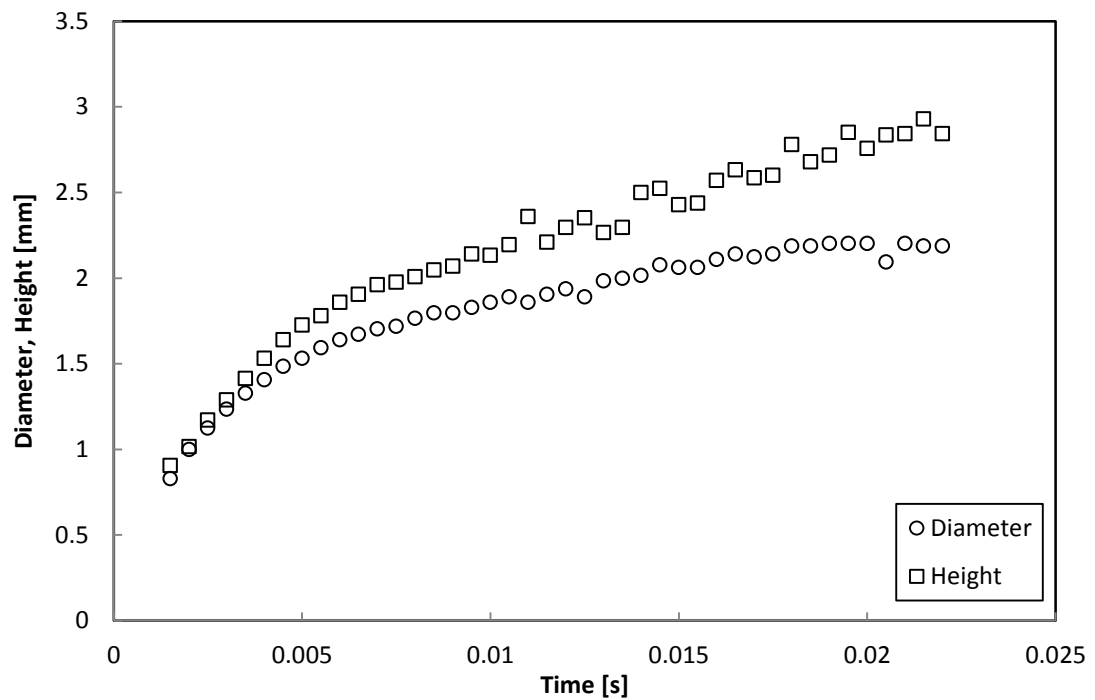


Figure 7.3: Bubble diameter and height plotted for the growth cycle of Bubble 1 of 14.

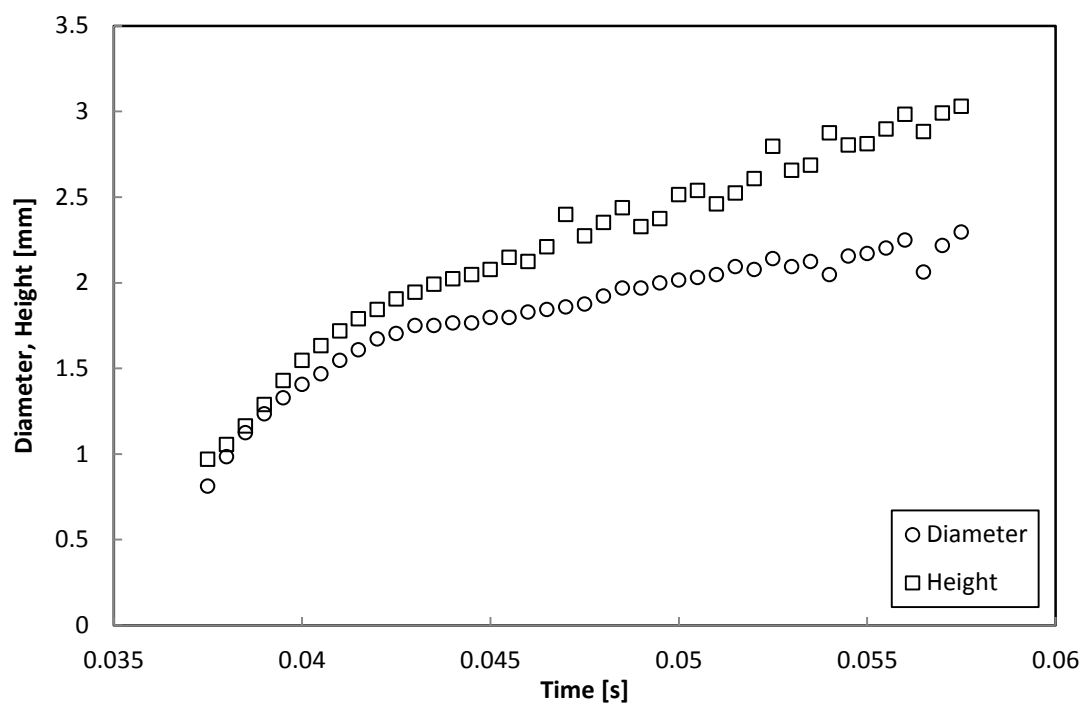


Figure 7.4: Bubble diameter and height plotted for the growth cycle of Bubble 2 of 14.

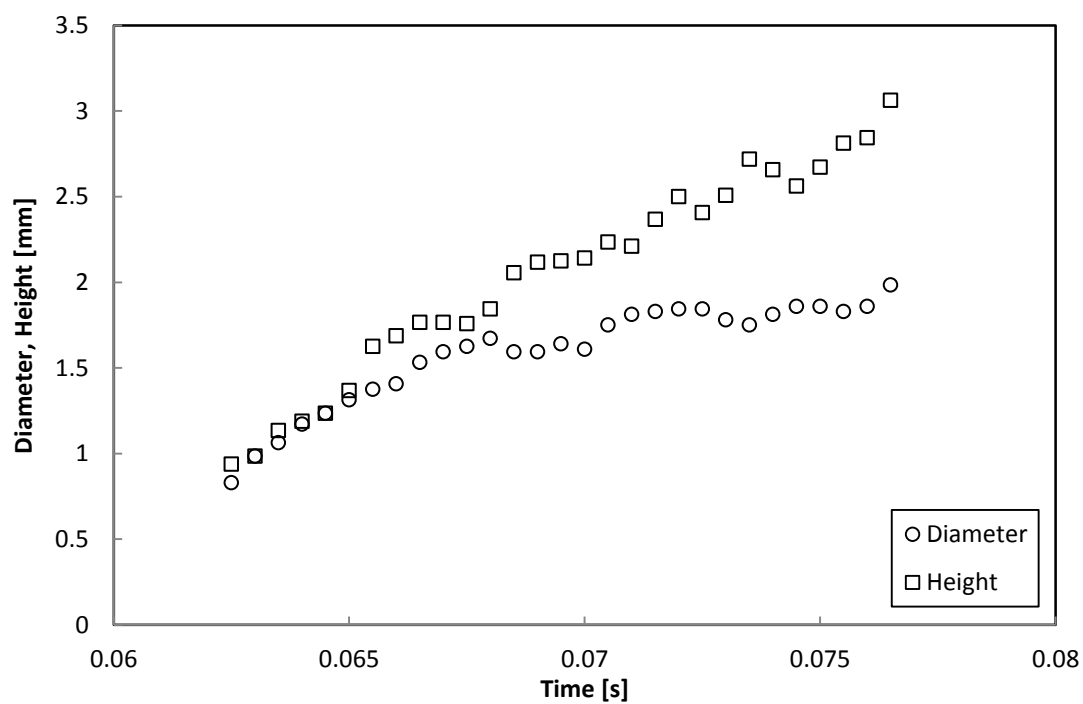


Figure 7.5: Bubble diameter and height plotted for the growth cycle of Bubble 3 of 14.

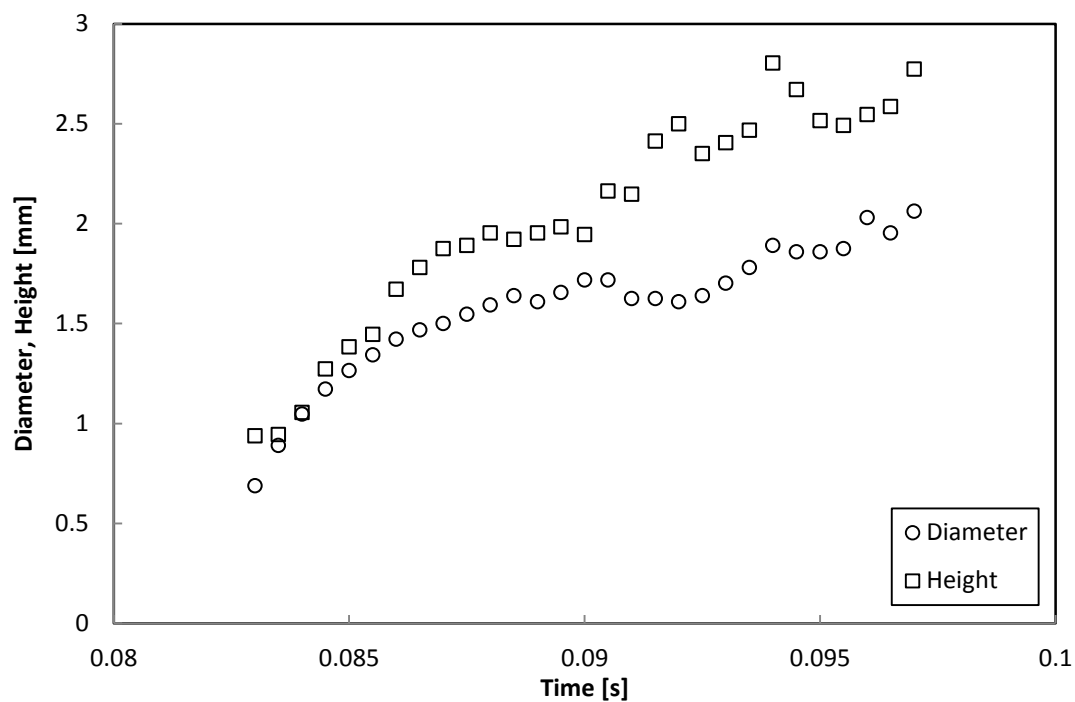


Figure 7.6: Bubble diameter and height plotted for the growth cycle of Bubble 4 of 14.

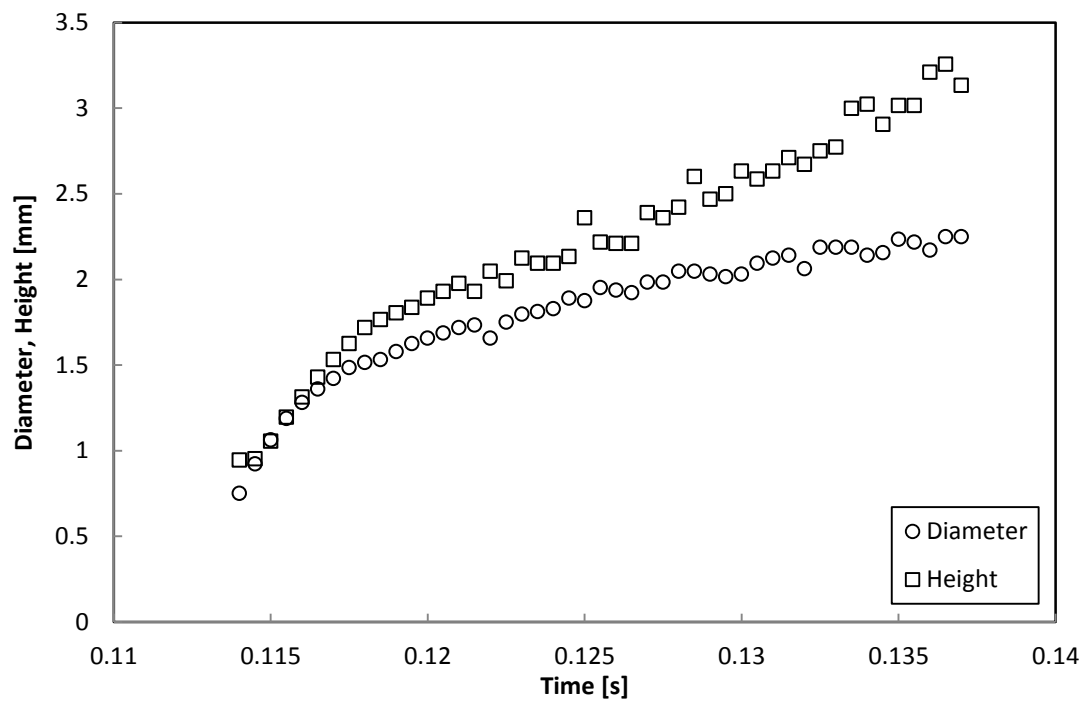


Figure 7.7: Bubble diameter and height plotted for the growth cycle of Bubble 5 of 14.

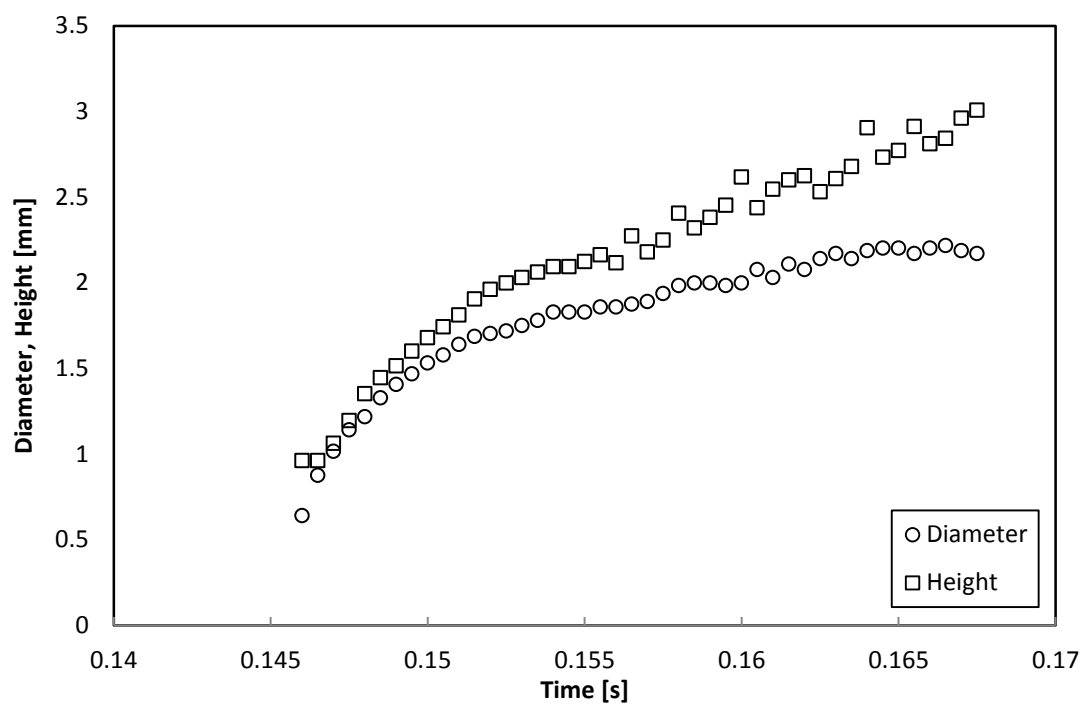


Figure 7.8: Bubble diameter and height plotted for the growth cycle of Bubble 6 of 14.

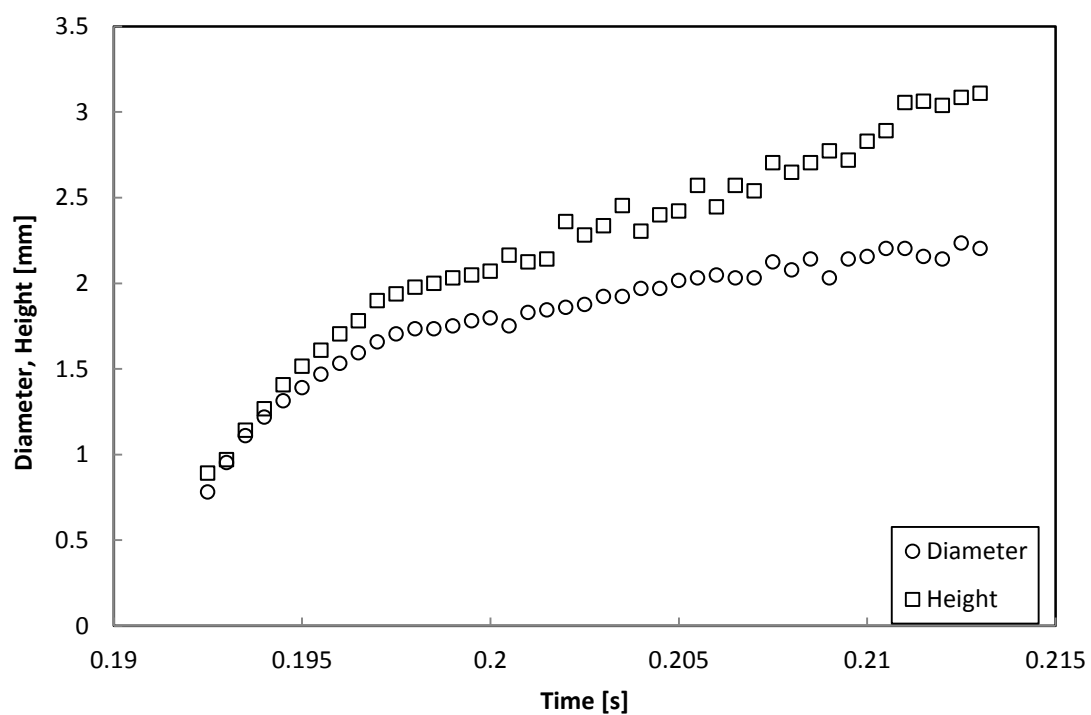


Figure 7.9: Bubble diameter and height plotted for the growth cycle of Bubble 7 of 14.

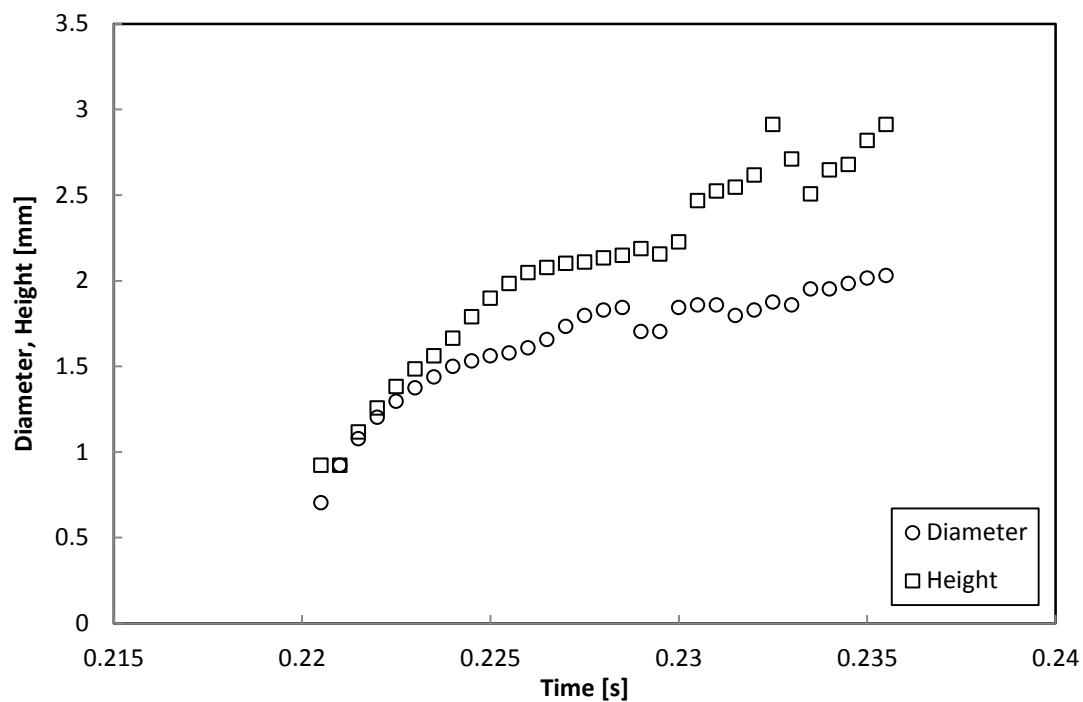


Figure 7.10: Bubble diameter and height plotted for the growth cycle of Bubble 8 of 14.

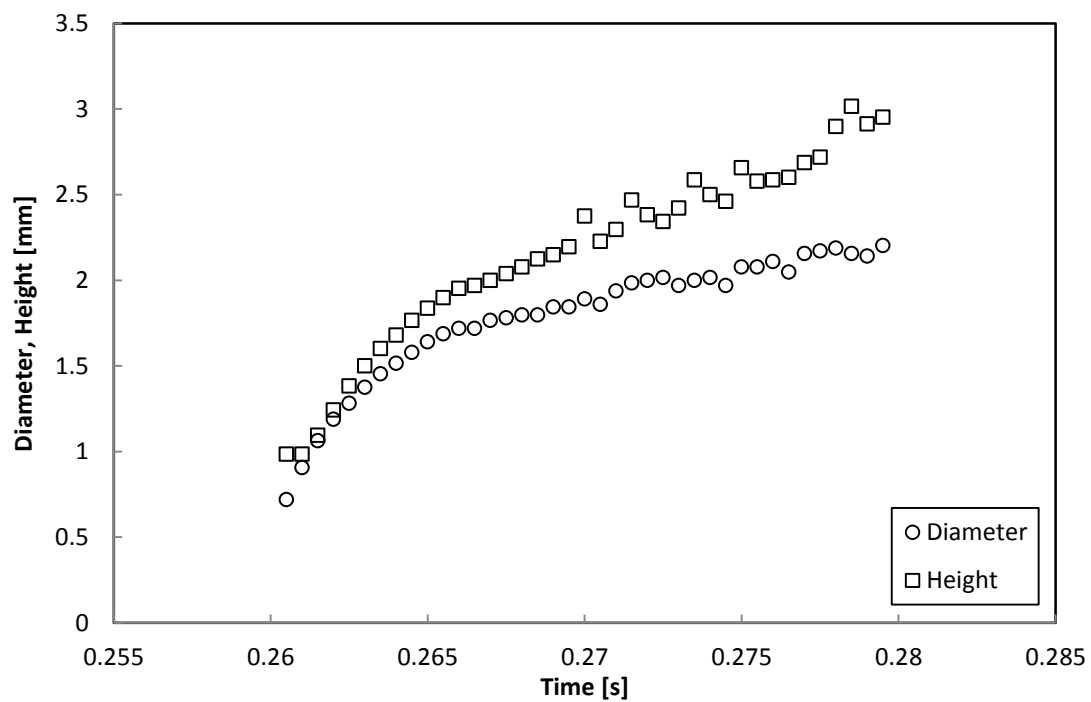


Figure 7.11: Bubble diameter and height plotted for the growth cycle of Bubble 9 of 14.

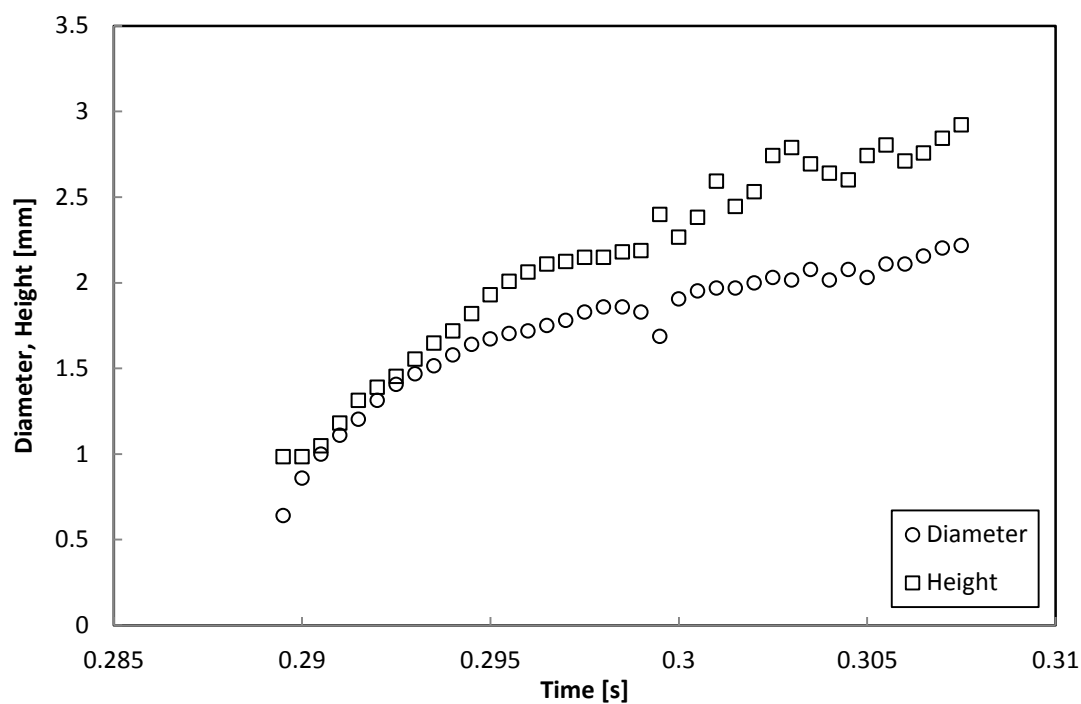


Figure 7.12: Bubble diameter and height plotted for the growth cycle of Bubble 10 of 14.

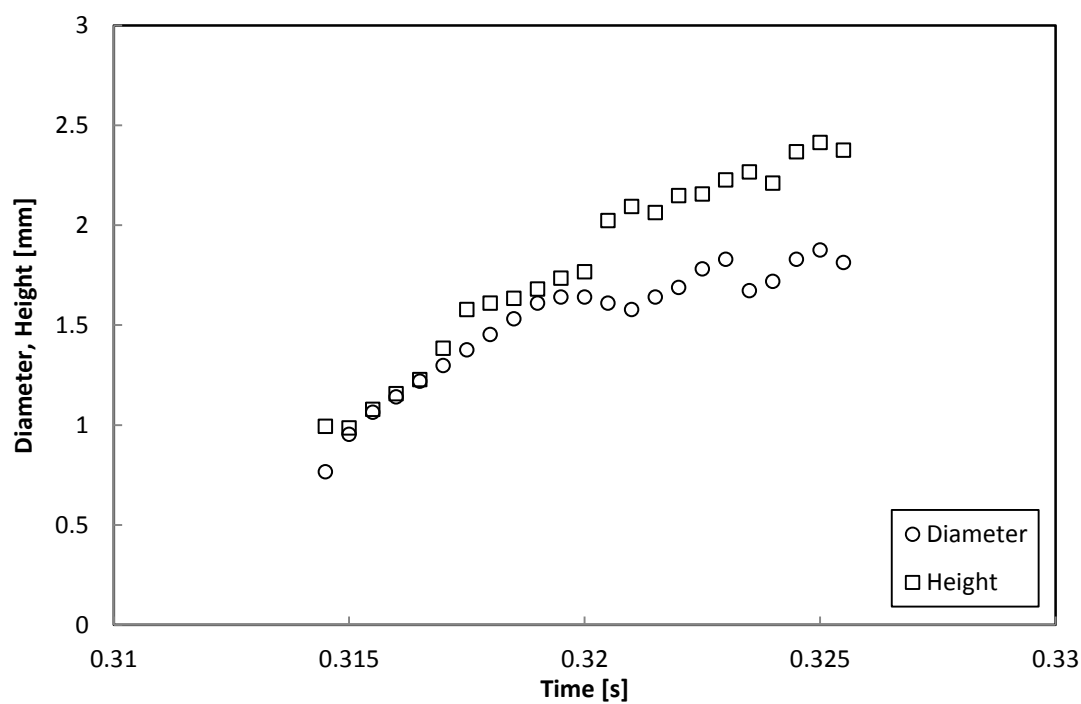


Figure 7.13: Bubble diameter and height plotted for the growth cycle of Bubble 11 of 14.

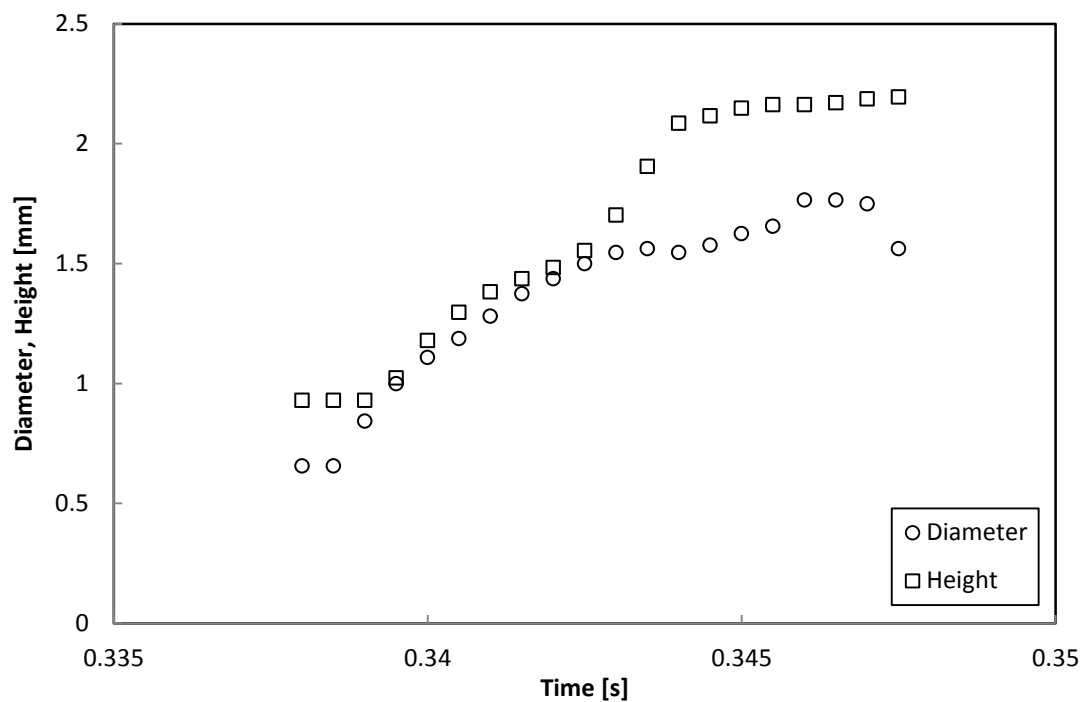


Figure 7.14: Bubble diameter and height plotted for the growth cycle of Bubble 12 of 14.

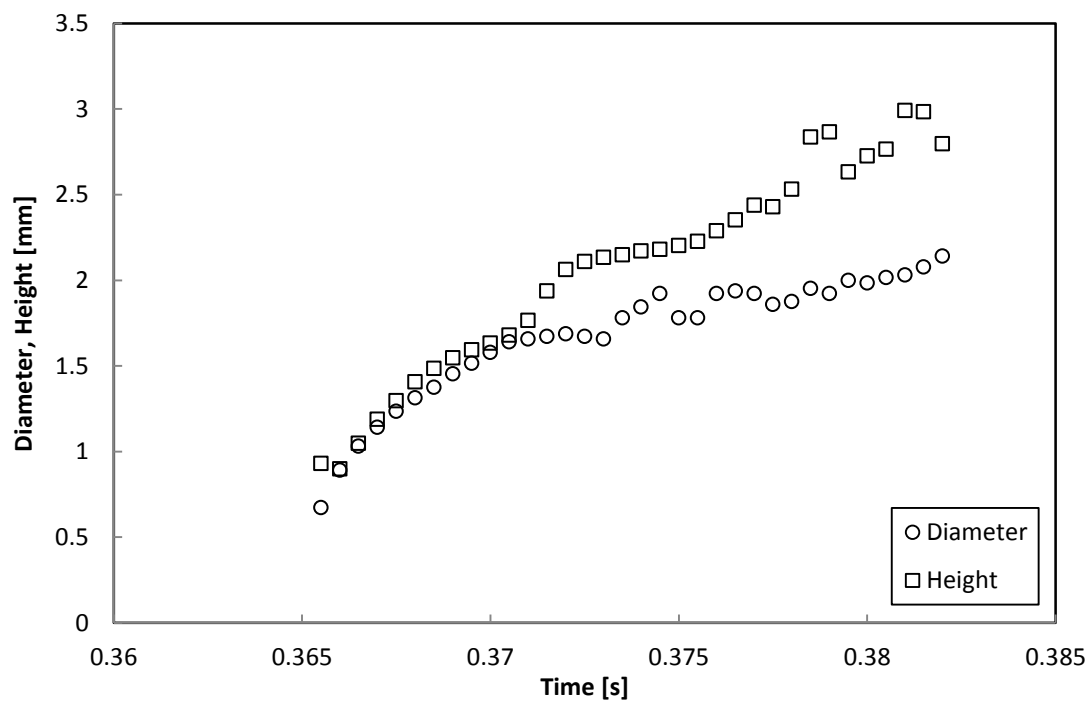


Figure 7.15: Bubble diameter and height plotted for the growth cycle of Bubble 13 of 14.

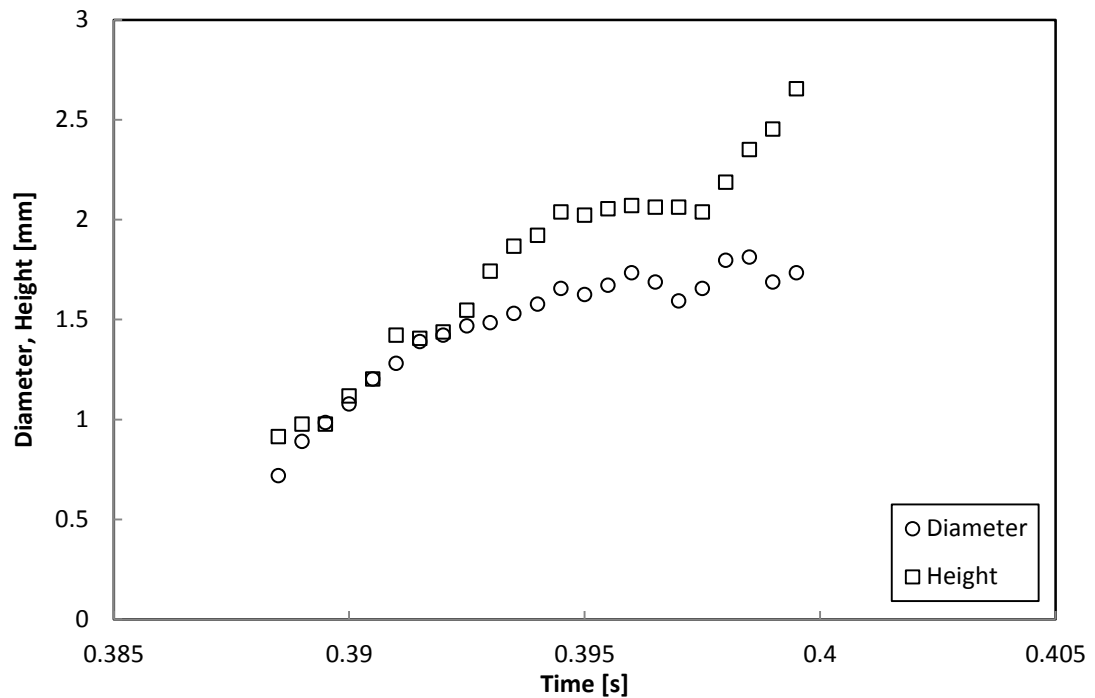


Figure 7.16: Bubble diameter and height plotted for the growth cycle of Bubble 14 of 14.

Applying the bubble diameter and height data to the force model (Eq. 7.4) yields predictions for liquid velocities. Velocities are reported on a per bubble basis for total, x-component, and y-component results; however, average values for the 14 bubble span are considered the best indicator of the influence a single bubble has on liquid velocities. The region of influence width used for the PTV is reflected in the model as the diameter when calculating *area of influence* (Eq. 7.5). Results for the three regions of interest are displayed in Table 7.1-Table 7.3 below.

$$A_{inf} = \frac{\pi}{4} (n\bar{d})^2 ; \quad n = 1, 2 \text{ or } 3 \quad (\text{Eq. 7.5})$$

Table 7.1: Velocity predictions made by the semi-empirical model with an area of influence of 1 average bubble diameter ($n=1$). Velocity predictions for each bubble and for the combined 14 bubbles are shown.

Bubble #	 Velocity [mm¹s⁻¹]	x-Velocity [mm¹s⁻¹]	y-Velocity [mm¹s⁻¹]
1	68.17	36.80	57.38
2	70.56	38.09	59.39
3	77.47	41.82	65.21
4	77.35	41.76	65.11
5	82.99	44.80	69.85
6	68.47	36.97	57.63
7	75.77	40.91	63.78
8	69.39	37.46	58.41
9	73.07	39.45	61.51
10	71.08	38.37	59.83
11	55.87	30.17	47.03
12	48.39	26.12	40.73
13	64.97	35.08	54.69
14	64.44	34.79	54.24
Average	69.14	37.33	58.20
Uncertainty	±2.40	±1.30	±2.02
Min	48.39	26.12	40.73
Max	82.99	44.80	69.85

Table 7.2: Velocity predictions made by the semi-empirical model with an area of influence of 1 average bubble diameter (n=2). Velocity predictions for each bubble and for the combined 14 bubbles are shown.

Bubble #	 Velocity mm¹s⁻¹	x-Velocity mm¹s⁻¹	y-Velocity mm¹s⁻¹
1	48.20	27.64	39.49
2	49.89	28.61	40.87
3	54.78	31.42	44.87
4	54.69	31.37	44.80
5	58.68	33.65	48.07
6	48.41	27.77	39.66
7	53.58	30.73	43.89
8	49.07	28.14	40.20
9	51.67	29.63	42.33
10	50.26	28.82	41.17
11	39.51	22.66	32.37
12	34.22	19.62	28.03
13	45.94	26.35	37.64
14	45.56	26.13	37.33
Average	48.89	28.04	40.05
Uncertainty	±2.40	±1.38	±2.02
Min	34.22	19.62	28.03
Max	58.68	33.65	48.07

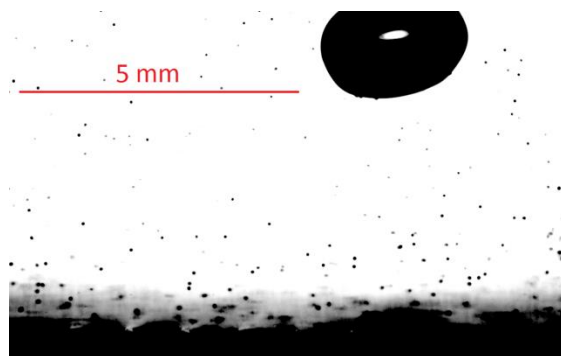
Table 7.3: Velocity predictions made by the semi-empirical model with an area of influence of 1 average bubble diameter (n=3). Velocity predictions for each bubble and for the combined 14 bubbles are shown.

Bubble #	 Velocity mm¹s⁻¹	x-Velocity mm¹s⁻¹	y-Velocity mm¹s⁻¹
1	39.36	24.60	30.72
2	40.74	25.47	31.80
3	44.73	27.96	34.91
4	44.66	27.92	34.86
5	47.91	29.95	37.40
6	39.53	24.71	30.85
7	43.75	27.35	34.15
8	40.06	25.04	31.27
9	42.19	26.37	32.93
10	41.04	25.65	32.03
11	32.26	20.17	25.18
12	27.94	17.46	21.81
13	37.51	23.45	29.28
14	37.20	23.26	29.04
Average	39.92	24.95	31.16
Uncertainty	±2.40	±1.50	±1.87
Min	27.94	17.46	21.81
Max	47.91	29.95	37.40

7.3. Particle Tracking Velocimetry

The following series of images were excerpted from the original high-speed video. The series spans 23.5 milliseconds for the frames in the range of [-7280 to -7233].

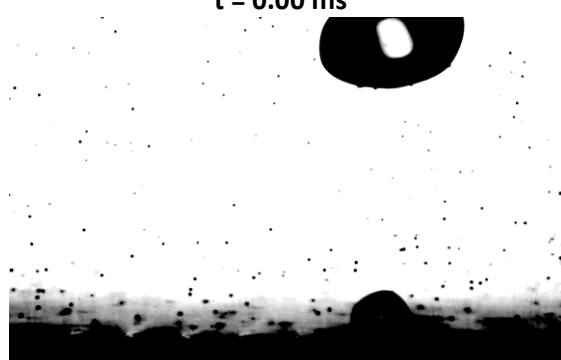
Figure 7.17: Series of 48 frames of the adiabatic single bubble growing and departing the structured surface. $P_{\text{injection}} \approx 0.14$ bar, gage; $V \approx 0.01$ Lpm; $\alpha = 30^\circ$; exposure time = $50 \mu\text{s}$; Aperture 100% open; Focus Middle; FOV = 10 mm x 6.25 mm.



t = 0.00 ms



t = 0.50 ms



t = 1.00 ms



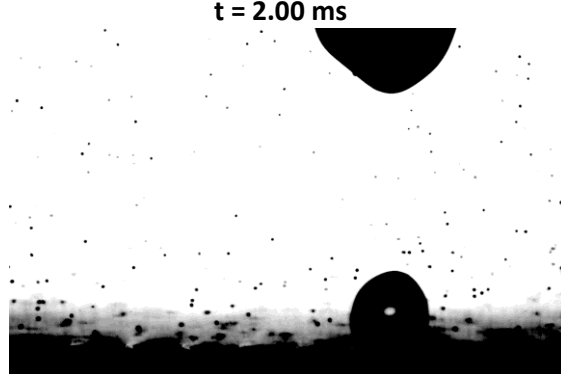
t = 1.50 ms



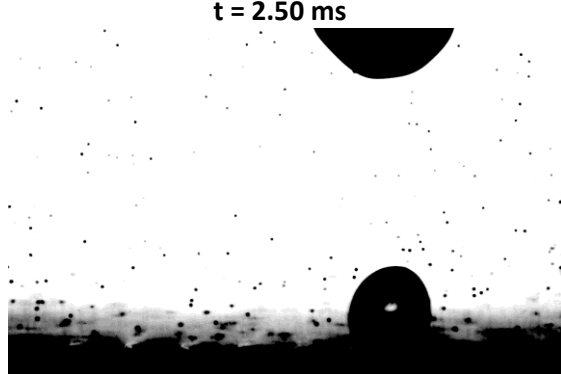
t = 2.00 ms



t = 2.50 ms



t = 3.00 ms



t = 3.50 ms

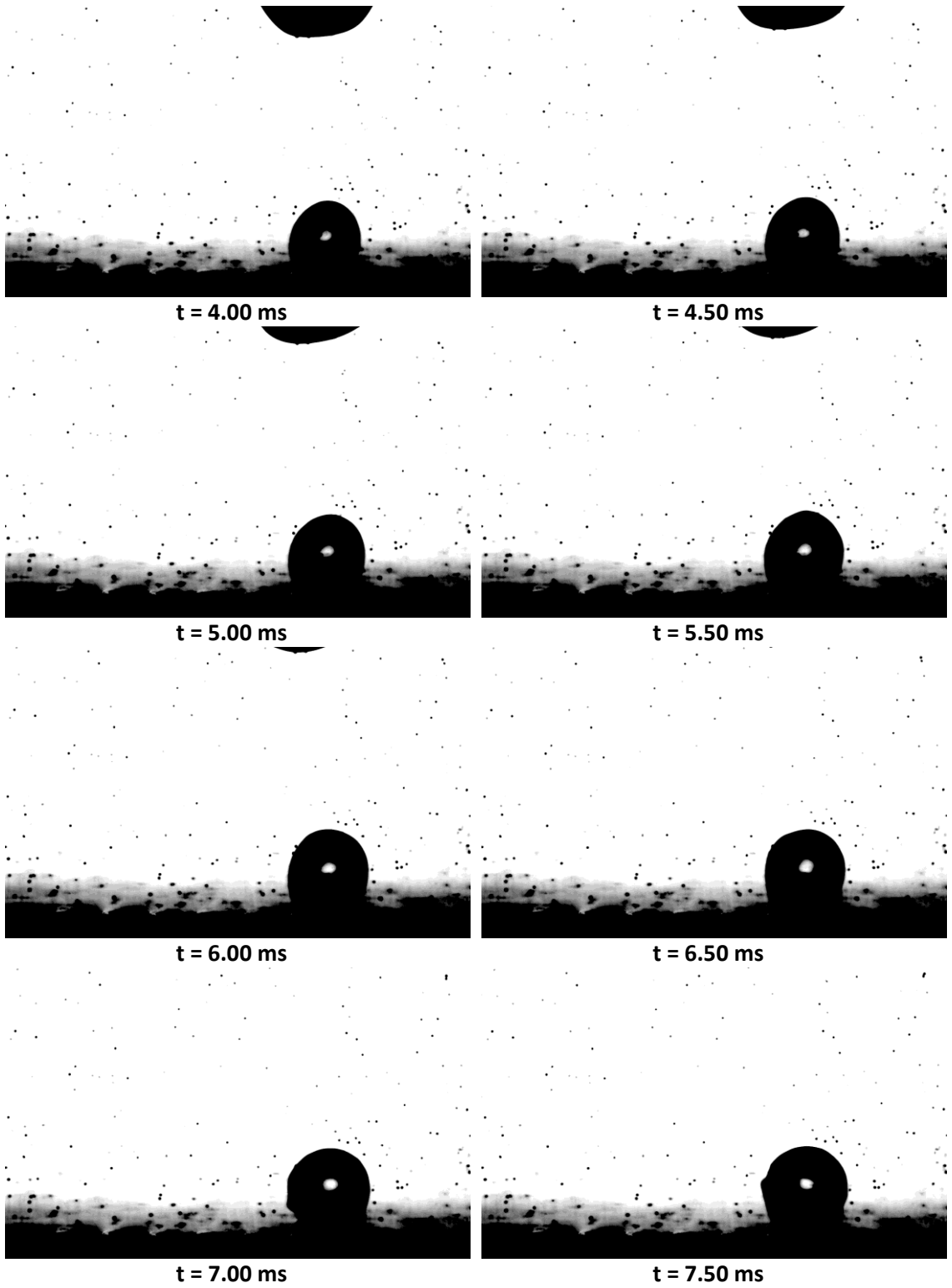


(Figure 7.17 continued)

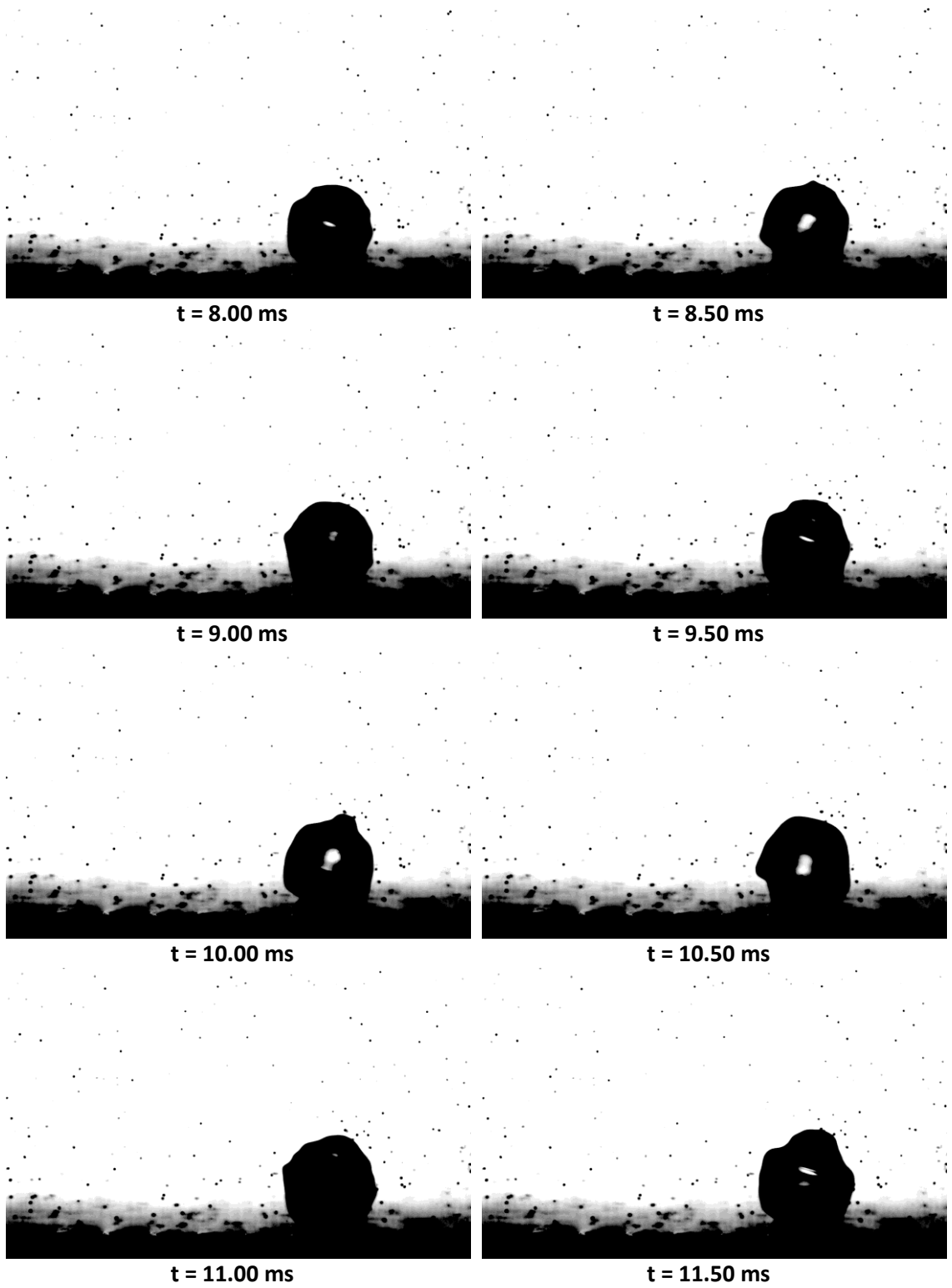


(Figure 7.17 continued)

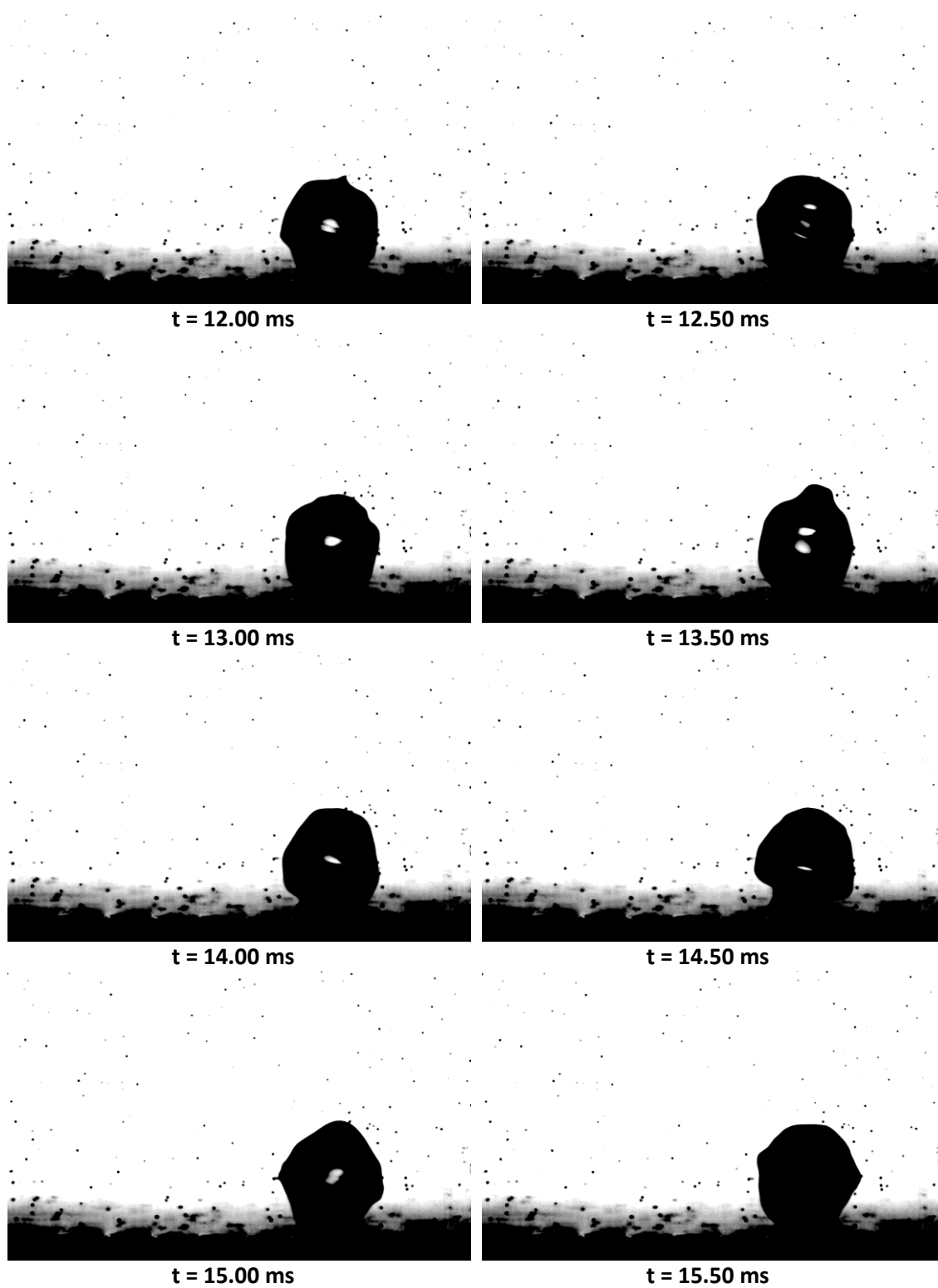


(Figure 7.17 continued)

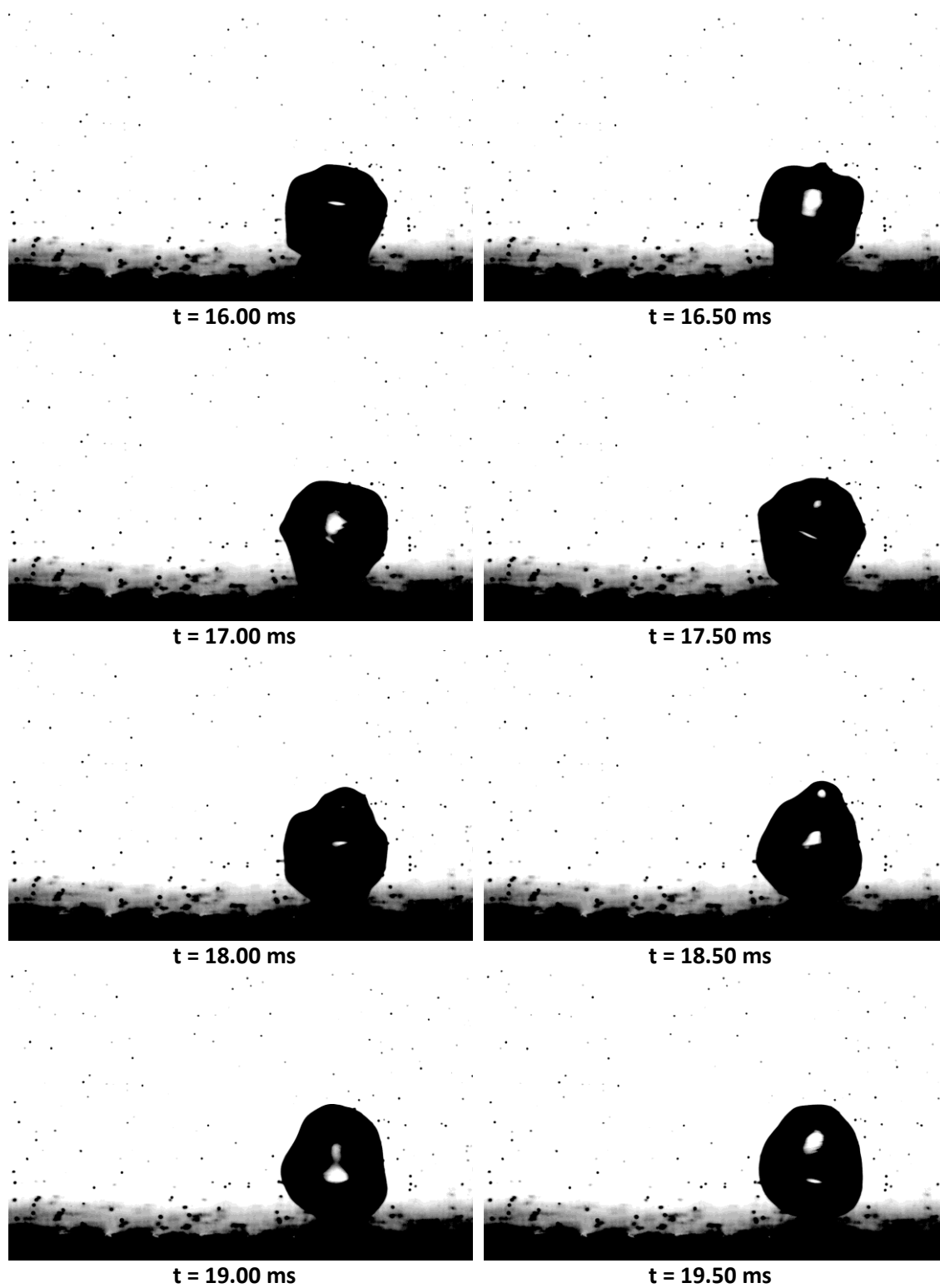


(Figure 7.17 continued)

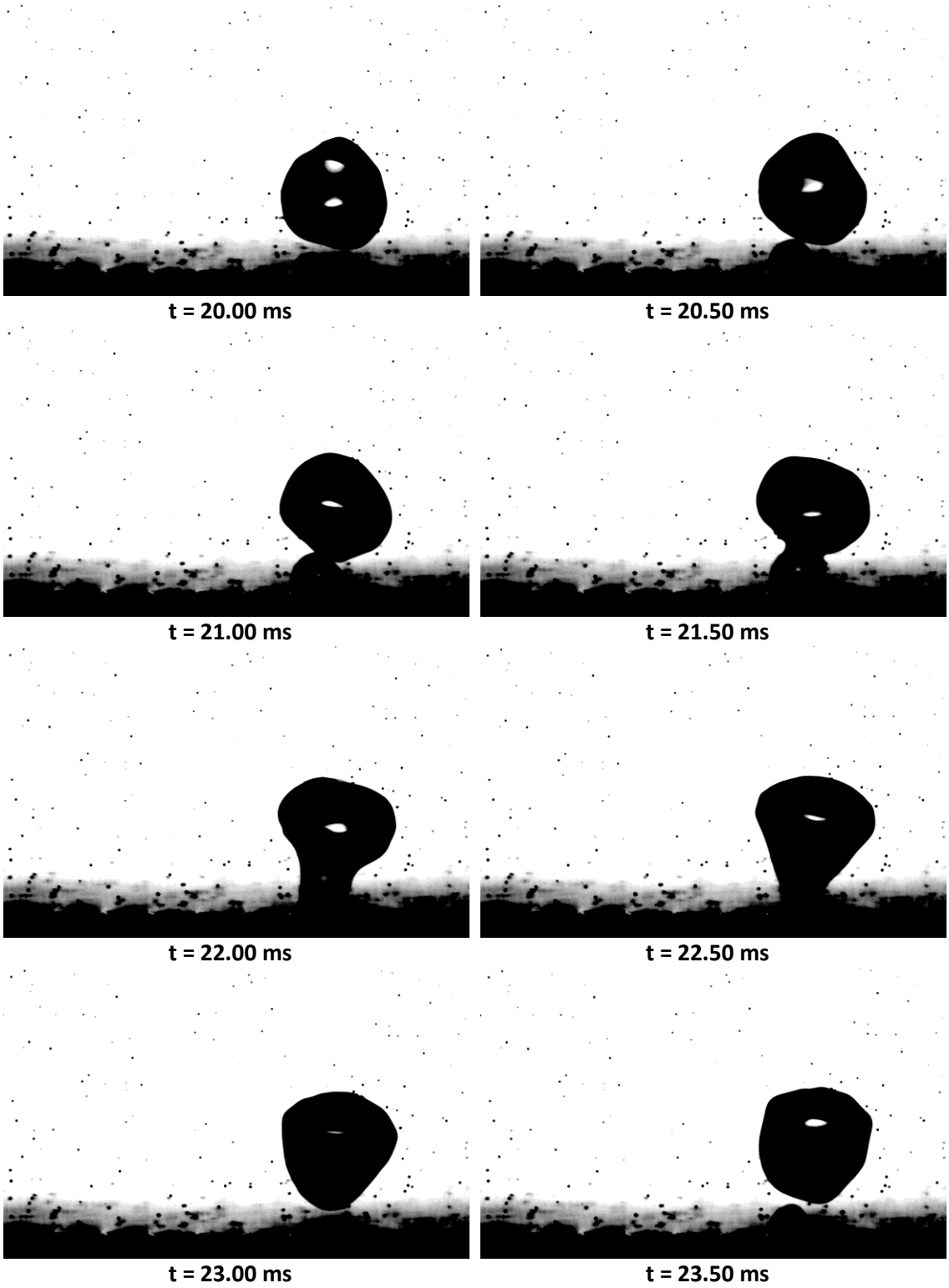
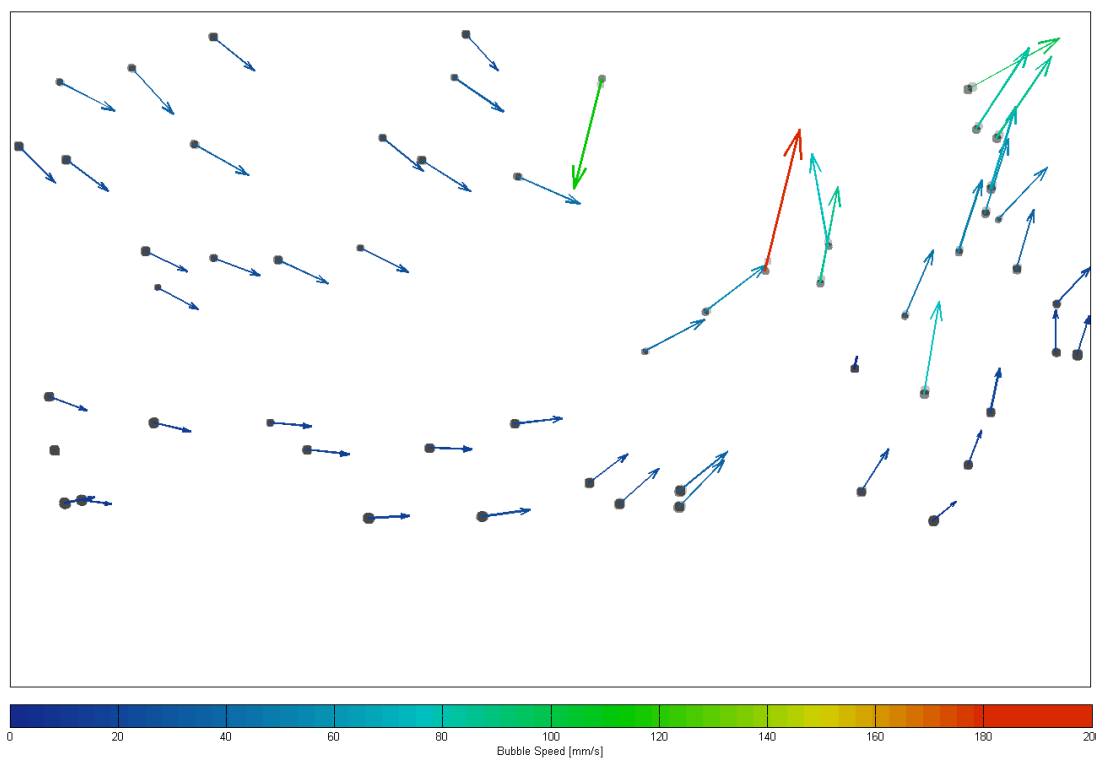


(Figure 7.17 continued)

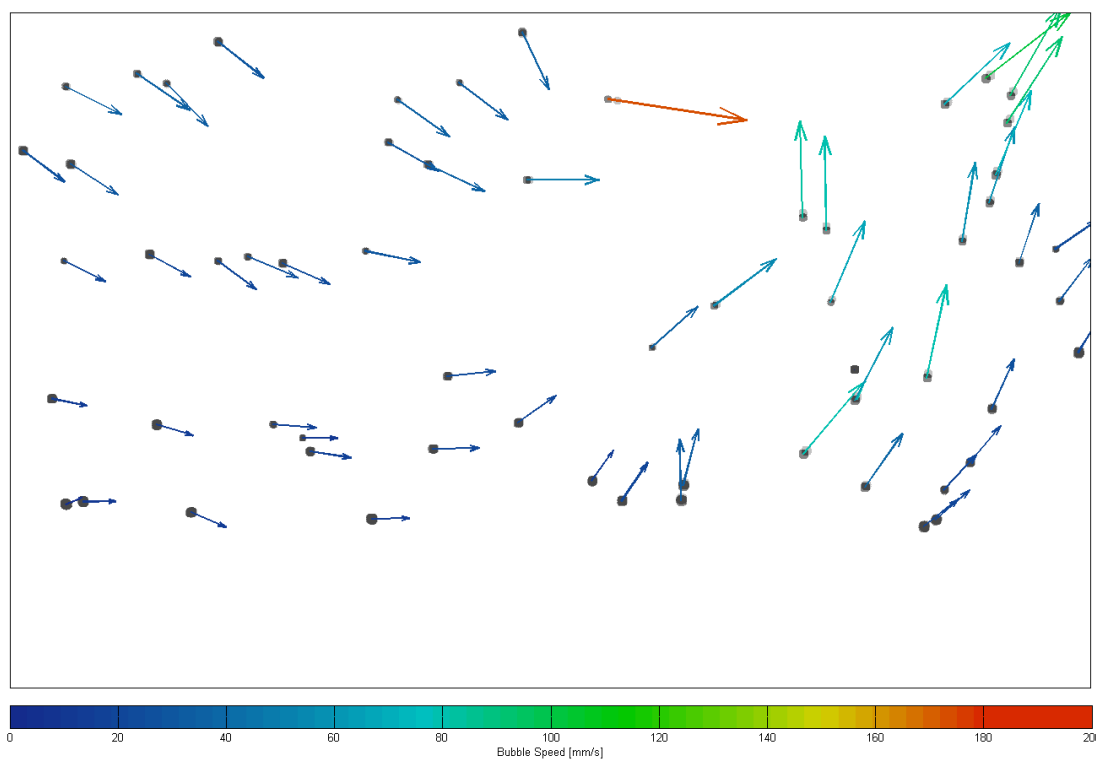
Figure 7.17 shows the growth and departure of a single bubble from a cavity on the asymmetric structured surface. It is apparent in the images that the bubble grows rapidly in height—normal to the shallow face of the ratchet. As the bubble continues to grow, the shape of the bubble undulates rapidly and unpredictably ($t = 12.00$ ms to 14 ms). Often when the bubble departs the surface it coalesces with the subsequent bubble ($t = 20$ ms to 22 ms). Despite being approximately 2 mm in diameter at departure, it travels initially from left to right before continuing vertically out of the field of view.

Particle tracking velocimetry was completed for all 800 frames in the video. The results from this analysis show slow moving particles traveling left to right across the field of view caused by the slow recirculation within the pool. As these bubbles approach the region where the bubble is growing, they are accelerated upwards at an angle as a result of bubble growth. In the interest of space, a sequence of only eight frames is shown to illustrate the PTV results.

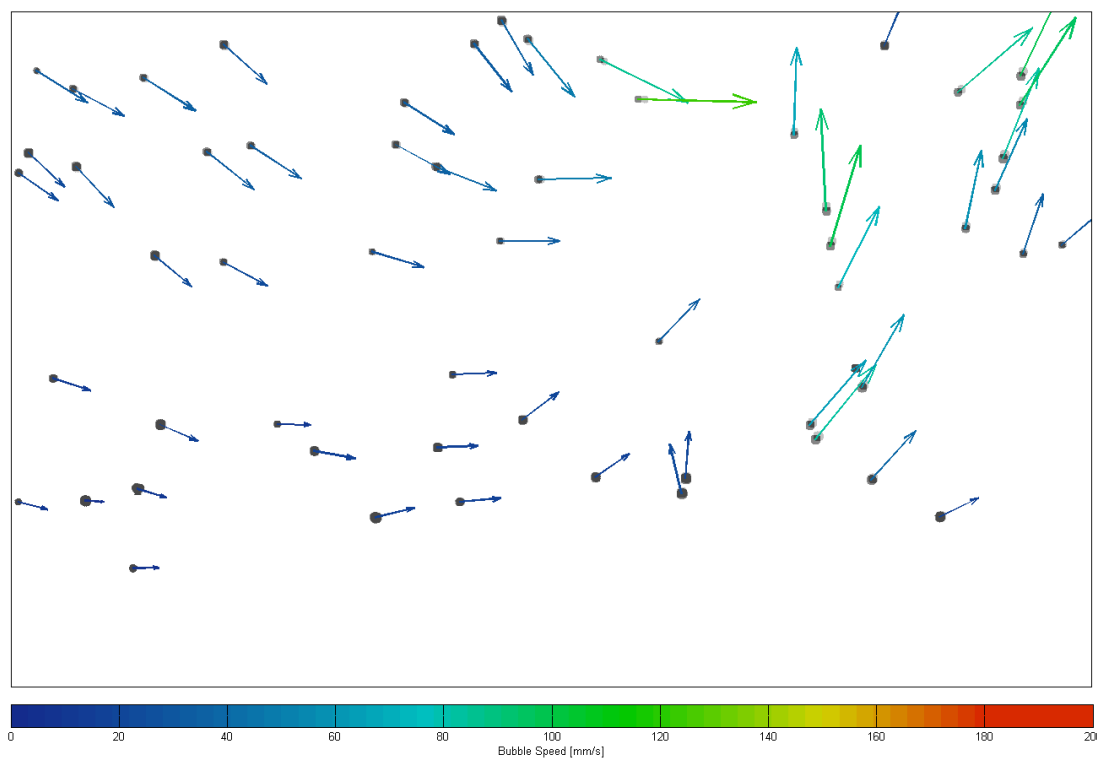
Figure 7.18: Series of 8 frames of particle tracking results during the growth of a bubble on the surface. $P_{\text{injection}} \approx 0.14$ bar,gage; $V \approx 0.01$ Lpm; $\alpha = 30^\circ$; exposure time = $50 \mu\text{s}$; Aperture 100% open; Focus Middle; FOV = 10 mm x 6.25 mm. Color bars shown indicate particle velocity.



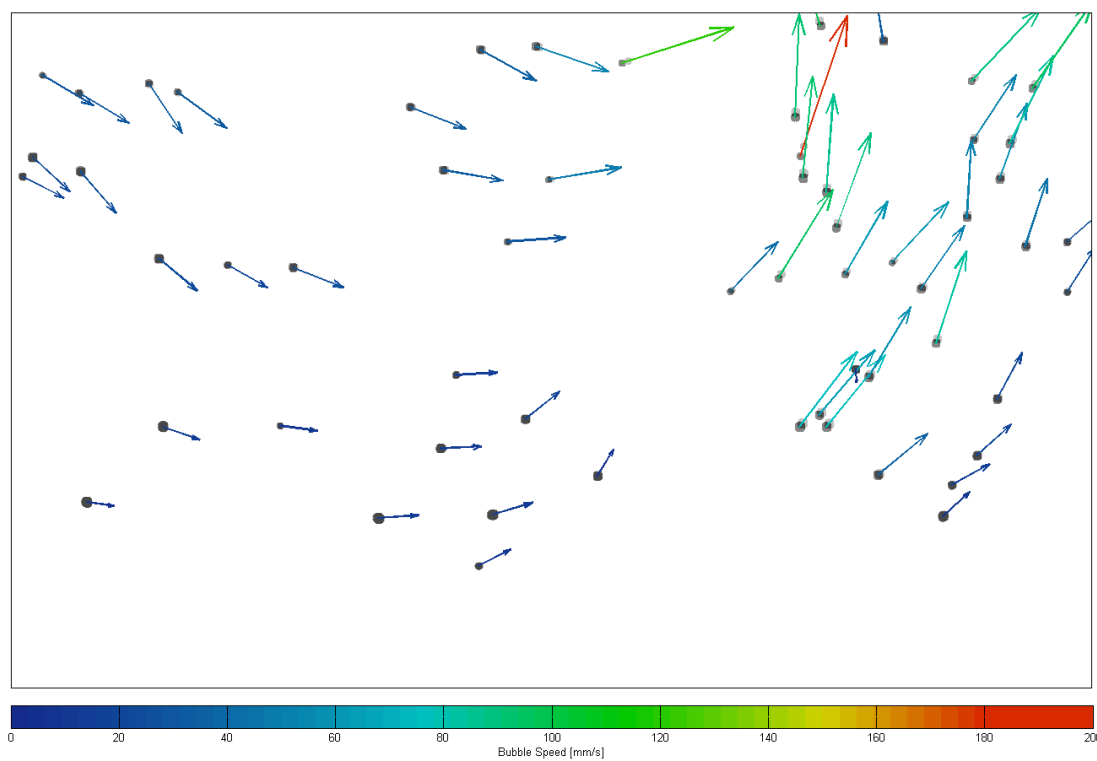
$t = 0.0$ ms



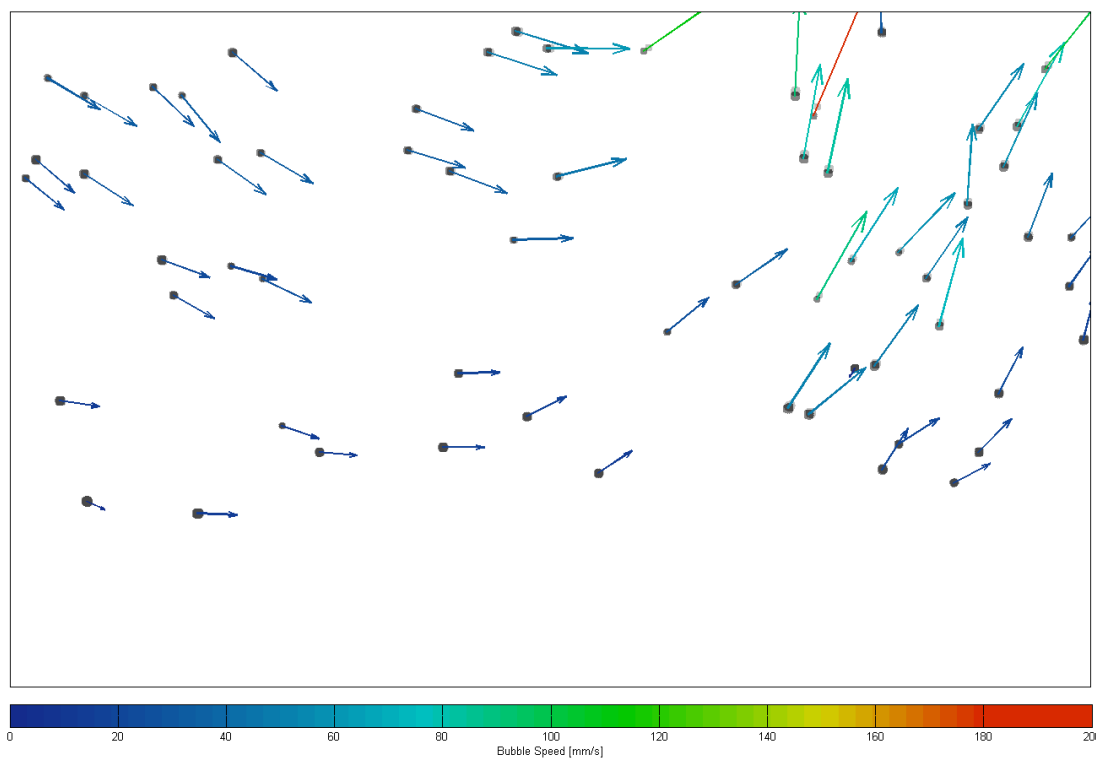
$t = 2.0$ ms



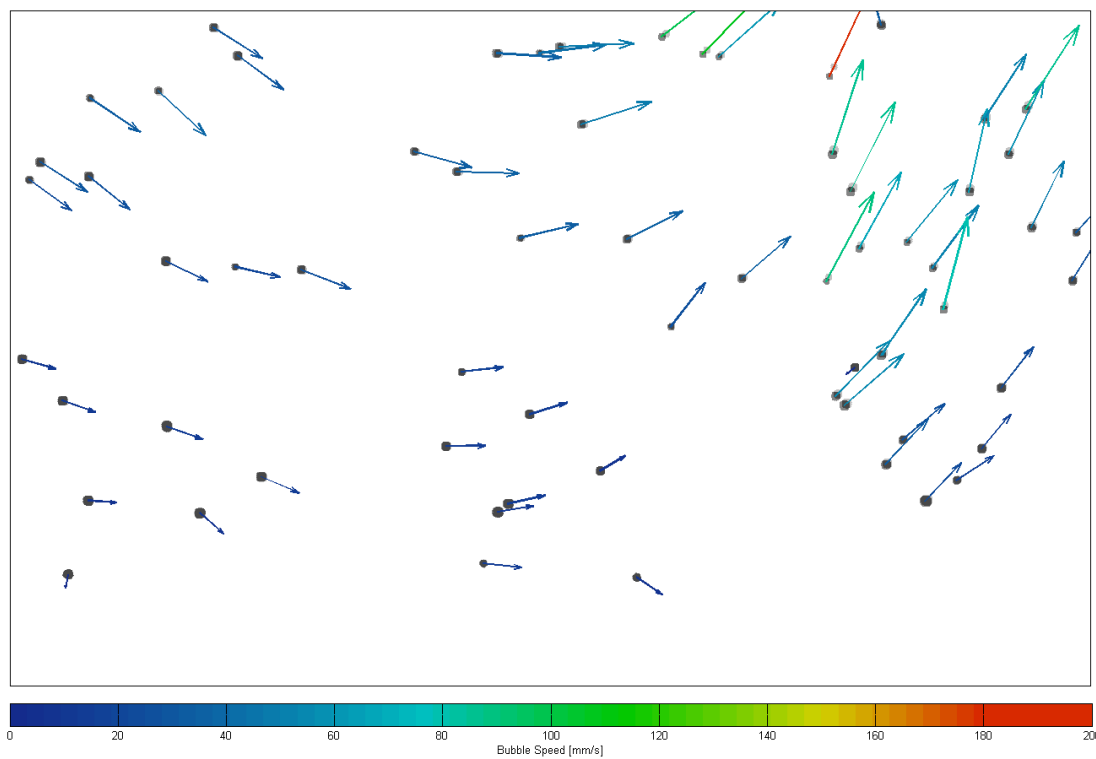
$t = 4.0$ ms



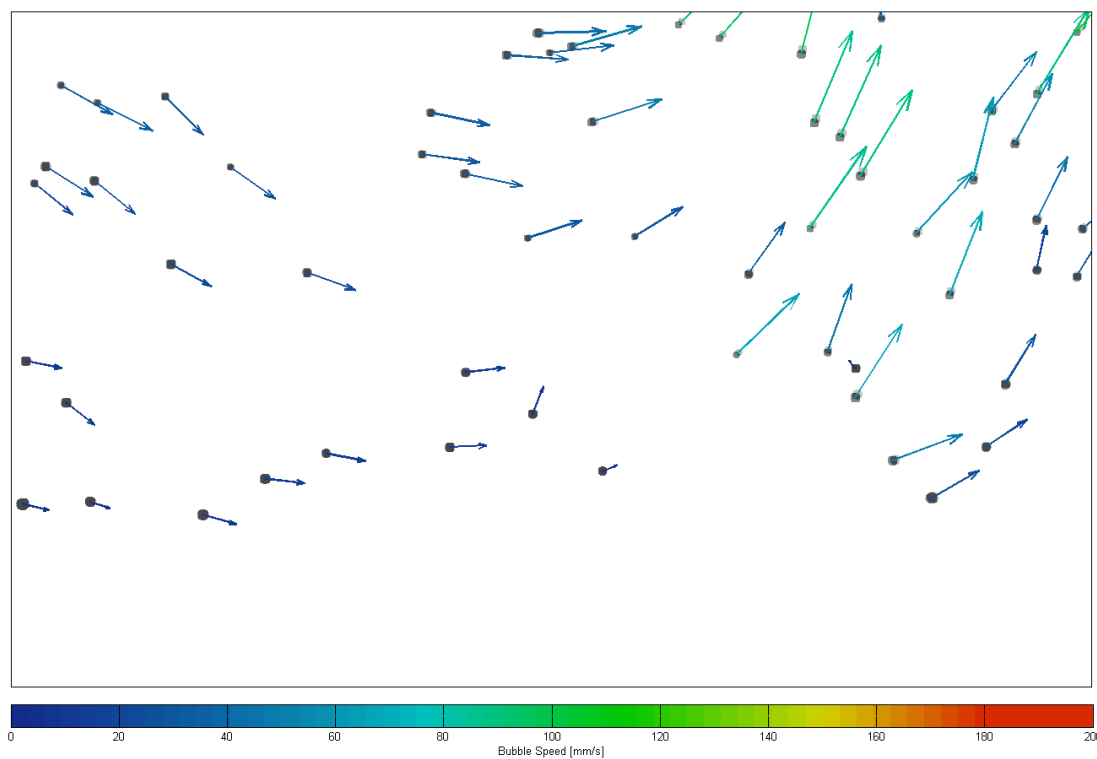
$t = 6.0$ ms



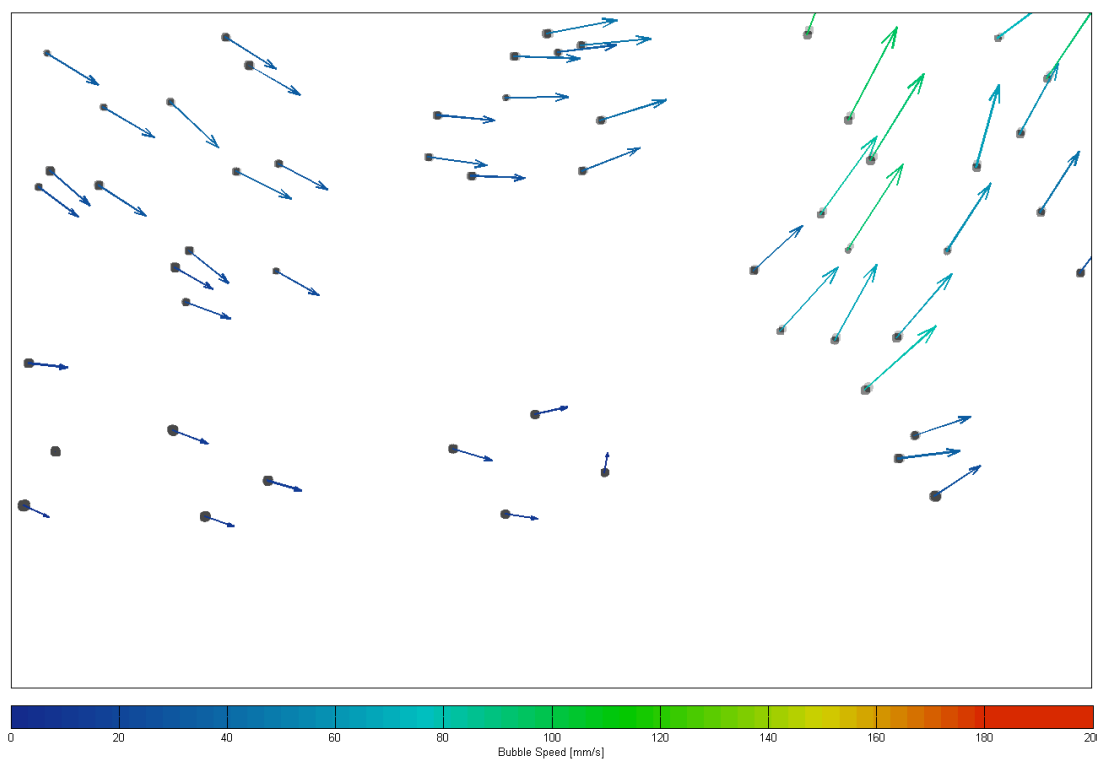
$t = 8.0$ ms



$t = 10.0$ ms



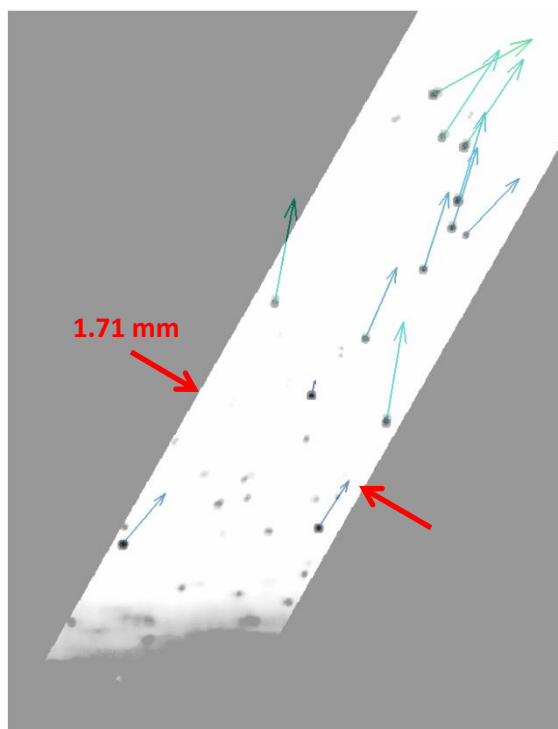
$t = 12.0$ ms



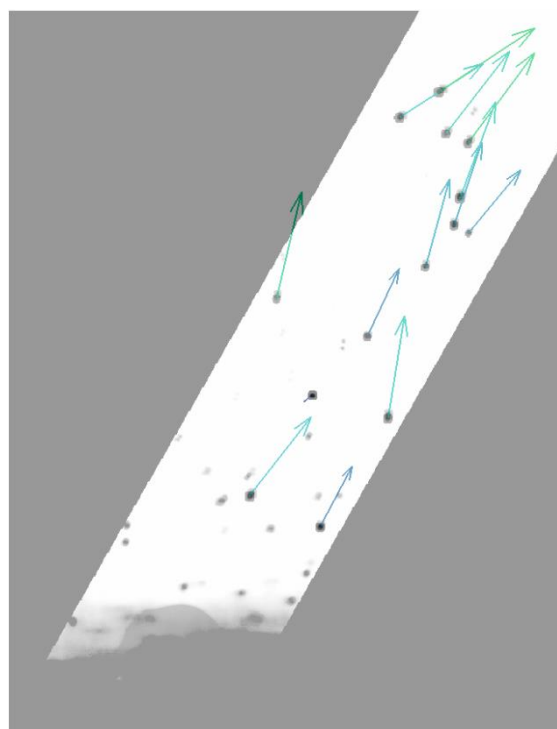
$t = 14.0$ ms

Performing particle tracking velocimetry with a restricted analysis area eliminates irrelevant seed particles from the field of view, limiting the analysis to only consider fluid velocities in close proximity to the bubble. For the results shown, the region of interest is set to 1.71 mm wide—equal to one average bubble diameter. Particles appear in the frames with vectors indicating direction and magnitude. A sequence of composite images shows the original bubble in the same field of view to compare bubble activity with resultant fluid velocities.

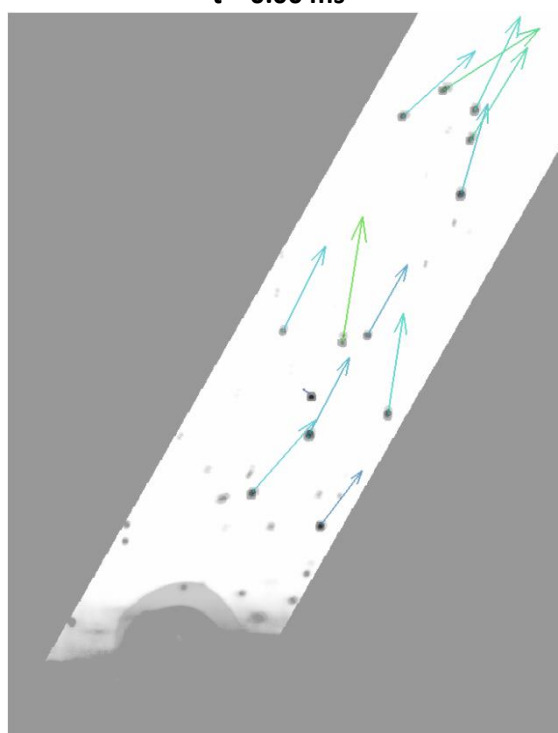
Figure 7.19: Series of 48 frames of a single bubble growing and departing the structured surface with particle tracking results overlaid. $P_{\text{injection}} \approx 0.14$ bar,gage; $V \approx 0.01$ Lpm; $\alpha = 30^\circ$; exposure time = $50 \mu\text{s}$; Aperture 100% open; Focus Middle; FOV = $1.71 \text{ mm} \times 6.25 \text{ mm}$ at 30° .



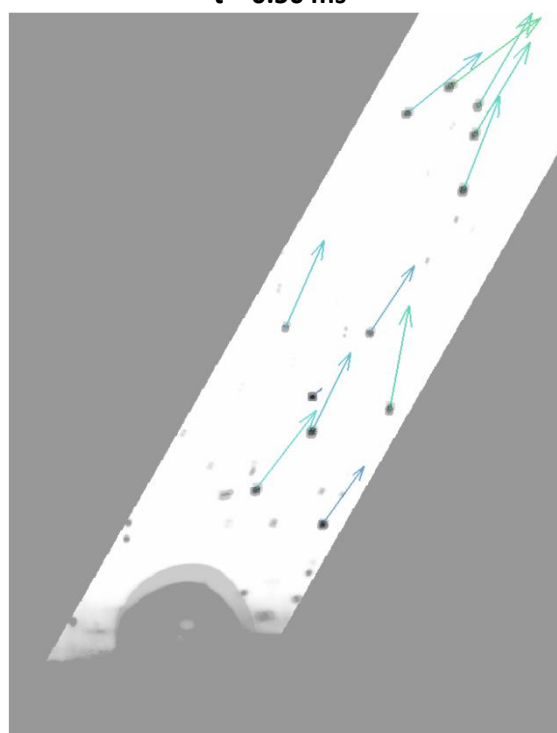
$t = 0.00$ ms



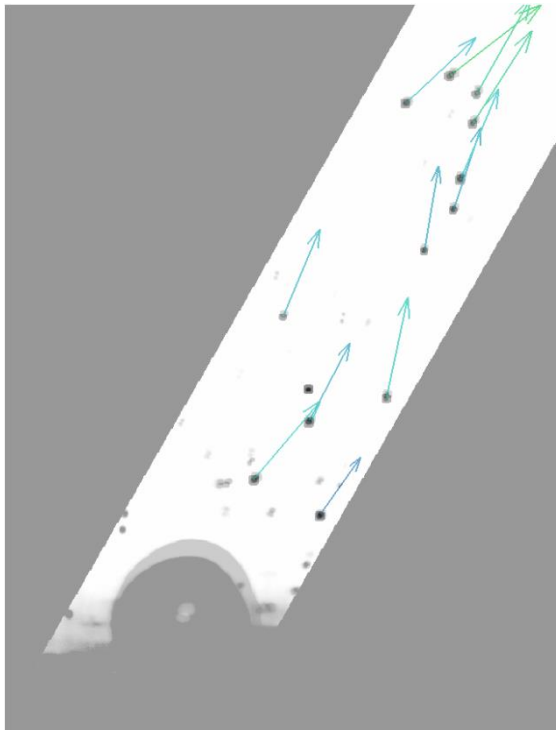
$t = 0.50$ ms



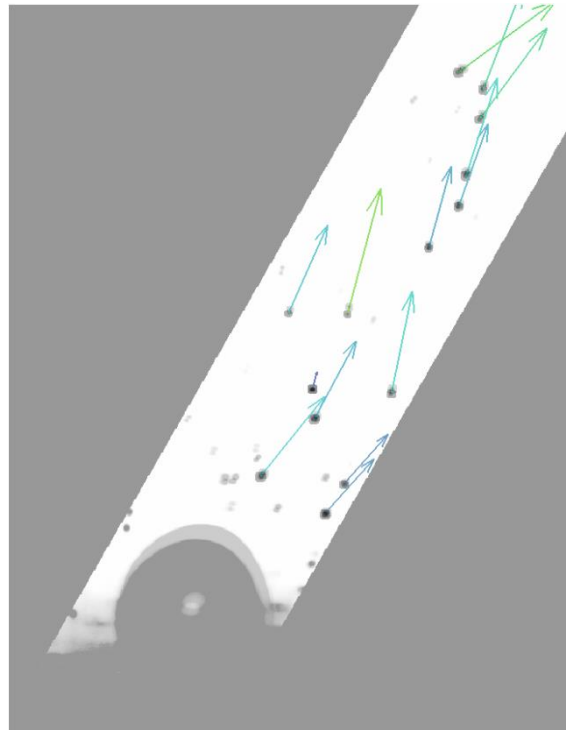
$t = 1.00$ ms



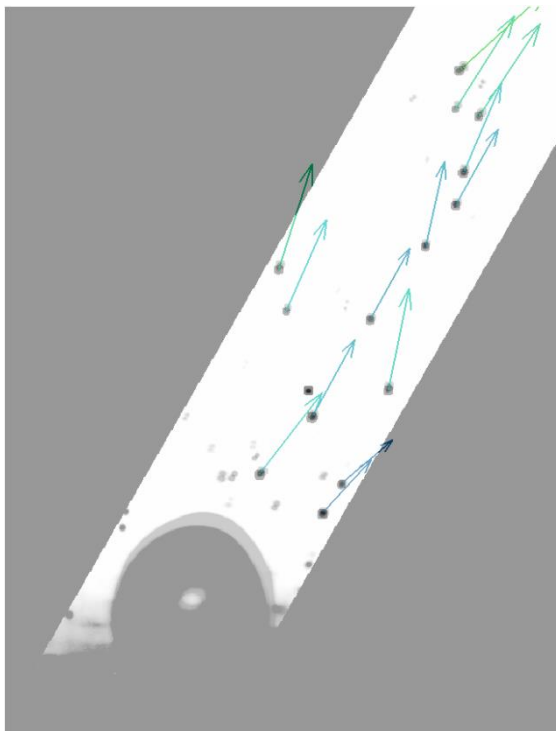
$t = 1.50$ ms



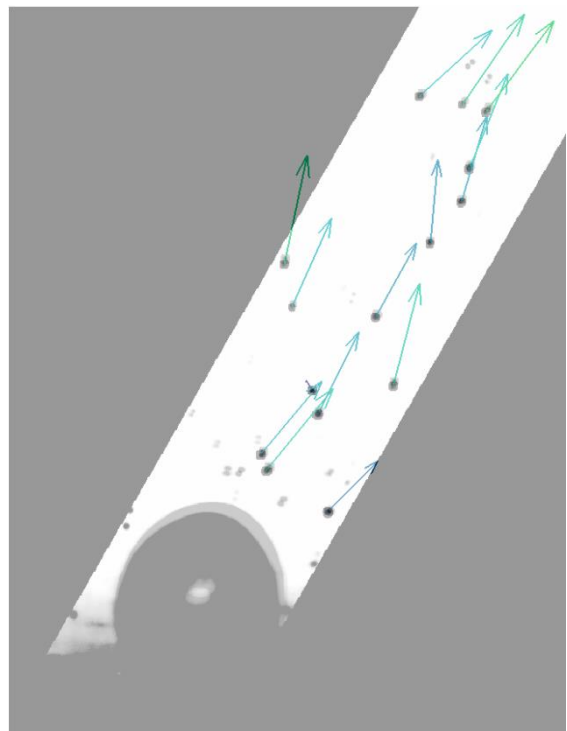
t = 2.00 ms



t = 2.50 ms

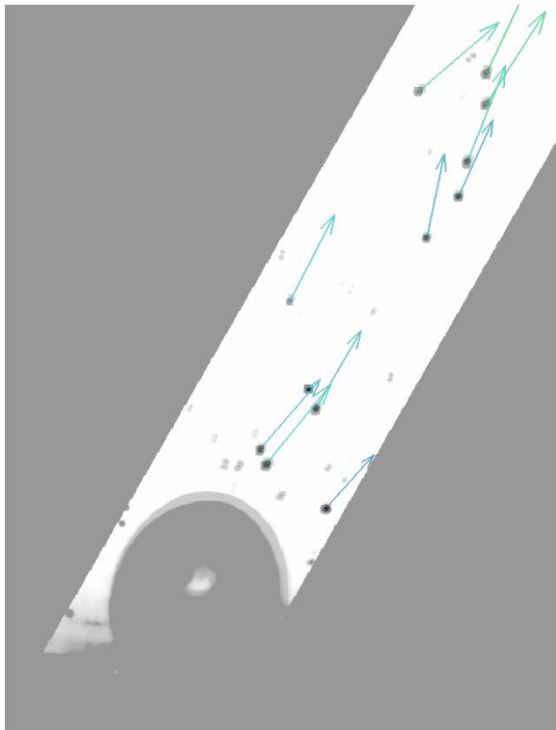


t = 3.00 ms

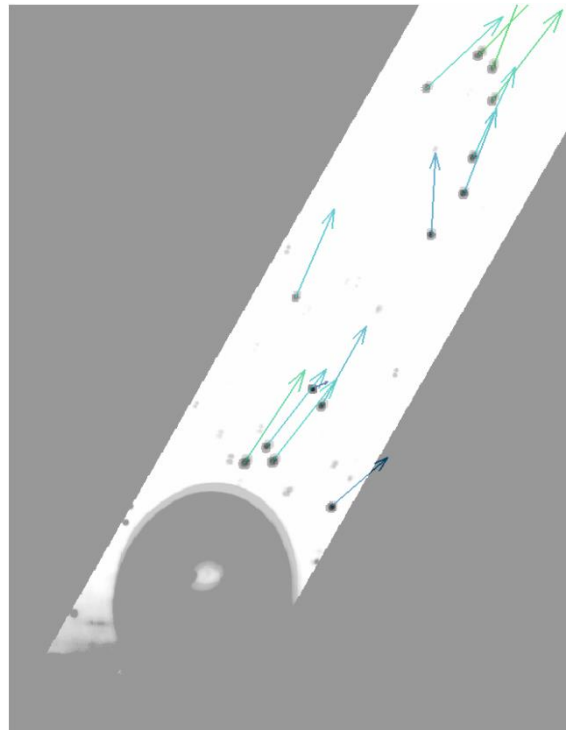


t = 3.50 ms

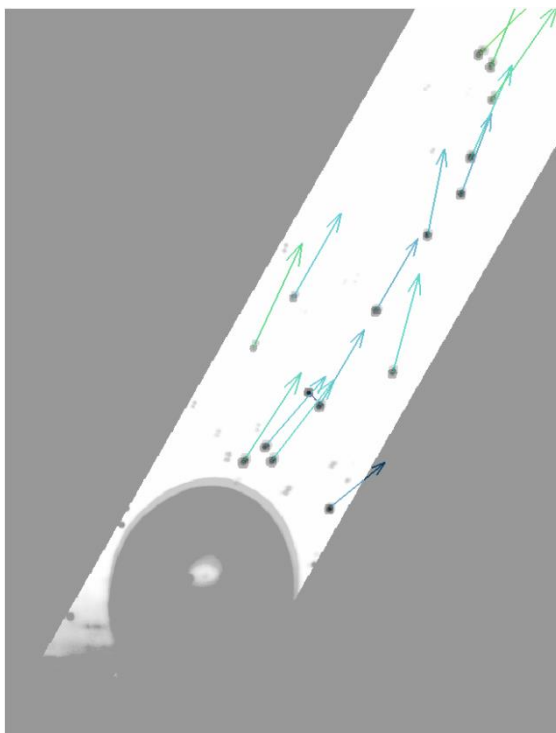
(Figure 7.19 continued)



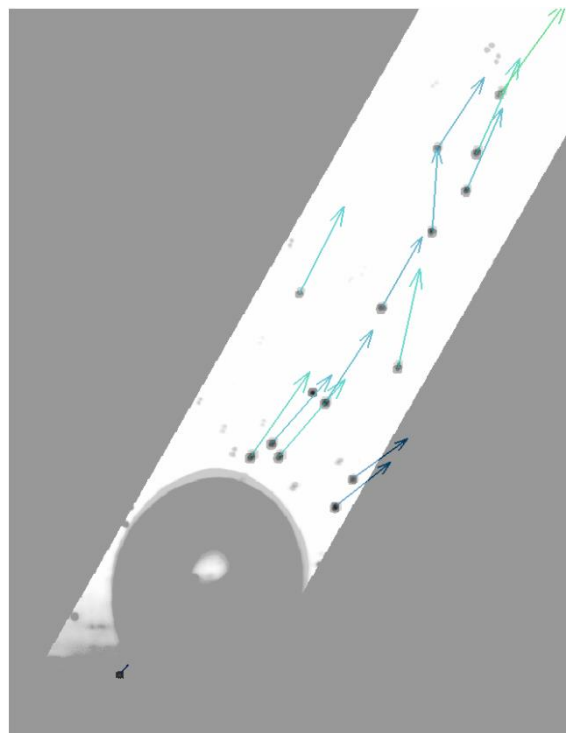
t = 4.00 ms



t = 4.50 ms

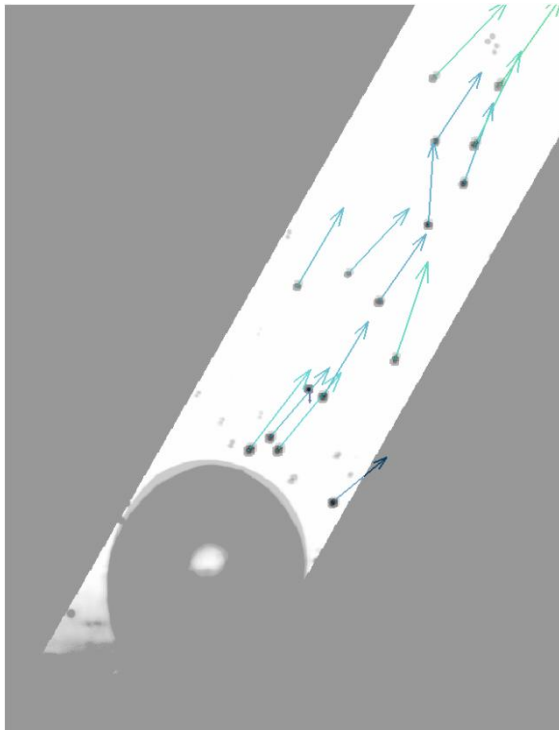


t = 5.00 ms

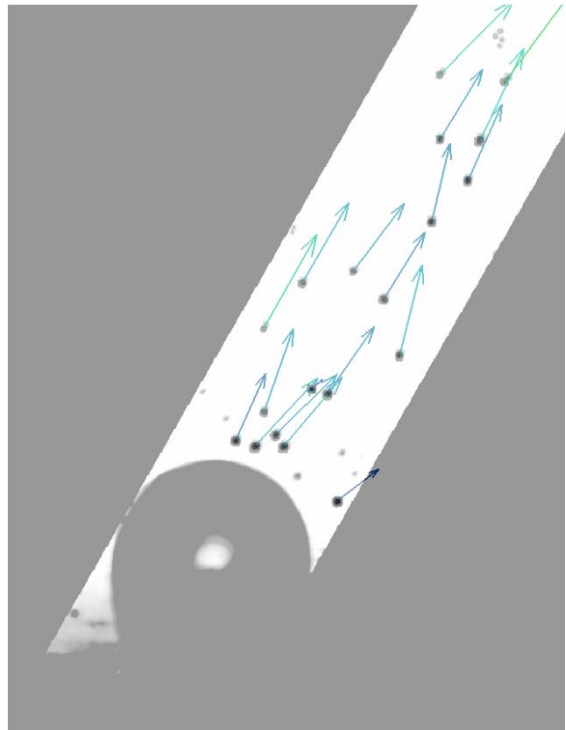


t = 5.50 ms

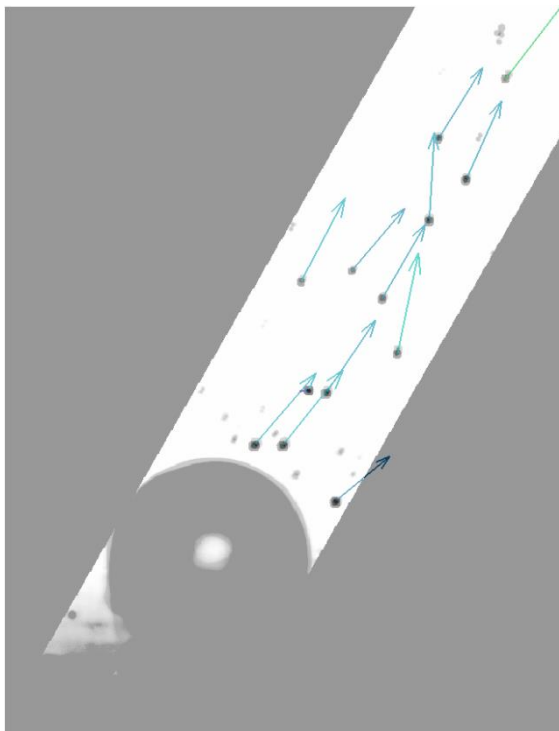
(Figure 7.19 continued)



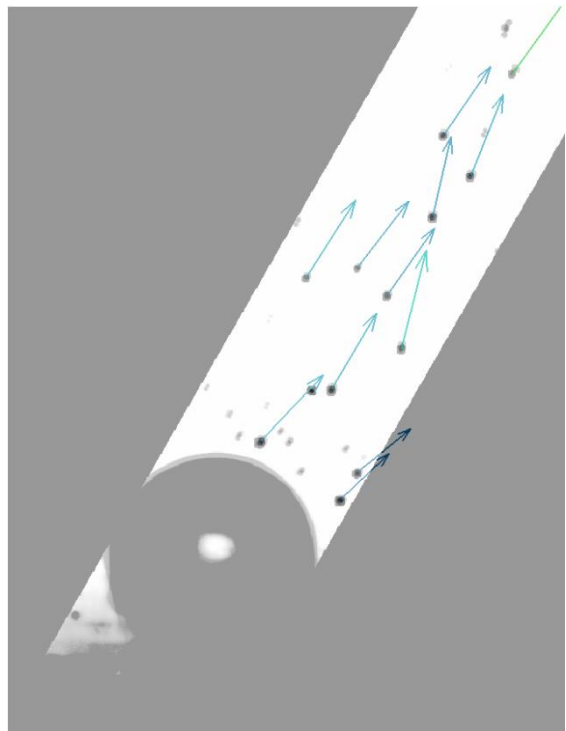
t = 6.00 ms



t = 6.50 ms

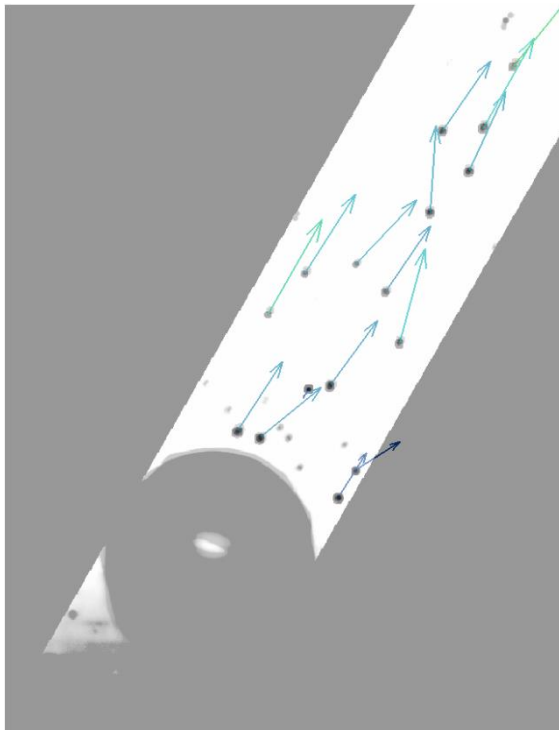


t = 7.00 ms

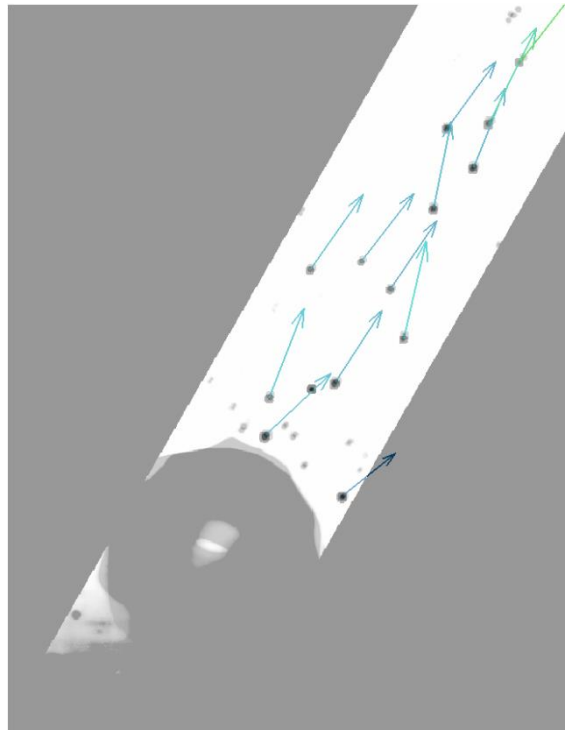


t = 7.50 ms

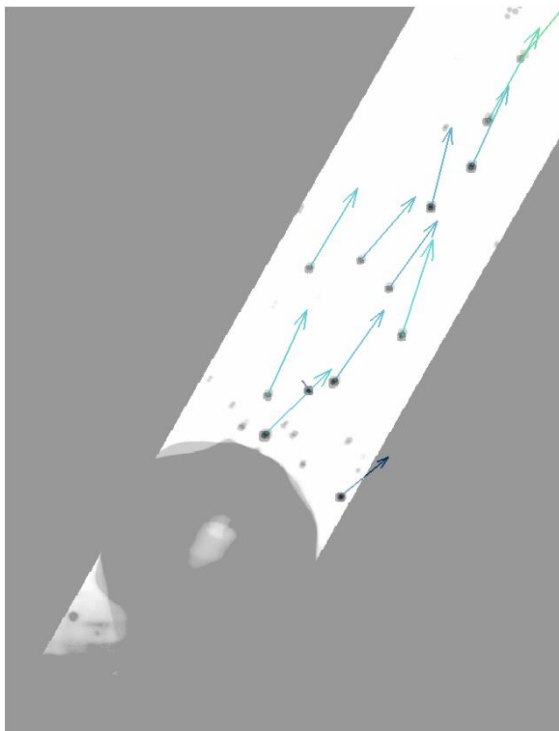
(Figure 7.19 continued)



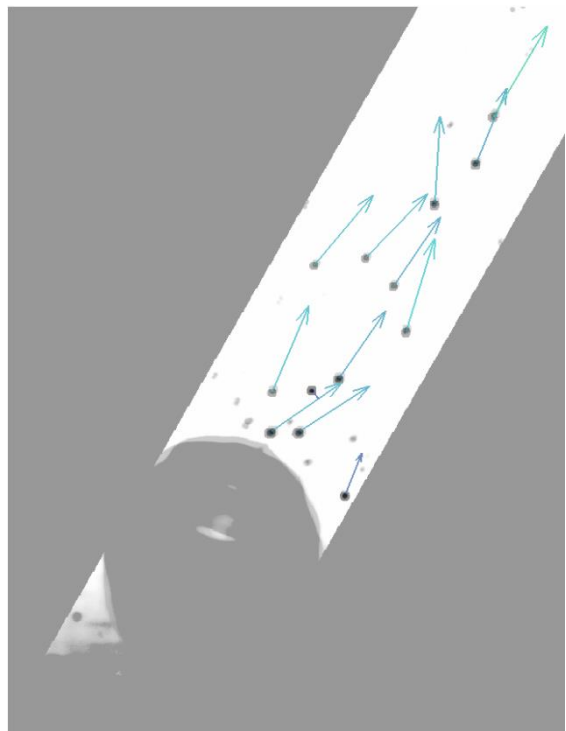
t = 8.00 ms



t = 8.50 ms

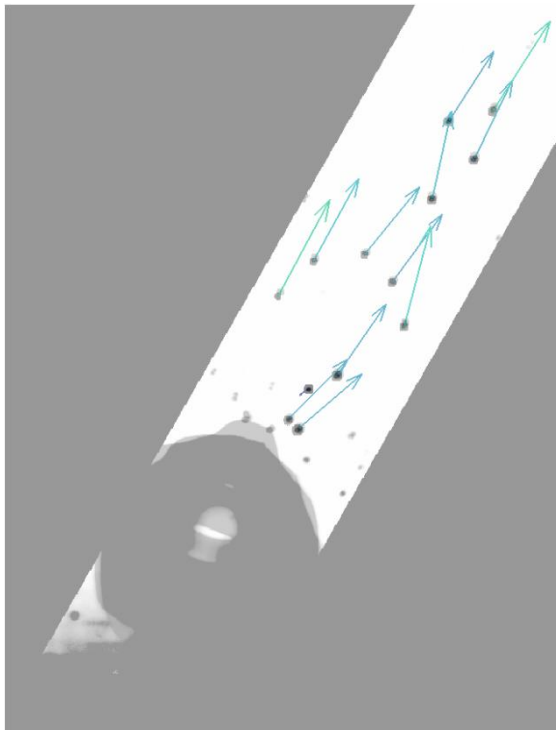


t = 9.00 ms

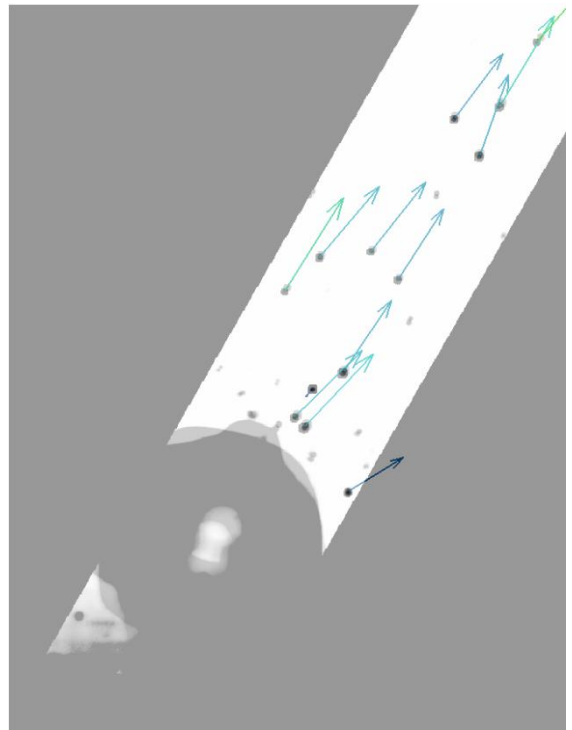


t = 9.50 ms

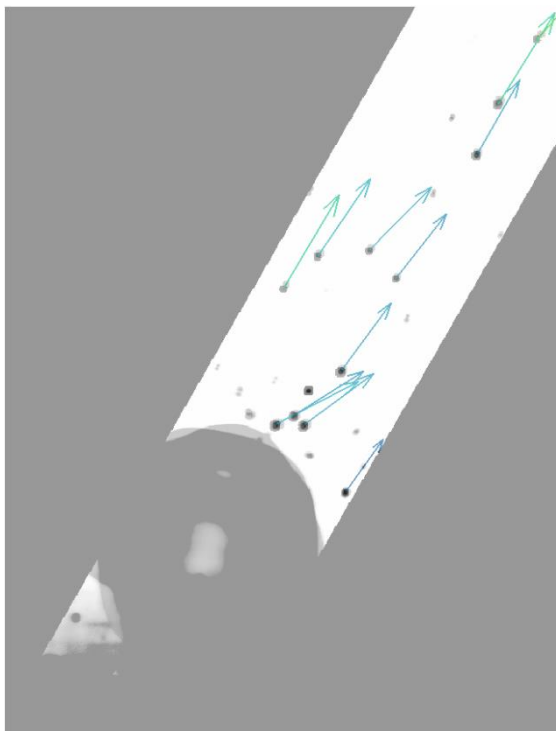
(Figure 7.19 continued)



t = 10.00 ms



t = 10.50 ms



t = 11.00 ms

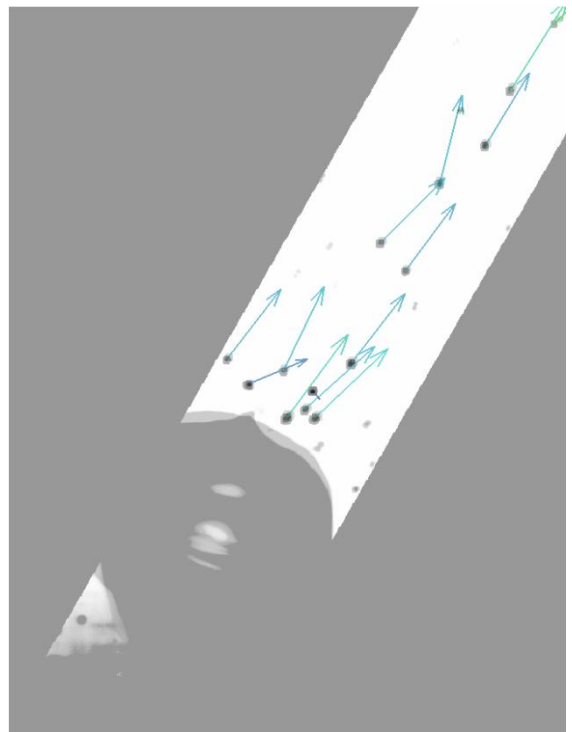


t = 11.50 ms

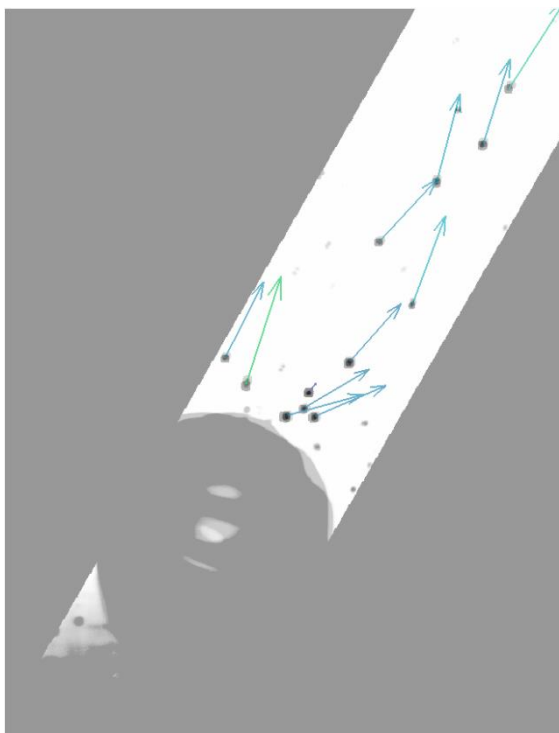
(Figure 7.19 continued)



t = 12.00 ms



t = 12.50 ms

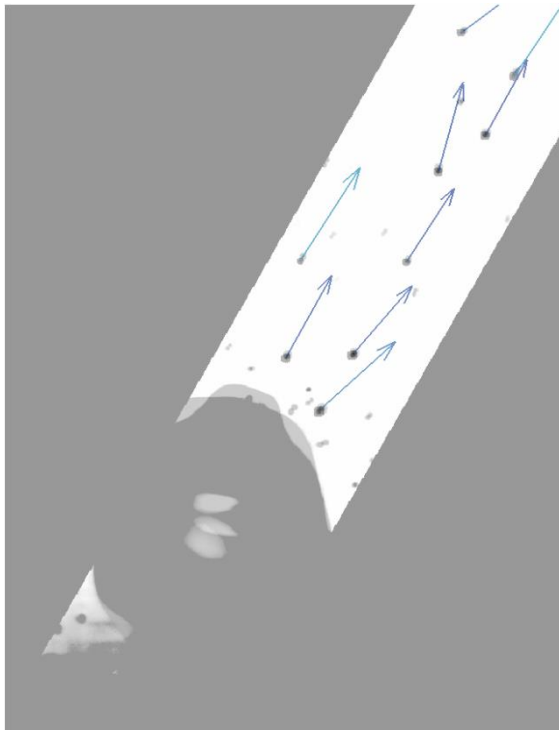


t = 13.00 ms

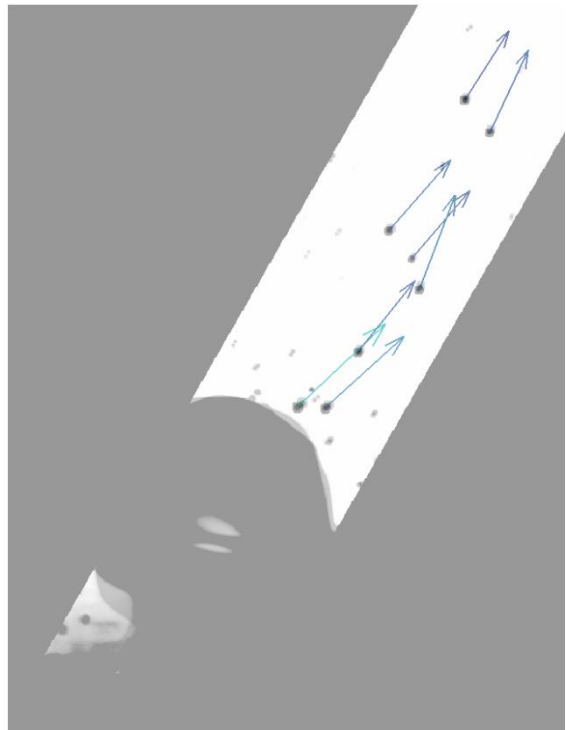


t = 13.50 ms

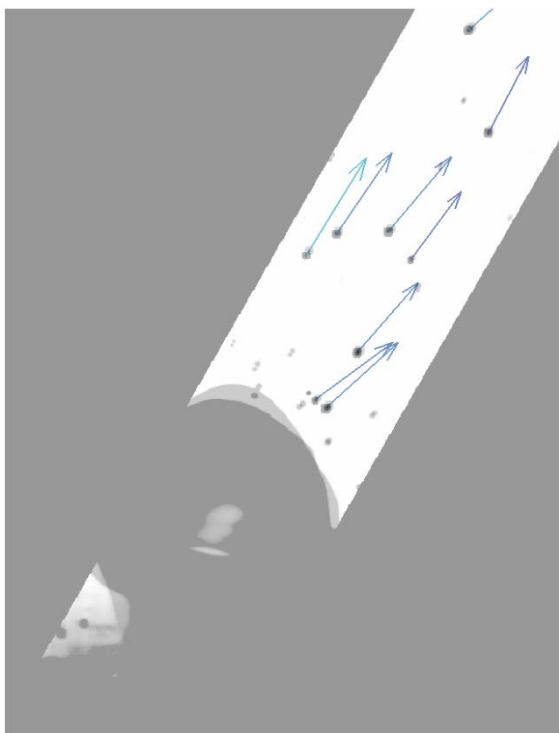
(Figure 7.19 continued)



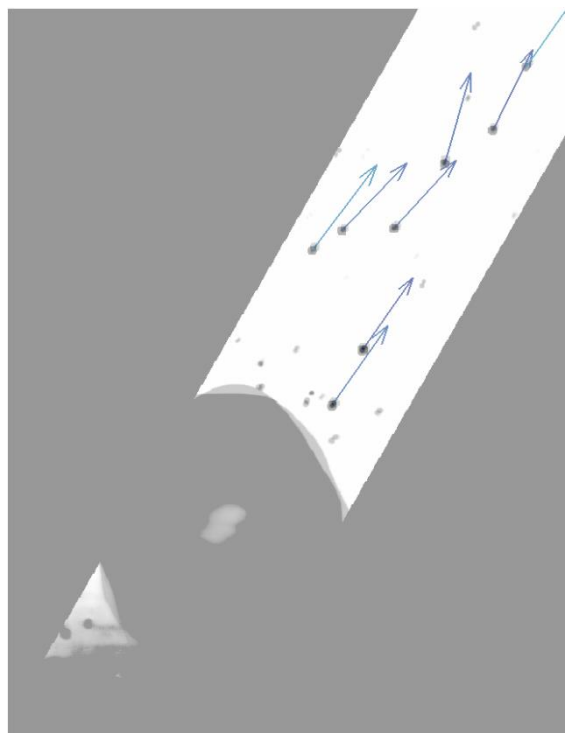
t = 14.00 ms



t = 14.50 ms

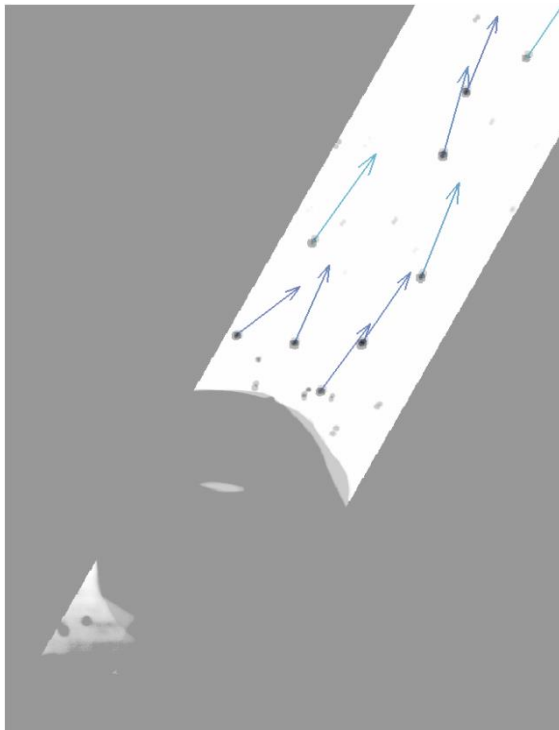


t = 15.00 ms

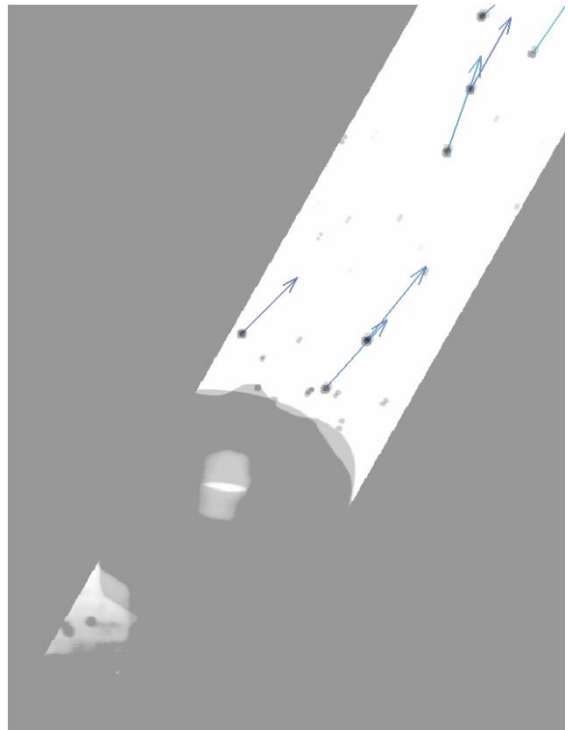


t = 15.50 ms

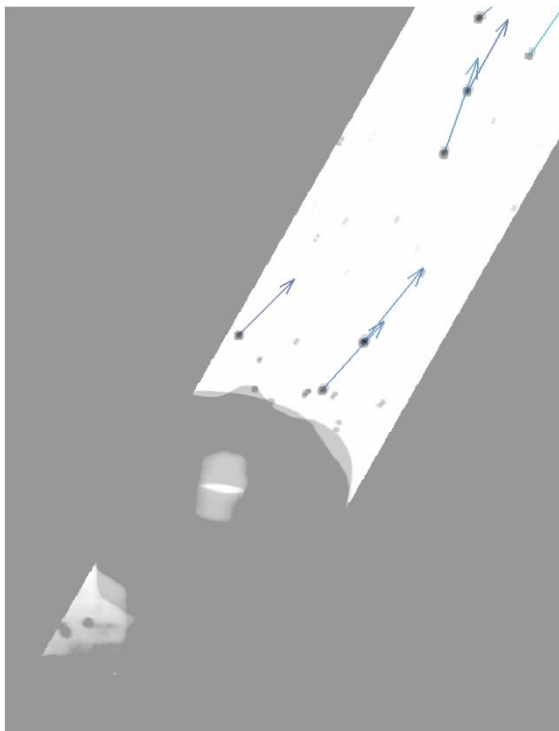
(Figure 7.19 continued)



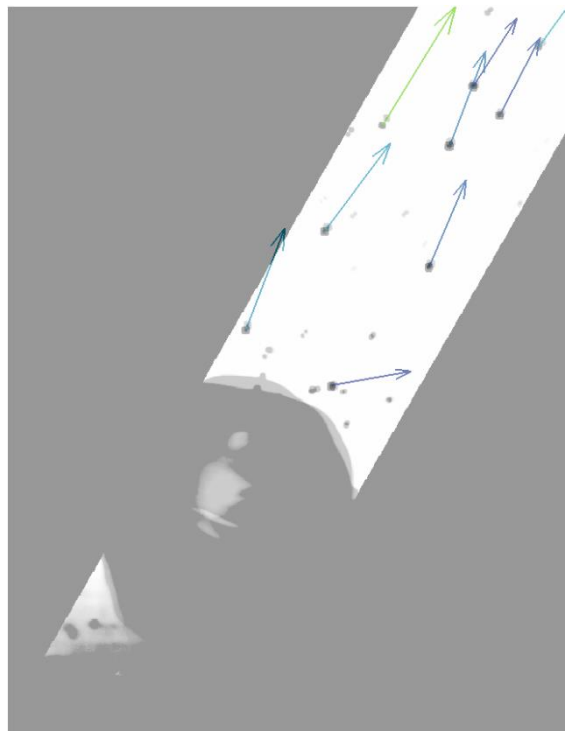
t = 16.00 ms



t = 16.50 ms

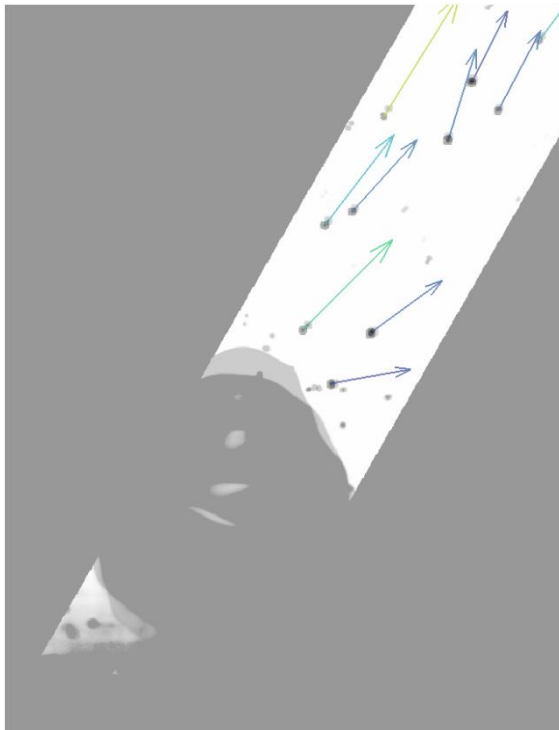


t = 17.00 ms

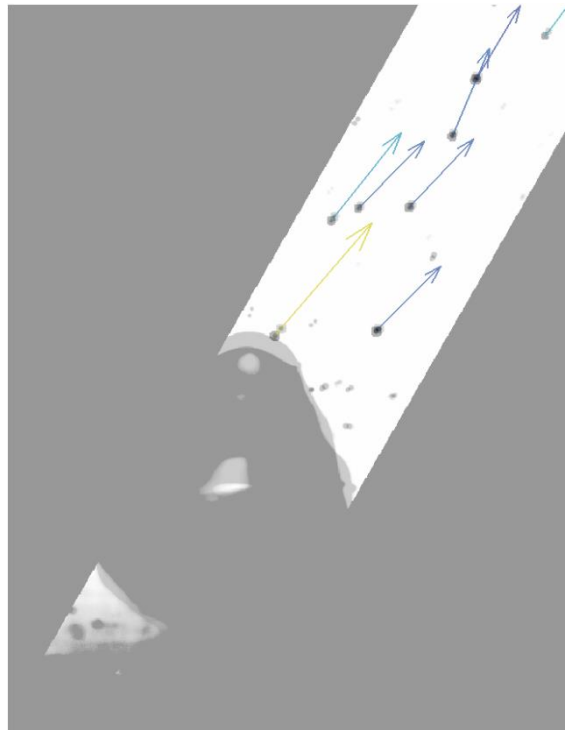


t = 17.50 ms

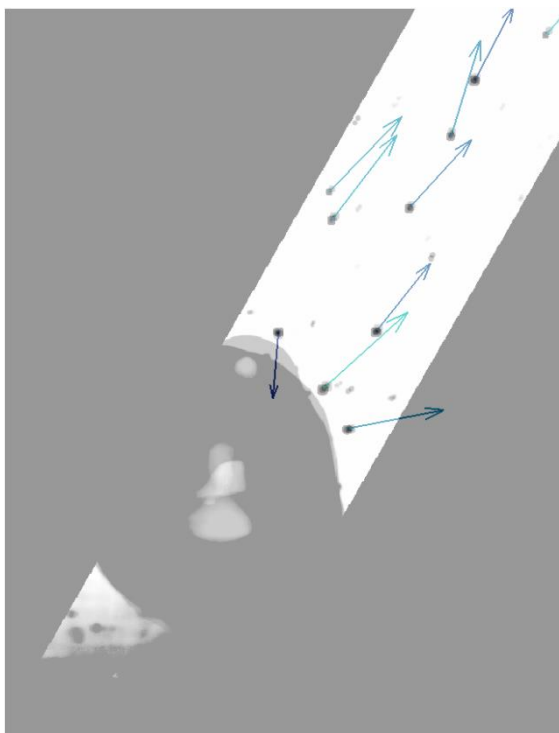
(Figure 7.19 continued)



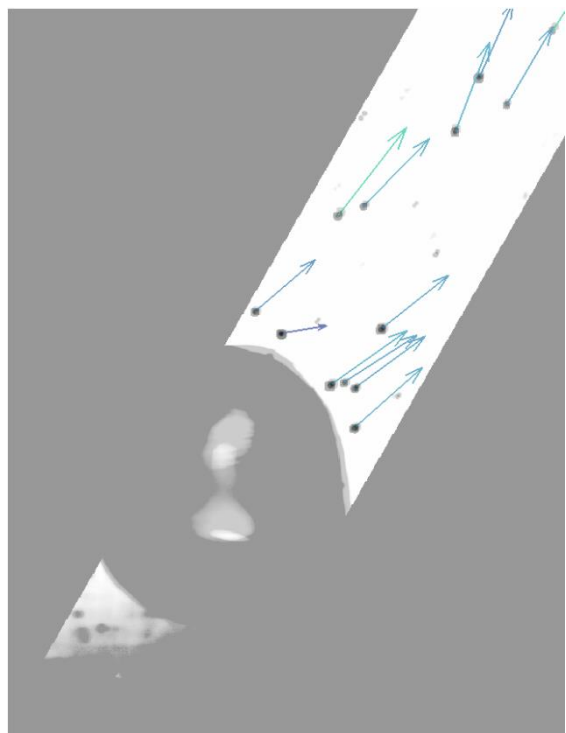
$t = 18.00$ ms



$t = 18.50$ ms

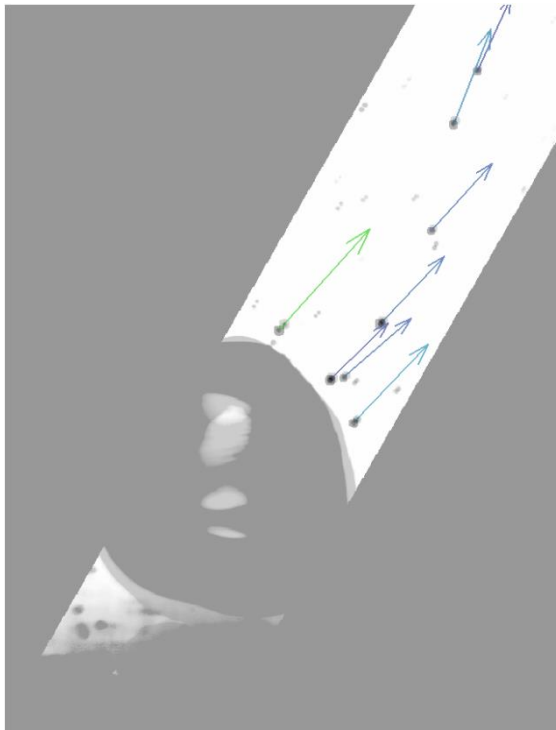


$t = 19.00$ ms

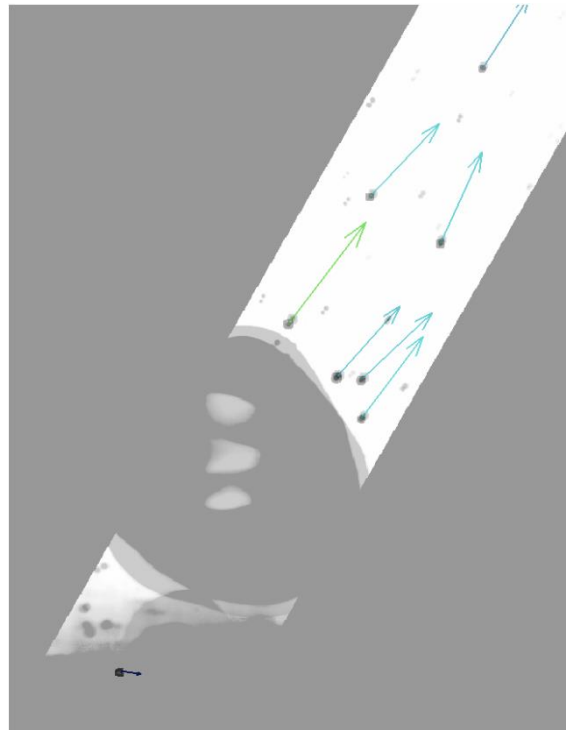


$t = 19.50$ ms

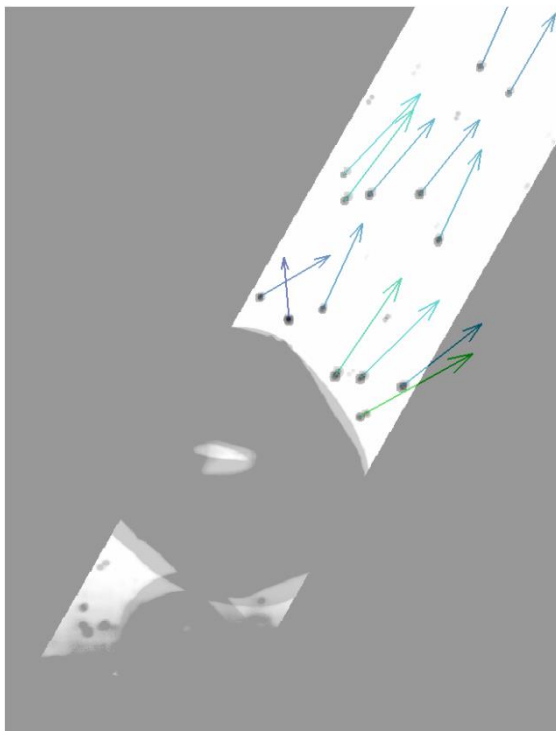
(Figure 7.19 continued)



t = 20.00 ms



t = 20.50 ms

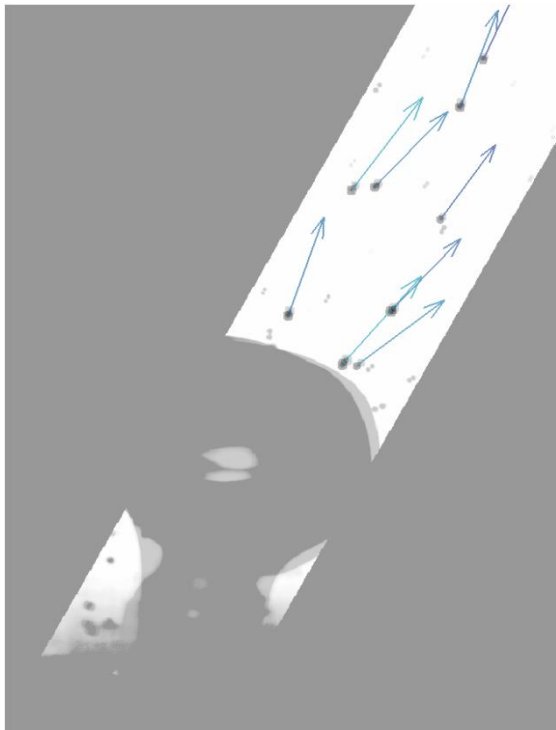


t = 21.00 ms

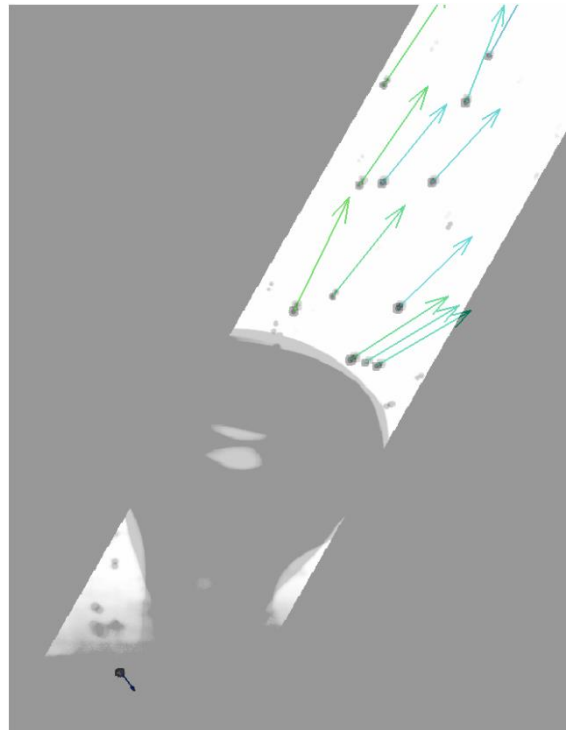


t = 21.50 ms

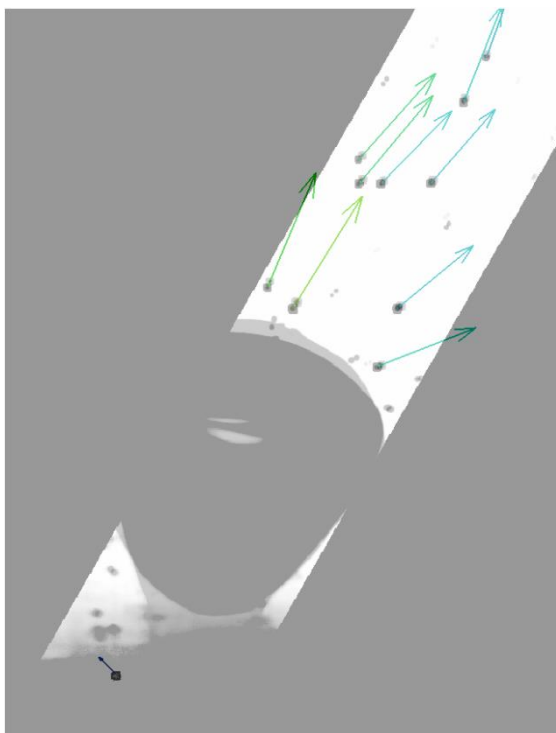
(Figure 7.19 continued)



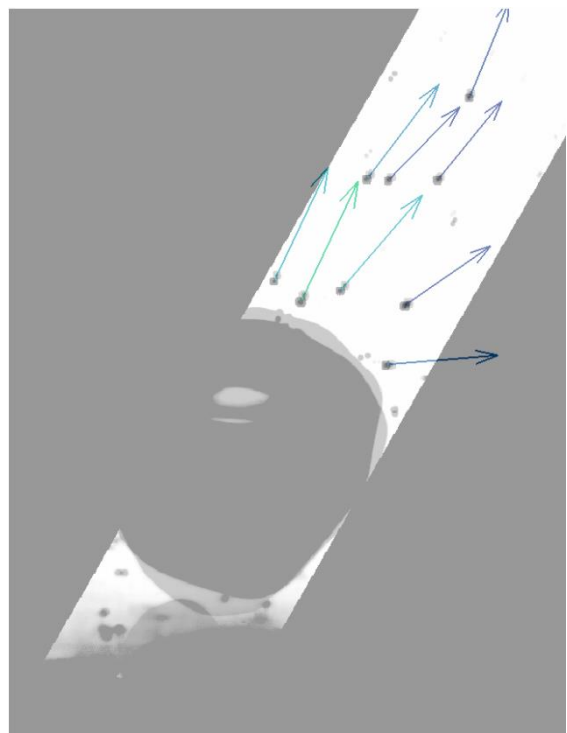
t = 22.00 ms



t = 22.50 ms



t = 23.00 ms



t = 23.50 ms

(Figure 7.19 continued)

Figure 7.19 clearly shows the single bubble growing within the region of interest during the early part of its cycle ($t = 0.5$ ms to 3.5 ms). It is not until approximately 7 ms after its inception does the bubble grow wider than the cropped region. The region of interest was set at 1.71 mm (0.067 in.) wide which is equal to the average bubble diameter as it remains on the surface.

Only the seed particles within the region of interest are tracked in the PTV algorithm. This restriction ensured that the calculated velocities were due to the bubble growth in the region in close proximity to the bubble. Most particles exhibit clear angled motion at approximately 30 degrees from vertical. In some cases, particles tend to travel at angles less than or greater than 30 degrees, especially when a particle is in close proximity to the interface of a bubble during rapid growth (early in the cycle). Some frames contain fewer visible seed particles than others as particles enter and exit the shallow depth of field (80 μm) of the high-speed camera. This out of plane velocity is not captured with the particle tracking velocimetry; thus, the results of this analysis are an underestimate for total velocity imparted to the liquid.

The images in Fig. 7.19 only contain the growth and departure of one bubble; however, 800 frames of high-speed video were analyzed with PTV. Average velocities of all seed particles present for each frame were computed and are shown in Fig. 7.20. As expected, fluid velocities fluctuate significantly throughout the 0.4 seconds as the fluid accelerates during periods of growth and decelerates during waiting periods. A moving average with a period of ten is overlaid onto the data to clarify how the velocities vary with time. Furthermore, horizontal bars located at the global average velocity indicate periods of time where a bubble was growing at the surface. There were a total of 14 distinguishable bubble growth and departures during the segment of video. The most defined spikes in the velocity data correspond near to when bubbles were growing on the surface—qualitatively confirming the hypothesis that the fluid region is accelerated in the region near the bubble during its growth phase. Many more than 14 increases in fluid velocity are apparent which can be attributed to the bubbles that do not have a complete growth cycle and, rather, coalesce with the preceding bubble just above the surface. Another source of velocity fluctuations are the

undulations of the bubble interface just before departure. These rapid changes in interface shape were observed to affect particle direction and velocity.

Particle tracking velocimetry was repeated twice using regions of interest measuring two and three diameters in width while maintaining the 30 degree rotated orientation. Figures 7.21 and 7.22 show global velocity, similar to Fig. 7.20, for their respective region of interest widths. It is important to notice that as the region of interest widens, the average velocity decreases because seed particles further from the active bubble travel at lower velocities and reduce the global average. Equations 7.6-7.8 show how velocities are computed in the PTV algorithm where n is the number of particles tracked in the frame.

$$V_x = \frac{\left(\frac{\sum_1^n dx}{n}\right)}{dt} \quad (\text{Eq. 7.6})$$

$$V_y = \frac{\left(\frac{\sum_1^n dy}{n}\right)}{dt} \quad (\text{Eq. 7.7})$$

$$|V| = \sqrt{V_x^2 + V_y^2} \quad (\text{Eq. 7.8})$$

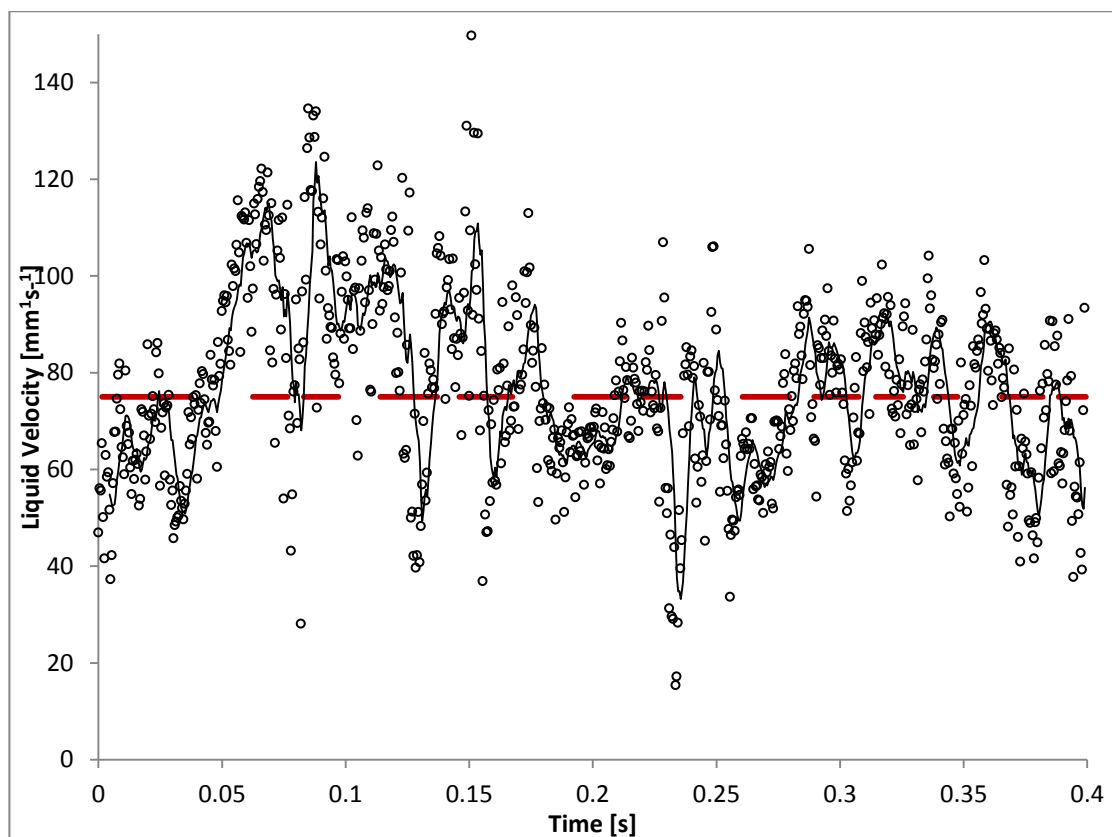


Figure 7.20: Time series of magnitude of average seed particle velocity calculated by PTV for 0.4 seconds of the adiabatic single-bubble high-speed video with a 1-Dia ROI. The solid black line indicates a moving average with a period of 10. Horizontal red bars indicate time ranges for which a bubble was growing on the surface.

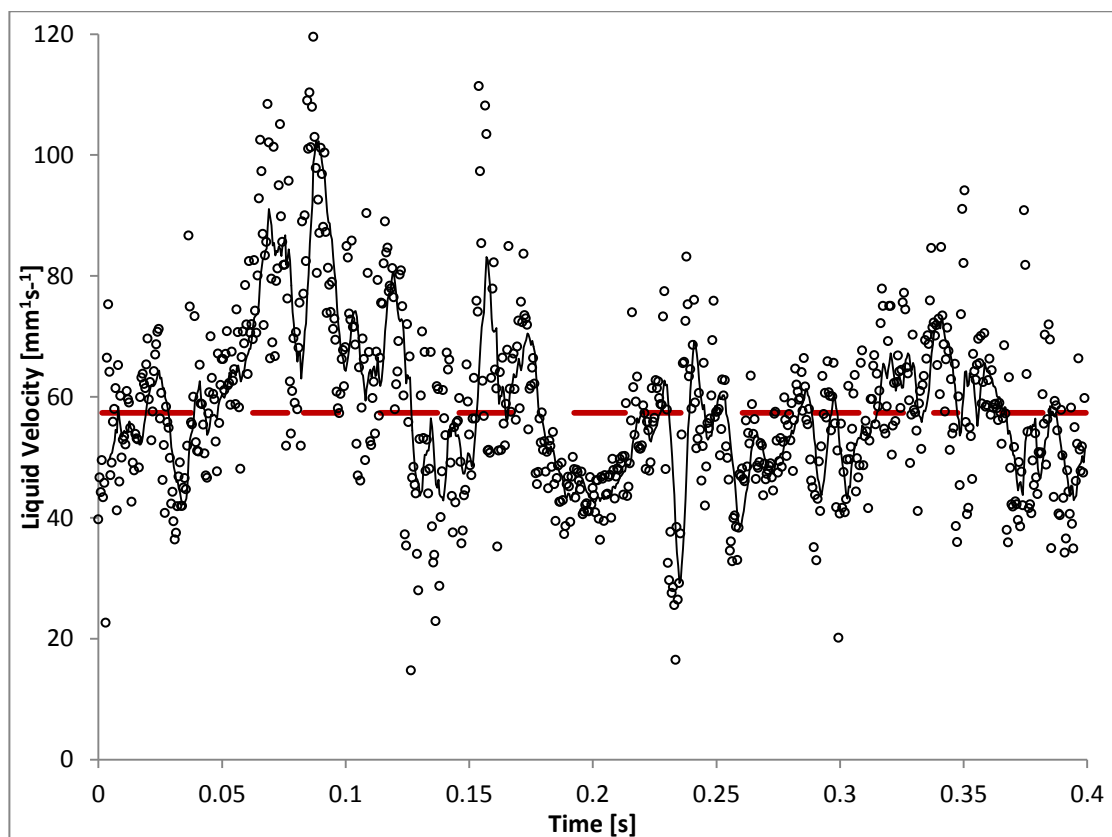


Figure 7.21: Time series of magnitude of average seed particle velocity calculated by PTV for 0.4 seconds of the adiabatic single-bubble high-speed video with a 2-Dia ROI. The solid black line indicates a moving average with a period of 10. Horizontal red bars indicate time ranges for which a bubble was growing on the surface.

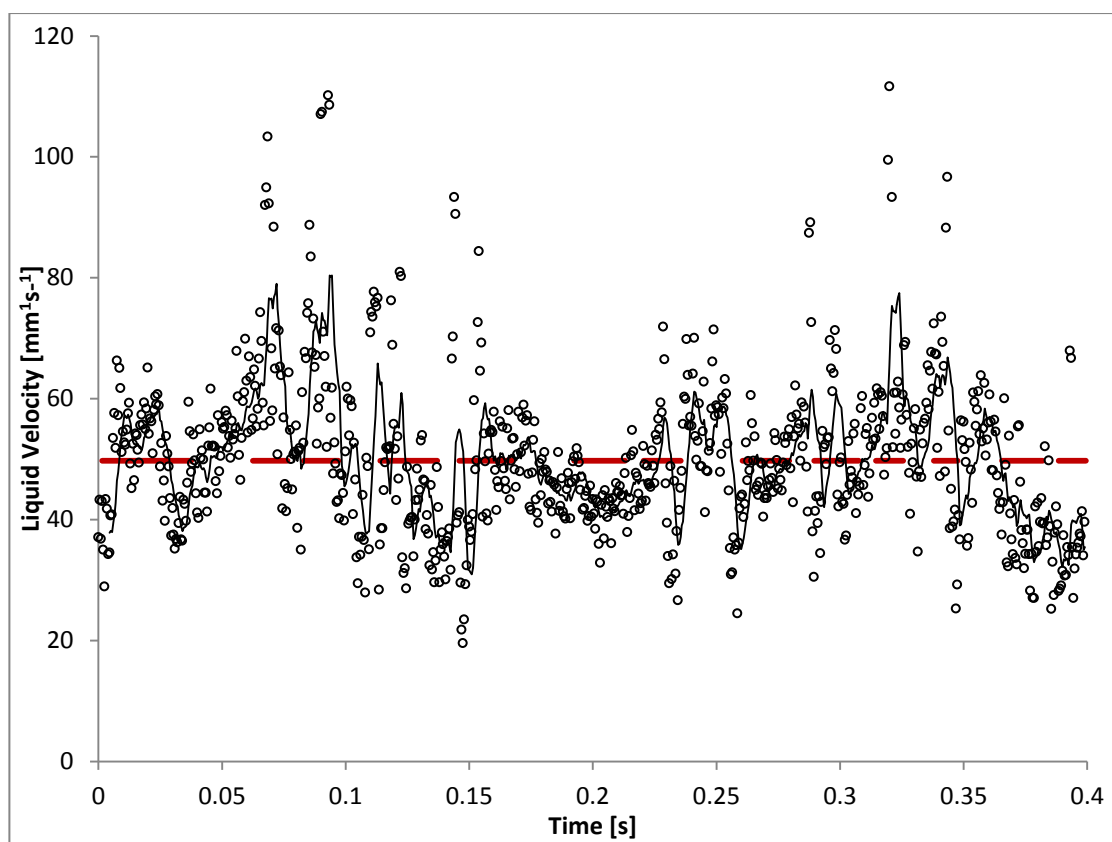


Figure 7.22: Time series of magnitude of average seed particle velocity calculated by PTV for 0.4 seconds of the adiabatic single-bubble high-speed video with a 3-Dia ROI. The solid black line indicates a moving average with a period of 10. Horizontal red bars indicate time ranges for which a bubble was growing on the surface.

Average velocities of the particles in each frame were output from the results of all three ROI widths. Table 7.4 and Fig. 7.23 summarize the resultant velocity data. The angle from the vertical, θ , reported is the average direction of seed particles determined by the PTV algorithm.

Table 7.4: Average fluid velocity values over 800 frames (0.4 s) in the three varying region of interest widths. Total magnitude of the velocity, x-component, y-component, and direction are all provided.

Unit		<i>n</i>		
		1	2	3
 Velocity 	mm¹s⁻¹	74.98	57.35	49.76
x-Velocity	mm¹s⁻¹	41.33	32.91	30.72
y-Velocity	mm¹s⁻¹	62.57	46.96	38.68
θ	deg	32.68	35.00	38.69

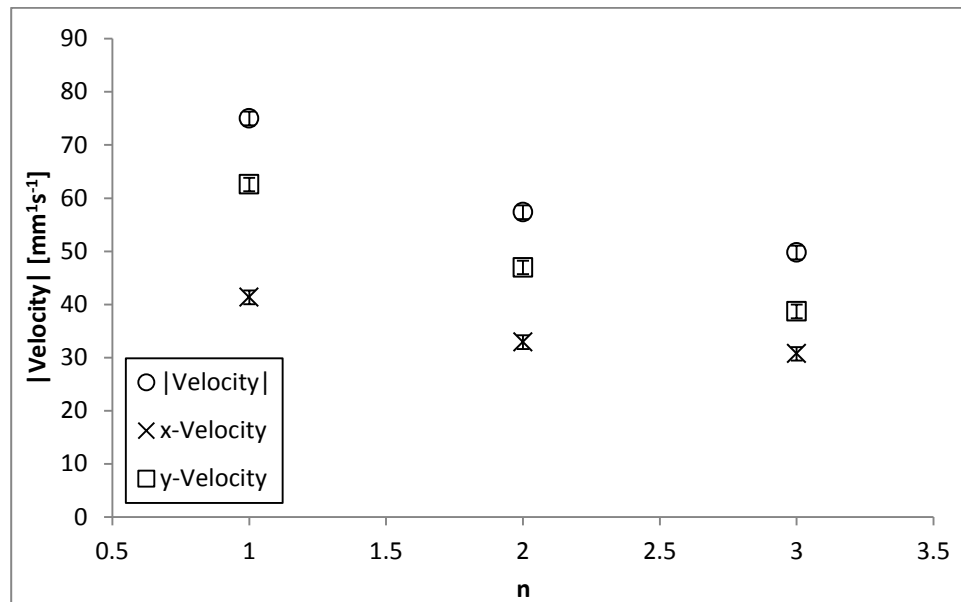


Figure 7.23: Average fluid velocity plotted as a function of region of interest width. Total magnitude of the velocity, x-component, y-component, and direction are each shown. Error bars are shown and are $\pm 1.28 \text{ mm}^1\text{s}^{-1}$ for all data points.

7.4. Model Validation

The purposes of performing particle tracking velocimetry analysis on the high-speed video data with three regions of interest in conjunction with calculating predicted fluid velocities with three corresponding areas of influence were to not only validate the semi-empirical model as a reliable means of predicting liquid net lateral velocities caused by the single bubble emanating from the structured surface, but also to determine the area of influence of a single bubble. By comparing the results of the previous two sections, the model is validated and an area of influence is established. Figure 7.24 and Table 7.5 below combines the results from both the particle tracking velocimetry and semi-empirical model. Figure 7.25 and Table 7.6 below show the percent deviation between the model predictions of velocity and the particle tracking velocimetry results.

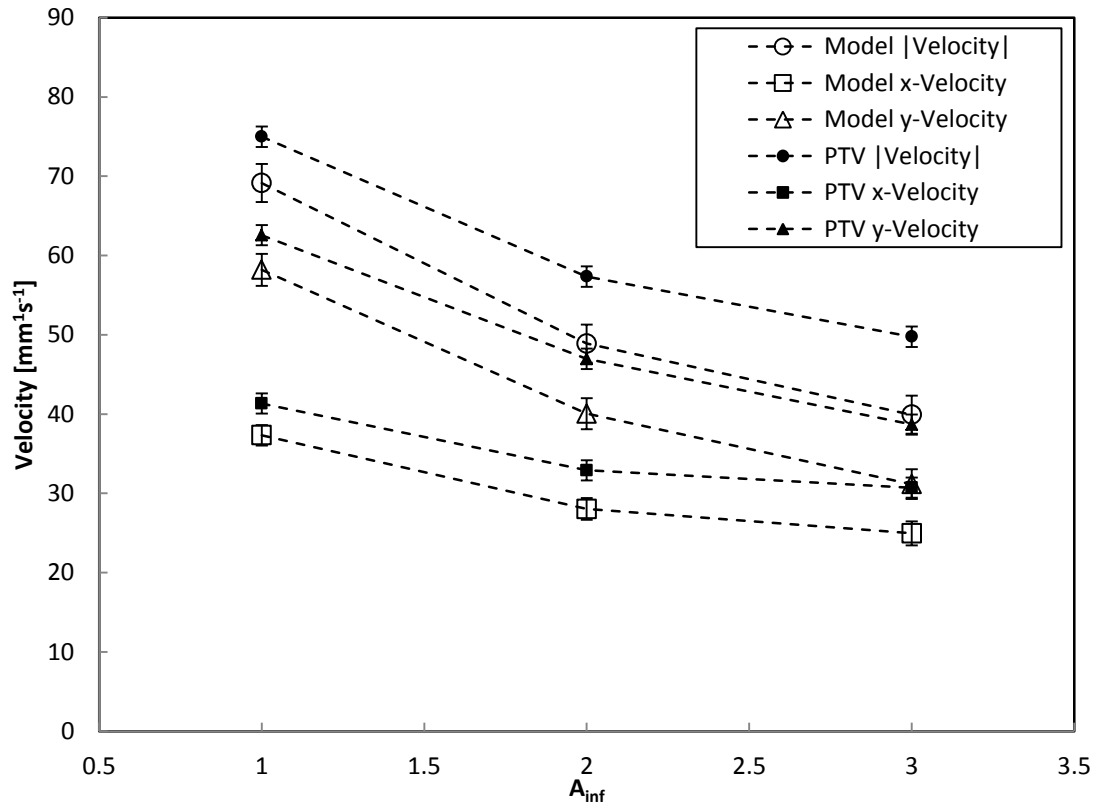


Figure 7.24: Comparison of particle tracking velocimetry results and model results. Error bars are indicated for the model results.

Table 7.5: Values of velocities with uncertainty errors shown for the comparison between PTV and model results.

	n	Velocity	Uncertainty	x-Velocity	Uncertainty	y-Velocity	Uncertainty
		mm^1s^{-1}	mm^1s^{-1}	mm^1s^{-1}	mm^1s^{-1}	mm^1s^{-1}	mm^1s^{-1}
PTV	1	74.98	1.28	41.33	1.28	62.54	1.28
	2	57.35	1.28	32.91	1.28	43.04	1.28
	3	49.76	1.28	30.72	1.28	33.48	1.28
Model	1	64.19	2.40	37.33	1.30	58.20	2.02
	2	48.89	2.40	28.04	1.38	40.05	1.97
	3	39.92	2.40	24.95	1.50	31.16	1.87

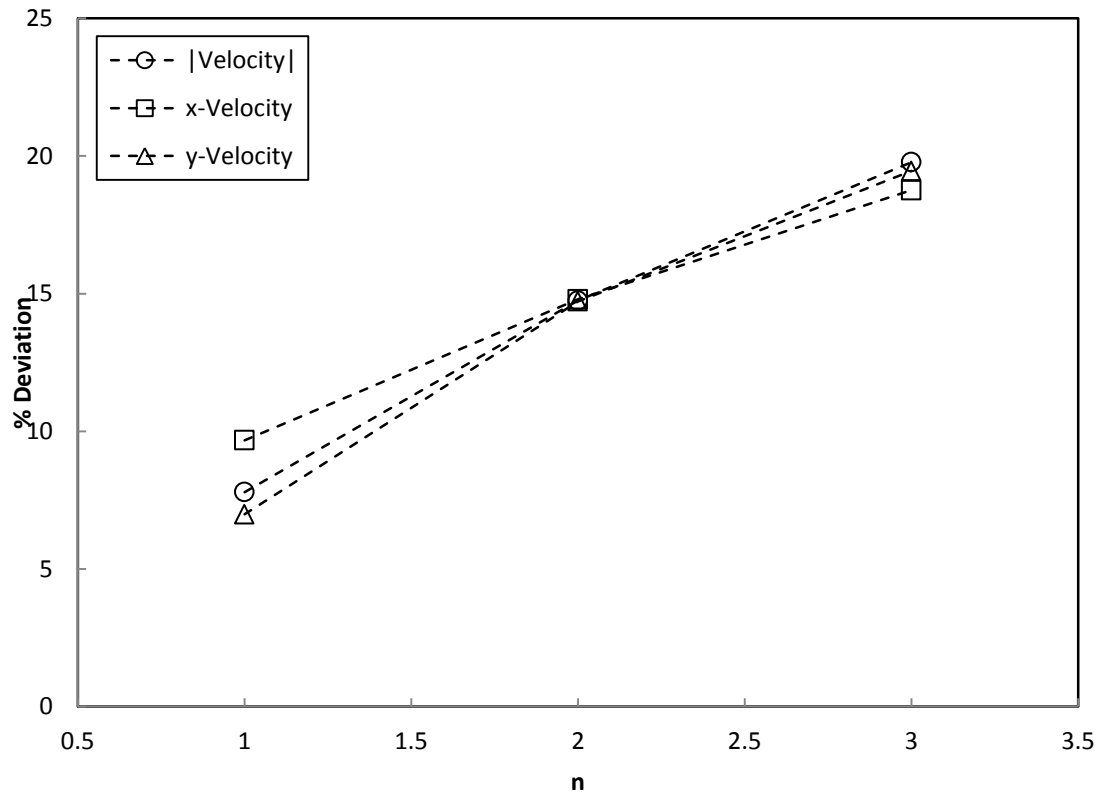


Figure 7.25: Percent deviation of the model predictions from the particle tracking velocimetry. Deviations are shown for three areas of interest.

Table 7.6: Values of percent deviation of the model predictions from the particle tracking velocimetry for all three areas of interest.

		n		
		1	2	3
% Deviation	Velocity	7.79	14.74	19.77
	x-Velocity	9.68	14.80	18.76
	y-Velocity	6.98	14.72	19.45

Figure 7.24 clearly shows that the semi-empirical model follows the trend seen in the results of the particle tracking velocimetry—that is, as the area of influence decreases velocity increases. Both the PTV model results change similarly between varying areas of influence, indicating that the model does in fact reliably predict the influence of a bubble on the surrounding liquid. However, with larger areas of influence ($n = 2$ and 3), there exists a discrepancy between PTV and model results—nearly $7 \text{ mm}^1\text{s}^{-1}$ (13.8 %) for the three bubble diameter case. As area of influence is decreased, the discrepancy reduces as the PTV algorithm and model tend to converge to the same value. In fact, an area of influence of one average bubble diameter yields velocities by both means that are statistically equal as indicated by the overlapping error bars and the low deviation values; hence, suggesting this as the correct area of influence.

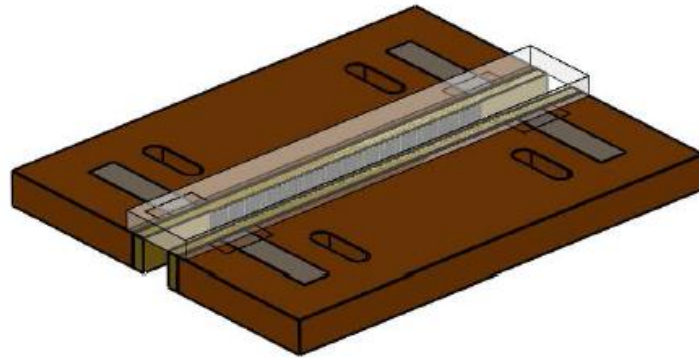
PART II: Open-Channel Pump

8. EXPERIMENTAL FACILITY

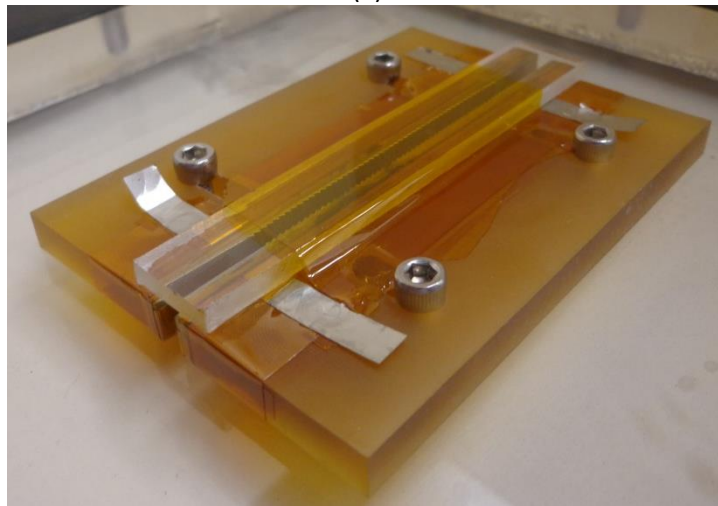
This section presents the facility used to perform open-channel pump experiments. A rectangular cross section channel was mounted in a chamber partially filled with FC-72. The vertical walls of the channel have a saw-tooth topography oriented to preferentially move the fluid lengthwise down the channel using bubble slugs. Visualization of the bubble slugs within the channel was done to not only characterize the regimes of flow, but also to measure the slug velocities. These measurements will be used to create a model to predict slug velocities based on fluid properties, bubble shape, and surface geometry. Component assemblies to discuss include the: test section, test chamber, high-speed imaging, lighting, data acquisition, and auxiliary components.

8.1. Test Section Assembly

The open channel, shown in Fig. 8.1, has a rectangular cross section of variable hydraulic diameter. The vertical walls feature saw-tooth microstructures and the top and bottom walls of the channel are transparent to permit illumination and imaging. The assembly consists of two halves which are mirror-image components. Each half consists of three components: the insulator, heater, and structured surface. Each will be described in detail here.



(a)



(b)

Figure 8.1: The test section assembly shown in (a) solid model and (b) as installed during testing.

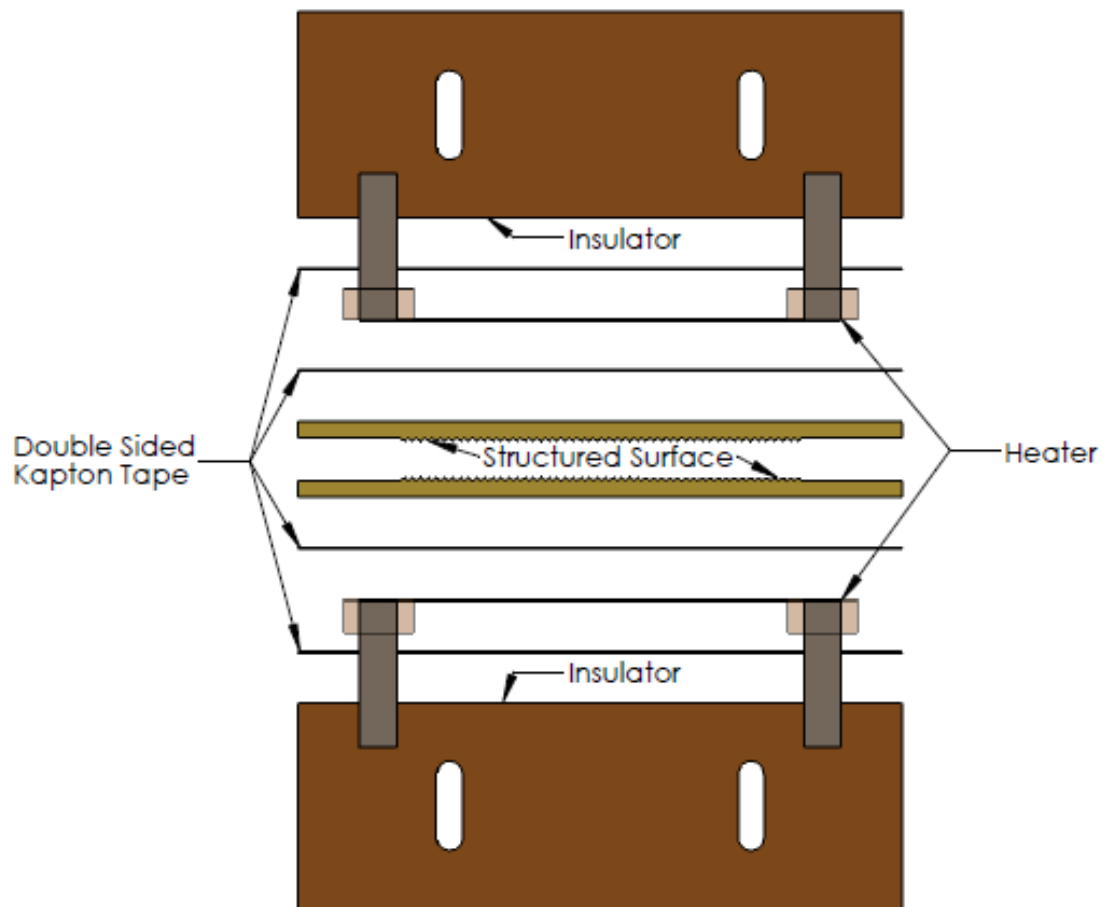


Figure 8.2: Solid model of the test section assembly exploded to show individual layers.

The heater and structured surface of each half are mounted to the insulator using double-sided Kapton tape as shown in Fig. 8.2. Electrical heater leads are bent over the insulator. The polycarbonate ceiling measures 76.2 mm (3.0 in.) in length 12.7 mm (0.5 in.) in width and 3.175 mm (0.125 in.) in height. It is installed after the structured surfaces are parallel and the desired channel width. For the data presented in this thesis, the widths tested are 4.5 mm (0.177 in.) and 2.25 mm (0.089 in.). The distance is measured with a pair of digital calipers at each end of the ratcheted surface and is the distance from peak to peak, rather than trough to trough.

The structured surfaces were machined first and are similar to the structured surface of the adiabatic single-bubble experiment. It is machined from brass and has a saw-tooth pattern

on the vertical. In this case, there are 50 ratchets with a pitch of 1.02 mm (0.04 in.) and a shallow face angle of 30 degrees (Fig. 8.3). The structured surface measures, 76.2 mm (3.0 in.) in length, 5.5 mm (0.22 in.) in width and 2.0 mm (0.079 in.) in base height plus an additional 0.44 mm (0.017 in.) height of the ratchets. Nucleation sites are created on the top surface by media blasting the ratchets with 60-120 μm (0.002-0.005 in.) particles. Unlike the adiabatic single-bubble experiment which has only one nucleation site per ratchet, the channel structured surface has nucleation sites covering the entirety of the ratchets. However, because of the saw-tooth geometry, shallow sloping faces account for more surface area than the steep faces. Therefore, the uniform blasting of the surface creates a greater number of nucleation sites on shallow faces.

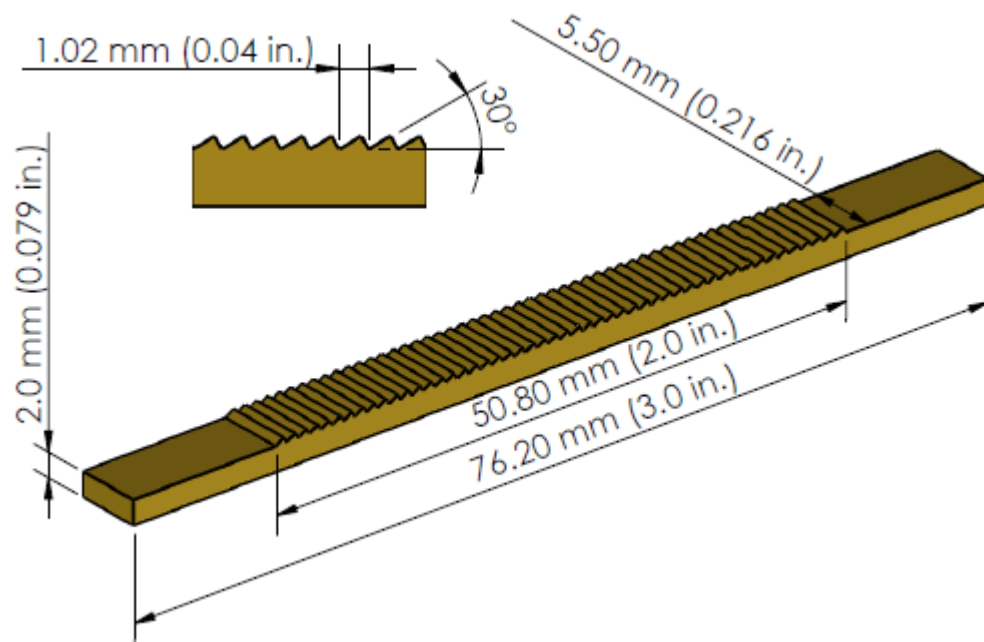
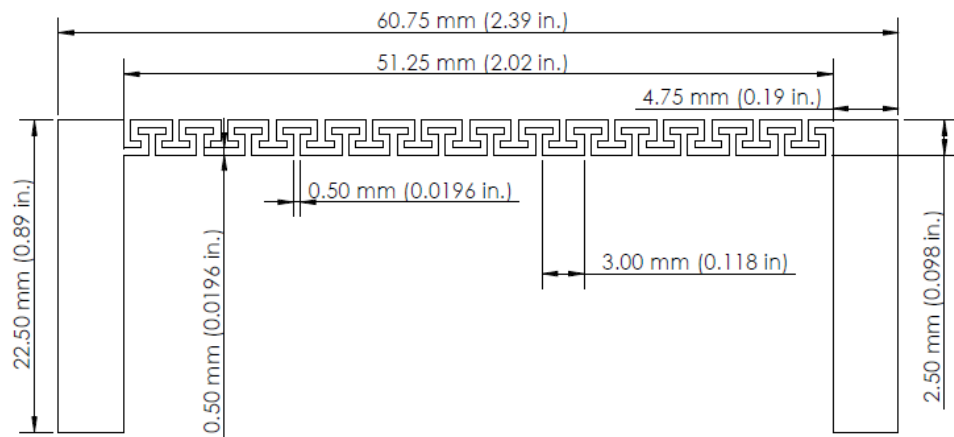


Figure 8.3: Structured surface machined from brass shown with dimensions.

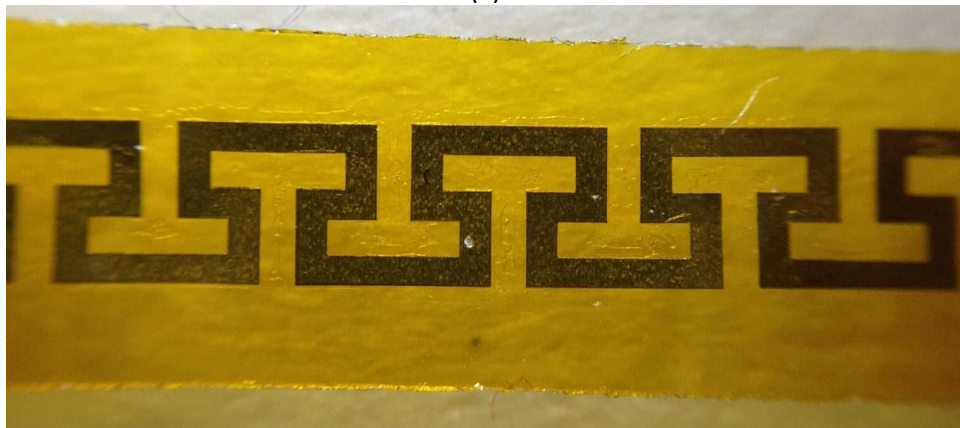
The insulator is a polyetherimide (Ultem 1000) block measuring 76.2 mm by 25.4 mm by 5.5 mm (3.0 in. by 1.0 in. by 0.217 in.) and features two slots for #4 socket head cap screws. These slots allow for the individual halves of the assembly to be moved—setting the distance between the two structured surfaces. Ultem 1000 was chosen for its low thermal conductivity of 0.22 W/m·K (0.127 BTU/ft·hr·°F) and high heat deflection temperature of 210

°C (410 °F) [12]. Lower conductivity ensures that the majority of the heat generated by the heaters is transferred to the structured surfaces. The high heat deflection temperature ensures that the insulator is capable of withstanding continuous operation without mechanical failure.

The heaters in the test section assembly are made from Inconel Alloy 600 foil. Each heater was laser cut from 25.4 μm (0.001 in.) foil into the serpentine pattern shown in Fig. 8.4. The two large tabs at the ends of the serpentine pattern are the electrical leads. These tabs were made large in relation to the heated area to ensure that no boiling would occur outside the desired area.



(a)



(b)

Figure 8.4: Inconel 600 heater shown with (a) dimensions and (b) in a photo taken with a macro lens after the heater has been laminated with Kapton tape.

Once the shape of the heater is cut, the Inconel is laminated between two strips of Kapton tape. This not only gives the heater strength and protection from tearing, but also provides a dielectric barrier between the heater and structured surface. The heater leads are left without lamination in the area of the electrical connections. Resistances for the heaters are measured at 12.35Ω and 13.34Ω and are wired in series (Fig. 8.5). The design resistance for the heater based on Eq. 8.1 was 12.39Ω . The discrepancy of the second heater is most likely do to a small variation in either the thickness or width of the serpentine heater as a very small variation in these dimensions results in large changes in resistance. Thickness and width could each be varied by surface defects or laser cutting inaccuracy. An example calculation is provided in Appendix C. Brass #10-32 machine screws with colloidal silver coated tips clamp the heater leads against the insulator to make electrical contacts. The two heaters are connected outside of the test chamber with a bridge between two of the brass screw heads. The added resistance of this bridge, at 0.04Ω , is small, but shown in the wiring diagram regardless.

$$R = \rho \frac{l}{t \cdot W} \quad (\text{Eq. 8.1})$$

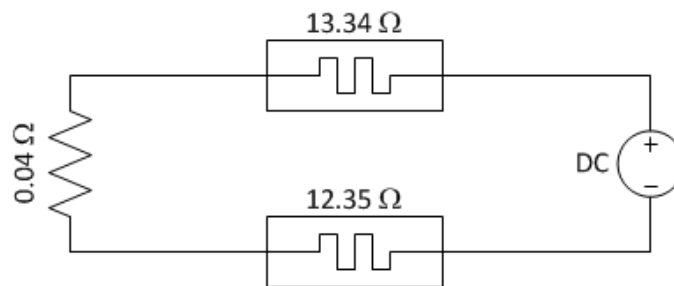


Figure 8.5: Wiring diagram for the heaters in the test section. Heater and contact resistances are shown.

8.2. Test Chamber

The test chamber serves several purposes. First, it is the support for the two halves of the test section assembly. It provides a closed chamber allowing the pressure to be varied as desired. The top and bottom surfaces are clear, allowing for light to be supplied from the top, and high-speed imaging from the bottom. And lastly, it has ample space for the required fittings and accessories. Figures 8.6 and 8.7 illustrate the construction of the test chamber and the ports in the top sheet.

The chamber is constructed from three sheets of polycarbonate measuring 152.4 mm (6.0 in.) square and 12.7 mm (0.5 in.) thick. The center sheet has #10-32 threaded holes along the square perimeter and its center section is milled out, leaving a 127 mm (5.0 in.) square opening. This sheet is fused to the bottom sheet, which has the appropriate #4-40 mounting holes for the test section assembly. Locating pins were installed in two corners for the fusing process to ensure correct alignment. The top sheet has threaded holes for all of the necessary ports, as well as countersunk holes for mounting it to the bottom two sheets. To ensure an airtight seal, an EPDM gasket is fashioned to reside between the center and top sheets.

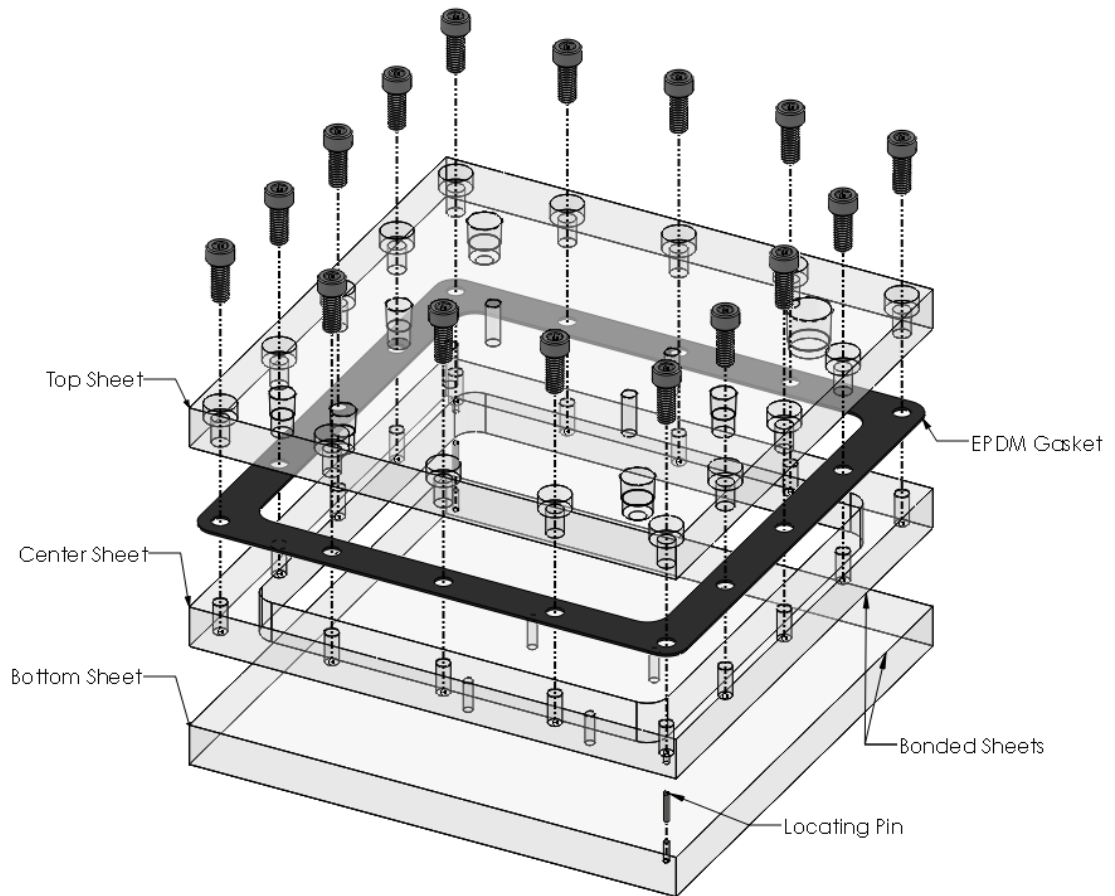


Figure 8.6: The construction of the test chamber without any components installed.

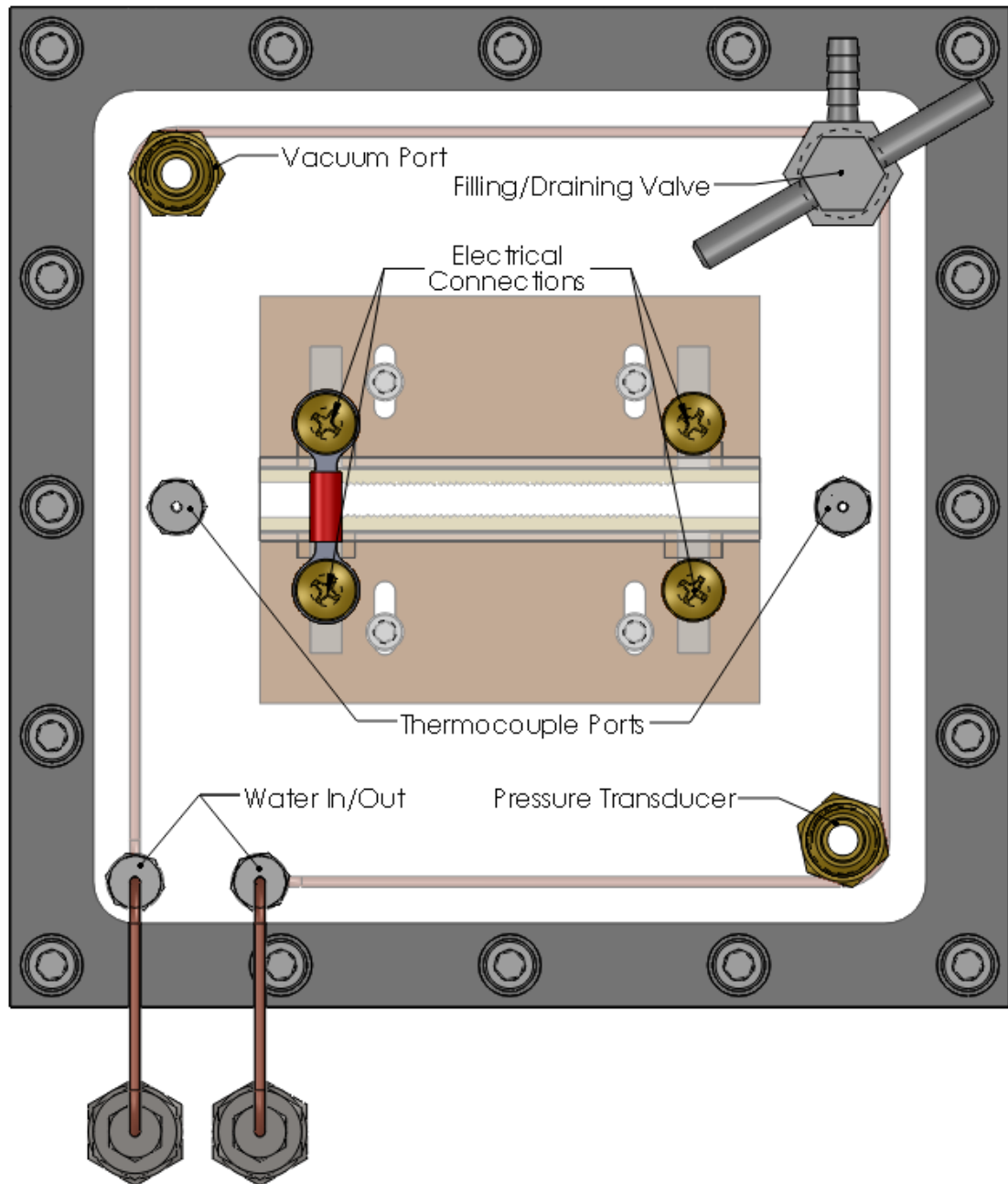


Figure 8.7: Top view of the test chamber designating the uses and location of ports in the top plate.

Because the channel is imaged from the underside, the test chamber must be elevated above the laser table top. A stage (Fig. 8.8) with the center section with a vacant center section

allows for imaging through the bottom sheet while raising the test chamber 157.5 mm (6.2 in.). Two aluminum toe clamps secure the test chamber to the stage at opposite corners.

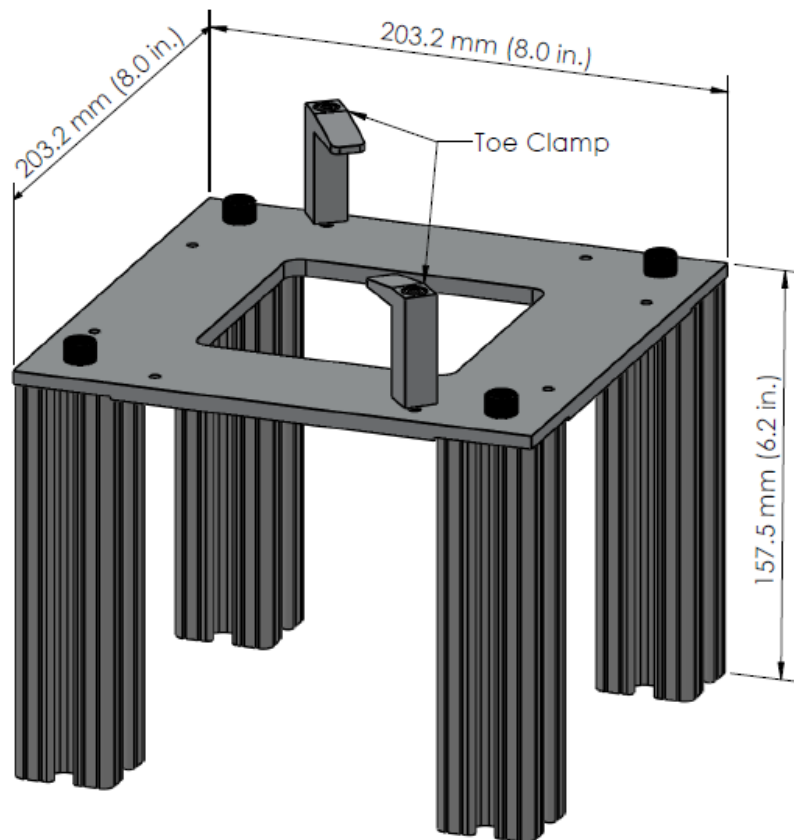
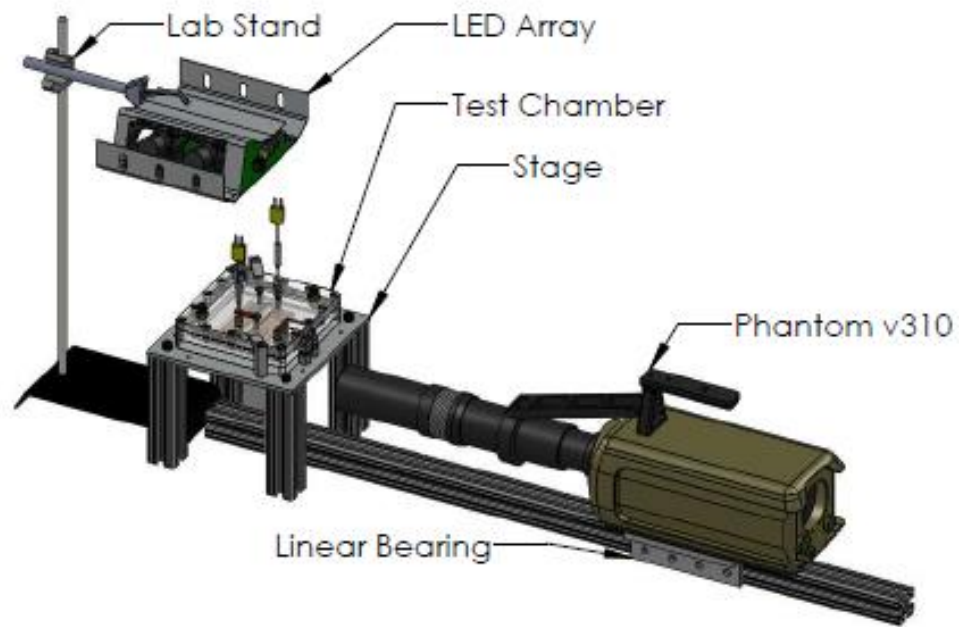


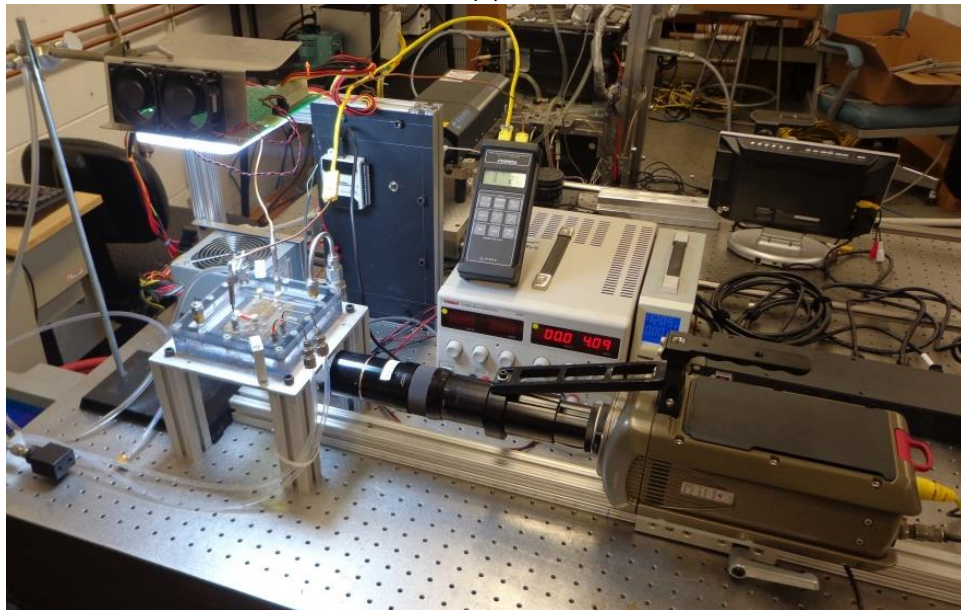
Figure 8.8: Stage and toe clamps used to elevate and secure the test chamber.

8.3. Test Facility

The test facility was assembled on a laser table starting with the camera rail (T-slotted aluminum extrusion) being bolted to the table surface. The stage straddles the far end of the rail directly over prism. The stage was not fixed to the table, allowing it to be adjusted throughout testing. Figure 8.9 shows the orientation of the components as during testing.



(a)



(b)

Figure 8.9: Experimental facility for the open-channel pump experiment (a) with major components labeled and (b) as configured during testing.

In addition to the parts already described, several components are used to make the experiment functional. These two components are a vacuum system and a heated-refrigerated bath circulator.

The vacuum system (Fig. 8.10a) consists of a 249 W (1/3 HP) vacuum pump mounted on a 113.5 L (30 gallon) compressed air tank (Make: Speedaire). This unit provides the test chamber with a source of vacuum to lower the pressure in the chamber—effectively altering the saturation temperature of the working fluid.

A Thermo Haake (Model: C30P) heated-refrigerated bath circulator (Fig. 8.10b) filled with de-ionized water supplies the cooling/heating coil within the chamber with liquid to alter and maintain pool temperature. It is fed into the chamber in a closed loop system (refer to Fig. 8.7 'Water In/Out').

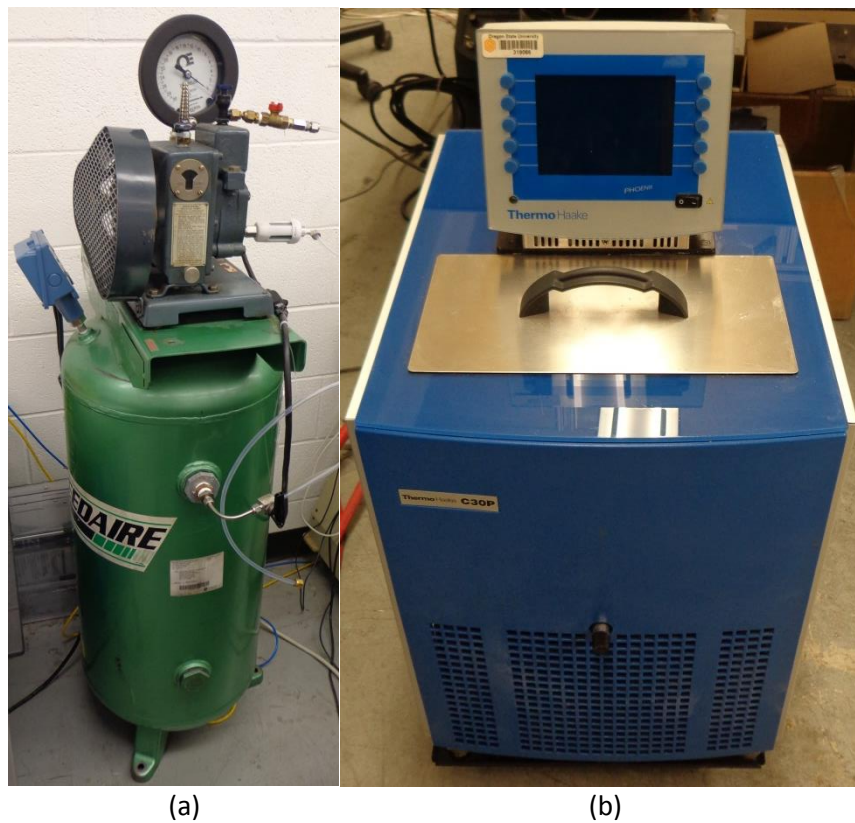


Figure 8.10: Auxiliary components required to run the channel pump experiment.(a) The Speedaire vacuum system. (b) The Thermo Haake heated-refrigerated bath circulator.

8.4. High Speed Imaging & Lighting

As in the adiabatic single-bubble experiment, high-speed imaging is used to capture bubble movement is accomplished using a Vision Research Phantom v310 in combination with an Infinity K2/SC microscope lens paired with CF-2 or CF-3 objectives. The camera is supported by a T-slotted aluminum extrusion and its distance from the target is adjusted with a double flange linear bearing designed for the extrusion as shown in Fig. 8.9a. Videos are captured and saved using Vision Research's Phantom Camera Control (PCC 1.3) software.

To avoid having to mount the camera vertically and risk damaging it, the Phantom v310 is mounted in a horizontal position and imaging of the channel is achieved by focusing through a 20 mm (0.787 in.) N-BK7 right angle prism with an antireflective coated hypotenuse (Thor Labs PS 908H-A). The prism is supported by a rotation platform (Thor Labs RP01) mounted to the same T-slotted frame rail as the v310 using a custom bracket to align the microscope lens with the prism (Fig. 8.11).

The optical method used to capture the images is shadowgraphy. Backlighting is supplied by a custom designed array of LEDs cantilevered above the test chamber using a standard lab stand and clamp. The 625 LEDs are powered by a 350W ADX computer power supply and cooled by two 12 VDC brushless fans.

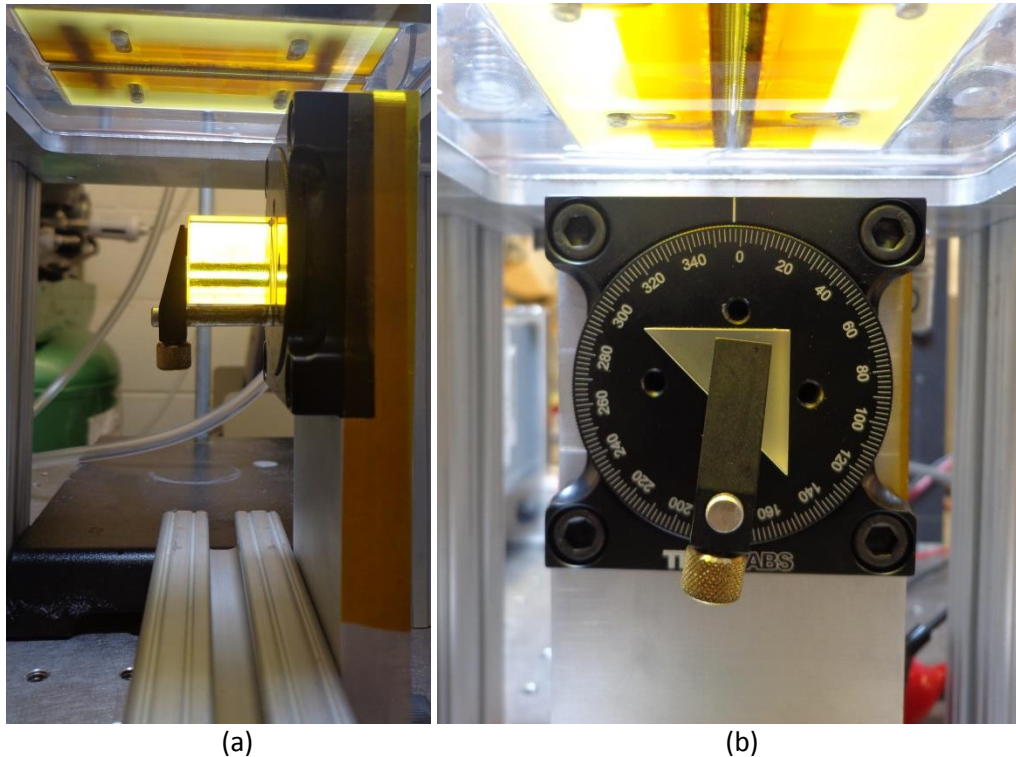


Figure 8.11: Thor Labs right angle prism as configured during testing. (a) Representative view from camera perspective showing channel in field of view through the prism. (b) Side view of prism, rotation platform, and toe clamp.

8.5. Data Acquisition (DAQ)

In order to quantify that states at which experimental videos are taken, a number of sensors are employed. Data recorded includes: pool temperature, heater voltage and current, and chamber pressure.

Pool temperature is measured using two Omega K-type thermocouples located outside of the channel as to not interfere with the flow within. They are secured with Swagelok pipe fittings through the top sheet of the test chamber. The temperature is displayed on a handheld Omega thermometer. Power input is read directly from the DC power supply used to control the heaters. Pressure is measured with an Omega pressure transducer and is secured at its designated port in the top sheet. The pressure transducer is powered by a DC

power supply. Data is read in LabVIEW using a National Instruments DAQ board. Table 8.1 below identifies all of the data acquisition components.

Table 8.1: List of components used for data acquisition.

Name	Make	Model	Measurand/Use	Range
K-Type Thermocouple (2)	Omega	TJ36-CAIN-116U-3-SMPW-M	Pool Temperature	-200-1250°C
Thermometer	Omega	HH23	Pool Temperature	J/K/T
DC Power Supply	Tenma	72-6909	Heater Power	0-300 W
Pressure Transducer	Omega	PX302-100AV	Chamber Pressure	0-100 psia
DC Power Supply	Tenma	72-8350	PX302 Power	0-100 W
DAQ Board	National Instruments	USB-6009	Chamber Pressure	-10-10V

9. EXPERIMENTAL PROCEDURES

This chapter describes the experimental procedures used to perform the open-channel pump experiments. There are two distinct regimes of operation—flashing and diabatic—for capturing data and each will be distinguished here. In the flashing method the chamber is lowered to a sub-atmospheric pressure such that the saturation temperature and pool temperature are equal. This is referred to as flash boiling or flash testing. The diabatic method uses the Inconel heaters behind the structured surface to heat the fluid within the channel to achieve boiling.

9.1. Start-up

For both the flashing and diabatic methods, much of the procedures are identical. It is indicated clearly when a procedure is dedicated for only one method of testing.

9.1.1. Spacing the Test Section Assembly

If not already at the desired spacing, the test section must be adjusted within the chamber. The pressure transducer was removed from its port. Then, the top sheet was removed by removing the sixteen stainless steel socket head cap screws, being careful not to damage the gasket. This also removed the water loop, thermocouples, and electrical contacts from the chamber interior. The test section assembly is secured with four #4-40 stainless steel socket head cap screws. After loosening these screws, the test section halves were adjusted and the distance between them was set using digital calipers. The screws were then retightened being careful not to shift the position of the halves. The distance was measured from the peaks of the ratchets as shown in Fig. 9.1 below. The test section assembly ceiling was then reinstalled with Kapton tape.

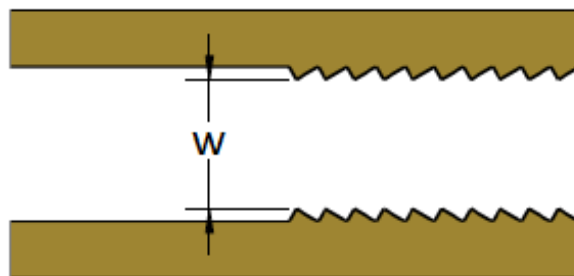


Figure 9.1: Channel width dimension definition.

Before reinstalling the top sheet of the chamber, the electrical contact screws were raised several turns. The top sheet was then set down into place and each of the electrical contact screws were slowly inserted until contact is made with the heater leads. Once all of the leads were in contact, the top sheet was tightened down. This process of setting the contact of the screws with the heater ensured that quality electrical contact is made and that the heaters were not damaged.

9.1.2. Securing the Chamber

With the chamber sealed, the chamber was placed on the stage such that it was square and centered. Alignment marks measured out onto the stage surface made this process repeatable. The toe clamps were then tightened onto the chamber to prevent it from shifting. The pressure transducer, lines to and from the bath circulator and vacuum line were all connected to their respective ports. If the testing included the diabatic method, the power leads from the heater DC power supply were attached to the brass electrical contacts with alligator clips.

9.1.3. Filling the Chamber

The working fluid for the open-channel pump was 3M's perfluorohexane (FC-72). This dielectric, highly wetting, and volatile fluid is stored in a freezer at approximately $-20\text{ }^{\circ}\text{C}$ ($-4\text{ }^{\circ}\text{F}$) to prevent evaporation. The vacuum system was isolated from the chamber by closing the valve at the tank and the vacuum pump was turned on—setting a pressure (absolute) in the

tank to 0.5-0.7 bar (7.25-10.15 psi). Ensuring that the fill/drain valve is closed, the chamber was opened to the vacuum tank and the fill tube was submerged into the FC-72 container. The fill/drain valve was then opened slowly to allow FC-72 to flow into the chamber. The flow was stopped by closing the fill/drain valve once the height of the fluid was several millimeters above the top of the test section assembly ceiling. The valve at the vacuum tank was then closed to isolate the chamber. Any remaining fluid in the fill tube was either drained back to the FC-72 container or into the chamber. Opening the fill/drain valve reestablished atmospheric pressure in the chamber and this value was recorded for reference. The container of FC-72 was resealed and returned to the freezer.

9.1.4. High-Speed Camera and Lighting

The camera was first attached to the linear bearing using two of the mounting holes located on the bottom and the linear bearing is slid onto the T-slotted rail. The Infinity K2/SC microscope lens, CF-3 or CF-2 objective, and lens brace are all subsequently installed. The starting procedure for the v310 was the same for the open-channel pump as it was for the adiabatic single-bubble. Refer to Part II for these procedures.

Once the software is ready, lens aperture is set to 100% open, the LED array is turned on, and the camera's position and focus are adjusted until the structured surface becomes visible. The stage is adjusted such that the field of view (FOV) desired is attained. For the data presented in this thesis, the FOV is region referred to as 'center-exit' and is displayed in Fig. 9.2.

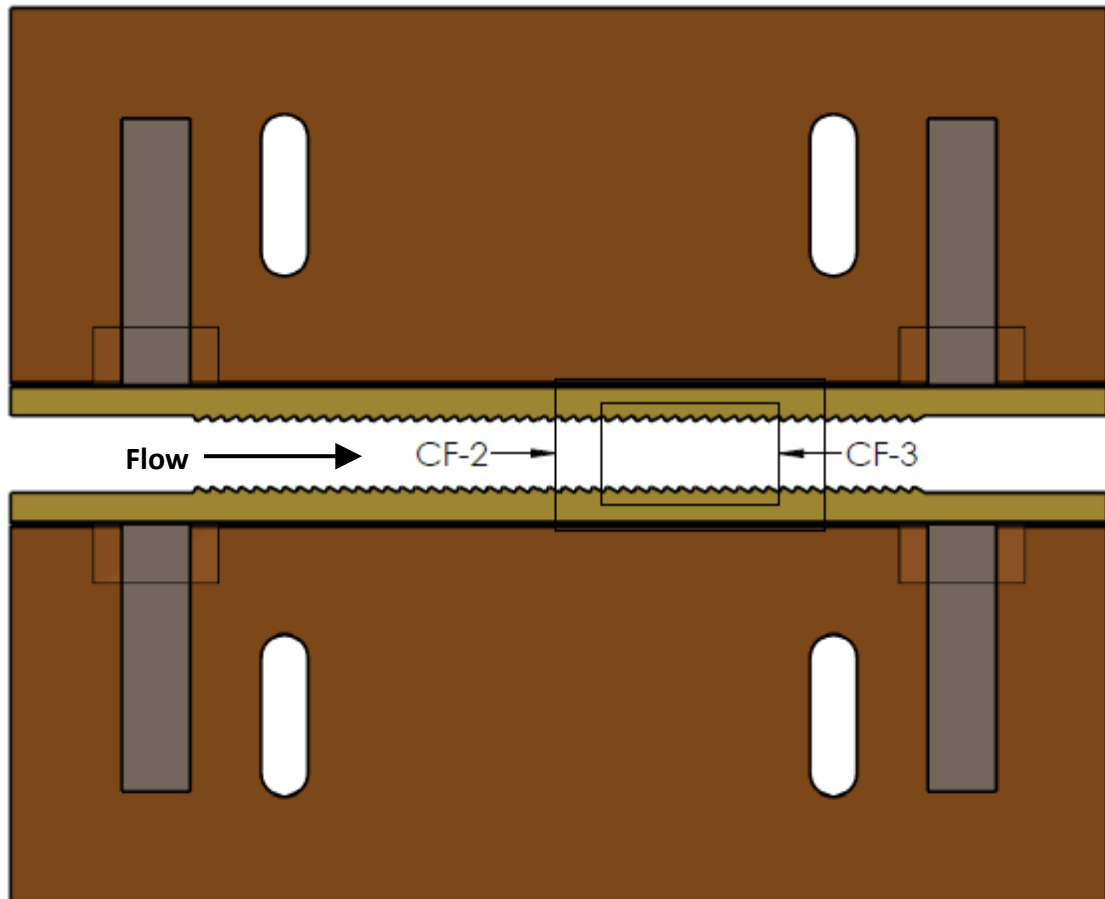


Figure 9.2: Field of view for the two different microscope objectives.

Table 9.1: Phantom Camera Control settings

Parameter	Setting
Image Resolution	1280 x 720 pixels
Sample Rate	500 frames per second
Exposure Time	90 μ s
Aperture	100% open
Focus	Far
Pixel Resolution	67 pix/mm (CF-2) 103 pix/mm (CF-3)

9.2. Flash Boiling

In order to achieve flash boiling, the pressure required to saturate the fluid in the chamber must be known. By reading the temperature from the thermometer, an estimate for the needed pressure was made using a plot of saturation temperature versus pressure for FC-72. This plot is included in Appendix D. The pressure in the tank was then set slightly below this estimate. Confirming that the fill/drain tube was closed, the vacuum tank valve was slowly opened to lower the pressure in chamber. The lower pressure affects two noticeable changes occur in the pool: the boiling was initially violent and chaotic and the pool temperature dropped to meet the saturation temperature for the given pressure. It was only after these two effects have stabilized that a high-speed video was recorded. Pressure and pool temperature was recorded along with the high-speed video and the chamber was reopened to atmospheric pressure. After many repetitions of this process, some FC-72 vapor was lost and was replaced using the appropriate filling procedures previously described. Furthermore, the bath circulator was utilized to both raise and lower the pool temperature between data sets as desired by adjusting the bath temperature.

9.3. Diabatic Boiling

The data presented in this thesis are identified by varying input heat fluxes and pool temperature. Heat flux was controlled by the heaters in the test section assembly. Because the heaters are wired in series they are controlled by the same DC power supply. Input heat flux was adjusted by increasing the input voltage on the power supply while keeping the current limiter at a maximum desired level (approximately 1.5 A).

Pool temperature was varied in several ways. To reach high pool temperatures, the bath circulator was set to 70 °C (158 °F) and the heaters are turned on to maintain boiling. This method took approximately one hour to reach a pool temperature of 38.7 °C (101.7 °F). For moderate pool temperatures, the bath circulator was set to 5 °C (41 °F) and the heaters were turned off between data sets as the heaters progressively raised pool temperature if left on.

For low pool temperatures, the bath circulator was set at 5 °C (41 °F) and data was taken immediately after the cold FC-72 is filled in the chamber.

9.4. Sub-Atmospheric Diabatic Boiling

For one data point presented, both the heaters and the vacuum system were utilized. This was necessary because it is not possible to maintain a low subcooling with only the test section heaters. For this data point, a steady pressure was set in the chamber that corresponded to a saturation temperature greater than the pool temperature. The heaters were adjusted to the desired power and a video was captured.

9.5. Capturing Videos

To capture a video of the bubbles traveling through the channel, the camera's RAM must be initialized. The RAM stores the preceding 8 GB of continuously recorded video which can be selected to save with the trigger function. When the camera is triggered, the camera activates the previously recorded images and displays them in the PCC software. For the camera settings chosen, the RAM memory captures 9129 images preceding the trigger, of 4000 frames in the range [-8000 to -4000] was saved for all of the data presented.

9.6. Shut-down

The shut-down procedure for this experiment is largely the reverse of the start-up procedures. Nonetheless, they are described below.

9.6.1. High-Speed Camera and Lighting

It is imperative to shut down the Phantom v310. Once the final high-speed video has completed saving, the Phantom Camera Control Software was closed, Ethernet cord removed from the laptop, and the power cable unplugged from the rear of the camera. For days of consecutive testing, the camera was left on the T-slotted rail with the appropriate lens cap installed. Otherwise, the Infinity lens was disassembled, removed, and stored. The

v310 was also removed from the facility, disconnected from the linear bearing, and stored as well. The linear bearing was replaced on the T-slotted rail. The LED array was shut off and rotated away from the test chamber.

9.6.2. Draining the Chamber

At the conclusion of testing, the heater power supply was disconnected from the heaters and shut off (diabatic testing only). The vacuum system was isolated from the test chamber and—if flash tests were performed—the chamber was vented to the atmosphere through the fill/drain valve. The vacuum line and pressure transducer were both disconnected and the toe clamps were loosened to free the test chamber. A cap was installed on the vacuum port to prevent spillage during the draining process. With the FC-72 storage container open and the fill/drain tube inserted, the test chamber was lifted and tilted to drain the FC-72 back into its container. The test chamber was then replaced on the stage and secured with the toe clamps.

10. DATA ANALYSIS

This chapter covers the data analysis completed for the results presented in Chapter 11 for the open channel pump. Description of measurement of pool subcooling, chamber pressure, and bubble location and tracking is presented. Calibrations and uncertainties for all of the measured values are also provided.

Pool subcooling and chamber pressure were used to quantify the state of the working fluid at each data point. Pool subcooling is defined as the difference between the saturation temperature of the working fluid (FC-72) and the pool temperature. Pool temperature was measured using a K-type thermocouple. Chamber pressure was measured using an Omega PX302 pressure transducer and was used to determine the saturation temperature of the fluid. Saturation temperature was found using fluid property data supplied by the manufacturer (3M).

10.1. Bubble Slug Tracking

From the high-speed videos, bubble slug position was determined using National Instruments Vision Assistant. Tracking of bubble position was necessary to determine the kinematics of slugs traveling in the channel. Two methods of analyses were performed on the videos. In the cases where entire bubble slugs were visible in the field of view (FOV), bubble centers of mass in the x -direction (CoM- x) were considered its position. For the cases where only a portion of the bubble slug was visible in the FOV, leading edge positions were considered tracking position.

10.1.1. Center of Mass Tracking

Tracking the center of mass began with a cropped version of the raw image. Original images were cropped to show only the channel width, leaving a top and bottom black region. The cropping was done in MATLAB for all images in a series. If necessary, the images were also slightly rotated such that the peaks of the ratchets were all horizontally aligned. This image (Fig. 10.1a) was then imported into the Vision Assistant software and binarized. Unwanted

regions were then removed using a series of functions. This was accomplished using 'Remove border objects', 'Remove small objects', and two particle filters to remove any remaining regions that were neither border objects nor small. After the aforementioned steps, only the interior region of the large bubble slug of interest remained in the image (Fig. 10.1b) as the outer edge of the bubble was indistinguishable from the ratchet surface. The center of mass of the bubble was then output by the software by its 'Particle Analysis' tool. These steps were done with batch processing for each frame of a distinguishable bubble slug traveling through the channel.

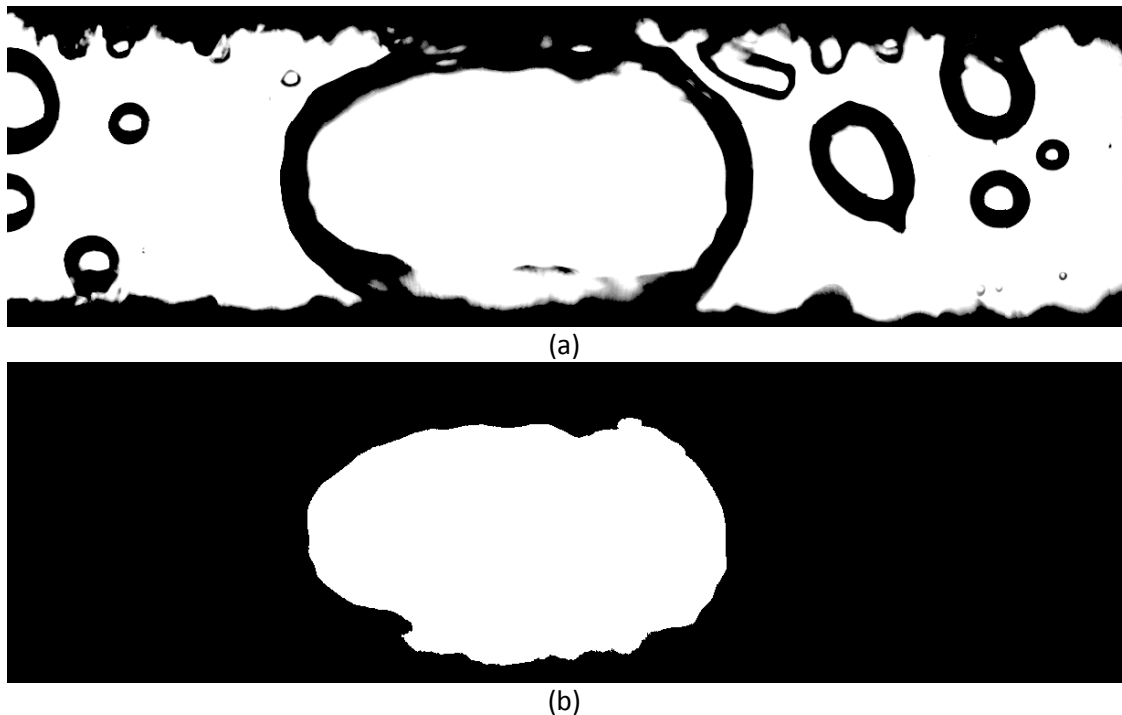
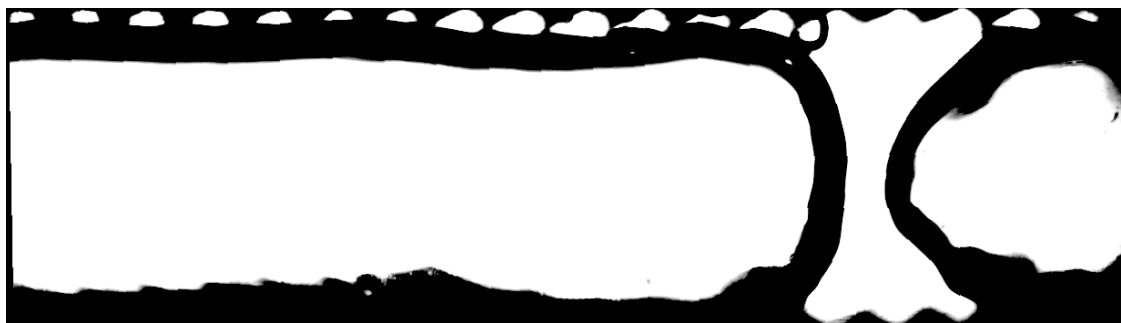


Figure 10.1: Example images from the image processing performed to track the center of mass of a bubble slug. (a) The cropped, raw image imported into Vision Assistant. (b) The bubble slug of interest after image processing.

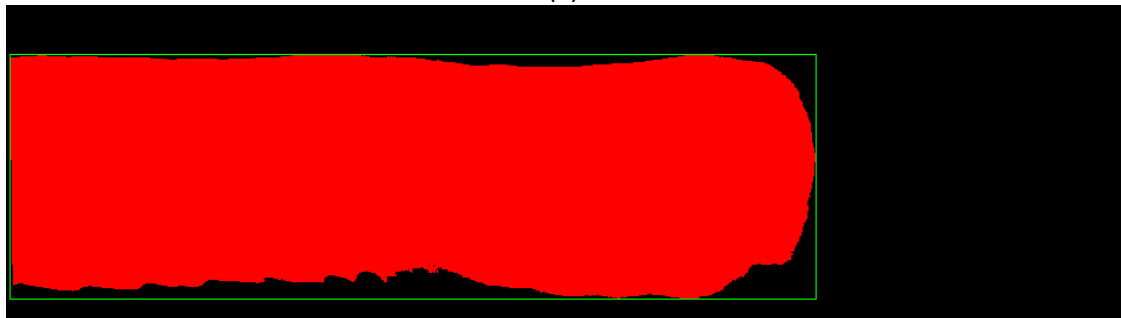
10.1.2. Leading Edge Tracking

Tracking leading edges of a bubble slug, was nearly identical to tracking centers of mass. Raw images were cropped in MATLAB to only show the width of the channel. Images were also

slightly rotated such that the peaks of the ratchets were all horizontally aligned. The images (Fig. 10.2a) were then imported to the Vision Assistant software and binarized. Border and small objects were removed with built in functions and any remaining objects were removed using particle filters based on their first pixel location and area. The position of the leading edge of the bubble slug was output by the 'Particle Analysis' tool as the bounding rectangle right edge horizontal pixel location. The bounding rectangle is defined by the software by the left, right, top, and bottom-most pixel of an object (Fig. 10.2b).



(a)



(b)

Figure 10.2: Example images from the image processing performed to track the leading edge of a bubble slug. (a) The cropped, rotated, raw image imported into Vision Assistant. (b) The bubble slug of interest after image processing. The bounding rectangle is shown in green.

10.1.3. Slug Velocity and Acceleration

Once the position of bubble slug was tracked by either its center of mass or leading edge it was plotted with respect to time. Velocity was calculated from the position data using a second order central differencing scheme with a time step equal to the time between ten frames of high speed video (20 ms). Equations 10.1-10.2 show the scheme used to determine velocity and Fig. 10.3 below shows how an example of velocity values with varying time steps.

$$v_i = \frac{x_{i+n} - x_{i-n}}{2 \cdot ndt} \quad (\text{Eq. 10.1})$$

where $n = 5$ and

$$dt = \frac{1}{fps} \quad (\text{Eq. 10.2})$$

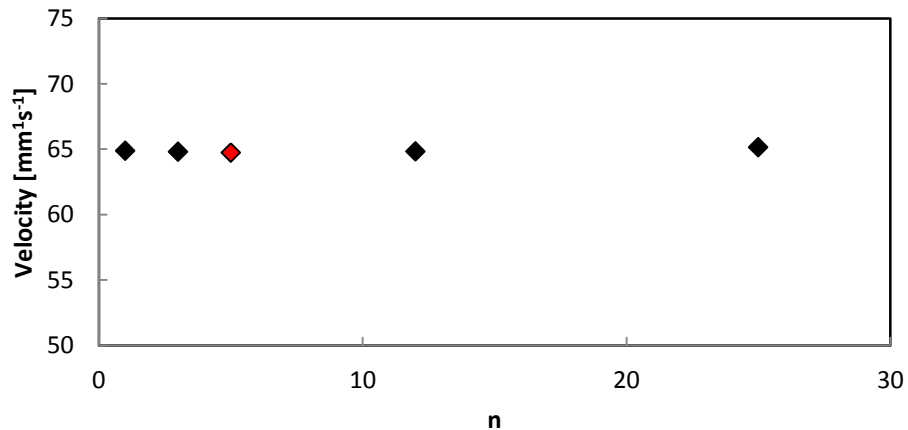


Figure 10.3: Plot of velocity with varying n for an example slug, the time step used in calculating the velocity of vapor slugs. The red data point indicates the $n = 5$ as used for the results presented.

10.2. Calibration and Uncertainty

To provide confidence in the results, calibrations and uncertainty analyses were performed. The instruments included in this section are the, pressure transducer, high-speed camera, thermocouple, and heater power supply. Calibrations were completed for both the high-speed camera and pressure transducer and thermocouple; however, manufacturers supplied accuracy was used for the power supply. The calibration for the Phantom v310 was identical for this experiment as it was for the adiabatic single-bubble and is not discussed here.

10.2.1. Pressure Transducer Calibration and Uncertainty

Calibration of the pressure transducer was performed in situ from 0.126 bar (3.73 inHg) to 1.01 bar (29.73 inHg) against an Omega test gauge (Model: PGT-60L-30V) as the standard. The accuracy uncertainty estimated at 0.0017 bar (0.05 inHg)—the resolution error of the analog gauge. The total uncertainty of the pressure transducer was equated to be the root sum of square of the standard gauge accuracy error, precision error of calibration, and curve fit error (RMSE). Total uncertainty of the pressure transducer was calculated to be 0.058 bar (1.7 inHg). This uncertainty was the bias error in pressure for the channel flow measurements.

Precision error for all calibration data points was calculated as the product of the student-t value and the standard deviation of the sample set. The maximum precision error of the calibration data points was used to evaluate the total error to the calibration range.

$$u_{Precision} = \sigma_p t_v \quad (\text{Eq. 10.3})$$

$$\sigma = \frac{1}{v} \sqrt{\sum_{i=1}^N (P_i - \bar{P})^2} \quad (\text{Eq. 10.4})$$

Curve fit error was evaluated as root mean square error, which takes the form shown below in Eq. 10.5.

$$RMSE = \sqrt{\frac{\sum_{i=1}^N (P_i - \bar{P})^2}{\nu}} \quad (\text{Eq. 10.5})$$

$$\nu = \text{degrees of freedom} = N - 1$$

Total error for the pressure transducer was then equated with the root sum of squares of the three sources of error.

$$u_{Total} = \sqrt{u_{Guage}^2 + u_{Precision}^2 + RMSE^2} \quad (\text{Eq. 10.6})$$

Each source of error, including total error is displayed in and the calibration curve is shown in

Table 10.1: Summary of uncertainty analysis of the Omega PX302 pressure transducer.

u_{Guage}	$u_{Precision}$	$RMSE$	u_p
0.0017 bar	0.0574 bar	0.0047 bar	0.058 bar

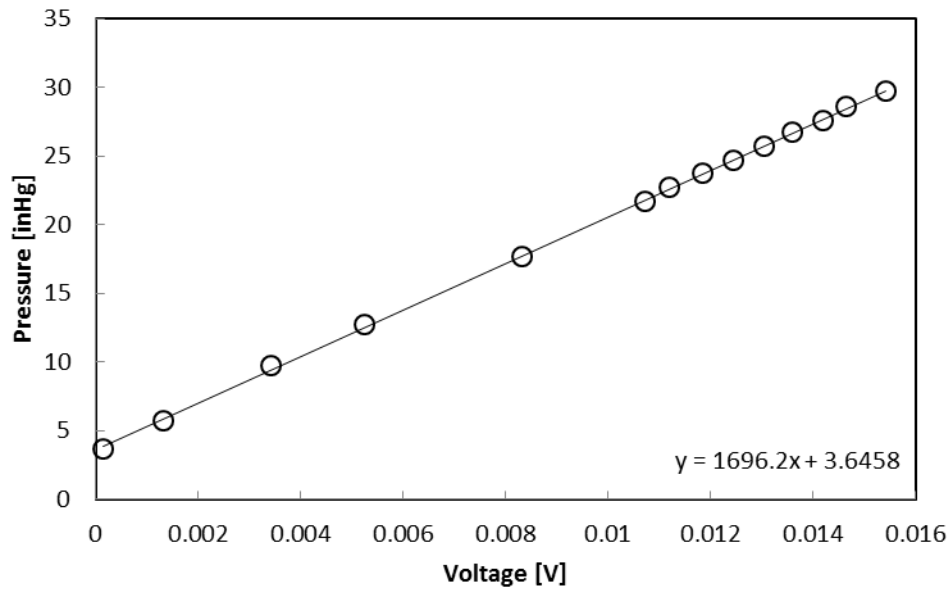


Figure 10.4: Calibration curve for the Omega PX302 pressure transducer.

10.2.2. K-type Thermocouple Uncertainty

The Omega K-type thermocouple was calibrated while connected to the Omega HH23 thermometer against the bath circulator which has an accuracy of 0.01 °C (0.018 °F). A total of ten data points in the range of pool temperatures tested in the chamber were used in the calibration. Total uncertainty of the thermocouple was calculated as the root sum of squares of the curve fit error (RMSE) and bias of the bath circulator. Table 10.2 and Fig. 10.5 show the calibration data for the K-type thermocouple.

Table 10.2: Summary of uncertainty analysis of the Omega K-Type thermocouple.

u_{bath}	$RMSE$	u_T
0.01 °C	0.14 °C	0.14 °C

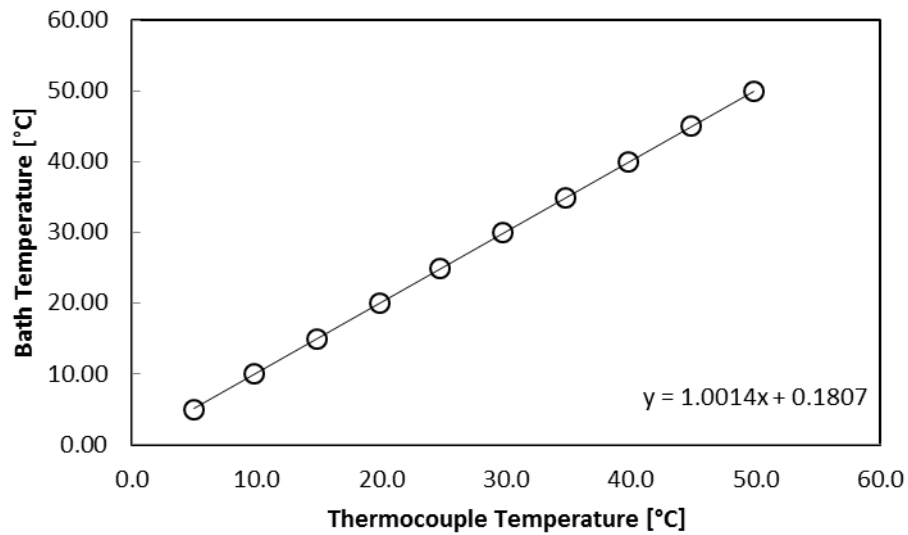


Figure 10.5: Calibration curve for the Omega K-type thermocouple.

10.2.3. Subcooling Uncertainty

As the subcooling is the difference between the saturation temperature of the working fluid and the pool temperature, the uncertainty in subcooling was determined as the root-sum-of-squares of the thermocouple uncertainty and the uncertainty in saturation temperature due to pressure uncertainty. This was determined as the local pressure dependence of saturation temperature multiplied by the uncertainty in pressure. Saturation temperature was found using product data; therefore the local pressure dependence was determined as the slope of the saturation temperature with respect to pressure using table values above and below the measured pressure. Uncertainty in saturation temperature is shown below in

$$u_{T_{sat}} = \left(\frac{T_{i+1} - T_{i-1}}{P_{i+1} - P_{i-1}} \right) u_P \quad (\text{Eq. 10.7})$$

10.2.4. Pixel Resolution Calibration and Uncertainty

Pixel resolution serves as a means to convert pixel measurements in image data to physical values. The data presented in this section of the thesis was taken over three different days; thus, a new pixel resolution was determined for each day to ensure the value was accurate for the given experimental conditions. A summary of how pixel resolution was calibrated and the uncertainty associated with it is presented here.

Each day that video data were taken, a sample frame containing the structured surface was taken during testing. An in situ calibration was then performed during post processing. Knowing the pitch of the ratchets, calibration of camera pixels to physical dimensions could be performed. Using National Instruments Vision Assistant, the region occupied by the ratchets was extracted from the image (Fig. 10.6), their centers of mass were calculated, and the pixel distance between each ratchet was calculated. The pixel resolutions used for each day of testing are shown below in Table 10.3.

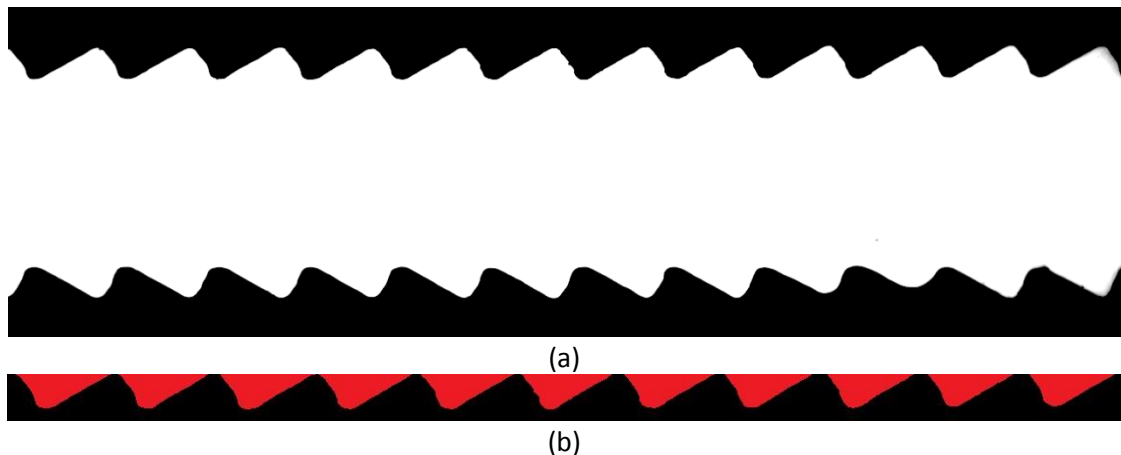


Figure 10.6: Example images used to determine pixel resolution for the high-speed videos. (a) Raw video frame is shown. (b) Top ratchets extracted in a binarized form for center of mass calculation.

Varying numbers of ratchets were visible, depending on the objective being used and the position of the camera; therefore, samples sizes also varied for these calculations. The uncertainty was determined using finite sample statistics using the equations shown below.

$$(res) = (res) \pm \sigma_{res} t_v \quad (\text{Eq. 10.8})$$

$$\sigma = \frac{1}{v} \sqrt{\sum_{i=1}^N [(res) - (\overline{res})]^2} \quad (\text{Eq. 10.9})$$

Table 10.3: Summary of pixel resolution. Each day of testing, objective, and focus position required an independent value. Uncertainties for each are additionally shown.

Day	Objective	Focus	DoF ν	t_ν	Average [pix/mm]	Uncertainty [pix]
Aug 2	CF-2	Far	24	2.064	67.65	4.00
Aug 5	CF-2	Far	29	2.045	67.36	2.39
Aug 6	CF-3	Far	19	2.093	102.98	1.98
Aug 28	CF-2	Near	8	2.306	107.32	1.87

10.2.5. Velocity Uncertainty

Uncertainty in velocity could be attributed to errors from image processing, pixel resolution, and camera frame rate. As most of the image processing was used to eliminate border objects and bubbles not of interest, it was found that varying image processing parameters had no effect on the locations of center of mass or leading edge for the vapor slugs. Velocity uncertainty was therefore evaluated as:

$$u_v = \sqrt{\left(\frac{\partial V}{\partial(\Delta x)} u_{\Delta x}\right)^2 + \left(\frac{\partial V}{\partial(\Delta t)} u_{\Delta t}\right)^2} \quad (\text{Eq. 10.10})$$

where $u_{\Delta t} \ll 1$; thus, the uncertainty in velocity is associated only with the pixel resolution uncertainty. Table 10.4 below shows the uncertainty in velocity for each day of testing where velocity results are presented.

Table 10.4: Summary of uncertainty in velocity for the three days of testing where velocity of slugs was calculated.

Day	Objective	Uncertainty [mm ¹ s ⁻¹]
Aug 2	CF-2	2.96
Aug 5	CF-2	1.77
Aug 6	CF-3	0.96

10.2.6. Heat Flux Uncertainty

The heat flux was calculated directly from the digital meters on the Tenma 72-6909 power supply. No calibration was performed for this device, but manufacturer data was applied to determine uncertainty. Heat flux was evaluated as shown in Eq. 10.11, where A_p is the projected area of the ratcheted surface and is assumed to be known with certainty. The uncertainty of a given heat flux was determined using the Kline and McClintock method (Eq. 10.12) for each heat flux reported.

$$q'' = \frac{V \cdot I}{A_p} \quad (\text{Eq. 10.11})$$

$$u_{q''} = \sqrt{\left(\frac{\partial q''}{\partial V} u_V\right)^2 + \left(\frac{\partial q''}{\partial I} u_I\right)^2} \quad (\text{Eq. 10.12})$$

11. RESULTS AND DISCUSSIONS

This section covers the results of the open channel-pump. Eight different experiments are presented. First, the results from all eight data set are presented qualitatively. Position, velocity, and acceleration data is then presented for each set. Finally, a model is proposed to predict bubble slug velocities within the channel pump.

11.1. Qualitative Visualization

Fifty high-speed videos of bubble motion in the channel were taken over three days of testing. A set of eight different videos were chosen for analysis which collectively illustrate what was observed for the all videos. The conditions for each test presented here are summarized in Table 11.1 and Fig. 11.1.

Table 11.1: Summary of conditions for each data set with uncertainties shown.

Day	Pressure [bar]	ΔT_{sub} [°C]	Voltage [V]	Current [A]	Heat Flux q'' [W ¹ cm ⁻²]	Channel Width [mm]	Operation Regime
Aug 2	1.006 ±0.058	43.3 ±1.7	27.7	1.06	5.22 ±0.09	4.50	Diabatic
Aug 2	1.009 ±0.058	27.7 ±1.7	14	0.55	1.37 ±0.04	4.50	Diabatic
Aug 2	1.009 ±0.058	22.1 ±1.7	20	0.77	2.74 ±0.06	4.50	Diabatic
Aug 2	1.009 ±0.058	21.5 ±1.7	7	0.28	0.35 ±0.02	4.50	Diabatic
Aug 2	1.009 ±0.058	17.7 ±1.7	14	0.55	1.37 ±0.04	4.50	Diabatic
Aug 2	0.572 ±0.058	5.8 ±2.7	9.1	0.36	0.58 ±0.02	4.50	Sub-atm.- Diabatic
Aug 5	0.998 ±0.058	26.8 ±1.7	14	0.55	1.37 ±0.04	2.25	Diabatic
Aug 6	0.291 ±0.058	-0.5 ±4.5	0	0	0	2.25	Flash

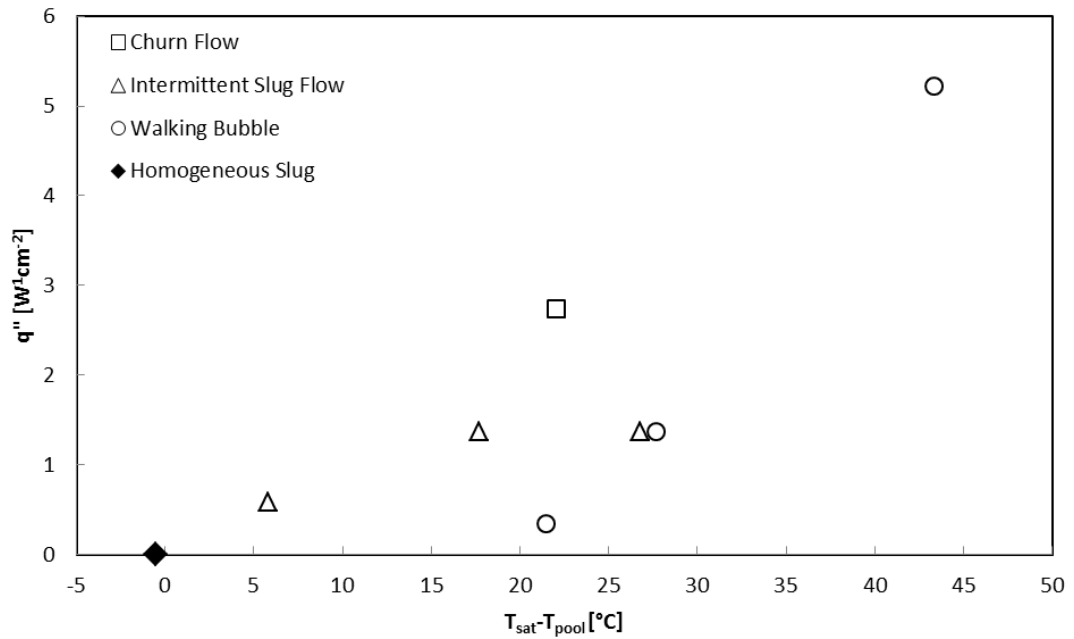


Figure 11.1: Plot of testing conditions of the channel pump. Error bars are excluded for clarity.

It was observed from the videos that four distinct regimes of channel flow existed. A set of images are shown for each regime witnessed to illustrate the characteristics of the flow. The regime of flow is dependent on the pool subcooling, heat flux input, and width of the channel. Due to the limitations of the experimental facility, not all combinations of heat flux and subcooling were achievable; thus, the boundaries of the regimes presented are not defined.

11.1.1. Churn Flow Regime

Churn flow is characterized by the presence of large unstable bubble slugs traveling rapidly through the channel in the preferential direction. These slugs are chaotic and unstable and the interface of the bubble is highly irregular. Mergers between the slug and surrounding smaller bubbles are a randomly occurring event. Often the slug interface distorts and circumvents other bubbles rather than coalescing. Furthermore, the slug often divides unexpectedly—splitting a trailing region off into an independent bubble.

Churn flow was observed in testing conditions with moderate to high heat flux ($>2.0 \text{ W}^1\text{cm}^{-2}$), moderate sub-cooling ($15\text{-}30 \text{ }^\circ\text{C}$), and a channel width of 4.5 mm such as the condition where $P = 1.009 \pm 0.058 \text{ bar}$, $\Delta T_{\text{sub}} = 22.1 \pm 1.73 \text{ }^\circ\text{C}$, $q'' = 2.74 \pm 0.06 \text{ W}^1\text{cm}^{-2}$, and $w = 4.5 \text{ mm}$. Figure 11.2 shows a sequence of frames demonstrating churn flow.

Figure 11.2: Sequence of 20 frames exhibiting churn flow. $P = 1.006 \pm 0.058$ bar, $\Delta T_{\text{sub}} = 22.1 \pm 1.73$ °C, $q'' = 2.74 \pm 0.06$ W¹cm⁻², $w = 4.5$ mm, Diabatic Operation, 500 fps, Exposure Time = 90 μ s, Aperture 100% open, Far Focus.



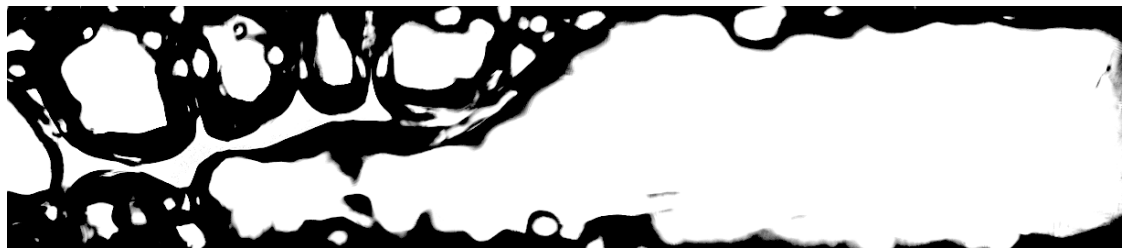
t = 0.0 ms



t = 2.0 ms



t = 4.0 ms



t = 6.0 ms



t = 8.0 ms

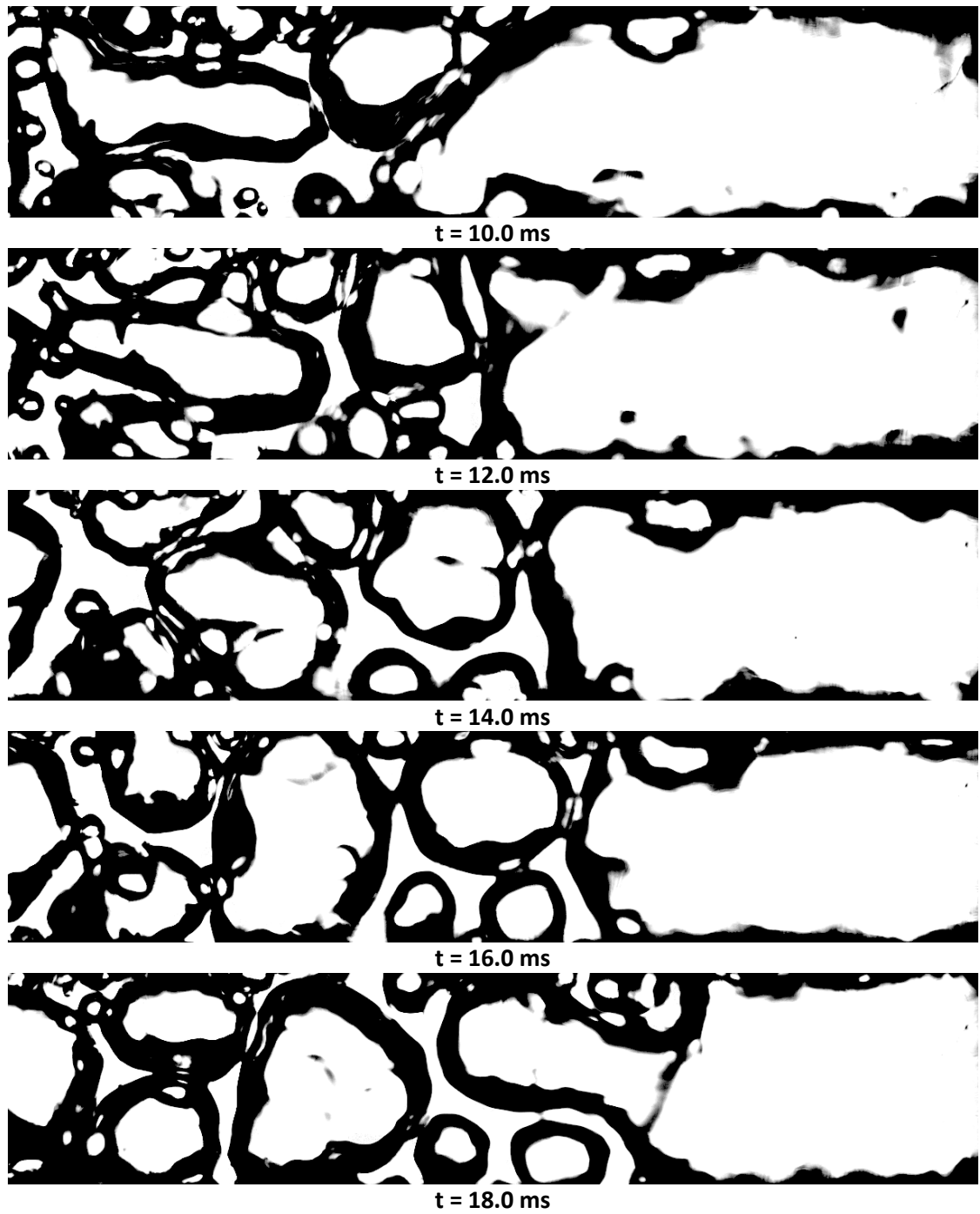


(Figure 11.2 continued)

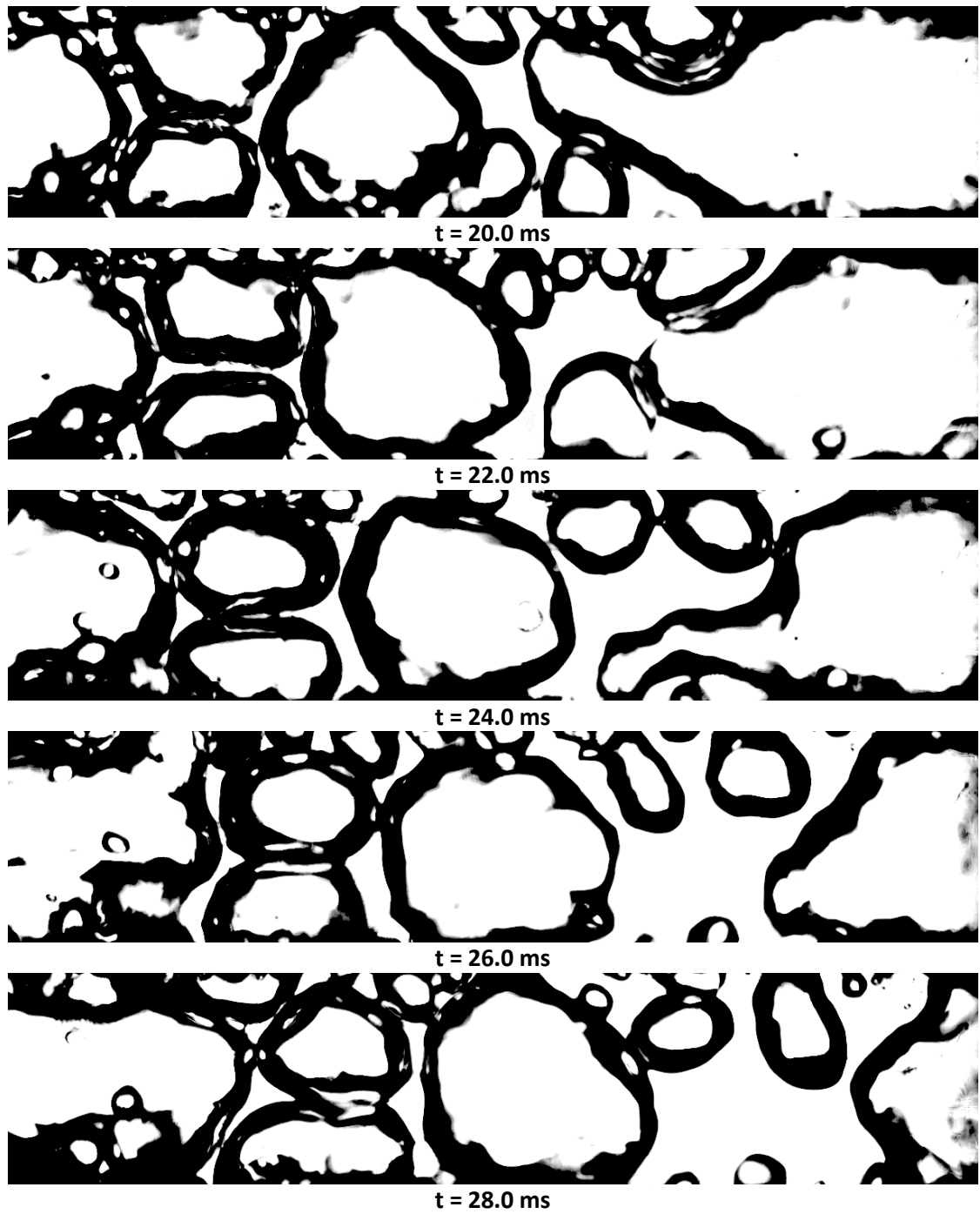


(Figure 11.2 continued)

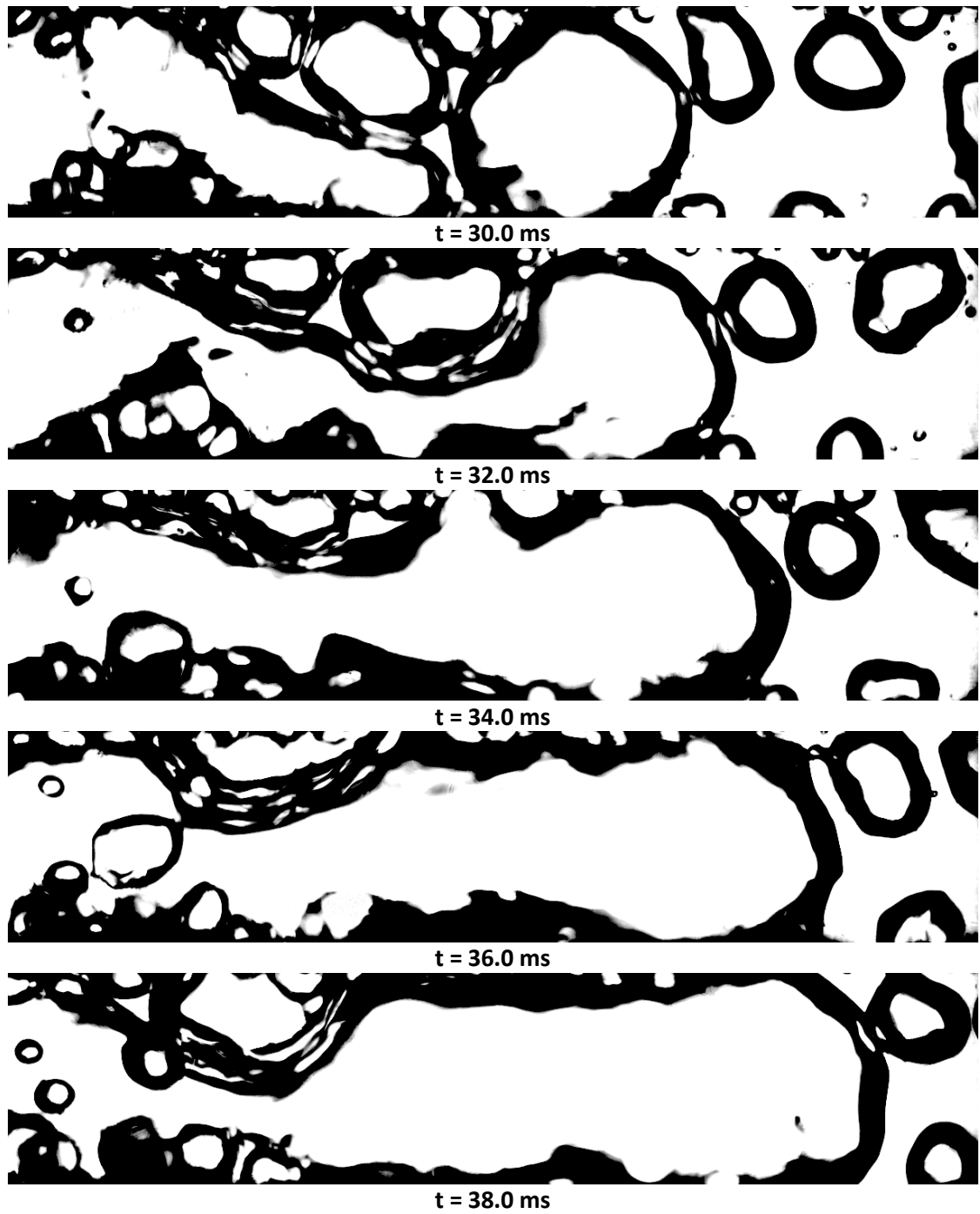


(Figure 11.2 continued)

11.1.2. Intermittent Slug Flow Regime

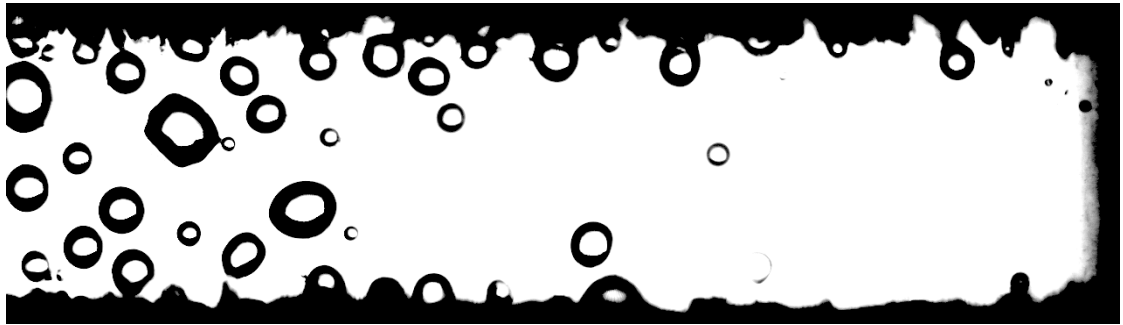
Intermittent slug flow in the channel presents itself as a cyclic flow. After a previous slug departs the field of view, the channel is mostly occupied by liquid. Production of small bubbles transitions the channel into what appears to be bubbly flow. The small bubbles coalesce, forming large bubbles which span the width of the channel. Once a large bubble interface reaches the structured surfaces on either side of the channel, it begins to accelerate down the channel, progressively merging with the other large bubbles to form a slug. The cycle repeats after the slug passes from the field of view.

Data presented in this thesis exhibiting slug flow include:

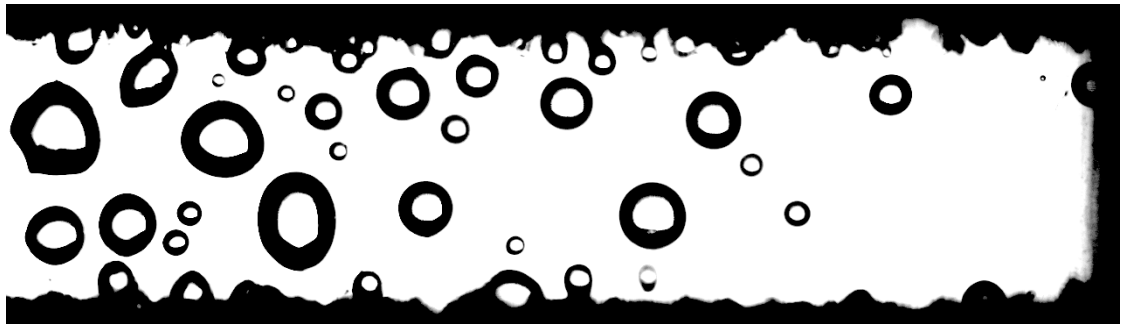
- $P = 1.009 \pm 0.058$ bar, $\Delta T_{\text{sub}} = 17.7 \pm 1.73$ °C, 1.37 ± 0.04 W¹cm⁻², $w=4.5$ mm
- $P = 0.998 \pm 0.058$ bar, $\Delta T_{\text{sub}} = 26.8 \pm 1.73$ °C, 1.37 ± 0.04 W¹cm⁻², $w=2.25$ mm
- $P = 0.572 \pm 0.058$ bar, $\Delta T_{\text{sub}} = 5.8 \pm 0.4.5$ °C, 0.58 ± 0.02 W¹cm⁻², $w=4.5$ mm

Sequences of frames are subsequently shown in Figs. 11.3-11.5 for each data condition exhibiting slug flow. Note that slug flow is achieved for two cases with identical heat fluxes; however, with channel width reduced a higher subcooling is required to maintain this flow regime. Furthermore, when chamber pressure is reduced to achieve a lower subcooling, a lower heat flux is required to produce slug flow. The last example appears to be on the cusp of slug flow—approaching to enter wispy flow (not seen in the channel flow experiments), but is classified as intermittent slug flow due to its periodic nature.

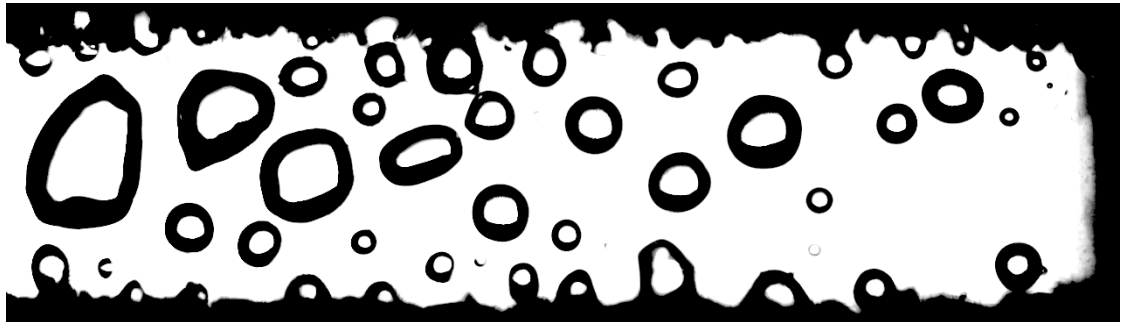
Figure 11.3: Sequence of 21 frames exhibiting intermittent slug flow. $P = 1.009 \pm 0.058$ bar, $\Delta T_{\text{sub}} = 17.7 \pm 1.73$ °C, $q'' = 1.37 \pm 0.04$ W¹cm⁻², $w = 4.5$ mm, Diabatic Operation, 500 fps, Exposure Time = 90 μs, Aperture 100% open, Far Focus.



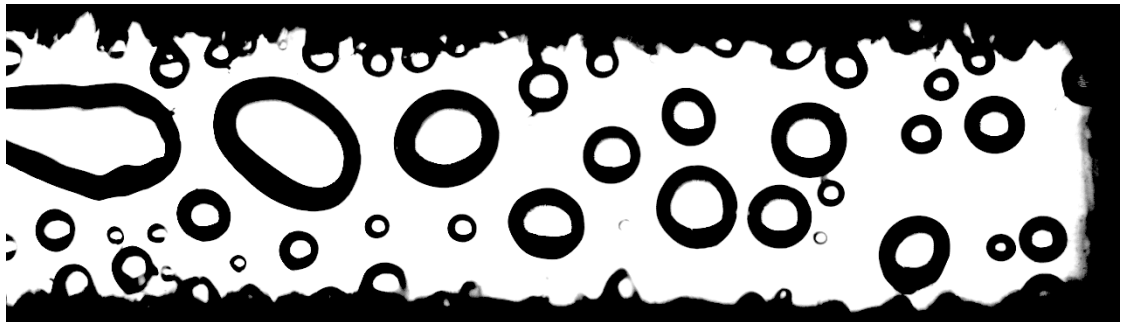
$t = 0.0 \text{ s}$



$t = 0.08 \text{ s}$



$t = 0.16 \text{ s}$



$t = 0.24 \text{ s}$

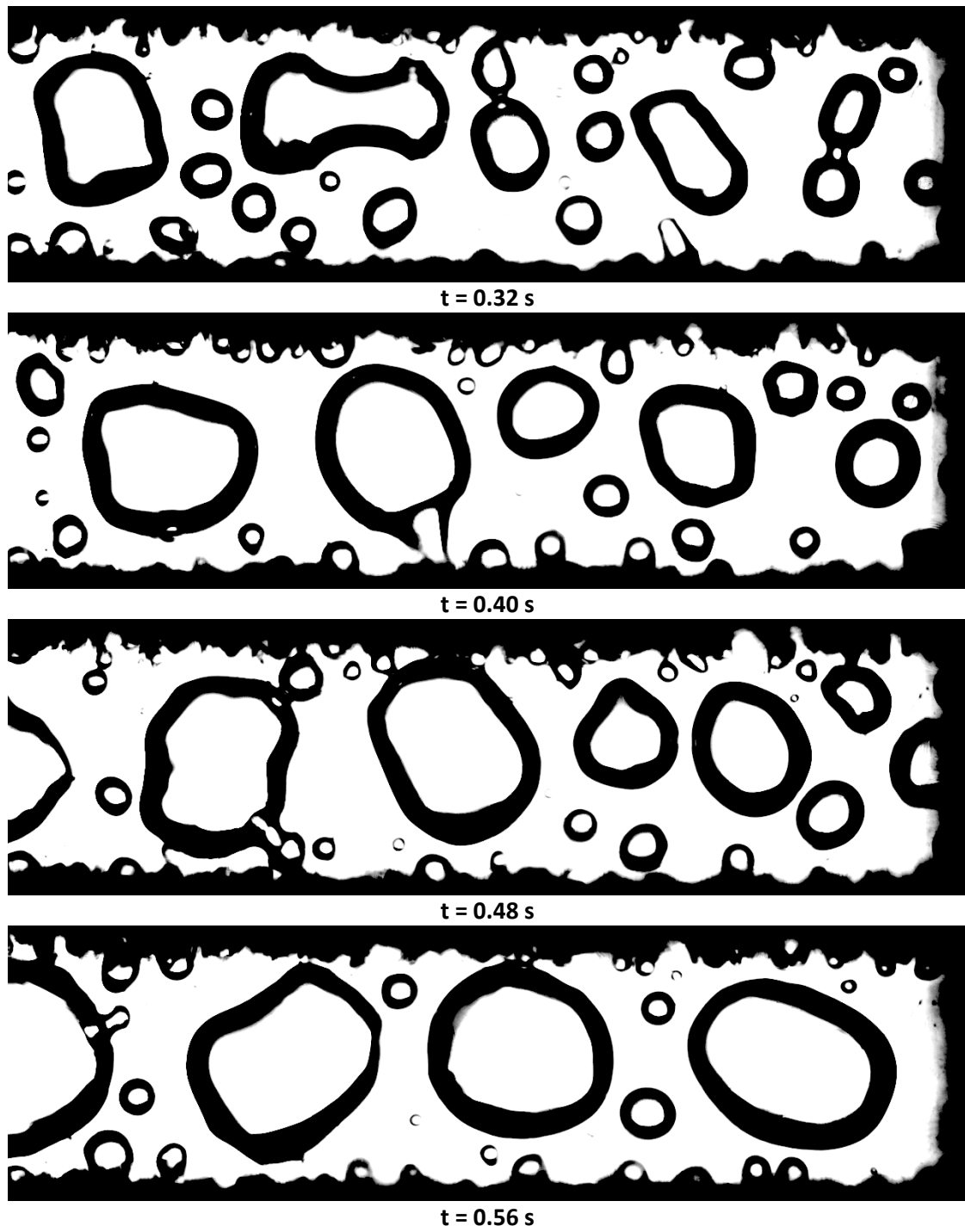
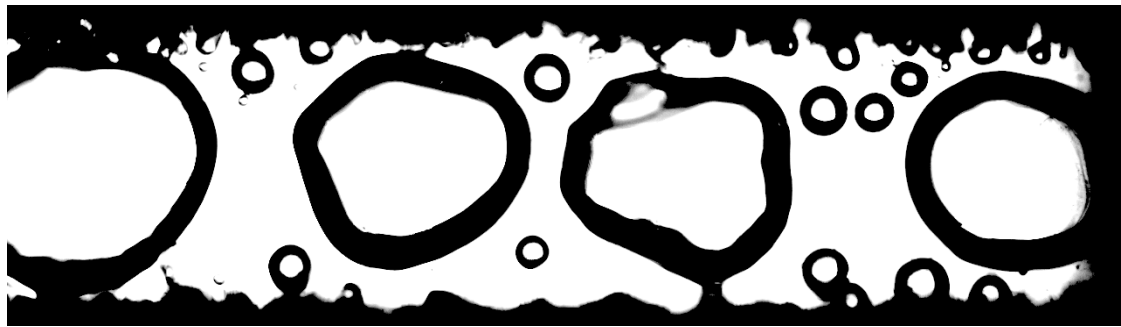


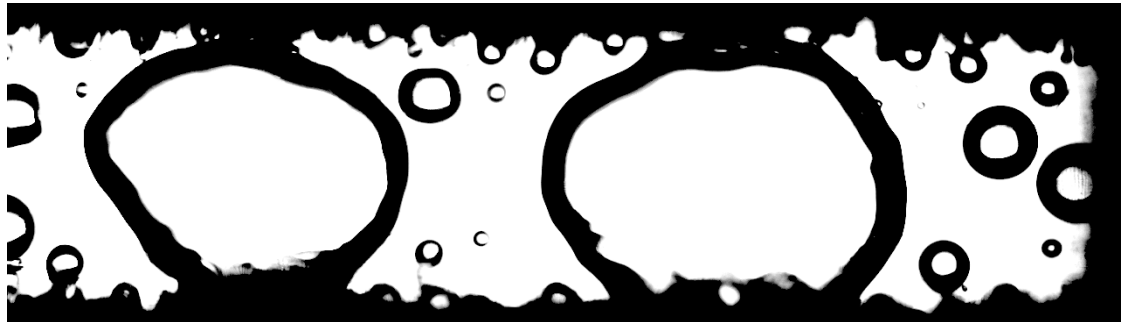
(Figure 11.3 continued)



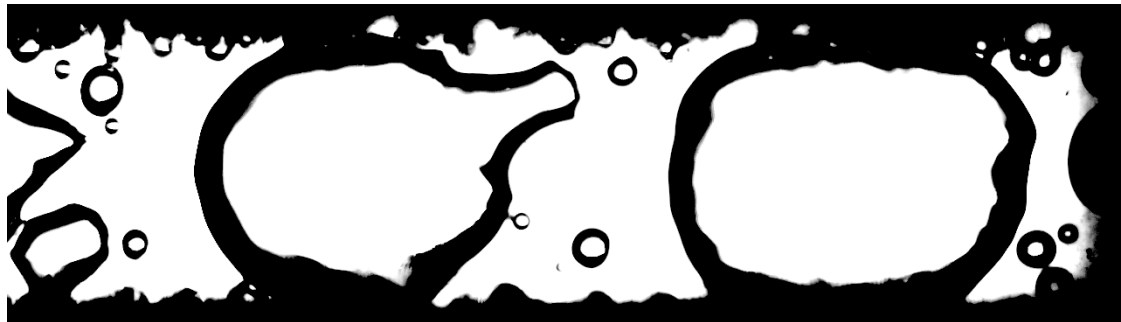
$t = 0.64 \text{ s}$



$t = 0.72 \text{ s}$



$t = 0.80 \text{ s}$



$t = 0.88 \text{ s}$

(Figure 11.3 continued)



$t = 0.96 \text{ s}$



$t = 1.04 \text{ s}$

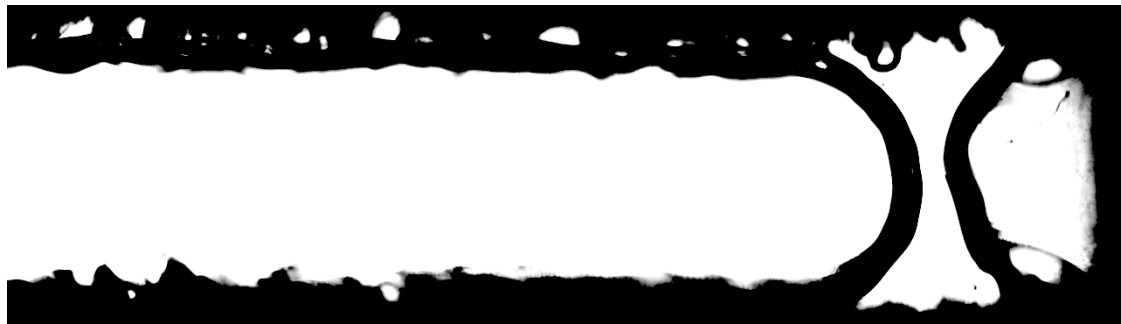


$t = 1.12 \text{ s}$

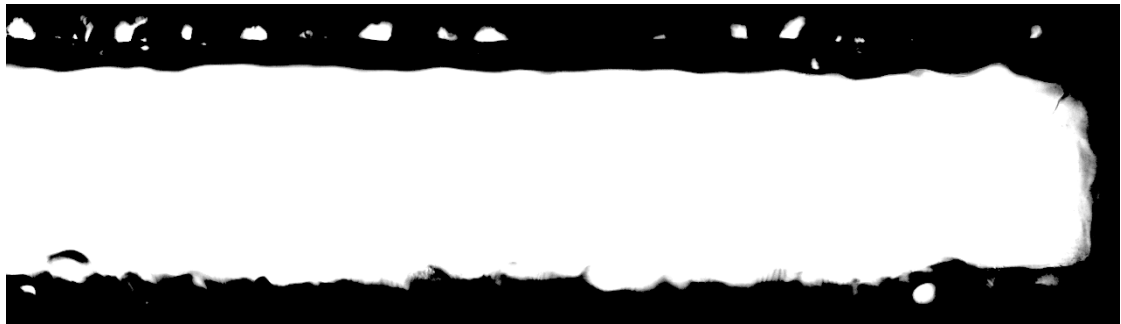


$t = 1.20 \text{ s}$

(Figure 11.3 continued)



$t = 1.28 \text{ s}$



$t = 1.36 \text{ s}$



$t = 1.44 \text{ s}$



$t = 1.52 \text{ s}$

(Figure 11.3 continued)



$t = 1.6 \text{ s}$

(Figure 11.3 continued)

Figure 11.4: Sequence of 20 frames exhibiting intermittent slug flow. $P = 0.998 \pm 0.058$ bar, $\Delta T_{\text{sub}} = 26.8 \pm 1.73$ °C, $q'' = 1.37 \pm 0.04$ W¹cm⁻², $w = 2.25$ mm, Diabatic Operation, 500 fps, Exposure Time = 90 μs, Aperture 100% open, Far Focus.

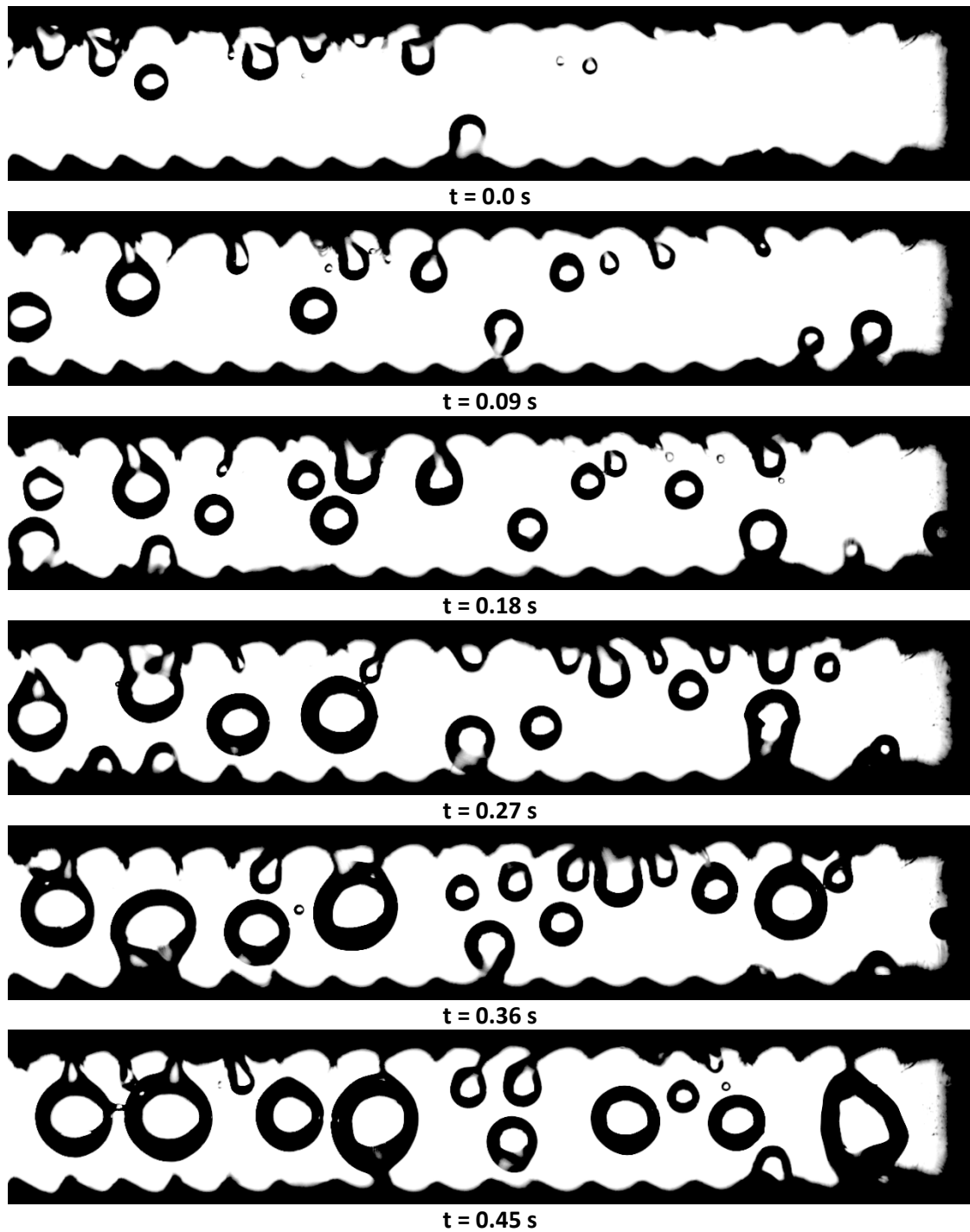


(Figure 11.4 continued)

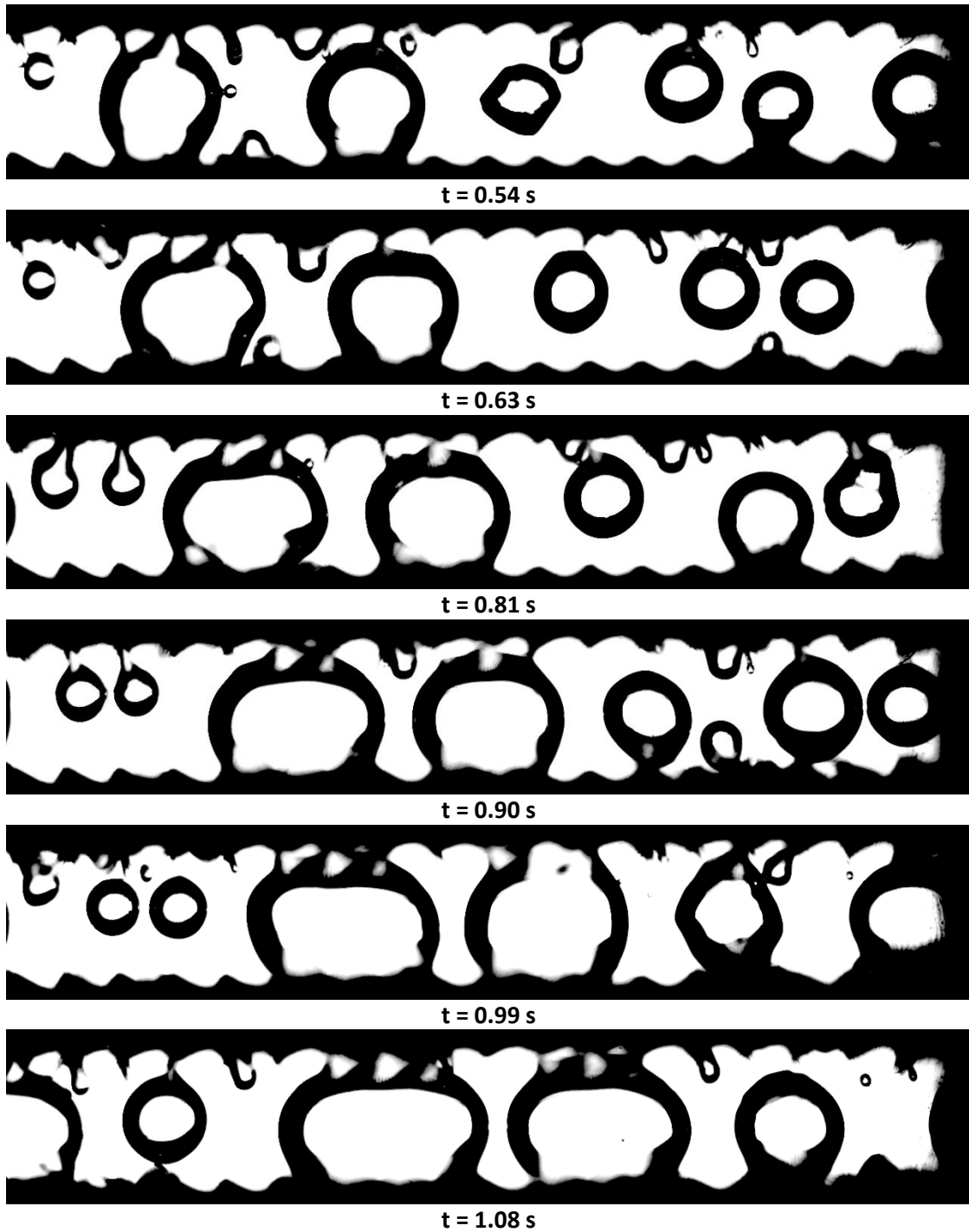


(Figure 11.4 continued)

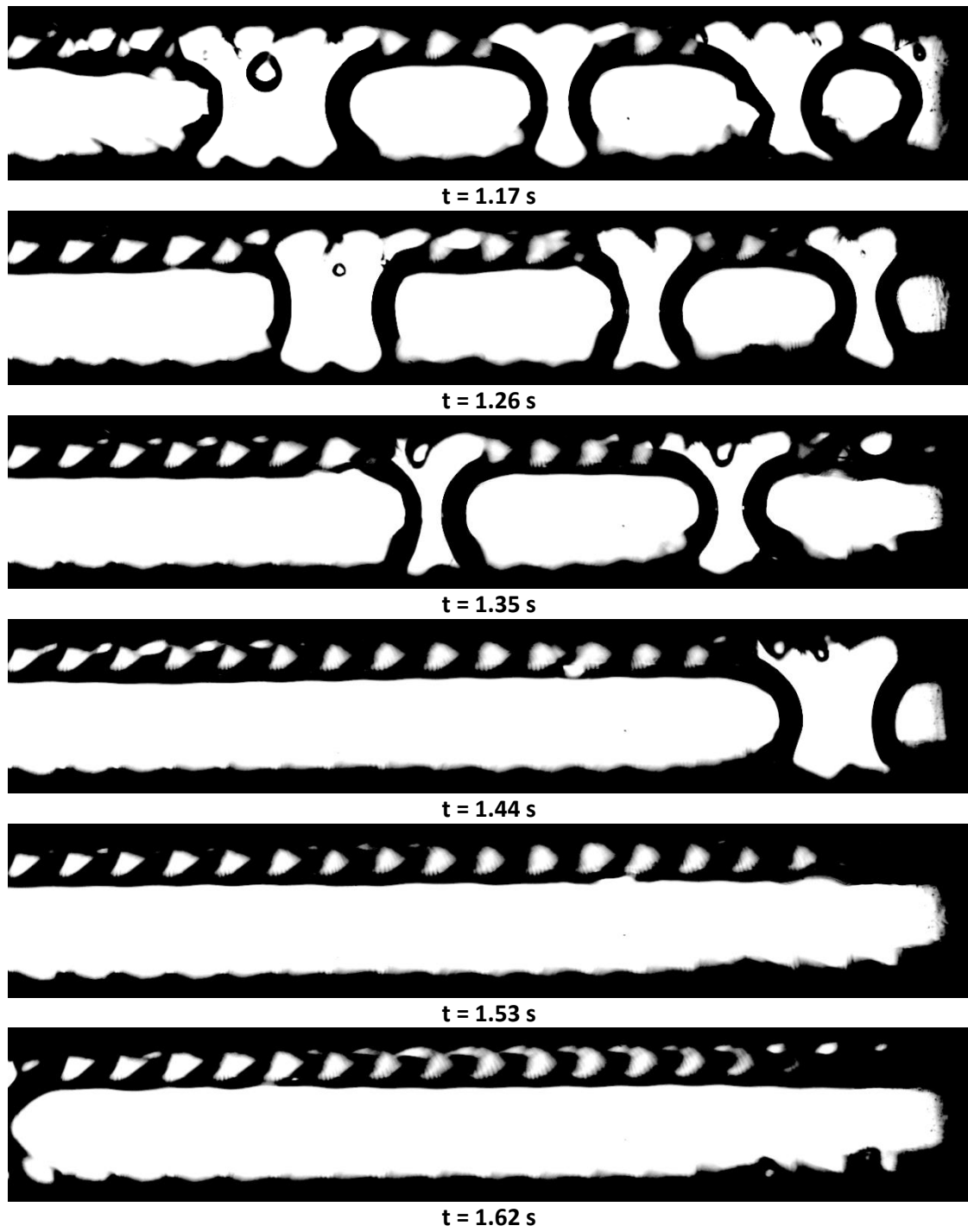


(Figure 11.4 continued)



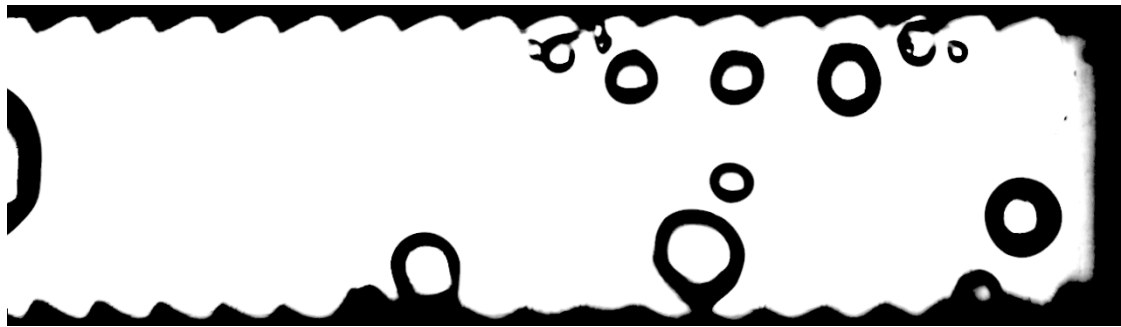
$t = 1.71 \text{ s}$



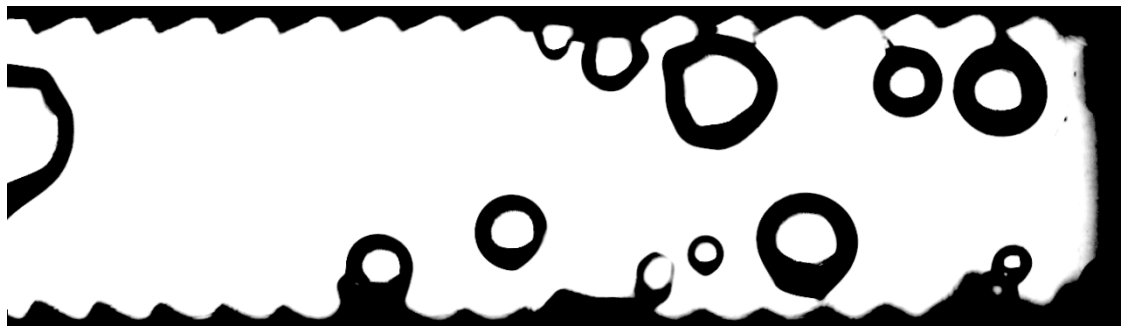
$t = 1.80 \text{ s}$

(Figure 11.4 continued)

Figure 11.5: Sequence of 13 frames exhibiting intermittent slug flow. $P = 0.572 \pm 0.058$ bar, $\Delta T_{\text{sub}} = 5.8 \pm 2.7$ °C, $q'' = 0.58 \pm 0.02$ W¹cm⁻², $w = 4.5$ mm, Sub-atmospheric Diabatic Operation, 500 fps, Exposure Time = 90 μs, Aperture 100% open, Far Focus.



$t = 0.0 \text{ s}$



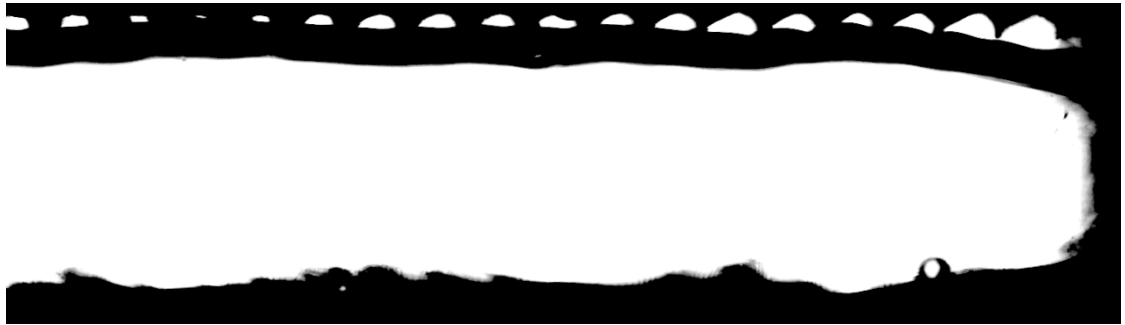
$t = 0.08 \text{ s}$



$t = 0.16 \text{ s}$



$t = 0.24 \text{ s}$



$t = 0.32 \text{ s}$



$t = 0.40 \text{ s}$



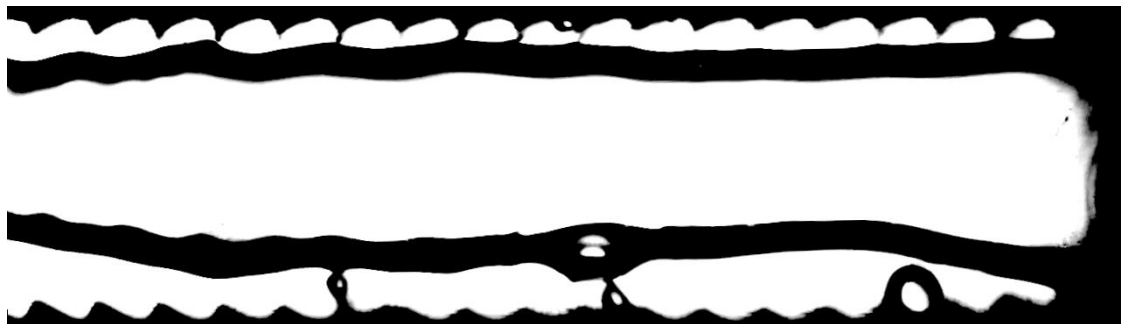
$t = 0.48 \text{ s}$



$t = 0.56 \text{ s}$



$t = 0.64 \text{ s}$



$t = 0.72 \text{ s}$



$t = 0.80 \text{ s}$

11.1.3. Walking Bubble Regime

The walking bubble regime initially appears very similar to slug flow. Small bubbles emanating from the structured surface occupy the channel and coalesce when in close proximity to another small bubble. These intermediate size bubbles appear to “bounce” or “roll along the wall as they continue to collect smaller bubbles and grow until it spans the width of the channel. The large bubbles slowly travel along the channel continuing to gather smaller bubble, but never growing larger than the field of view.

Sequences of frames are subsequently shown in Figs. 11.6-11.8 for each data condition exhibiting the walking bubble flow regime. This regime occurs when the conditions of the experiment inhibit rapid bubble production, i.e. long waiting periods between bubbles. Such conditions occur at a high subcooling and moderate to high heat fluxes or at moderate heat fluxes and low heat fluxes.

Data presented in this thesis exhibiting the walking bubble flow regime include:

- $P = 1.006 \pm 0.058$ bar, $\Delta T_{\text{sub}} = 43.3 \pm 1.73$ °C, 5.22 ± 0.09 W¹cm⁻², $w=4.5$ mm
- $P = 1.009 \pm 0.058$ bar, $\Delta T_{\text{sub}} = 27.7 \pm 1.73$ °C, 1.37 ± 0.04 W¹cm⁻², $w=4.5$ mm
- $P = 1.009 \pm 0.058$ bar, $\Delta T_{\text{sub}} = 21.5 \pm 1.73$ °C, 0.35 ± 0.02 W¹cm⁻², $w=4.5$ mm

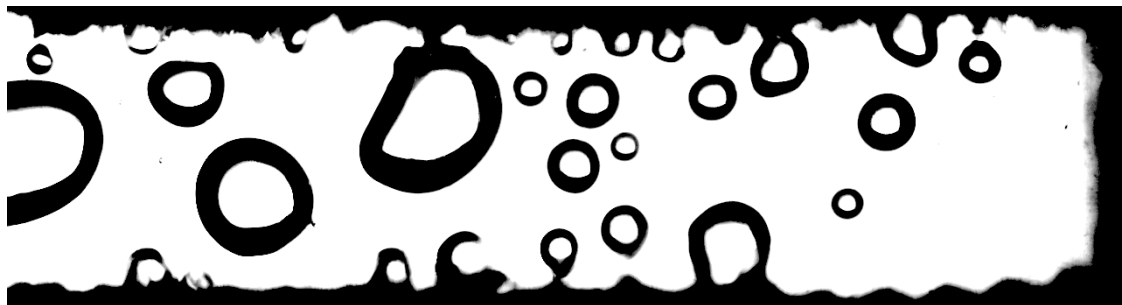
Figure 11.6: Sequence of 20 frames exhibiting walking bubble flow. $P = 1.006 \pm 0.058$ bar, $\Delta T_{\text{sub}} = 43.3 \pm 1.73$ °C, $q'' = 5.22 \pm 0.09$ W¹cm⁻², $w = 4.5$ mm, Diabatic Operation, 500 fps, Exposure Time = 90 μ s, Aperture 100% open, Far Focus.



$t = 0.0 \text{ s}$



$t = 0.07 \text{ s}$



$t = 0.14 \text{ s}$



$t = 0.21 \text{ s}$



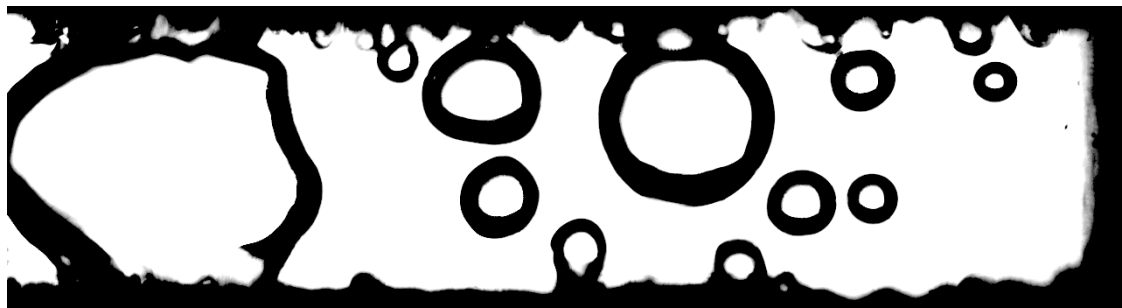
(Figure 11.6 continued)



$t = 0.56 \text{ s}$



$t = 0.63 \text{ s}$



$t = 0.70 \text{ s}$



$t = 0.77 \text{ s}$

(Figure 11.6 continued)

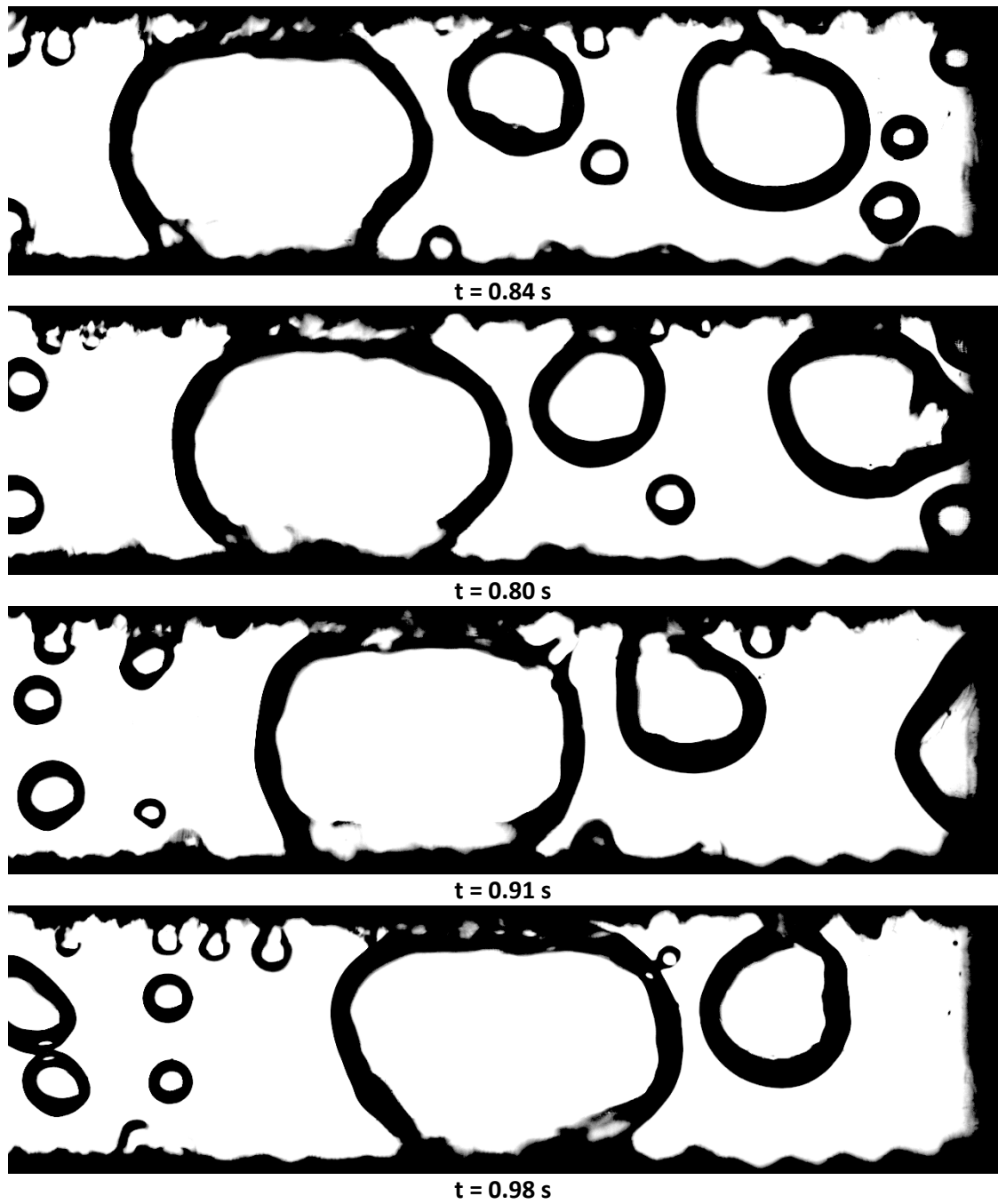


(Figure 11.6 continued)



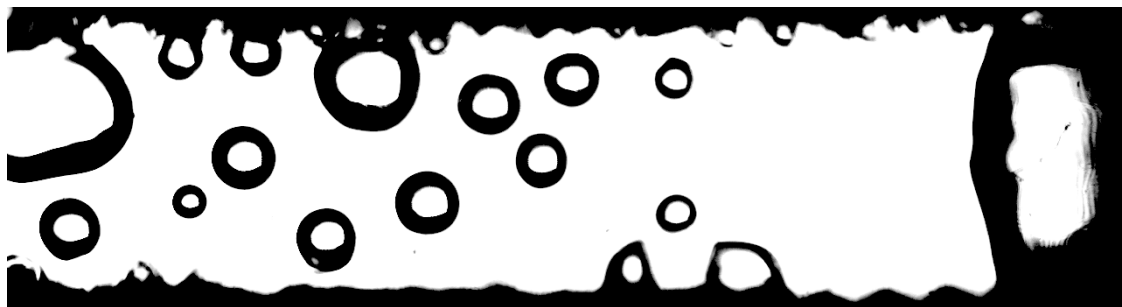
$t = 1.05 \text{ s}$



$t = 1.12 \text{ s}$



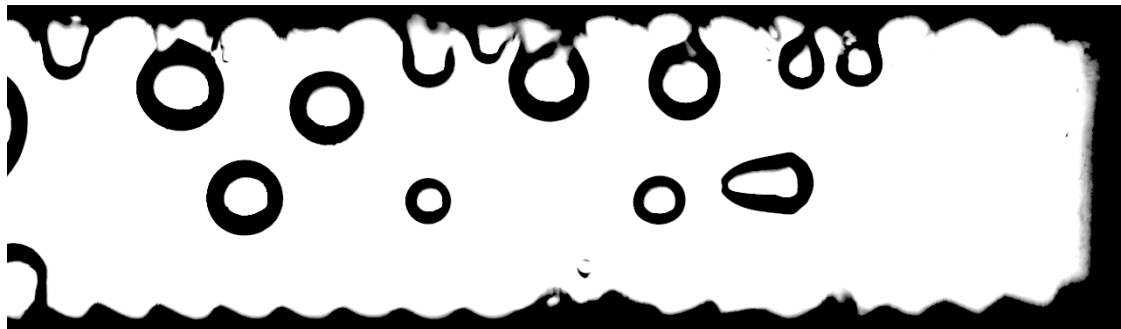
$t = 1.19 \text{ s}$



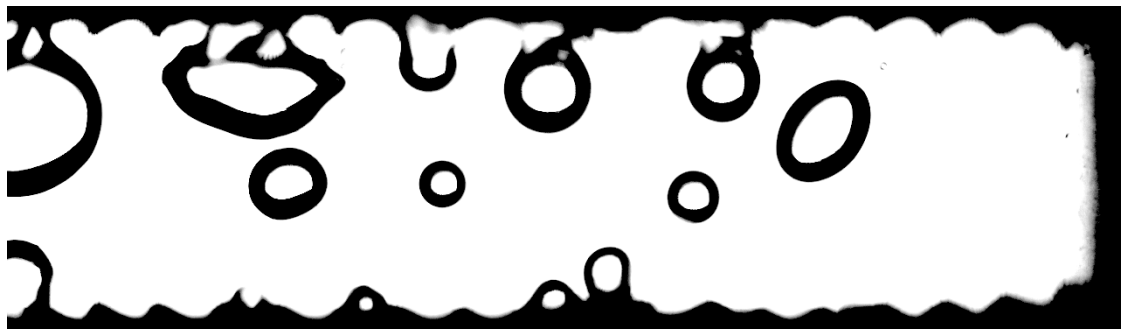
$t = 1.26 \text{ s}$

(Figure 11.6 continued)

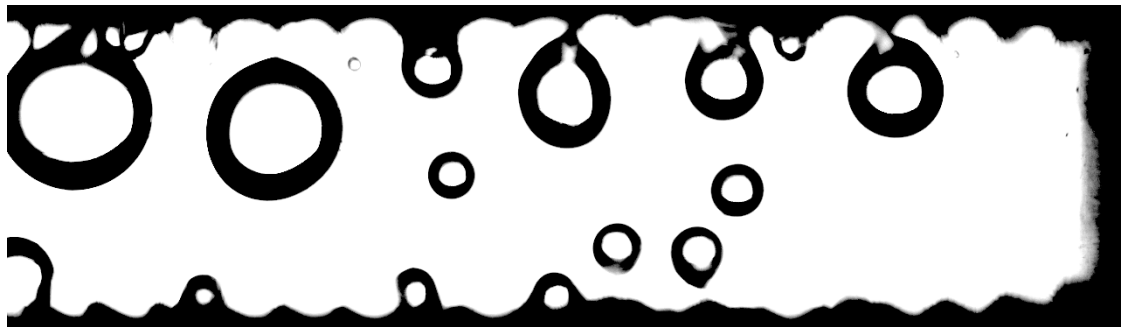
Figure 11.7: Sequence of 20 frames exhibiting walking bubble flow. $P = 1.006 \pm 0.058$ bar, $\Delta T_{\text{sub}} = 27.7 \pm 1.73$ °C, $q'' = 1.37 \pm 0.04$ W¹cm⁻², $w = 4.5$ mm, Diabatic Operation, 500 fps, Exposure Time = 90 μs, Aperture 100% open, Far Focus.



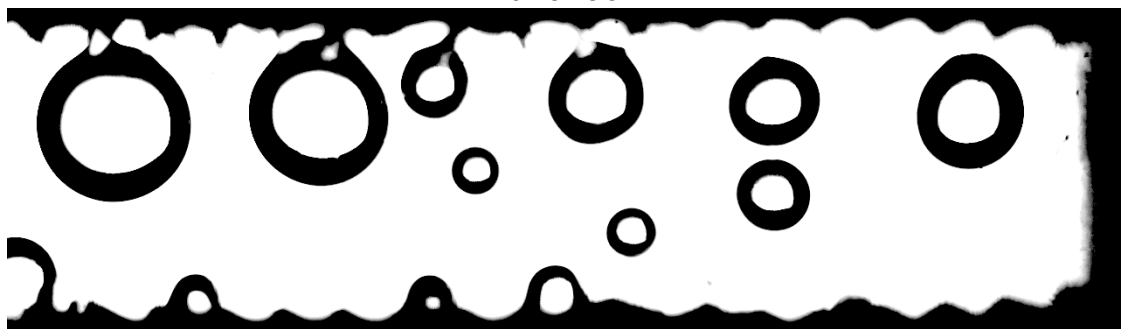
$t = 0.00 \text{ s}$



$t = 0.10 \text{ s}$



$t = 0.20 \text{ s}$



$t = 0.30 \text{ s}$

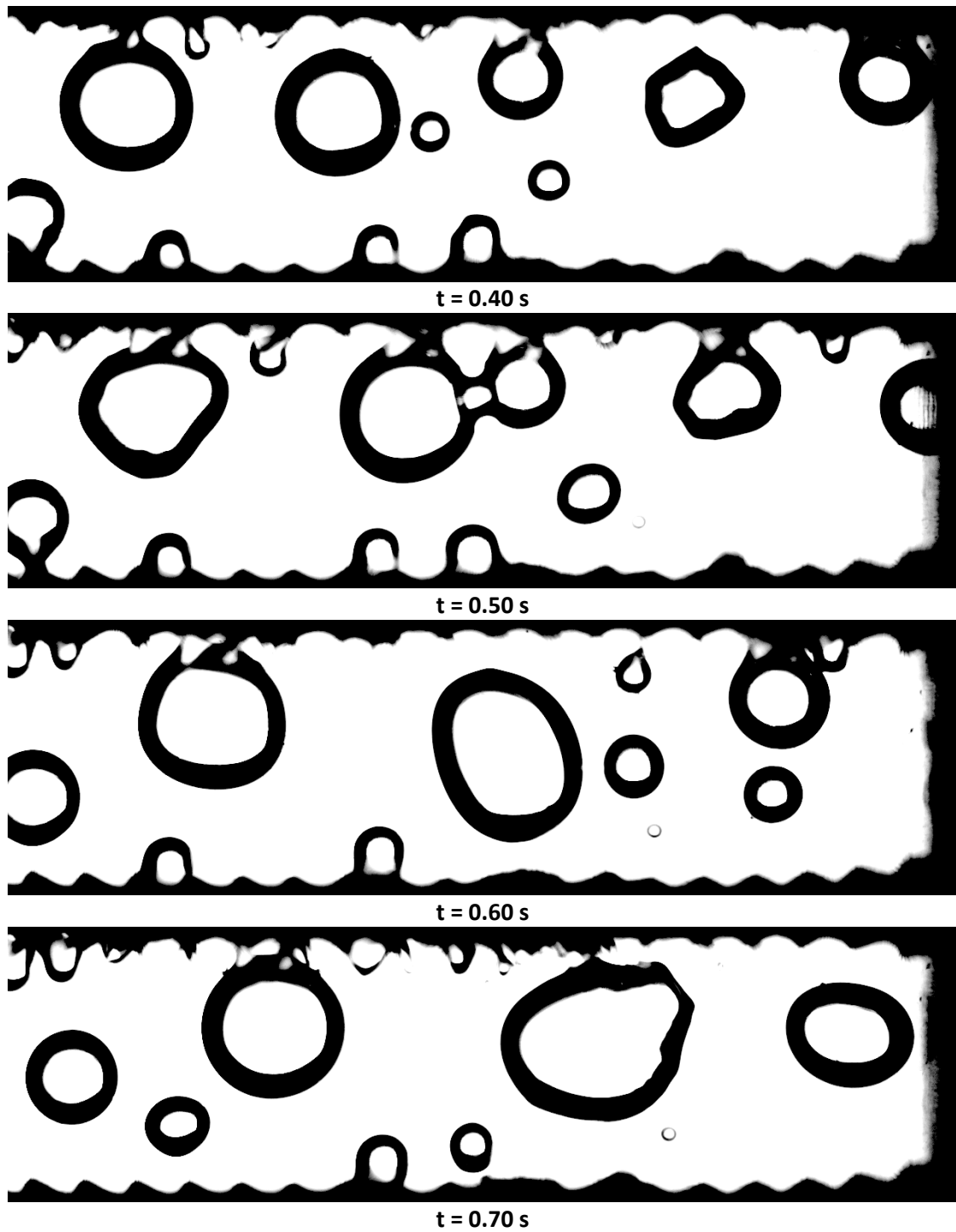


(Figure 11.7 continued)

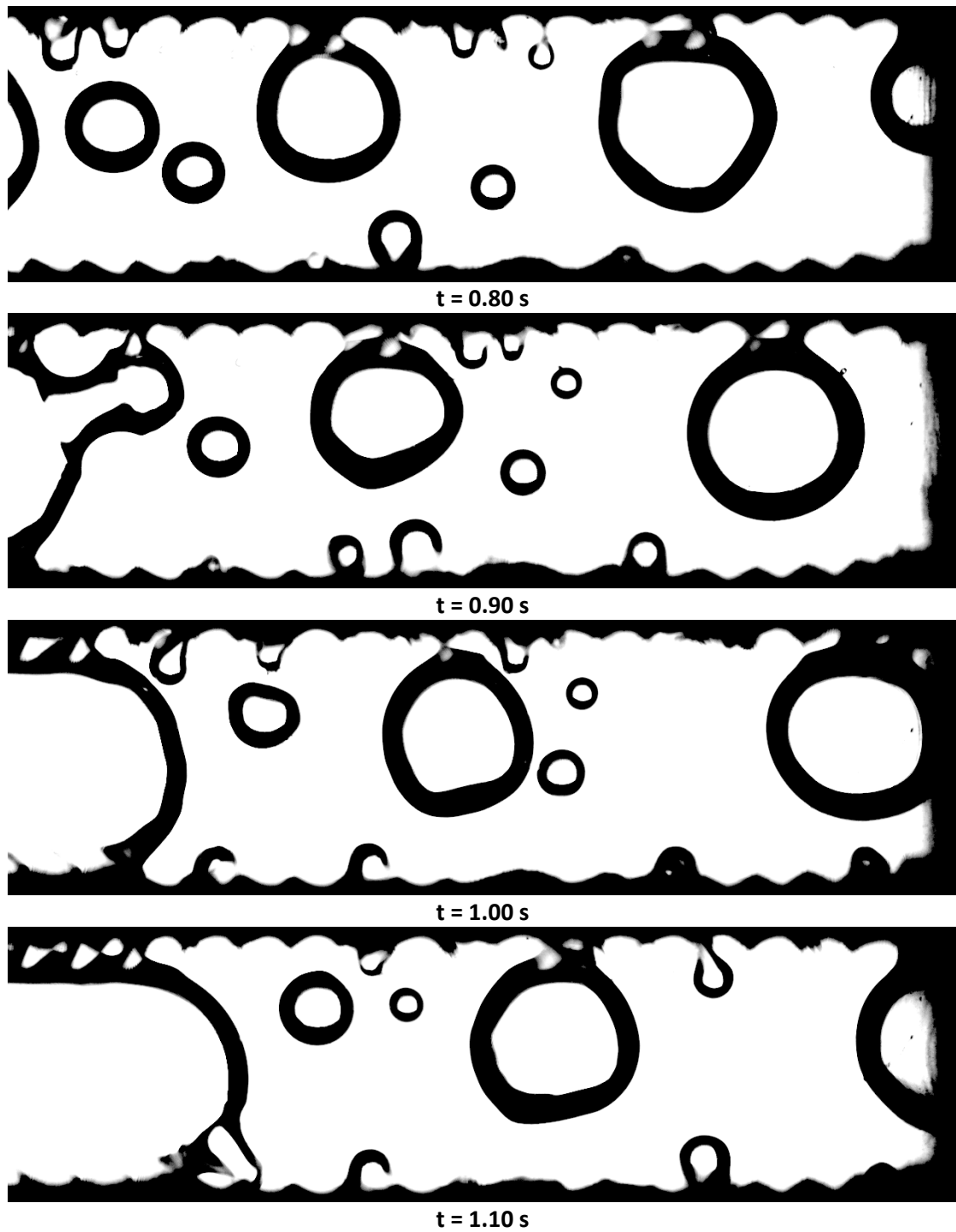


(Figure 11.7 continued)

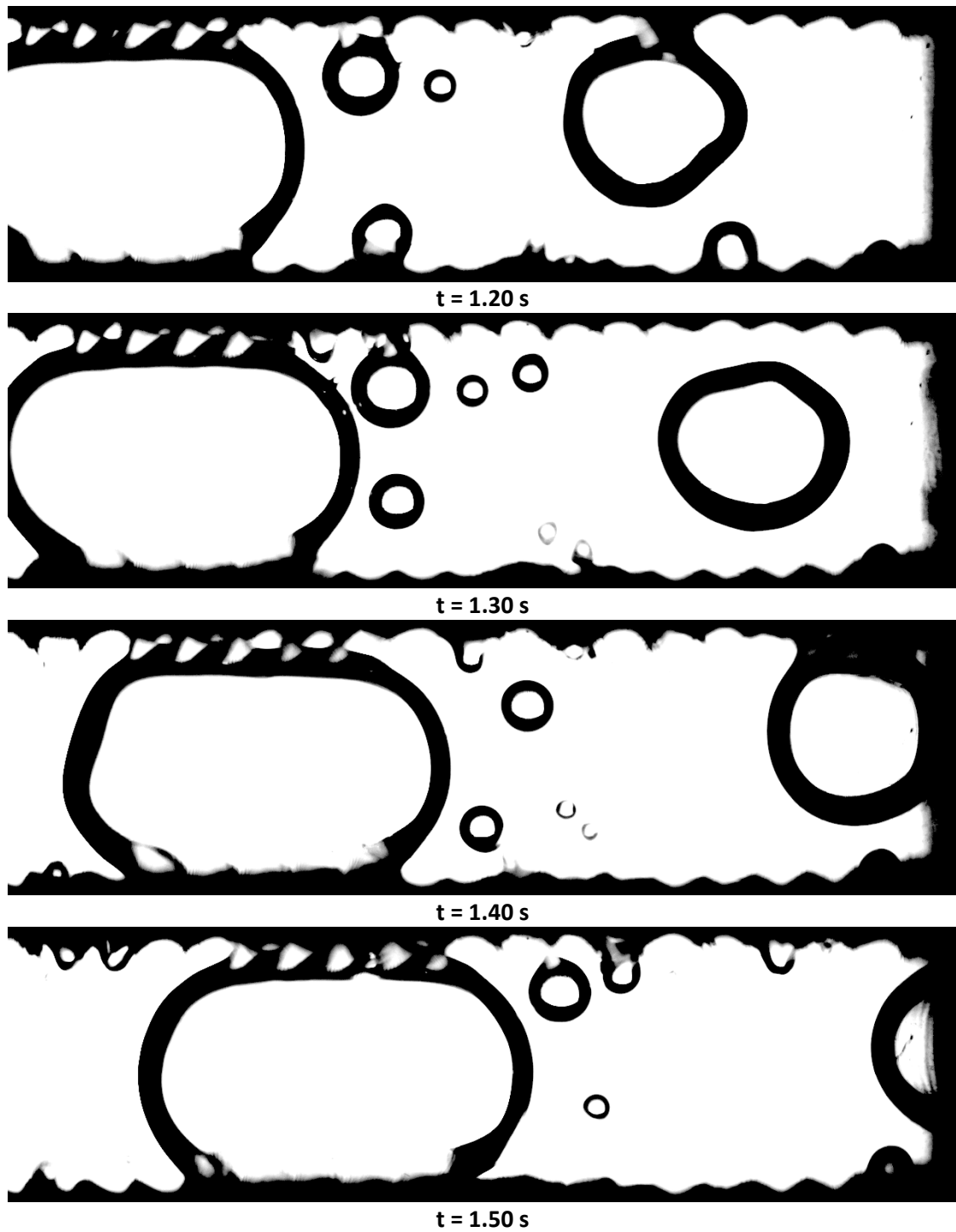


(Figure 11.7 continued)

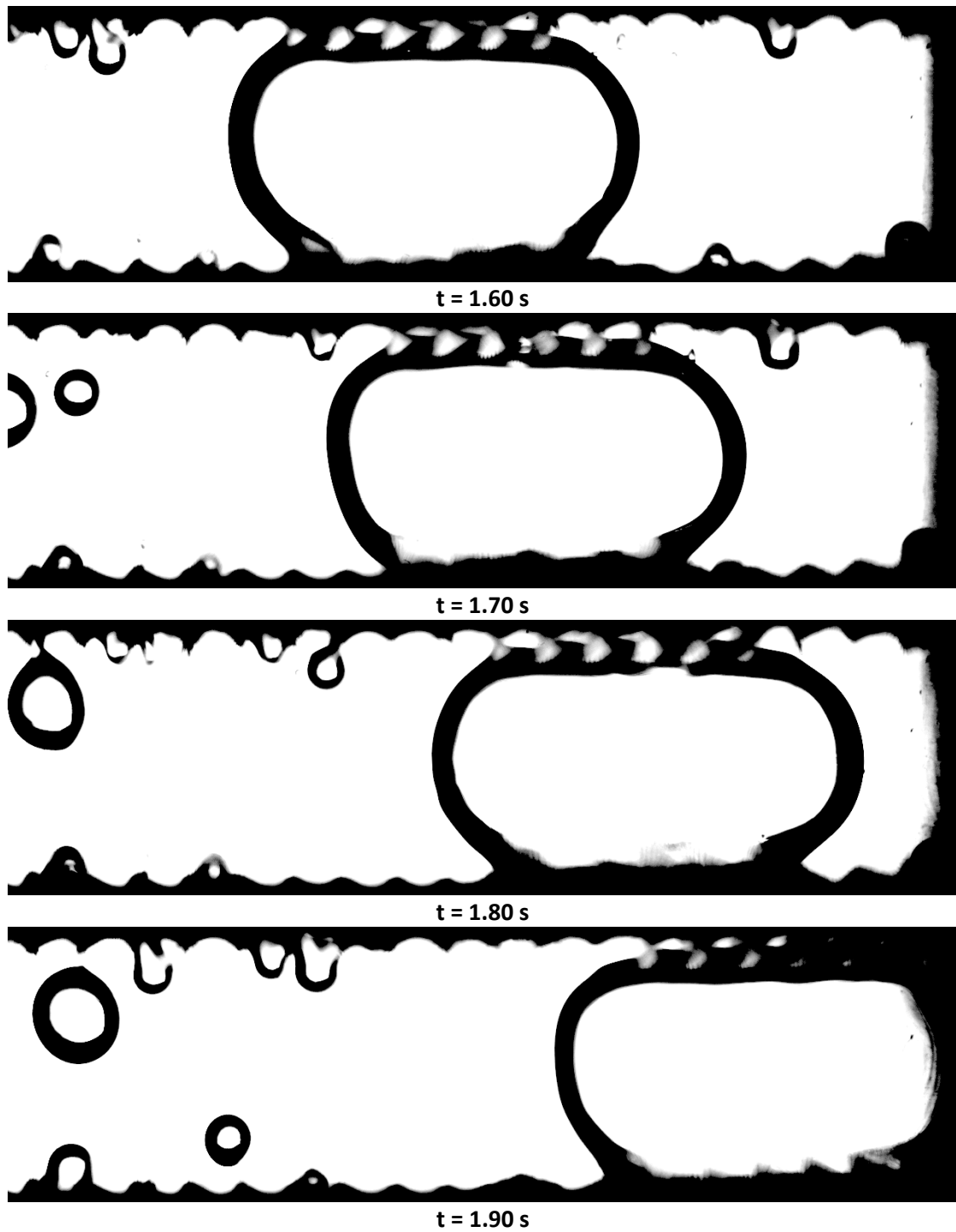


(Figure 11.7 continued)

Figure 11.8: Sequence of 20 frames exhibiting walking bubble flow. $P = 1.006 \pm 0.058$ bar, $\Delta T_{\text{sub}} = 21.5 \pm 1.73$ °C, $q'' = 0.35 \pm 0.02$ W¹cm⁻², $w = 4.5$ mm, Diabatic Operation, 500 fps, Exposure Time = 90 μs, Aperture 100% open, Far Focus.

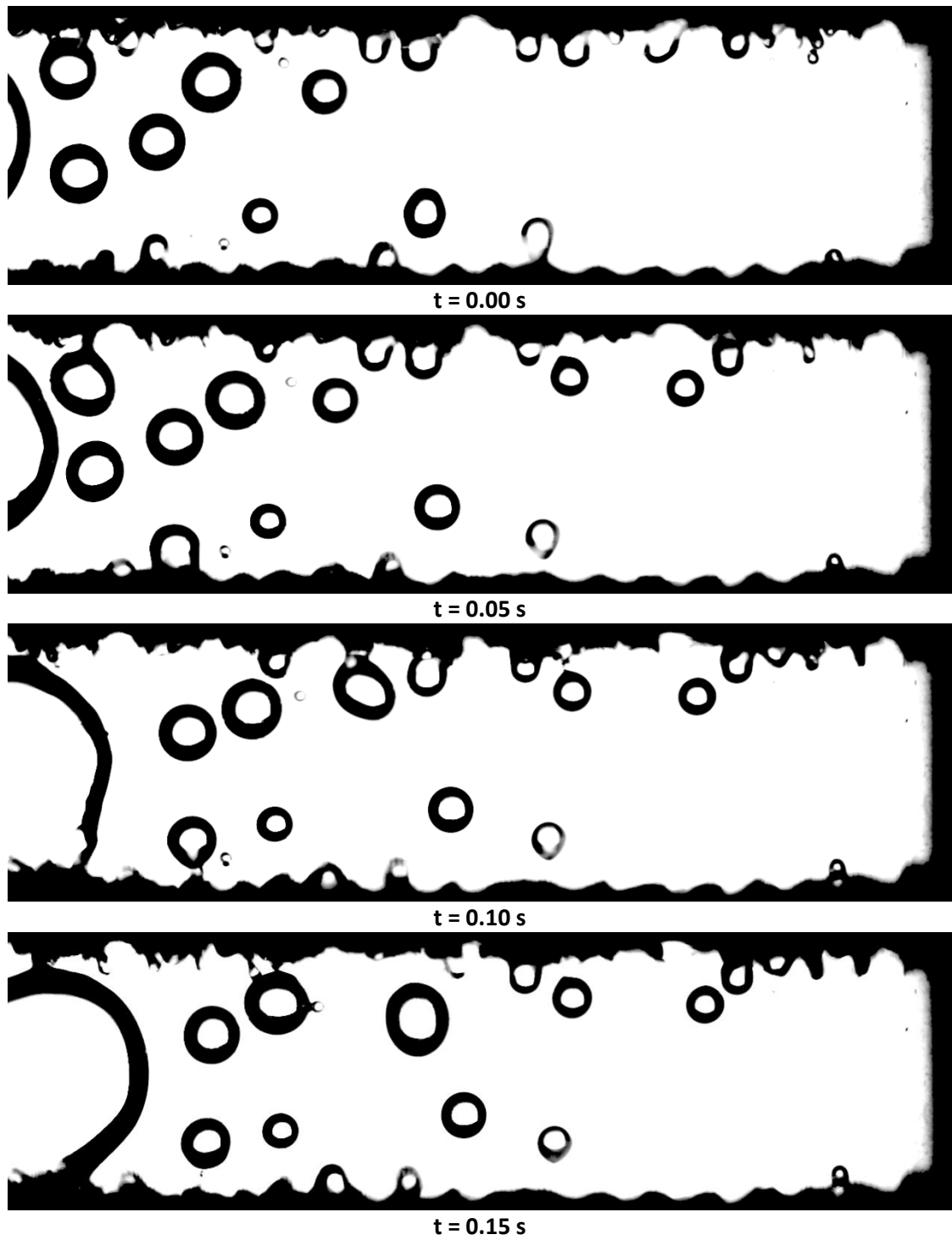


(Figure 11.8 continued)

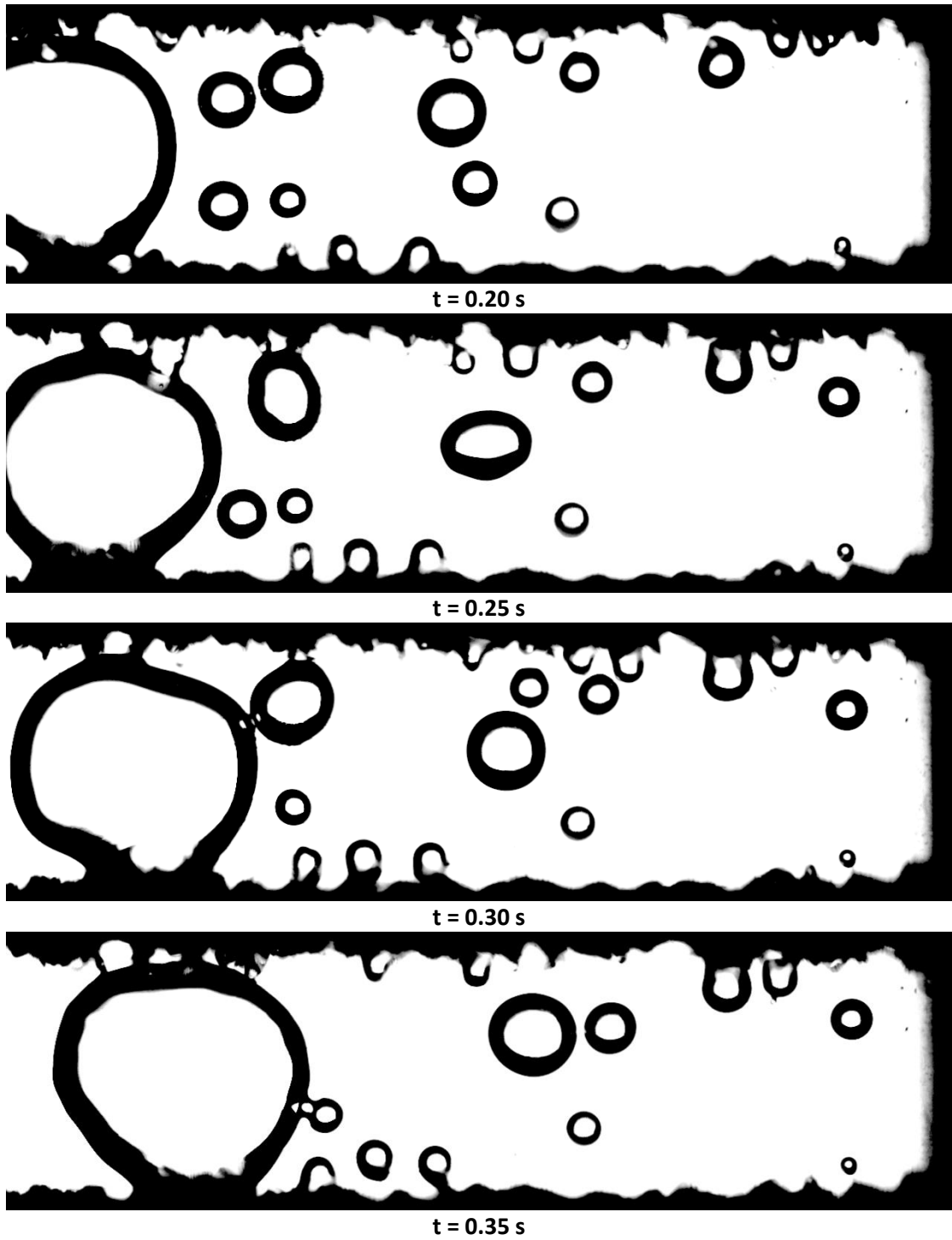


(Figure 11.8 continued)

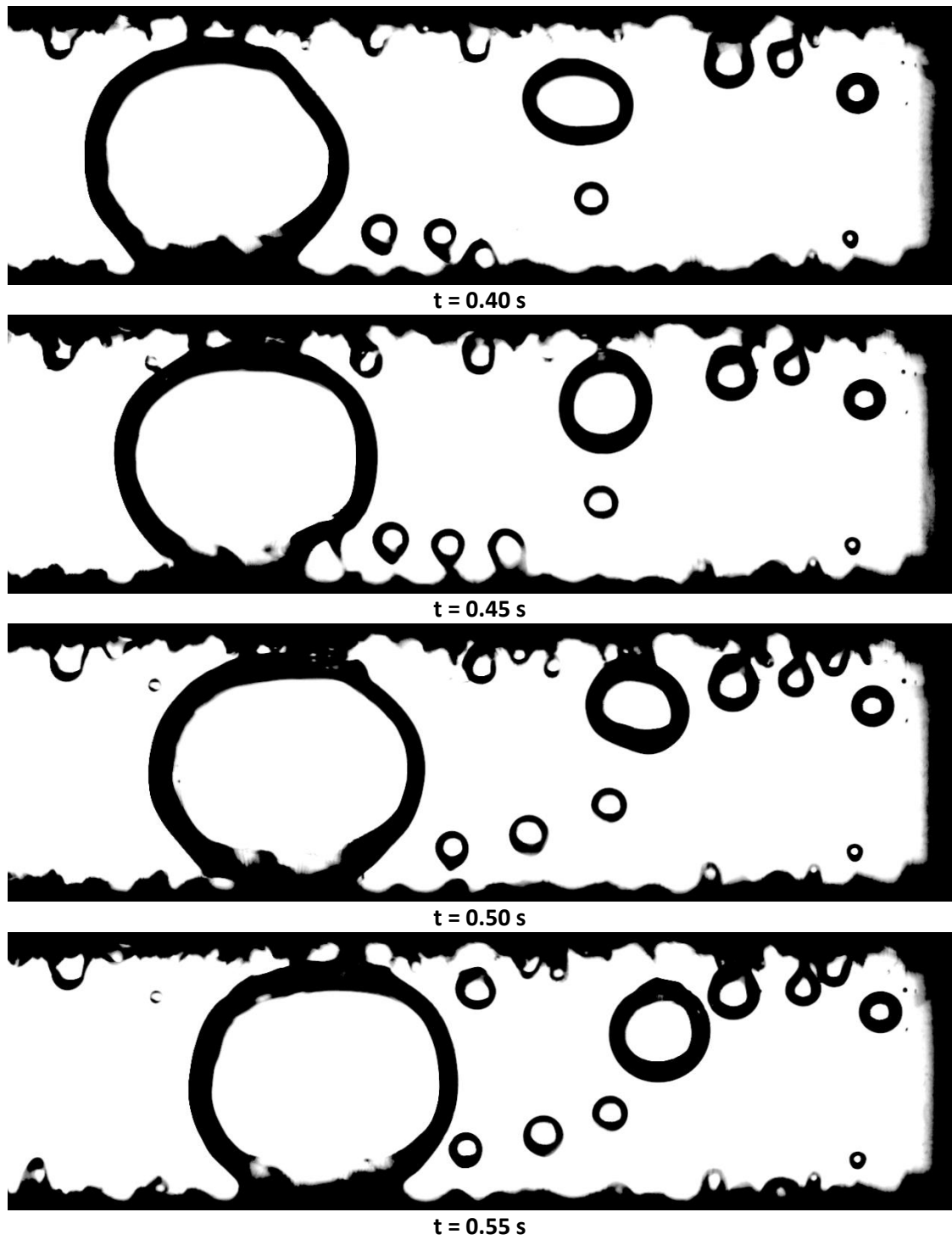


(Figure 11.8 continued)

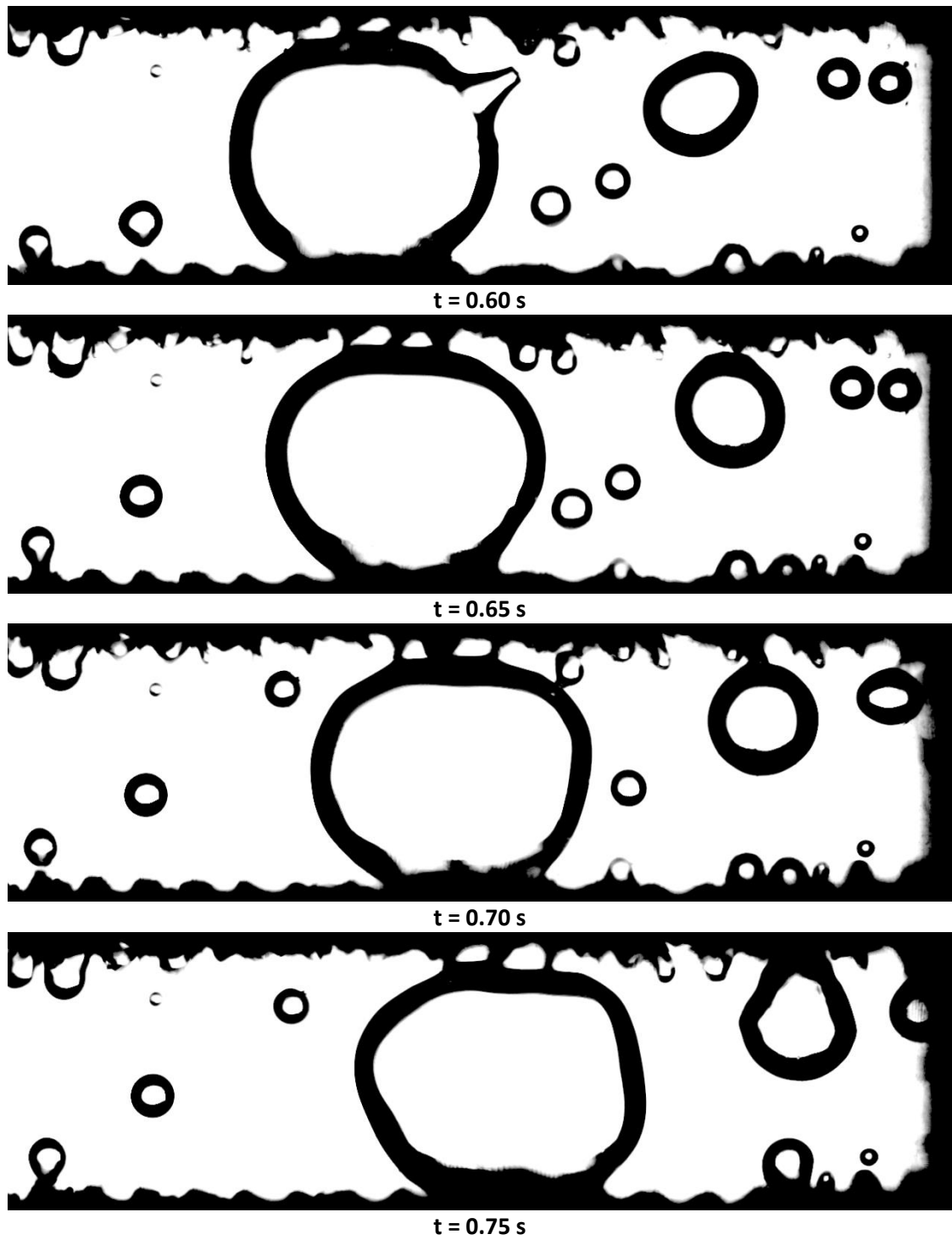


(Figure 11.8 continued)

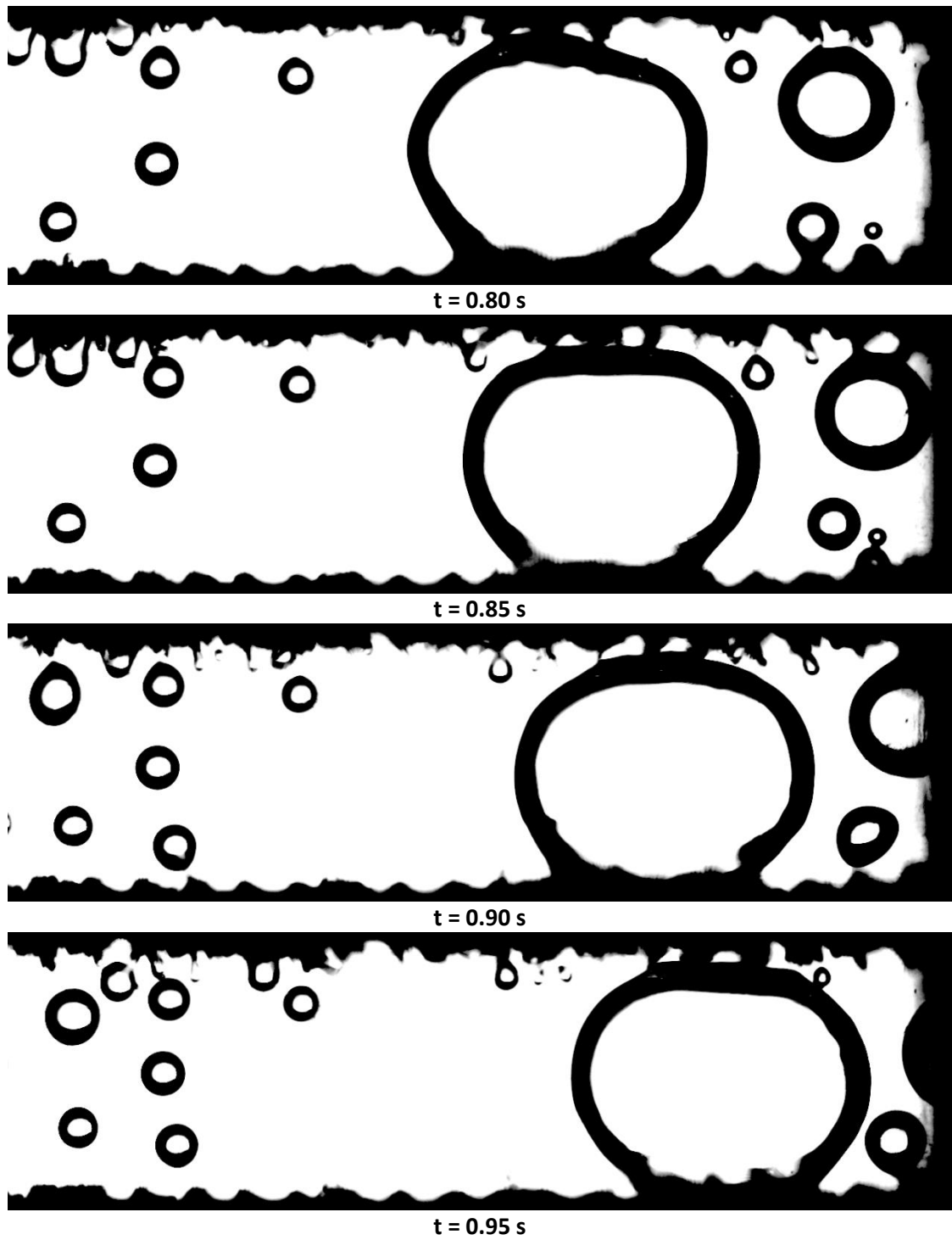


(Figure 11.8 continued)

11.1.4. Homogeneous-Slug Flow Regime

The last flow regime observed occurs with flash boiling conditions. Flash boiling homogeneous nucleation in the channel is caused by lowering the pressure in the chamber sufficiently to saturate or slightly superheat the liquid. Before homogeneous nucleation occurs, the channel is void of vapor. The inception of boiling is spontaneous, but once initiated, slugs travel through the channel in a cyclic nature. The period of the slug traveling through the chamber and the wait time between slugs is markedly consistent. The homogeneous nucleation tends to begin out of the field of view to the left, but the slug initially appears near the flow-wise center of the channel, grows quickly in both directions, and rapidly accelerates to the right once the slug occupies approximately one-third to one-half of the channel length. Although almost unnoticeable in the images, the slug “pulses” as it travels through the channel—slightly growing and shrinking in diameter. Homogeneous-slug flow was repeatable and consistent between flash boiling tests. The results presented in these these exhibiting the homogeneous flow boiling were under the following condition: $P = 0.291 \pm 0.058$ bar, $\Delta T_{\text{sub}} = -0.5 \pm 4.5$ °C, $q'' = 0$ W¹cm⁻², and $w = 2.25$ mm. A sequence of frames for the test the exhibiting homogeneous-slug flow regime is shown below in Fig. 11.9. Note that the time step is not constant between all frames as it takes approximately one second for the slug to pass.

Figure 11.9: Sequence of 13 frames exhibiting homogenous-slug flow. $P = 0.291 \pm 0.058$ bar, $\Delta T_{\text{sub}} = -0.5 \pm 4.5$ °C, $q'' = 0$ W¹cm⁻², $w = 2.5$ mm, Flash Boiling, 500 fps, Exposure Time = 90 μs, Aperture 100% open, Far Focus.

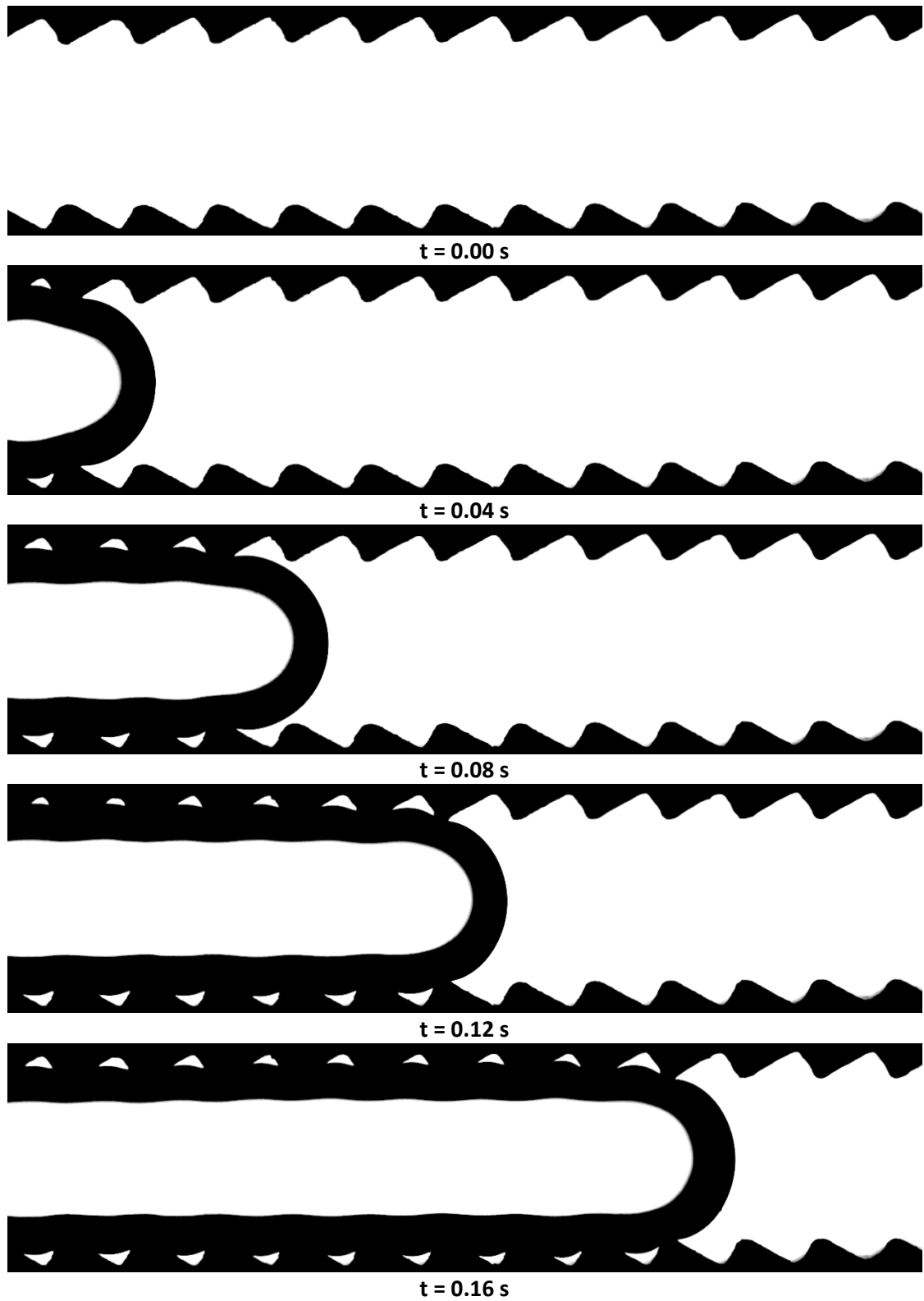


(Figure 11.9 continued)

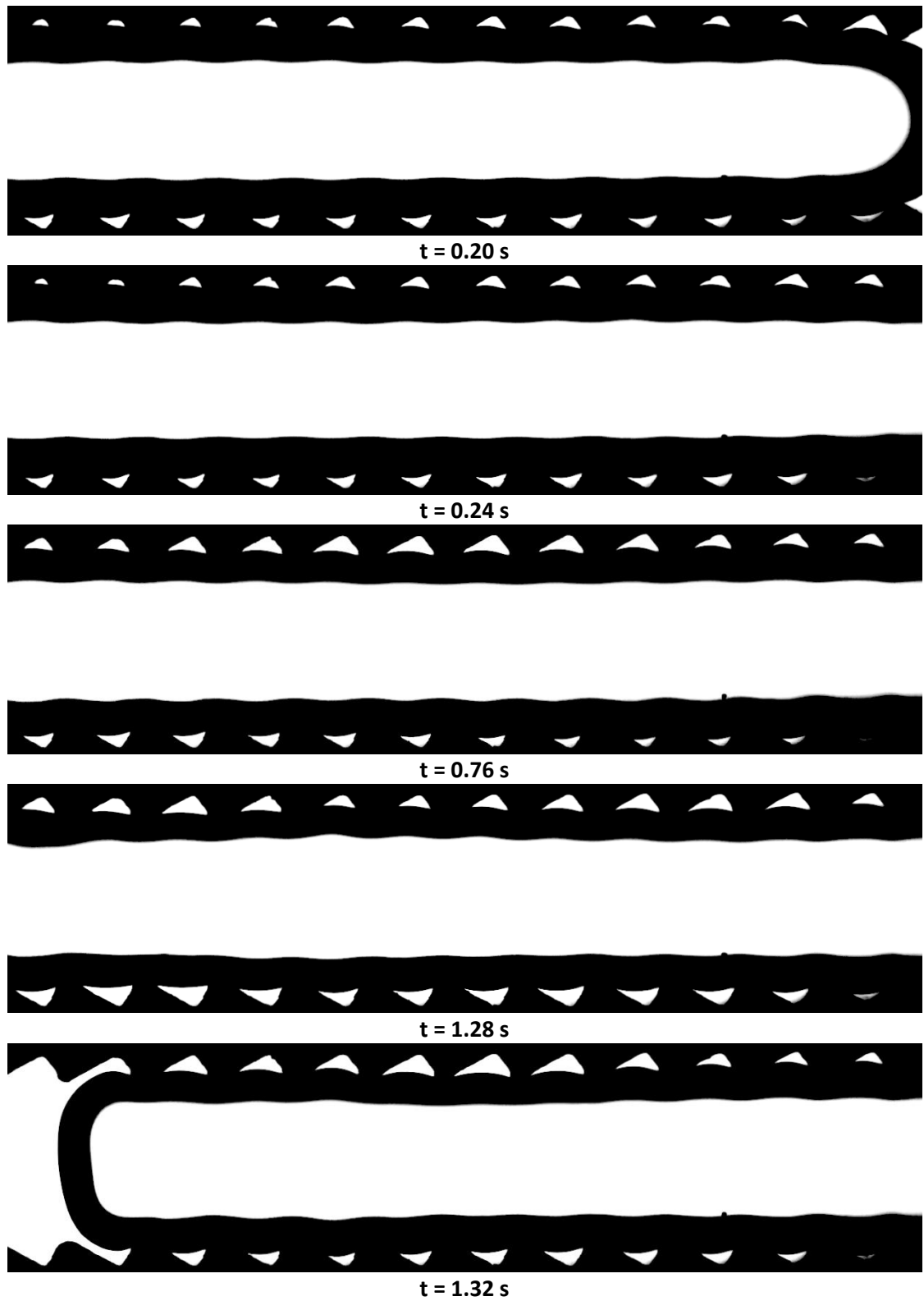


(Figure 11.9 continued)

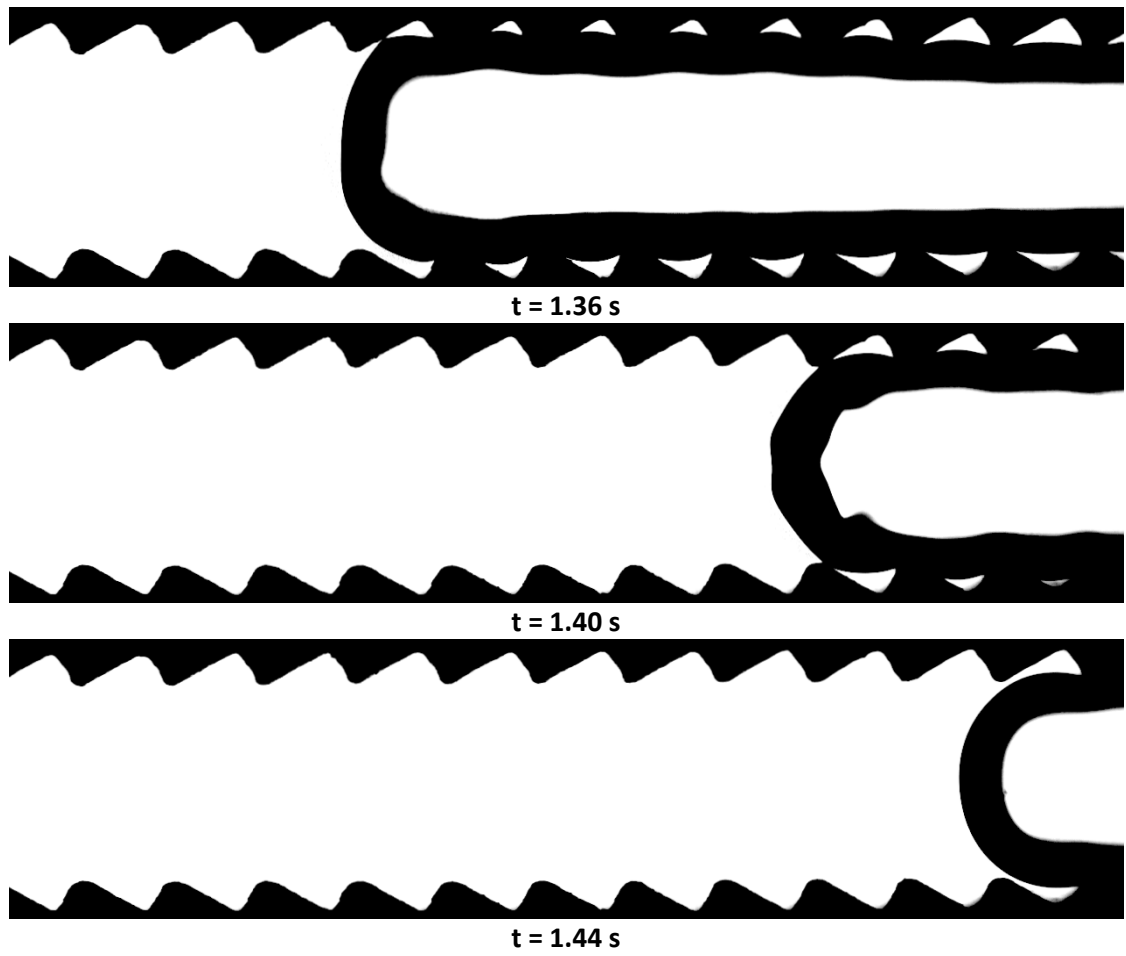


(Figure 11.9 continued)

11.2. Bubble-Slug Kinematics

Using the images processing and data analysis described in Section 10.1, the slug position and velocity results are presented individually. For all figures following in this section, every tenth data point is plotted for clarity.

11.2.1. Churn Flow

The unstable and chaotic nature of the churn flow is evident in the position (Fig. 11.10) and velocity (Fig. 11.11) results. Large jumps in the position data are associated with the occurrence of a merger. The slug occasionally travels in the reverse direction briefly due to bubble interactions and slug divisions. Only major slug structures were tracked with the assumption that the flow in the channel is dominated by their activity. Slugs were only tracked for approximately two seconds as the activity in the channel is more rapid than in other regimes

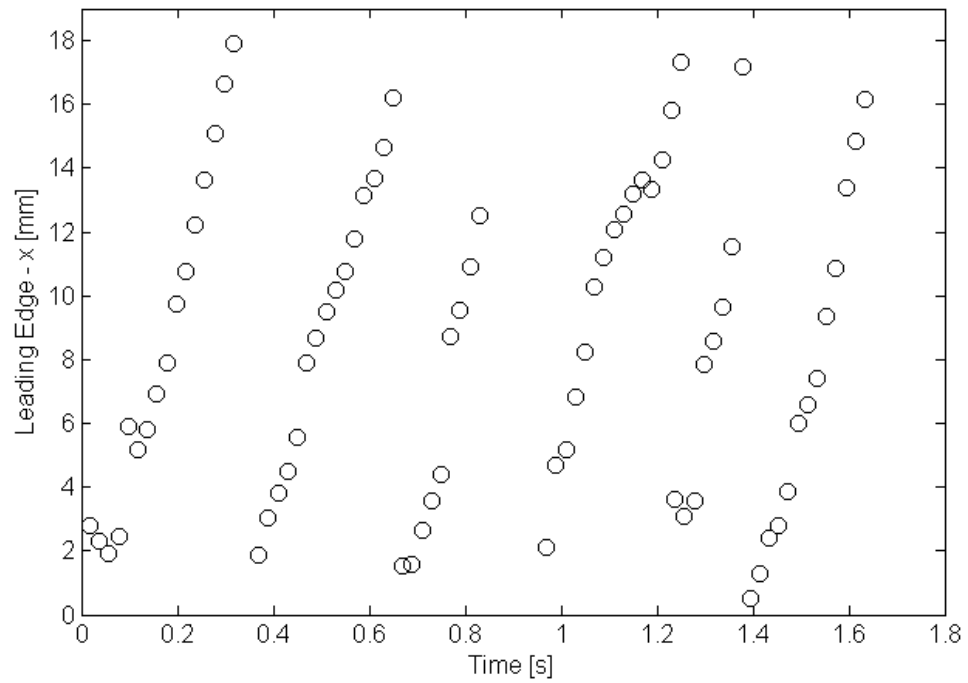


Figure 11.10: Position data of six slugs in the churn flow regime. $P = 1.006 \pm 0.058$ bar, $\Delta T_{\text{sub}} = 22.1 \pm 1.73$ °C, $q'' = 2.74 \pm 0.06$ W¹cm⁻², $w = 4.5$ mm, Diabatic Operation, 500 fps, Exposure Time = 90 μ s, Aperture 100% open, Far Focus.

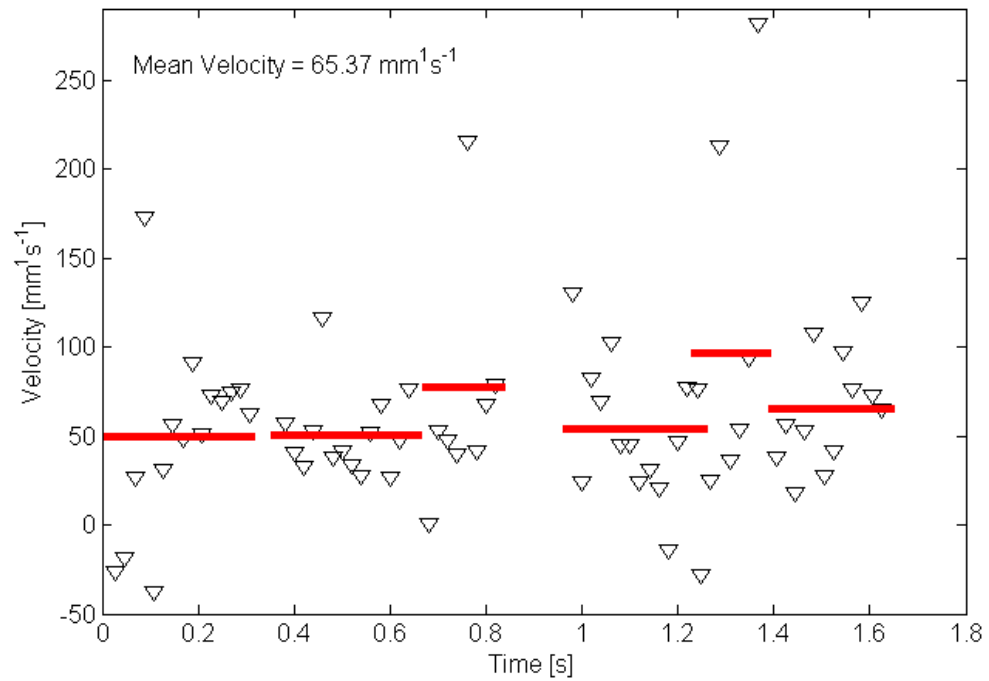


Figure 11.11: Velocity results of six slugs in the churn flow regime. Horizontal red bars indicate mean velocity for each slug and mean velocity of all slugs is shown in the annotation. $P = 1.006 \pm 0.058$ bar, $\Delta T_{\text{sub}} = 22.1 \pm 1.73$ °C, $q'' = 2.74 \pm 0.06$ W¹cm², $w = 4.5$ mm, Diabatic Operation, 500 fps, Exposure Time = 90 μ s, Aperture 100% open, Far Focus.

11.2.2. Intermittent Slug Flow

Intermittent slug flow is markedly less chaotic than churn flow visually; however, large jumps in position caused by mergers. Velocity values tend to be near the average value; however, high velocity outliers are apparent due to mergers. Figures 11.13 and 11.15 have limited vertical axes to omit several high values of velocity for clarity.

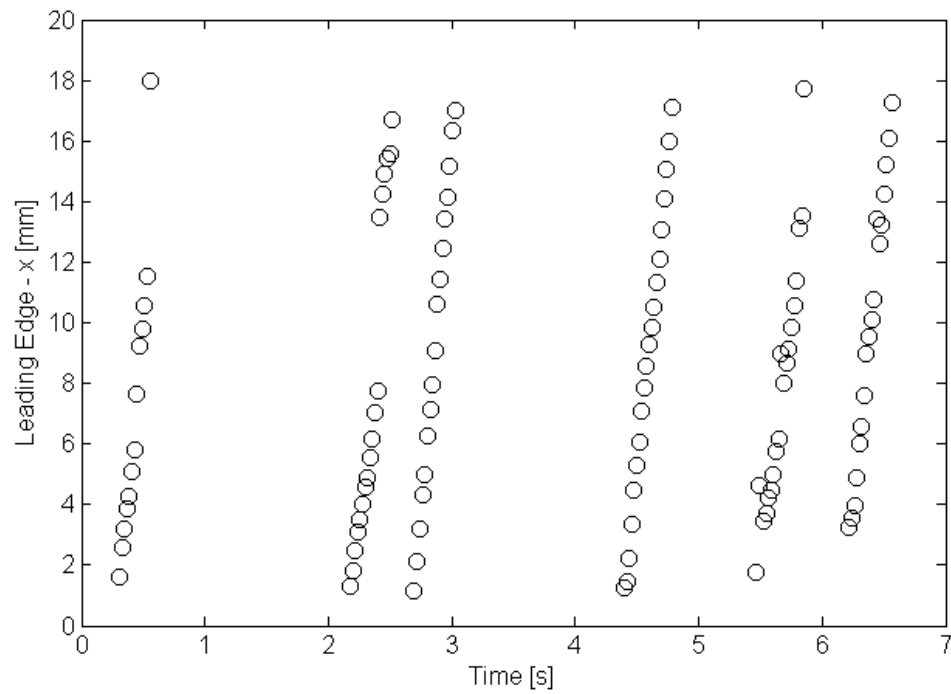


Figure 11.12: Position data of six slugs in the intermittent slug flow regime. $P = 1.009 \pm 0.058$ bar, $\Delta T_{\text{sub}} = 17.7 \pm 1.73$ °C, $q'' = 1.37 \pm 0.04$ W^1cm^{-2} , $w = 4.5$ mm, Diabatic Operation, 500 fps, Exposure Time = 90 μs , Aperture 100% open, Far Focus.

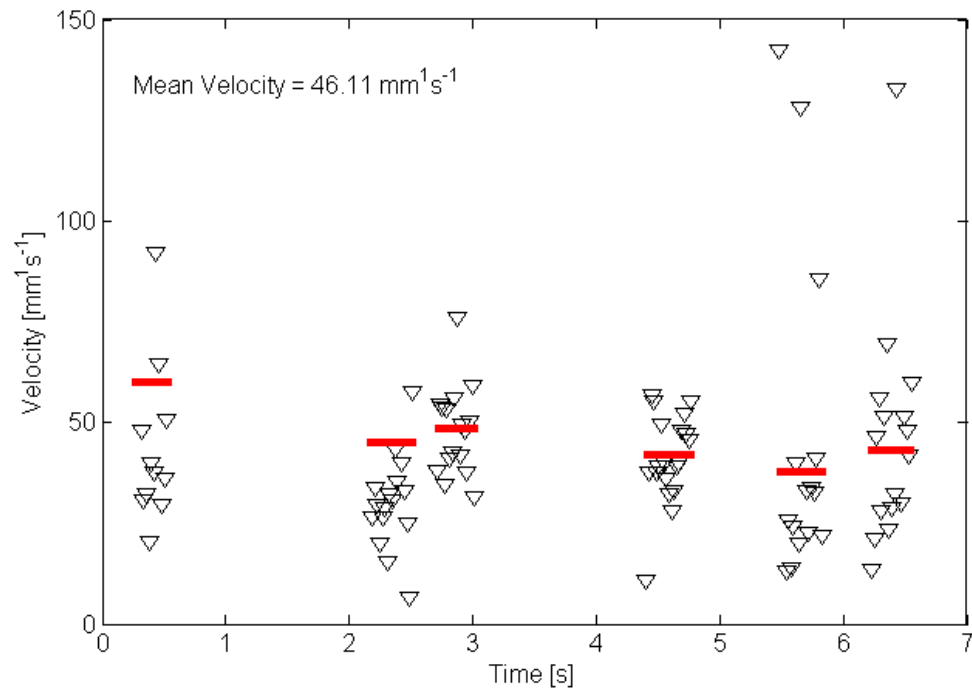


Figure 11.13: Velocity results of six slugs in the intermittent slug flow regime. Horizontal red bars indicate mean velocity for each slug and mean velocity of all slugs is shown in the annotation. $P = 1.009 \pm 0.058$ bar, $\Delta T_{\text{sub}} = 17.7 \pm 1.73$ °C, $q'' = 1.37 \pm 0.04$ W¹cm⁻², $w = 4.5$ mm, Diabatic Operation, 500 fps, Exposure Time = 90 μ s, Aperture 100% open, Far Focus.

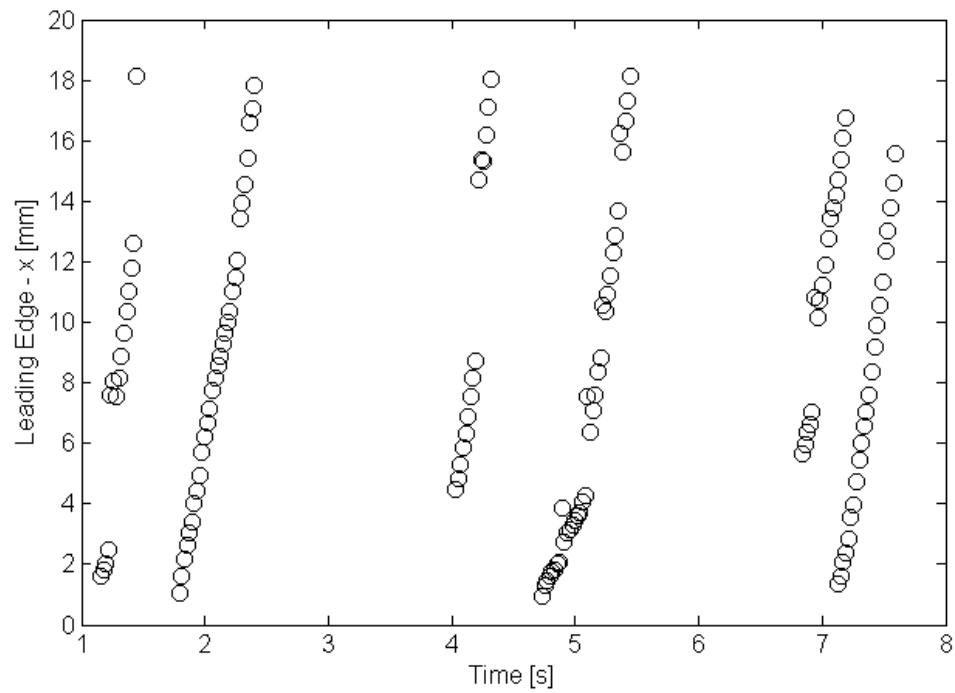


Figure 11.14: Position data of six slugs in the intermittent slug flow regime. $P = 0.998 \pm 0.058$ bar, $\Delta T_{\text{sub}} = 26.8 \pm 1.73$ °C, $q'' = 1.37 \pm 0.04$ W^1cm^{-2} , $w = 2.25$ mm, Diabatic Operation, 500 fps, Exposure Time = 90 μs , Aperture 100% open, Far Focus.

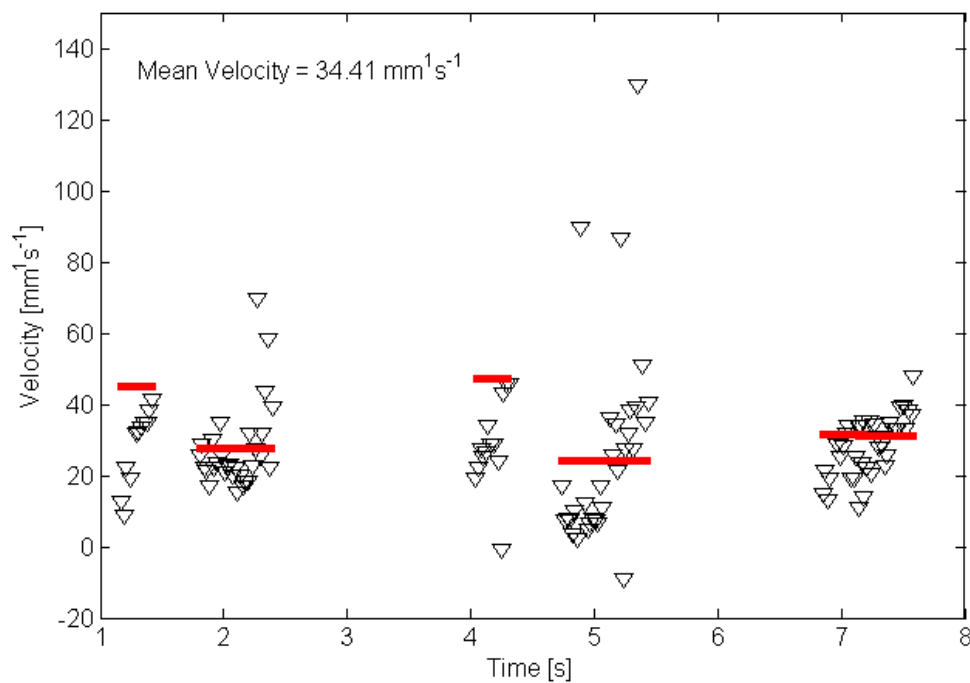


Figure 11.15: Velocity results of six slugs in the intermittent slug flow regime. Horizontal red bars indicate mean velocity for each slug and mean velocity of all slugs is shown in the annotation. $P = 0.998 \pm 0.058$ bar, $\Delta T_{\text{sub}} = 26.8 \pm 1.73$ °C, $q'' = 1.37 \pm 0.04$ W¹cm⁻², $w = 2.25$ mm, Diabatic Operation, 500 fps, Exposure Time = 90 μ s, Aperture 100% open, Far Focus.

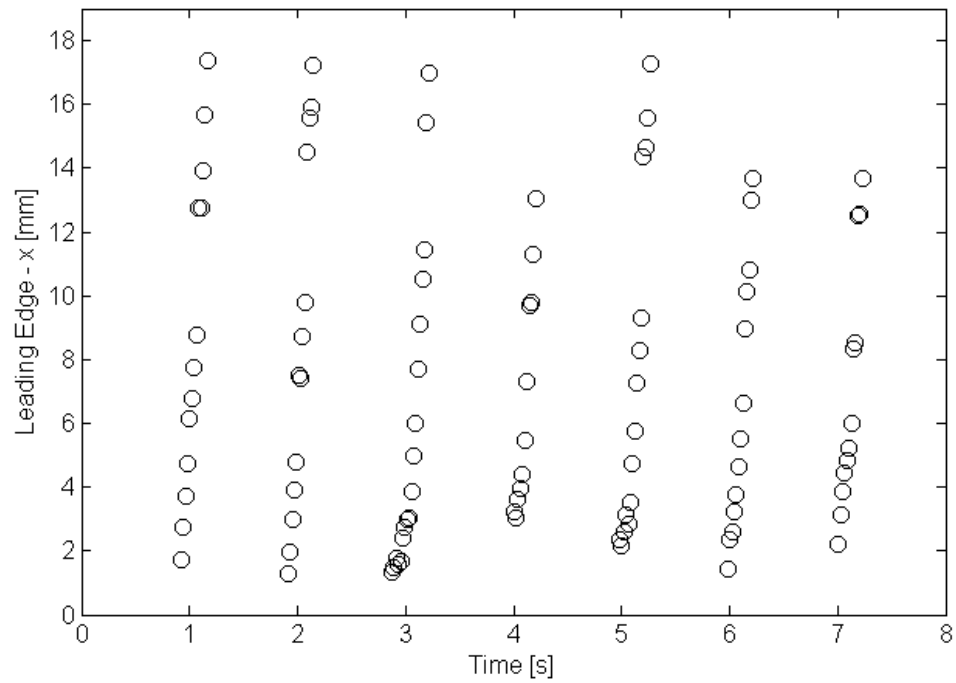


Figure 11.16: Position data of seven slugs in the intermittent slug flow regime. $P = 0.572 \pm 0.058$ bar, $\Delta T_{\text{sub}} = 5.8 \pm 2.7$ °C, $q'' = 0.58 \pm 0.02$ W¹cm⁻², $w = 4.5$ mm, Sub-atmospheric Diabatic Operation, 500 fps, Exposure Time = 90 μ s, Aperture 100% open, Far Focus.

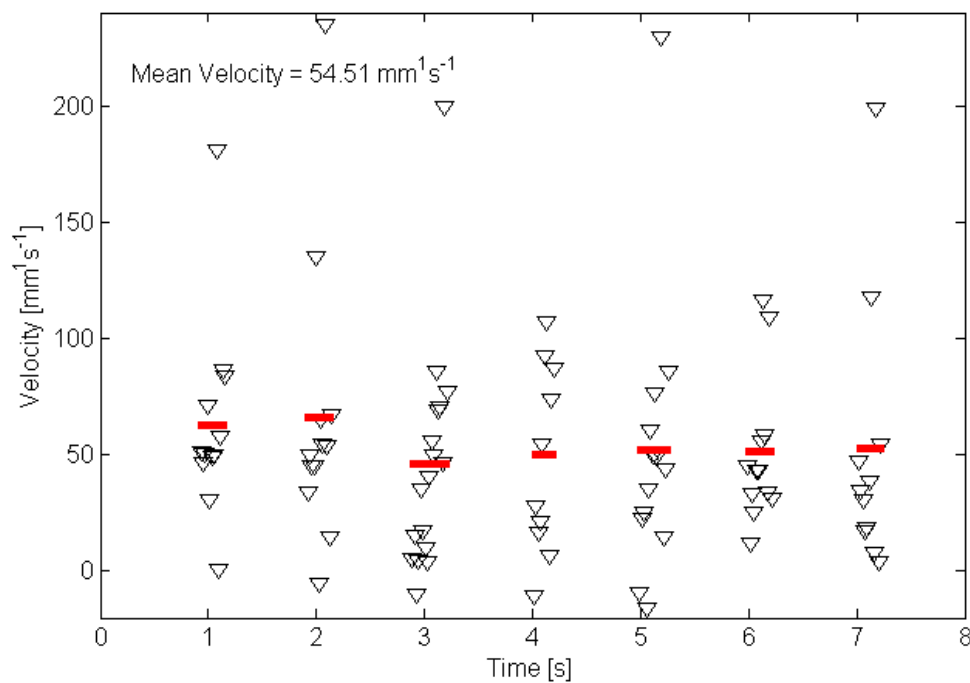


Figure 11.17: Velocity results of seven slugs in the intermittent slug flow regime. Horizontal red bars indicate mean velocity for each slug and mean velocity of all slugs is shown in the annotation. $P = 0.572 \pm 0.058 \text{ bar}$, $\Delta T_{\text{sub}} = 5.8 \pm 2.7 \text{ }^\circ\text{C}$, $q'' = 0.58 \pm 0.02 \text{ W}^1 \text{cm}^{-2}$, $w = 4.5 \text{ mm}$, Sub-atmospheric Diabatic Operation, 500 fps, Exposure Time = $90 \text{ } \mu\text{s}$, Aperture 100% open, Far Focus.

11.2.3. Walking Bubble Regime

The walking bubble regime is markedly less unstable than the churn and slug regimes. Position data features fewer mergers and bubbles do not travel in the reverse direction. Velocity values tend toward the average more consistently and no high velocity outliers exist.

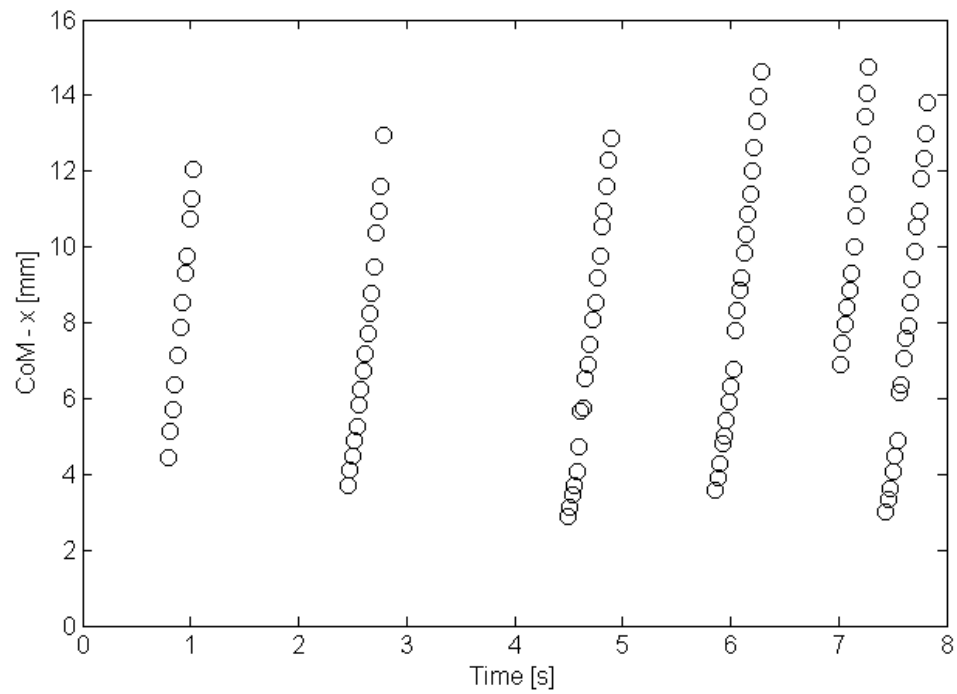


Figure 11.18: Position data of six bubbles in the walking bubble flow regime. $P = 1.006 \pm 0.058$ bar, $\Delta T_{\text{sub}} = 43.3 \pm 1.73$ °C, $q'' = 5.22 \pm 0.09$ W¹cm⁻², $w = 4.5$ mm, Diabatic Operation, 500 fps, Exposure Time = 90 μ s, Aperture 100% open, Far Focus.

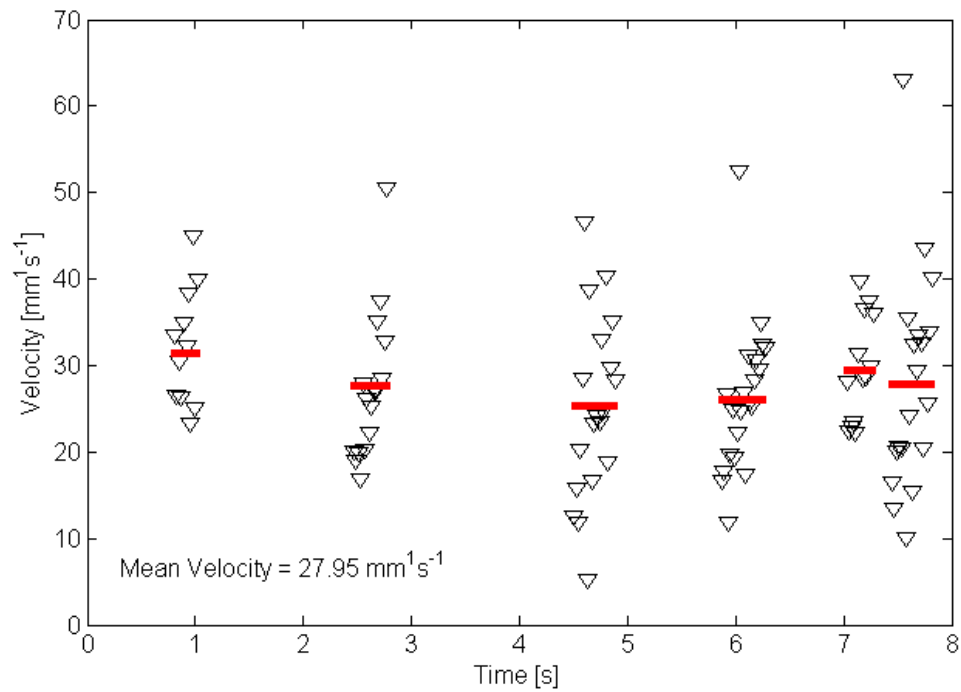


Figure 11.19: Velocity results of six bubbles in the walking bubble flow regime. Horizontal red bars indicate mean velocity for each bubble and mean velocity of all bubbles is shown in the annotation. $P = 1.006 \pm 0.058$ bar, $\Delta T_{\text{sub}} = 43.3 \pm 1.73$ °C, $q'' = 5.22 \pm 0.09$ W¹cm⁻², $w = 4.5$ mm, Diabatic Operation, 500 fps, Exposure Time = 90 μ s, Aperture 100% open, Far Focus.

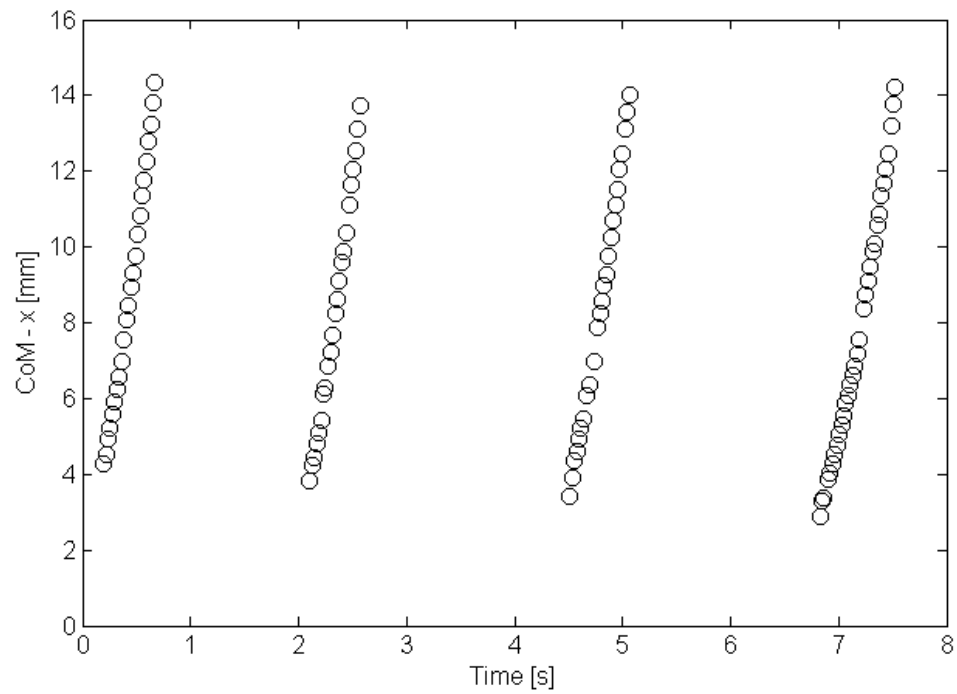


Figure 11.20: Position data of four bubbles in the walking bubble flow regime. $P = 1.009 \pm 0.058$ bar, $\Delta T_{\text{sub}} = 27.7 \pm 1.73$ °C, $q'' = 1.37 \pm 0.04$ W¹cm⁻², $w = 4.5$ mm, Diabatic Operation, 500 fps, Exposure Time = 90 μ s, Aperture 100% open, Far Focus.

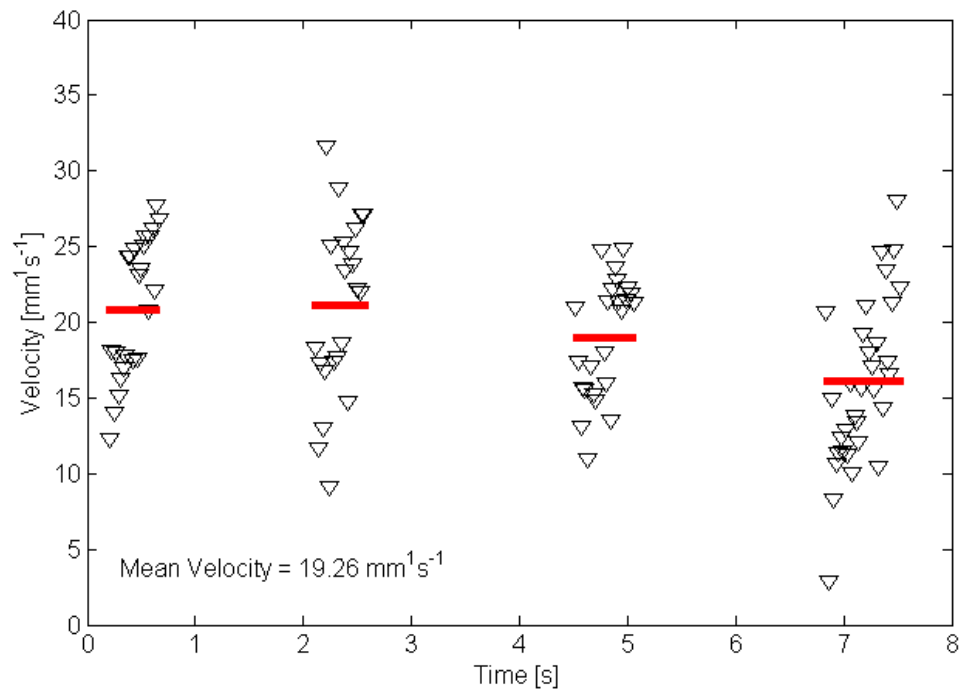


Figure 11.21: Velocity results of four bubbles in the walking flow regime. Horizontal red bars indicate mean velocity for each bubble and mean velocity of all bubbles is shown in the annotation. $P = 1.009 \pm 0.058$ bar, $\Delta T_{\text{sub}} = 27.7 \pm 1.73$ °C, $q'' = 1.37 \pm 0.04$ W¹cm⁻², $w = 4.5$ mm, Diabatic Operation, 500 fps, Exposure Time = 90 μ s, Aperture 100% open, Far Focus.

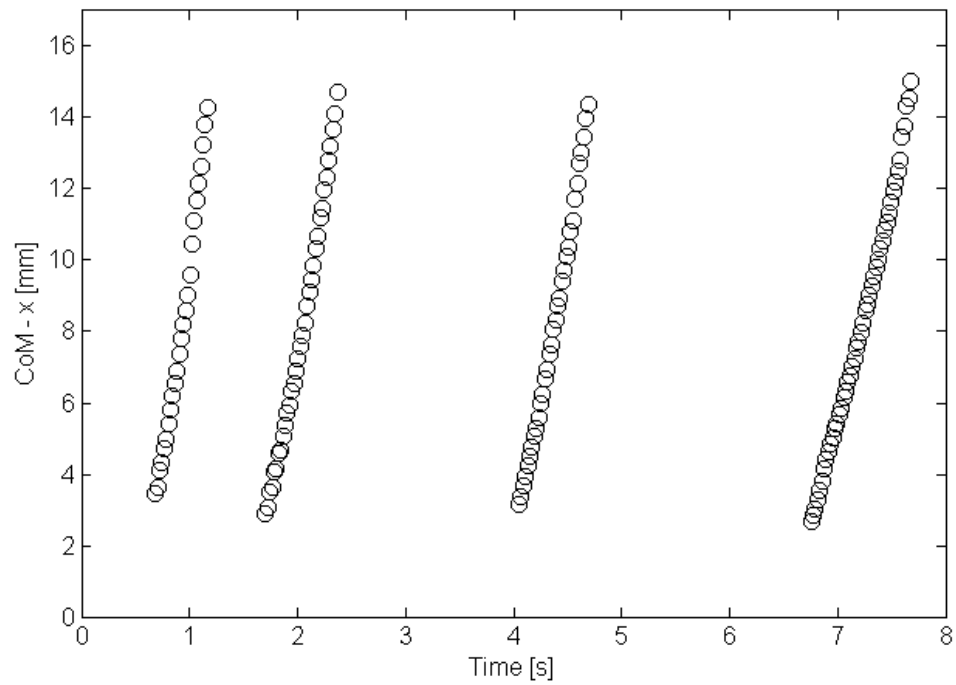


Figure 11.22: Position data of four bubbles in the walking bubble flow regime. $P = 1.009 \pm 0.058$ bar, $\Delta T_{\text{sub}} = 21.5 \pm 1.73$ °C, $q'' = 0.35 \pm 0.02$ W¹cm⁻², $w = 4.5$ mm, Diabatic Operation, 500 fps, Exposure Time = 90 μ s, Aperture 100% open, Far Focus.

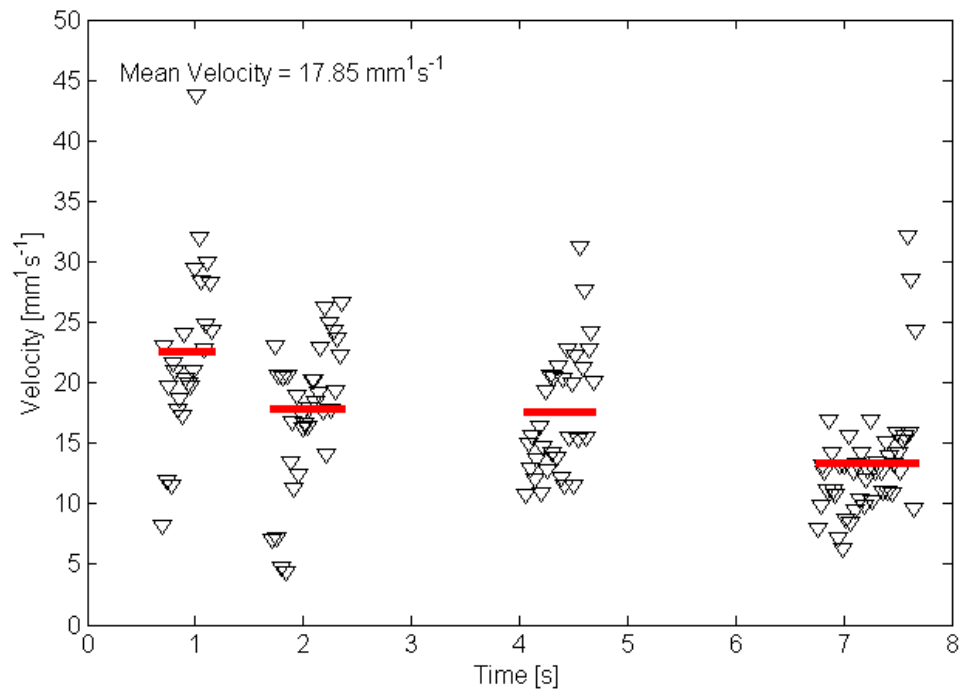


Figure 11.23: Velocity results of four bubbles in the walking flow regime. Horizontal red bars indicate mean velocity for each bubble and mean velocity of all bubbles is shown in the annotation. $P = 1.009 \pm 0.058$ bar, $\Delta T_{\text{sub}} = 21.5 \pm 1.73$ °C, $q'' = 0.35 \pm 0.02$ W¹cm⁻², $w = 4.5$ mm, Diabatic Operation, 500 fps, Exposure Time = 90 μ s, Aperture 100% open, Far Focus.

11.2.4. Homogeneous Slug Flow

Homogeneous slug flow is visually the cleanest and most stable flow tested and this can also be seen in the position data. The position of the slug with time is almost linear, indicating nearly constant velocity and no acceleration.

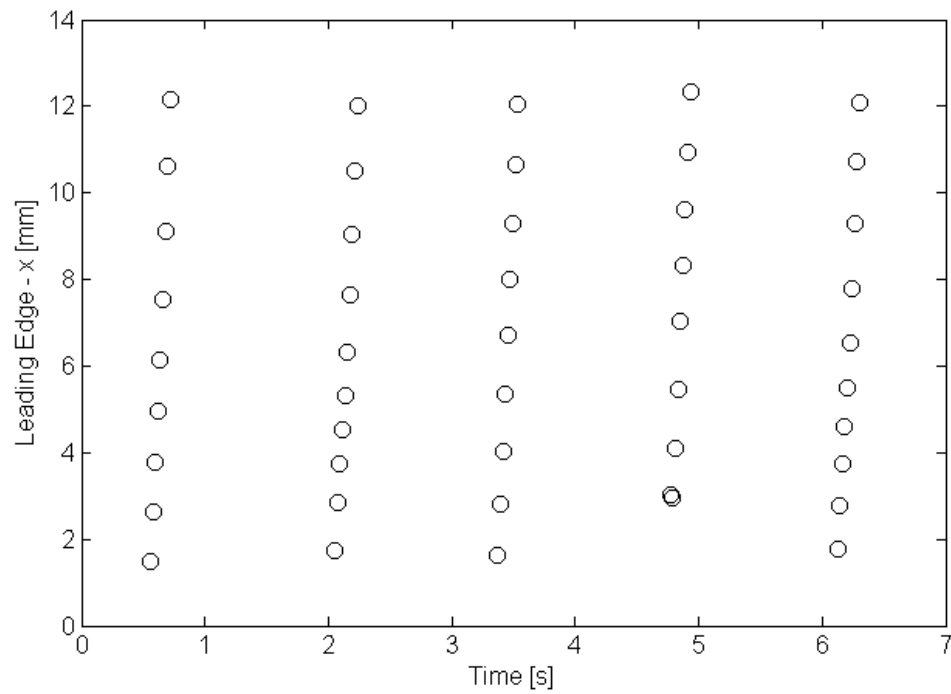


Figure 11.24: Position data of five slugs in the homogeneous slug flow regime. $P = 0.291 \pm 0.058$ bar, $\Delta T_{\text{sub}} = -0.5 \pm 4.5$ °C, $q'' = 0$ W¹cm⁻², $w = 2.25$ mm, Flash Boiling, 500 fps, Exposure Time = 90 μ s, Aperture 100% open, Far Focus.

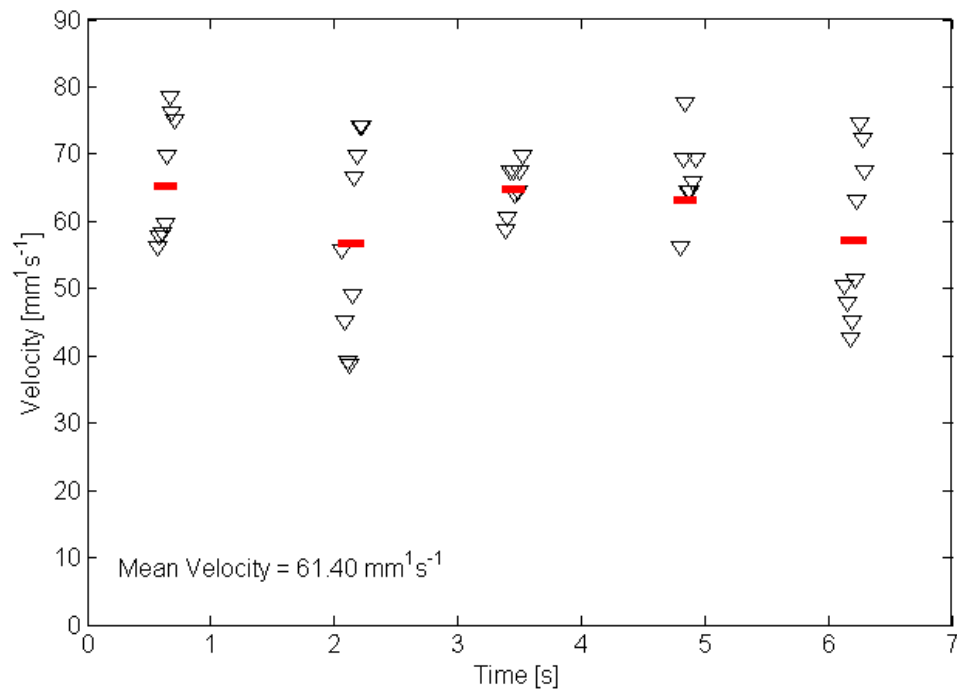


Figure 11.25: Velocity results of five slugs in the homogeneous slug flow regime. Horizontal red bars indicate mean velocity for each slug and mean velocity of all slugs is shown in the annotation. $P = 0.291 \pm 0.058$ bar, $\Delta T_{\text{sub}} = -0.5 \pm 4.5$ °C, $q'' = 0$ W¹cm⁻², $w = 2.25$ mm, Flash Boiling, 500 fps, Exposure Time = 90 μ s, Aperture 100% open, Far Focus.

11.3. Slug Transport Mechanism

The physical phenomenon of rapid transport of vapor slugs along the structured surface is not fully understood; however a preliminary model is presented in this section that explains driving force propelling the slugs. It is proposed that the asymmetric shape of the structured surface topography creates a pressure difference in the liquid over each ratchet and is the basis for driving flow.

As the bubble travels through the channel, it appears to be in contact with the ratcheted surface on either side of the channel; however, there exists a thin liquid layer that separates the bubble from the solid surface. To capture images of the liquid layer with the high-speed camera the backlighting configuration used in videos shown in Section 11.1 was switched to forward lighting thereby effectively reducing the shadow created by the concavity of the slug. The homogeneous slug flow (flashing) test presented previously was repeated with the new lighting setup. Liquid layer thickness was measured for a series of frames using National Instruments Vision Assistant software. One clearly viewable ratchet was selected as the region of interest for the analysis. An in-situ frame showing this ratchet with no slug present was chosen for analysis. The location and geometry of the ratchet was determined with edge detection (Fig. 11.26a-b). A series of forty-two consecutive frames was analyzed similarly to determine the radii of the bubble interface near the solid surface. The raw image with contrast enhanced is shown in Fig. 11.26c and radii of curvature were determined using circular edge detection (Fig. 11.26d). The dark ribbon (Fig. 11.26d) is not considered the slug interface as it crosses in front of the ratchet; thus, is assumed to be a thin film of fluid between the structured surface and the clear polycarbonate top wall of the channel.

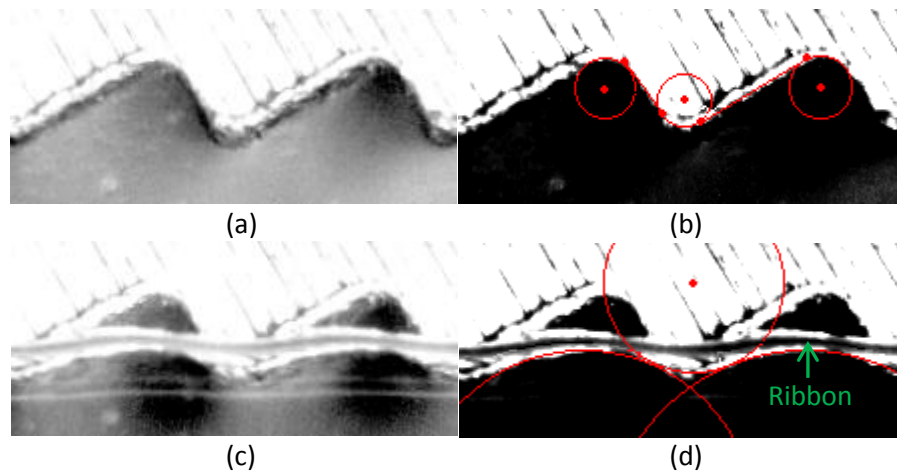


Figure 11.26: Example images of showing the determination of the liquid layer thickness. The four images shown are (a) the ratchet without a bubble present; (b) edge detection defining the ratchet location and geometry; (c) the ratchet with a bubble present; (d) the shape of the bubble near the ratchet surface.

With the radii and respective centers measured, the liquid layer thickness was calculated. Figure 11.27 shows a simplified image of the ratchets and bubble interface for clarity and Eqs. 11.1 and 11.2 show how thicknesses were determined.

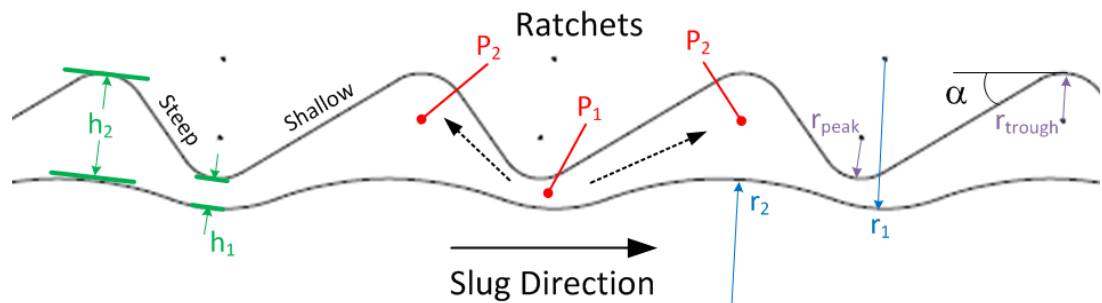


Figure 11.27: Schematic showing ratchet topography and the interface of the bubble. Annotations in green indicate layer thickness; blue indicate bubble radii; red indicate ratchet radii.

The thickness at the peak, h_1 , was determined as

$$h_1 = r_1 - r_{peak} - \sqrt{(x_1 - x_{peak})^2 + (y_1 - y_{peak})^2} \quad (\text{Eq. 11.1})$$

$$h_2 = r_{trough} - r_2 + \sqrt{(x_2 - x_{trough})^2 + (y_2 - y_{trough})^2} \quad (\text{Eq. 11.2})$$

Values of r_1 , r_2 , h_1 , and h_2 varied among the forty-two consecutive frames because, as mentioned before, the slug pulses as it travels along the channel. For the purpose of this analysis, average values over 42 frames are used. As indicated in Fig. 11.26d, r_2 was measured on both sides of the ratchet. After analysis the two measurements were statistically equivalent which confirms the assumption that the interface of the bubble is consistent from ratchet to ratchet. For all frames, r_2 was greater than r_1 . Average values of both are shown in Table 11.2.

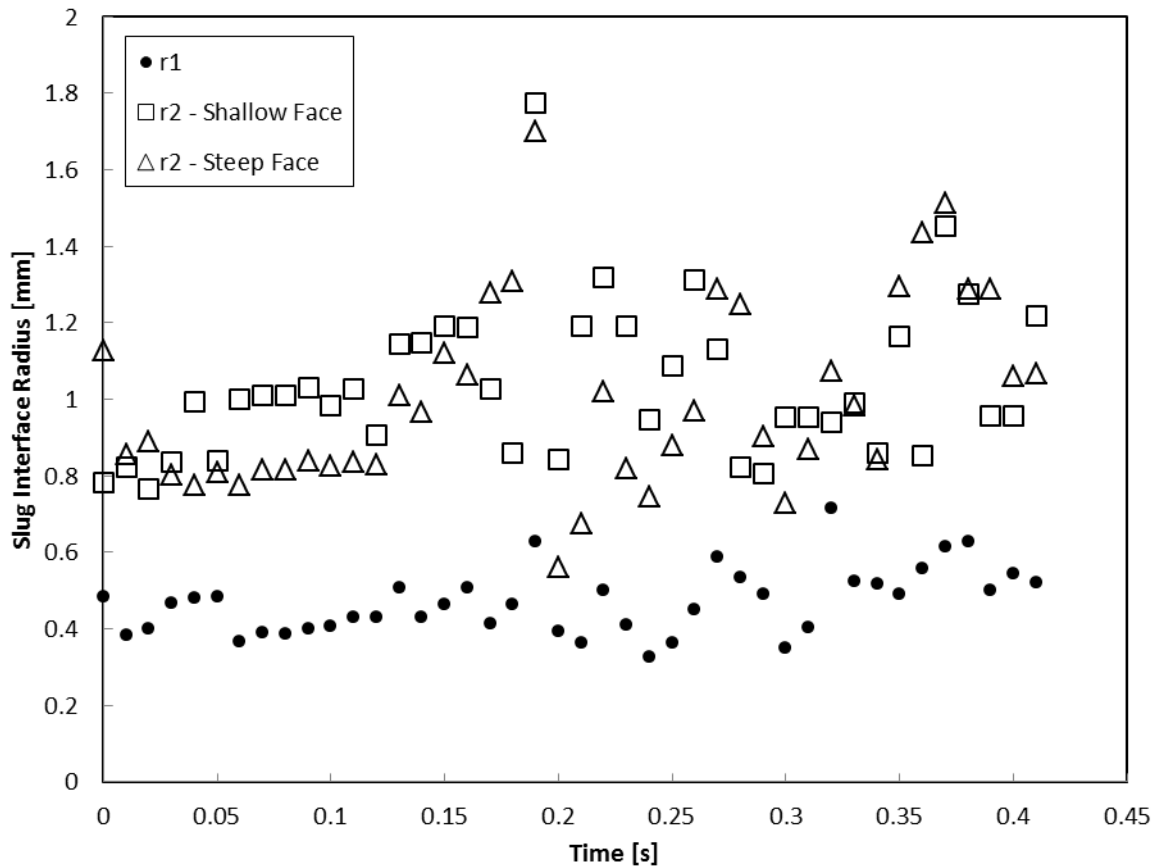


Figure 11.28: Radius measurements of the slug interface for a sequence of 42 consecutive frames.

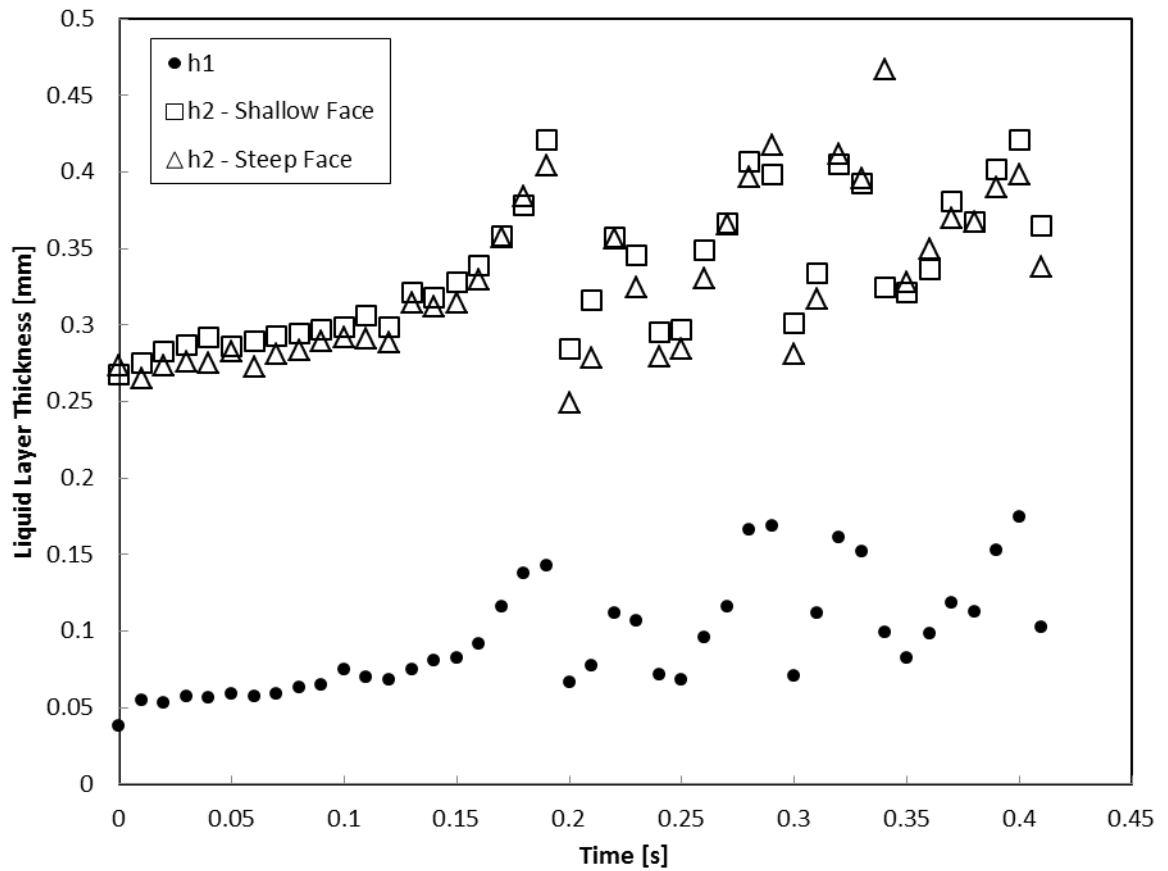


Figure 11.29: Liquid layer thickness between the slug and ratchet calculated for a sequence of 42 consecutive frames.

From the image processing it is seen that r_1 is concave and r_2 is convex. This indicates that the vapor pressure within the bubble at the peak, $P_{1,v}$, is lower than the local liquid pressure, $P_{1,l}$. Conversely, the vapor pressure within the bubble at the trough, $P_{2,v}$, is greater than the local liquid pressure, $P_{2,l}$. The pressure difference between the vapor and liquid at each location is determined using the Young-Laplace equation [11] as shown in Eqs. 11.3 and 11.4. Assuming the vapor pressure is equal throughout the bubble, a pressure difference between the peak and trough on either side of the ratchet is evaluated Eq. 11.5.

$$P_{1,l} - P_{1,v} = \frac{\sigma}{|r_1|} \quad (\text{Eq. 11.3})$$

$$P_{2,l} - P_{2,v} = \frac{\sigma}{|r_2|} \quad (\text{Eq. 11.4})$$

$$P_{1,l} - P_{2,l} = \sigma \left(\frac{1}{r_1} - \frac{1}{r_2} \right) \quad (\text{Eq. 11.5})$$

The shape of the slug interface is simplified such that the liquid layer thickness is constant over the ratchet and equal to the average of h_1 and h_2 . The ratchet shape is also simplified to have right angle corners at the peak and trough. The simplified geometry is shown in Fig. 11.30.

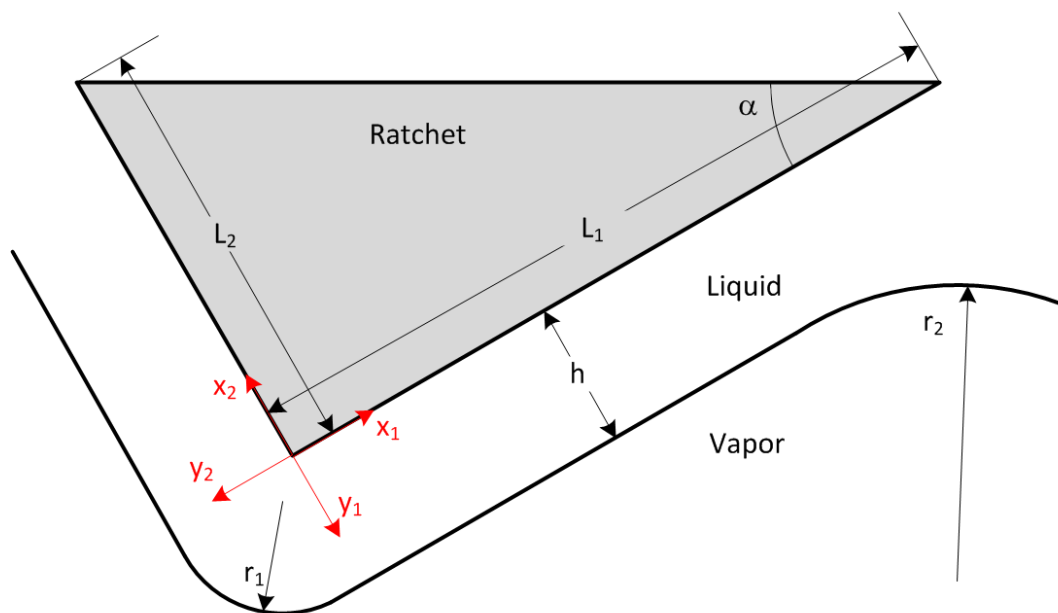


Figure 11.30: Simplified shape of the bubble interface and ratchet profile. Dimensions are shown for clarity.

The liquid layer between the ratchet is subjected to the pressure gradient created by the bubble interface shape. This gradient is used to determine the velocity profile in the liquid layer approximating fully developed Couette-Poiseuille flow along the shallow face of the ratchet. Shear force acting on the bubble is then determined by the shear stress at the liquid vapor interface. The velocity distribution in a fully developed Couette-Poiseuille flow is given by:

$$u(x_1) = \frac{1}{2\mu} \frac{\partial P}{\partial x_1} y^2 + c_1 y + c_2 \quad (\text{Eq. 11.6})$$

where the boundary conditions in terms of dimensions shown in Fig. 11.30 are:

$$u|_{y=0} = 0$$

$$u|_{y=h} = V$$

where V is the velocity of the slug.

After evaluating the constants c_1 and c_2 , the velocity profile in the liquid layer becomes:

$$u(x_1) = -\frac{1}{2\mu} \frac{\partial P}{\partial x_1} (hy - y^2) + \frac{V}{h} y \quad (\text{Eq. 11.7})$$

The shear stress on the on the slug by the liquid layer between the ratchet and slug is:

$$\tau_w = -\tau_{yx}|_{y=h} = -\mu \left. \frac{du}{dy} \right|_{y=h} = -\frac{h}{2} \frac{\partial P}{\partial x_1} - \frac{\mu V}{h} \quad (\text{Eq. 11.8})$$

Integrating the shear stress acting on the slug along the length of the ratchet face provides the total shear force per unit width.

$$\frac{F}{W} = - \int_0^{L_1} \tau_w dx = \left[\frac{\mu V}{h} + \frac{h}{2} \frac{\partial P}{\partial x_1} \right] L_1 \quad (\text{Eq. 11.9})$$

The component of this force acting in the direction of travel of the bubble (horizontal) is therefore:

$$F_{\Delta P1} = \left[\frac{\mu V}{h} + \frac{h}{2} \frac{\partial P}{\partial x_1} \right] L_1 W \cos \alpha \quad (\text{Eq. 11.10})$$

where α is 30° and L_1 is 0.880 mm.

Applying the same analysis to the steep slope of the ratchet using x_2 , y_2 , and L_2 , with the same liquid layer thickness an opposing force to the flow is found. Equation 11.11 shows the sum of the two forces per ratchet as they act on the slug.

$$F_{\Delta P} = \left[\frac{\mu V}{h} + \frac{h}{2} \frac{\partial P}{\partial x_1} \right] L_1 W \cos \alpha - \left[\frac{\mu V}{h} + \frac{h}{2} \frac{\partial P}{\partial x_2} \right] L_2 W \sin \alpha \quad (\text{Eq. 11.11})$$

where W is the width of the bubble interacting with the ratchets.

When applied to the channel configuration tested, $F_{\Delta P}$ must be double, as the slug is in interacting with both vertical walls structured with ratchets. Although the pressure drop from peak to trough is equal both the shallow and steep sides of the ratchet, a greater component of the shallow face force acts in the horizontal direction; thus, causing the slug to move in a preferential direction along the shallow slope of the ratchet.

The width of the bubble (W) interacting with the ratchets is then determined. From the homogeneous flow testing presented in Section 11.1.4, a black region can be seen at the

interface of the bubble (Fig. 11.31a). Due to the short depth of field ($80\ \mu\text{m}$) of the K2/SC lens, this dark region corresponds to the curvature of the bubble; thus, the white region is a flat liquid film in contact with the top wall of the channel. The flat region width is measured in Vision Assistant and is shown as in red in Fig. 11.31b. Assuming that the slug is symmetrical, this flat region is also equal to the region interacting with the ratchets on the side wall. This assumption is reasonable only for the flash testing as only these bubbles are consistent in shape throughout the video. Figure 11.32 is a schematic showing the width of a slug in the channel. This width is equivalent on all sides.

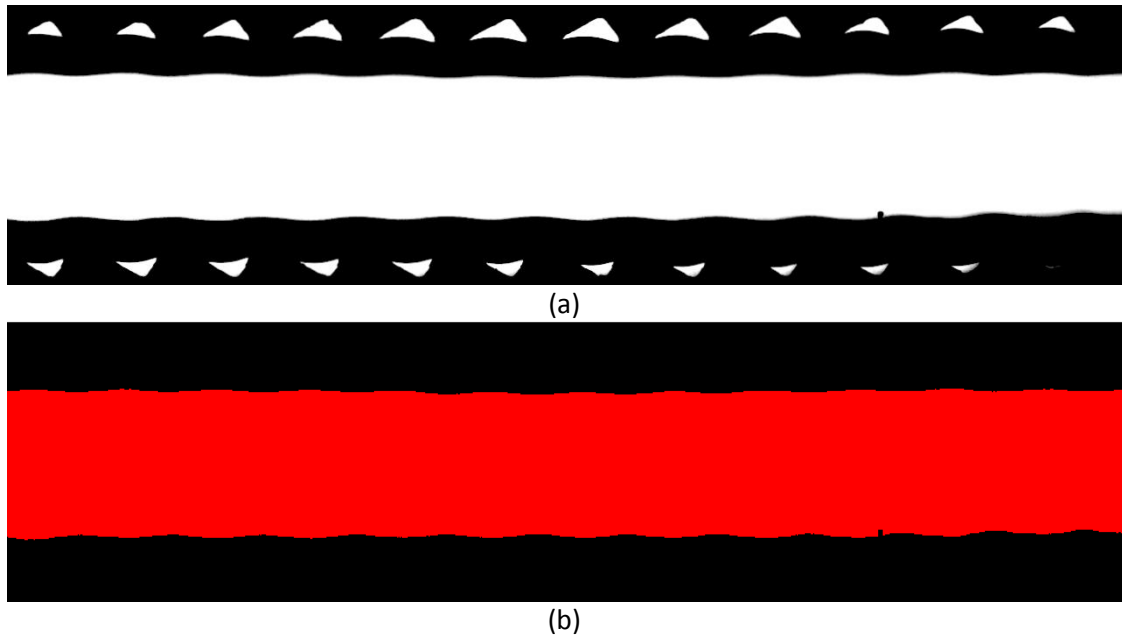


Figure 11.31: Image used to determine the width of slug interacting with the ratchet surface. (a) The raw image is shown. (b) The flat top region separated by a thin liquid layer from the top wall.

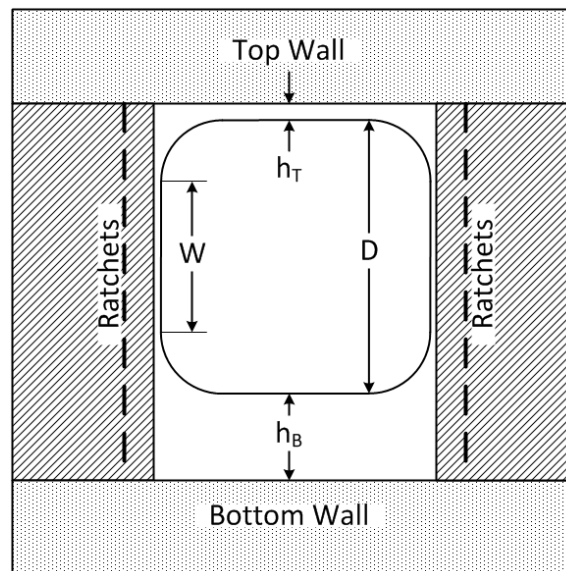


Figure 11.32: Schematic of a slug in the channel. View is looking down the channel. A simplified shape of the slug is shown. Not to scale.

Just as the net shear force in the liquid layer between the ratchet and slug propels the slug, shear force by the liquid layers at the top and bottom walls also opposes the movement of the slug. The opposing shear forces take the form shown in Eq. 11.12.

$$F_S = \mu V \left[\frac{1}{h_T} + \frac{1}{h_B} \right] L_3 W \quad (\text{Eq. 11.12})$$

$$L_3 = L_1 \cos \alpha + L_2 \sin \alpha$$

$$h_B = \text{Channel Height} - D$$

No measurements of the shear layer thickness (h_T , h_B) on the top or bottom wall could be made; therefore, an estimate is made for h_B based on the dimensions shown in Fig. 11.32 and h_T is unknown.

By setting the driving shear force (Eq. 11.11) equal to the opposing shear force (Eq. 11.12) an expression for equilibrium velocity is derived.

$$2 \left[\frac{\mu V}{h} + \frac{h}{2} \frac{\partial P}{\partial x_1} \right] L_1 \cos \alpha - 2 \left[\frac{\mu V}{h} + \frac{h}{2} \frac{\partial P}{\partial x_2} \right] L_2 \sin \alpha - \mu V \left[\frac{1}{h_T} + \frac{1}{h_B} \right] L_3 = 0 \quad (\text{Eq. 11.13})$$

Because the assumption was made that W is equal on all sides of the slug, it is no longer necessary for the analysis. The experimentally determined homogeneous flow regime results presented earlier yielded an average velocity for the slug of $61.4 \text{ mm}^1\text{s}^{-1}$. With the values summarized in Table 11.2 below, and h_T varying from 0-20 μm , velocity predictions are calculated for the slug.

Table 11.2: Variables used in predicting slug velocity. Not all variables are used in the final form of the equation, but are necessary in determining others.

Symbol	Value	Unit	Symbol	Value	Unit
μ	6.44×10^{-4}	$\text{N}^1 \text{s}^1 \text{m}^{-2}$	h_1	0.090	mm
σ	1.07×10^{-2}	$\text{N}^1 \text{m}^{-1}$	h_2	0.332	mm
ρ	1678.8	$\text{kg}^1 \text{m}^{-3}$	h	0.211	mm
L_1	0.880	mm	h_T	0-50	μm
L_2	0.508	mm	h_B	3.25	mm
L_3	1.02	mm	r_1	0.469	mm
α	30	$^\circ$	r_2	1.018	mm
W	1.59	mm	r_{peak}	0.128	mm
D	2.25	mm	r_{trough}	0.145	mm

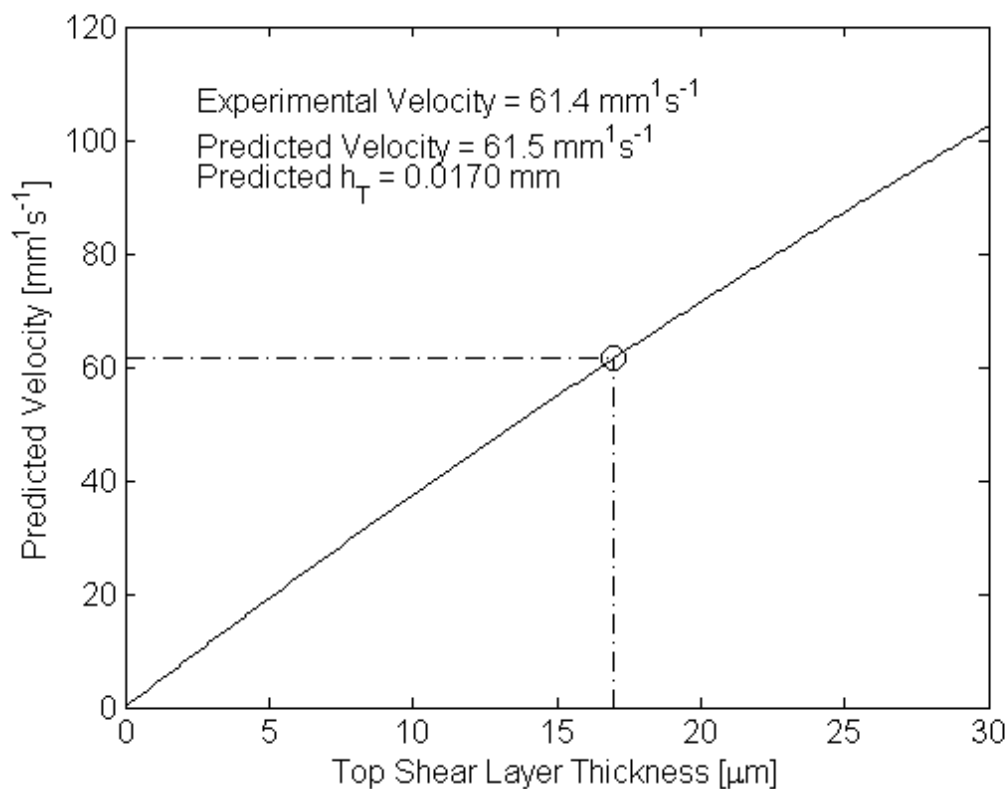


Figure 11.33: Plot of predicted velocity values for a range of top shear layer, h_T .

By matching the experimentally determined velocity with the predicted velocity, a predicted top shear layer thickness is determined to be $17 \mu\text{m}$. Now it is possible to vary the liquid layer thickness between the ratchet and slug. Predicted velocities are plotted as a function of liquid layer thickness illustrating its sensitivity. Liquid layer thickness is varied from 0.090 mm (h_1) to 0.332 mm (h_2) which corresponds to the minimum and maximum values measured, respectively.

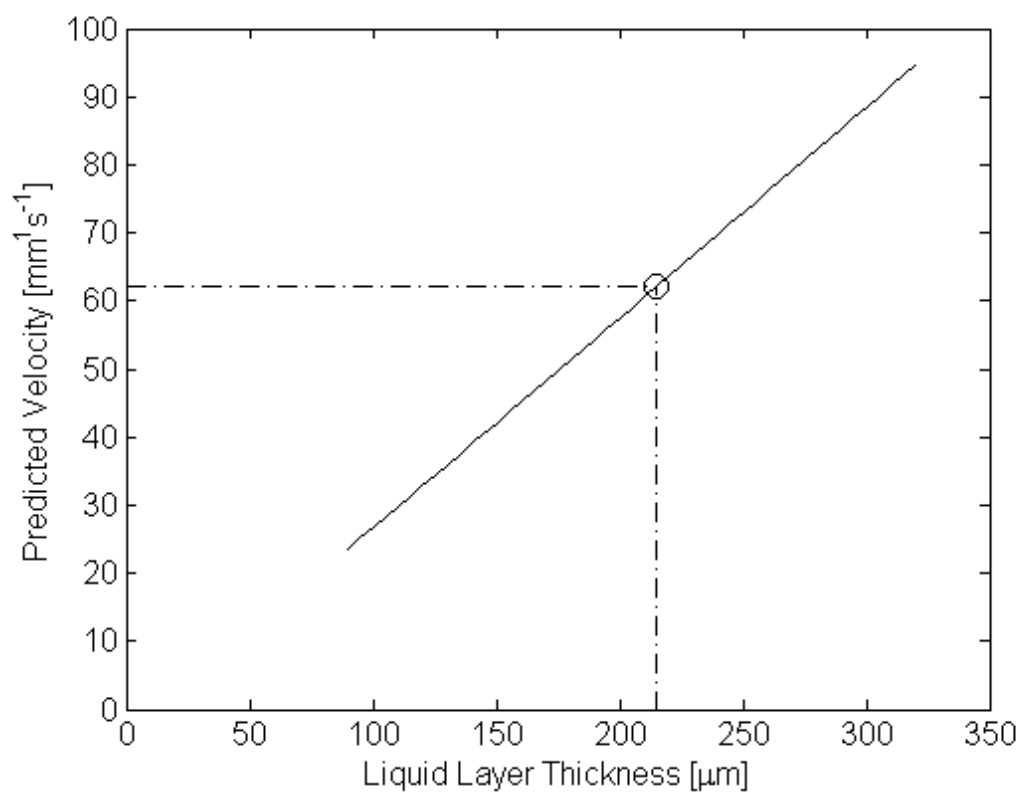


Figure 11.34: Plot of predicted slug velocity as a function of varying liquid layer thickness between the slug and ratchet. Liquid layer thickness, h , is varied from 0.090 mm to 0.332 mm.

12. CONCLUSIONS

The conclusions are divided into two sections—one for each part of this thesis.

12.1. Adiabatic Single-Bubble

The adiabatic single-bubble experiment was designed to confirm lateral fluid motion caused from bubble growth at the surface and to determine the extent of its influence. By growing bubbles from the surface with gas (nitrogen) injection rather than boiling, PTV could be easily performed.

The bubble growth force model results presented in Chapter 7.2 show that the rate of change in height of a bubble used influences the surrounding liquid by imparting momentum and accelerating the liquid. Because the bubble emanates from an asymmetric surface, preferential growth of the bubble occurs at an angle from vertical; hence, also accelerating the liquid in a preferred direction.

Particle tracking velocimetry incorporated into the experiment provided an accurate means of determining liquid velocities in the field of view of the camera. By restricting this field of view with a region of interest in the PTV algorithm, velocities directly above the single bubble were tracked. Varying the region of interest for the PTV algorithm directly related to the area of influence of a bubble, as the region of influence width was equal to multiples of the average bubble diameter of the single bubble.

The bubble growth force model was validated against PTV data by comparing predicted velocities made by the model and velocities measured the PTV for corresponding areas of influence and regions of interest. It was found that the correct region of interest was one average bubble diameter wide; thus, the area of influence of a bubble growing asymmetrically from the surface was equal to the projected area of a bubble with an average diameter. Resultant liquid velocities from the PTV results presented were determined to be $41.33 \text{ mm}^1\text{s}^{-1}$ in the x-direction, $62.57 \text{ mm}^1\text{s}^{-1}$ in the y-direction, and a total of $74.98 \text{ mm}^1\text{s}^{-1}$ at

32.68° from the vertical. The semi-empirical model with the determined area of influence predicted velocities with 7.79%, 9.68% and 6.98% deviation from the PTV results.

12.2. Open Channel Pump

The open channel pump was designed to prove that lateral motion could be applied as an innovative way to pump fluid passively with bubble motion. Asymmetric structures were incorporated into the vertical walls of a square channel with the ability to boil the fluid within diabatically or homogeneously.

The channel produced vapor slugs that traveled through the channel in the preferential direction (away from the shallow sloping faces of the ratchet structure). Four distinct regimes of flow were observed in the channel and vapor slugs were observed to move through the channel at velocities ranging from 13.4 mm¹s⁻¹ 96.3 mm¹s⁻¹.

Based on work done by Linke [6] on self-propelled Leidenfrost liquid droplets, a new model was proposed that was capable of predicting slug velocity. This new model postulates that a the asymmetric surface creates a pressure gradient in the thin liquid layer separating the slug from the solid surface which causes liquid motion in the preferential direction as in Couette-Poiseuille flow. The viscous shear force in the liquid layer then propels the vapor slug along the channel. Viscous drag from the top and bottom walls was assumed to oppose the motion of the bubble; however, the shear layer thicknesses could not be measured on either surface. Therefore, the bottom shear layer thickness was estimated based on channel geometry and top shear layer thickness was calculated.

13. Recommendations for Future Investigation

Recommendations for future investigation are divided into two sections—one for each part of this thesis.

13.1. Adiabatic Single-Bubble

Future investigation regarding the adiabatic single bubble experiments mainly includes increasing the scope of the experiment. All data presented in this thesis was collected using a single injection port size with nitrogen as the injected gas. The semi-empirical model could be further validated by testing smaller and larger port sizes as well as changing the working gas to ammonia to simulate bubble collapse within the liquid. Furthermore, adding additional injection ports on adjacent ratchets would expand the experiment from single to multiple bubbles.

13.2. Open Channel Pump

The open channel pump shows great promise as a passively driven pump in applications such as thermal management in spacecraft and zero-gravity environments. For the channel pump to reach a stage to where it could be applied effectively, more investigation needs to be done.

First, the model for vapor slug movement needs strengthening. High-speed visualization with forward lighting implemented into the experiment would improve the images of the liquid layer between the vapor slug and structured surface for future tests. A high power lens ring light would supply front lighting through the prism in the current experimental facility; however, commercially available ring lights fall short of supplying enough light for the camera and lens combination. Furthermore, imaging lengthwise down the channel during flash tests would allow for measurements of the shear layers on the top and bottom surfaces to develop accurate viscous drag.

Modifications of the surface geometry should also be done to determine the limits of the asymmetry and its effectiveness of propelling vapor. As the slug velocity is partially opposed by the pressure differential on the steep side of the ratchet, the first modification should be changing the steep slope to vertical; theoretically eliminating any reverse flow in the liquid layer. Backflow in the channel could also be prevented by incorporating an orifice at the entrance.

A second generation channel pump should be redesigned and fabricated such that it could be incorporated into a closed loop system as a passive pump. This closed loop would simulate removing heat from a small electronic device. Such a closed loop experimental setup could quantify the pumping power and confirm its potential as a passive pumping device. This closed loop should be designed with micro-gravity testing in mind. The physical size should be small enough that it can be tested in a drop tower. Furthermore, the closed loop should be designed such that it could meet NASA's Reduced Gravity Program requirements for potential zero-gravity flights.

REFERENCES

- [1] Mukherjee S., Mudawar I., "Smart Pumpless Loop for Micro-Channel Electronic Cooling Using Flat and Enhanced Surfaces", *IEEE Transaction on Components and Packaging Technologies*, Vol. 26, No. 1, March 2003.
- [2] Kuo S., Shih C., Chang C., Chen S., "Bubble pump in a closed-loop system for electronic cooling", *Applied Thermal Engineering* 51 (2013), pp. 425-434.
- [3] Torniainen E. D., Govyadinov A. N., Markel D. P., Kornilovitch P. E., "Bubble-driven inertial micropump", *Physics of Fluids* 24, 2012, p. 122003.
- [4] Yin Z., Prosperetti A., "'Blinking bubble' micropump with microfabricated heaters", *Journal of Micromechanics and Microengineering* 15 (2005), pp. 1683-1691.
- [5] Incropera F. P., Dewitt D. P., Bergman T. L., Lavine A. S., "Fundamentals of Heat and Mass Transfer". John Wiley & Sons, Hoboken, NJ. 2007, p. 624
- [6] Linke H., Alemán B. J., Melling L. D., Taormina M. J., Francis M. J., Dow-Hygelund C. C., Narayanan V., Taylor R. P., and Stout A., "Self-Propelled Leidenfrost Droplets." *Physical Review Letters*. 96 (15), p. 154502.
- [7] Kapsenberg, F., Thiagarajan, N., Narayanan, V., Bhavnani, S.H., "Lateral Motion of Bubbles from Surfaces with Mini Ratchet Topography Modifications During Pool Boiling – Experiments and Preliminary Model", *Proceedings of 13th IEEE Intersociety Conference on Thermal and Thermomechanical Phenomena in Electronic Systems*, San Diego, CA, May 2012.
- [8] Kapsenberg, F., "Lateral Fluid Motion in Nucleate Boiling through Asymmetric Surface Structures", Thesis. Oregon State University, 2011.
- [9] Thiagarajan N., Kapsenberg F., Narayanan V., Bhavnani S. H., Ellis C. D., "Development of a Heat Sink With Periodic Asymmetric Structures Using Grayscale Lithography and Deep Reactive Ion Etching". *IEEE Electron Device Letters*, Vol. 33, No. 7, July 2012, pp. 1054-1056.
- [10] Thiagarajan N., "Investigation of Thermally-Actuated Pumping During Pool Boiling of a Dielectric Liquid on an Asymmetric Microstructured Silicon Heat Sink", Thesis. Auburn University, 2013.

- [11] Carey, Van P. "Liquid-vapor Phase-change Phenomena: An Introduction to the Thermophysics of Vaporization and Condensation Processes in Heat Transfer Equipment". Second ed., New York: Taylor and Francis, 2008.
- [12] ULTEM™ Resin 1000. SABIC Innovative Plastics Holding, 2013. PDF.
- [13] Freire, A. S., and Mikhail M., "Sphere Drag", Wolfram|Alpha, 1 Aug. 2010. Web. 20 Aug. 2013.
- [14] "Model K2/SC Long-Distance Microscope System", Product Manual. Infinity Photo-Optical Company, 2009.

APPENDICES

Appendix A. Preparing Cospheric Microspheres

Preparing Tween Solution

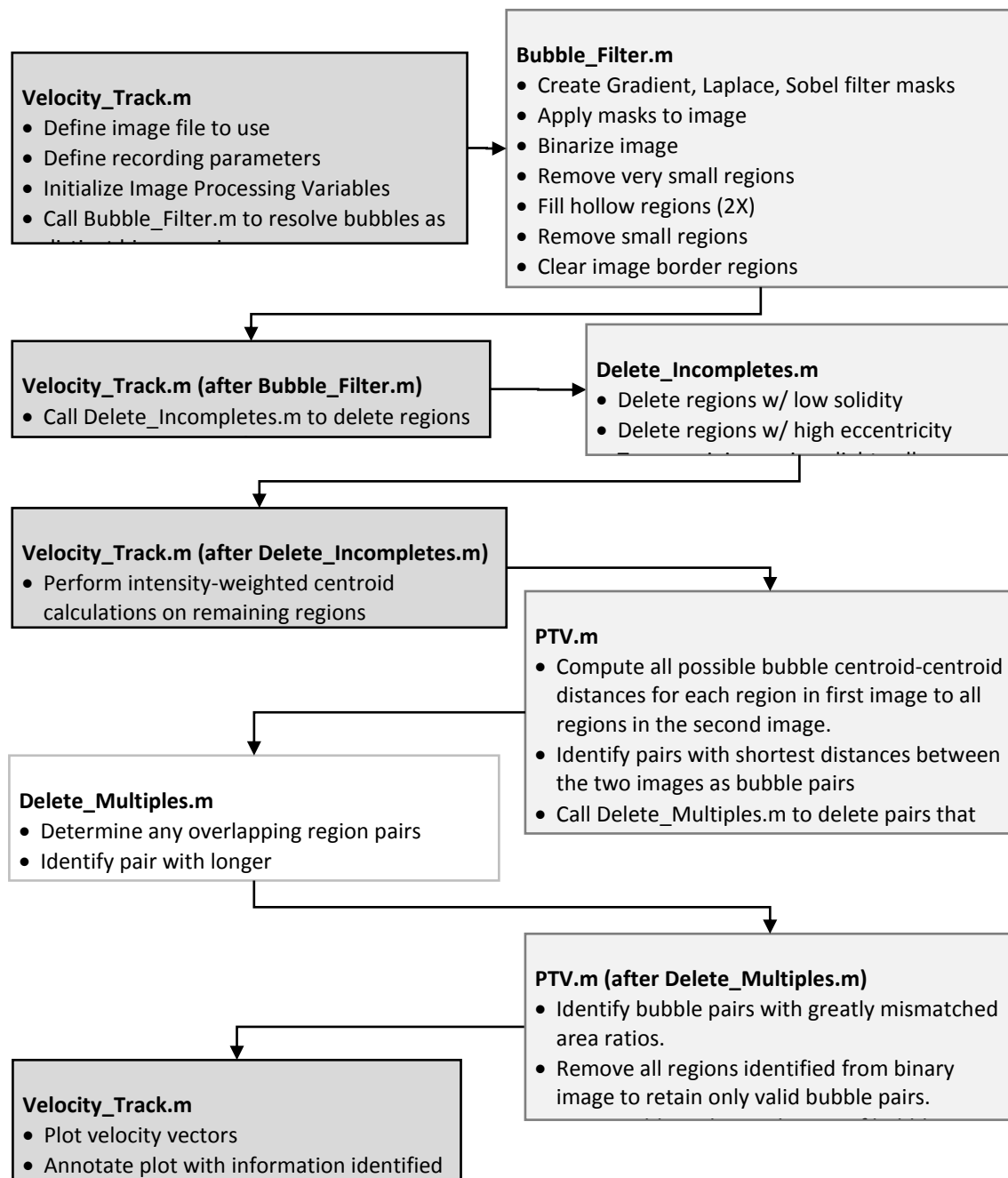
- Prepare a hot bath of tap water on a hotplate at a bath temperature of approximately 80 °C (176 °F)
- Into a clean jar, dispense 0.10g (0.0035 oz.) of Tween 80 with a pipette or syringe
- Add 99.90g (3.52 oz.) of deionized water to the jar for a total of 100g (3.53 oz.) of solution. The resulting solution is 0.1% Tween 80 by mass.
- Secure the jar lid.
- Holding it with either tongs or gloves, submerge the jar into the hot bath to a level where the two water lines approximately match. Hold in the water bath for 20-30 seconds.
- Remove the jar and gently swirl in a circular motion as to mix the solution.
- Repeat submersion and swirling process several times for 5-10 minutes until the no filaments of Tween 80 can be seen in the solution.
- Leave the solution to cool overnight

Suspending the Particles

- In a 1 dram vial, deposit 0.5g (0.018 oz.) of the microspheres (Product ID: WPMS-1.00 53-63um)
- Dispense 8 mL (0.27 oz.) of the 0.1% Tween80 solution using a pipette or syringe to create a 6.25% mixture of particles by mass. It is important to add the Tween solution to the spheres, not the spheres to the solution as the particles are hydrophobic and will remain floating on the surface, otherwise.
- Secure the cap to the vial and agitate the solution. Soap bubbles will be made.
- Label the solution and allow the particles to become wetted for 1-2 days.
- If the particles are not fully wetted after 2 days, shake the vial again and wait until the soap bubbles to disperse before using the solution.
- This solution can now be diluted to any desired concentration.

Appendix B. Bubble Tracking Algorithm

Courtesy of Florian Kapsenberg[8].



Appendix C. Inconel Heater Resistance

The following calculations are shown to demonstrate the sensitivity of the resistance of the Inconel 600 heaters made for the open-channel pump.

$$R = \rho \frac{l}{t \cdot W} \quad (\text{Eq. C.1})$$

$$\frac{\partial R}{\partial l} = \frac{\rho}{t \cdot W} \quad (\text{Eq. C.2})$$

$$\frac{\partial R}{\partial t} = -\frac{\rho \cdot l}{W} t^{-2} \quad (\text{Eq. C.3})$$

$$\frac{\partial R}{\partial W} = -\frac{\rho \cdot l}{t} W^{-2} \quad (\text{Eq. C.4})$$

$$\rho = 1.03 \mu\Omega \cdot m; \quad l = 152.75 \text{ mm}; \quad t = 25.4 \mu m; \quad W = 500 \mu m$$

The table below applies a 1 μm (2.54×10^{-5} in.) decrease in thickness, width, and length and shows the resulting change in resistance.

Table C.1: Change in resistance due to a 1 μm (2.54×10^{-5} in.) change in each heater dimension.

Dimension	ΔR [Ω]
Length	-0.0001
Thickness	0.4877
Width	0.0248

Appendix D. FC-72 Properties

Courtesy of 3M via electronic mail.

$$\mu = 1 \times 10^{-6} [(-2.6238 \times 10^4)T^2 + (7.0786 \times 10^{-2})T + 7.7884] \quad (\text{Eq. D.1})$$

$$\mu = [N \cdot s \cdot m^{-2}] \quad ; \quad T = [^{\circ}C]$$

Table D.2: Selected saturated data for FC-72.

T	P	T	P
[K]	[bar]	[K]	[bar]
250	0.018	302	0.358
252	0.021	304	0.389
254	0.025	306	0.422
256	0.028	308	0.458
258	0.033	310	0.496
260	0.038	312	0.536
262	0.043	314	0.579
264	0.049	316	0.624
266	0.056	318	0.672
268	0.063	320	0.723
270	0.071	322	0.777
272	0.080	324	0.833
274	0.090	326	0.893
276	0.101	328	0.956
278	0.113	330	1.023
280	0.126	332	1.093
282	0.140	334	1.166
284	0.155	336	1.243
286	0.171	338	1.324
288	0.189	340	1.410
290	0.208	342	1.499
292	0.229	344	1.592
294	0.251	346	1.691
296	0.275	348	1.793
298	0.301	350	1.901
300	0.328	352	2.013

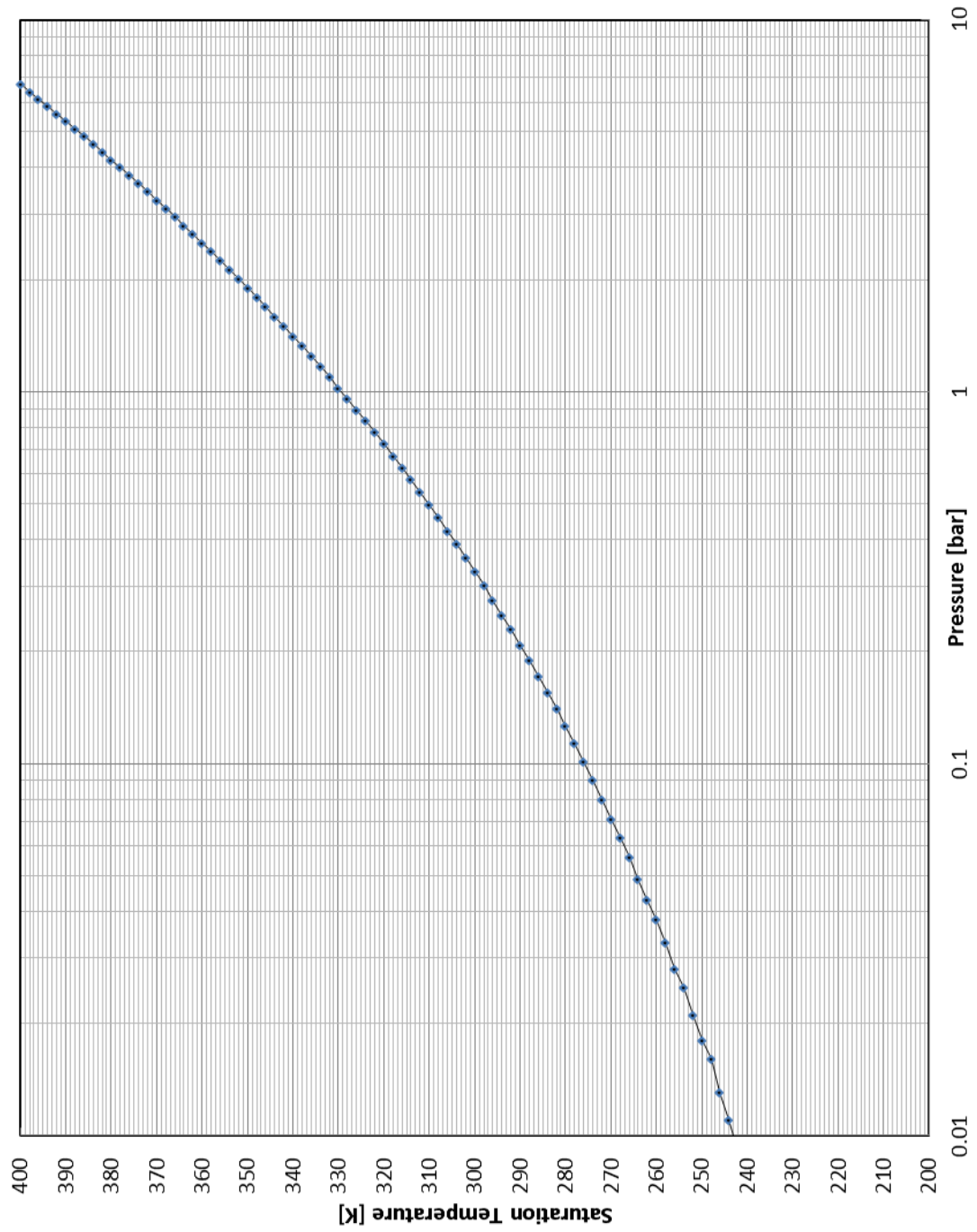


Figure D.1: Plot of FC-72 saturation temperature with respect to pressure.

